

ABSTRACT

COX, JR., WILLIAM CHARLES. Simulation, Modeling, and Design of Underwater Optical Communication Systems. (Under the direction of John Muth.)

Underwater free-space optical communications has the potential to provide high speed, low latency communications for undersea vehicles and sensors. This thesis describes the design and validation of a Monte Carlo numerical simulation tool for underwater optical communications systems. The simulation tool can also be used more generally for other systems that require calculations of the underwater light-field. The program, named Photonator, was validated experimentally in a laboratory tank where the absorption and scattering was controlled by the addition of Maalox to vary the water conditions from open ocean to turbid harbor water. These results were also compared with custom blue/green light emitting diode and laser transmitters and receivers that allowed the wavelength and field-of-view (FOV) to be controlled.

An emphasis was placed on understanding the requirements of point-to-point underwater communication links. Results are presented for on and off-axis received power for a series of receiver apertures and fields-of-view. Also presented are the scattering histograms at the receiver and the temporal bandwidth of each communication link. A two-term exponential power loss model is developed and compared with the simulated outputs to agreement within 30% over twelve orders of magnitude power loss. This type of power loss model is useful in constructing link budgets which are more accurate than the usual Beer's law assumption in water environments where scattering is appreciable.

Several results are presented that are of interest to the underwater optical systems designer:

1. The simulations and experiments show that the power gain from FOV and aperture changes of an optical system are independent in highly turbid waters.
2. A power-law relationship between FOV and received power is shown for turbid water environments for fields-of-view up to 45 degrees.
3. A systematic series of simulations show how the scattering orders at the receiver evolve as water quality is varied which provides a physical underpinning to understanding temporal dispersion of underwater pulses.
4. A systematic series of simulations shows how the temporal bandwidth of underwater optical communication systems varies strongly with the receiver field of view, but weakly with aperture size.

© Copyright 2012 by William Charles Cox, Jr.

All Rights Reserved

Simulation, Modeling, and Design of Underwater Optical Communication Systems

by
William Charles Cox, Jr.

A dissertation submitted to the Graduate Faculty of
North Carolina State University
in partial fulfillment of the
requirements for the Degree of
Doctor of Philosophy

Electrical Engineering

Raleigh, North Carolina

2012

APPROVED BY:

Edward Grant

Brian Hughes

C. Russell Philbrick

John Muth
Chair of Advisory Committee

DEDICATION

To Jamie, my Anne “with an ‘e’”.

BIOGRAPHY

William Cox is a North Carolina native, and a life-long engineer. His BS and MS degrees were obtained from NC State University in Electrical Engineering, with a focus on mechatronics and robotics. After graduating with a PhD in Electrical Engineering, with a focus on underwater optical communications, he will continue to live and work in North Carolina with his wife and children.

ACKNOWLEDGEMENTS

Thanks to ...

Mike Faircloth for constantly demanding I get a PhD.

Kory Gray, Brandon Cochenour, and Chris Altman for their encouragement, help, and input along the way.

Alan Laux, Alan Weidemann, Norm Farr, and Edouard Berrocal for their help with discussion and data to compare against.

Jim Simpson, I couldn't have done it without you. Truly.

My family for being patient with their perpetual student.

My advisor, John Muth. Your laid-back attitude helped me not to worry.

My son Charlie, Daddy will be home more now.

My wife Jamie, your love was never-ending. Who else would make me lunch and dinner to take to the lab day-in and day-out for all those years?

The Alpha and Omega, God only wise. Soli Deo Gloria.

TABLE OF CONTENTS

| | |
|--|-------------|
| List of Tables | viii |
| List of Figures | ix |
| Chapter 1 Introduction | 1 |
| Chapter 2 Overview of the State-of-the Art | 3 |
| 2.0.1 Freespace Optical Communication | 3 |
| 2.0.2 Underwater Freespace Optical Communication | 4 |
| 2.0.3 Monte Carlo Model of Terrestrial Light Transportation | 5 |
| 2.0.4 Monte Carlo Modeling of Light Underwater | 7 |
| 2.1 Conclusion | 7 |
| Chapter 3 Light Underwater | 8 |
| 3.1 Characterizing Light in Water | 8 |
| 3.2 Absorption | 10 |
| 3.3 Scattering | 10 |
| 3.4 Analytical Models | 11 |
| 3.5 Full System View of Light Reception | 13 |
| 3.5.1 Radiative Transfer Equation | 13 |
| 3.5.2 The Diffusion Length | 14 |
| 3.6 Conclusion | 15 |
| Chapter 4 Simulation of the Underwater Lightfield | 17 |
| 4.1 Overview of Monte Carlo Numerical Simulation | 17 |
| 4.2 Simulation Assumptions and Approximations | 18 |
| 4.3 Mechanics of the Photonator Simulation | 19 |
| 4.3.1 Initial Conditions | 19 |
| 4.3.2 Photon Propagation | 23 |
| 4.3.3 Moving the photons | 28 |
| 4.3.4 Photon Reception | 29 |
| 4.3.5 Determining Accuracy of the Simulation Output | 32 |
| 4.3.6 On-line Computation of Mean and Variance Statistics | 34 |
| 4.4 Determining Channel Bandwidth from Simulation | 36 |
| 4.5 Validating the Simulation Model | 40 |
| 4.5.1 Validation Against Mie Scattering from Fixed-Size Polystyrene Spheres | 40 |
| 4.5.2 Validation Against Off-Axis Power Measurements with Maalox as the Scattering Agent | 49 |
| 4.5.3 Validation Against Experimental Measurement of On-Axis Power vs. Water Turbidity | 49 |
| 4.5.4 Concluding the Validation | 60 |
| 4.6 Conclusion | 60 |

| | |
|---|------------|
| Chapter 5 Simulating Various Scenarios for Underwater Optical Communication | 62 |
| 5.1 Partitioning the Simulation Variable Space | 62 |
| 5.1.1 Receiver Aperture and Field of View | 64 |
| 5.2 Source Effects | 65 |
| 5.2.1 Transmitter/Receiver Misalignment | 65 |
| 5.2.2 Initial Conditions | 66 |
| 5.3 Geometric Loss | 68 |
| 5.4 Harbor Water - Absolute Received Power Versus Distance | 68 |
| 5.4.1 Geometric Loss in the Simulation | 70 |
| 5.4.2 Harbor I-type Water Power Loss | 71 |
| 5.4.3 Harbor II-type Water Power Loss | 72 |
| 5.4.4 Harbor III-type water power loss | 72 |
| 5.4.5 Average Power Loss for Harbor Waters | 73 |
| 5.4.6 Received power versus FOV for various Harbor water types | 73 |
| 5.4.7 Received power, normalized by receiver area versus FOV for various Harbor water types | 74 |
| 5.4.8 Figures | 75 |
| 5.5 Coastal Water - Absolute Received Power versus Distance | 110 |
| 5.6 Clear Water - Absolute Received Power versus Distance | 110 |
| 5.7 Clear and Coastal Water Received Power Figures | 111 |
| 5.8 Harbor Water - Scattering Orders at the Receiver | 121 |
| 5.8.1 Unnormalized Histogram of Scattering Orders | 122 |
| 5.8.2 Normalized Histogram of Scattering Orders | 124 |
| 5.8.3 Scattering Order Probability Versus Water Type | 124 |
| 5.8.4 Harbor Water Scattering Orders Figures | 125 |
| 5.9 Temporal Response | 138 |
| 5.9.1 Frequency Response of Harbor Water | 138 |
| 5.9.2 Temporal Response of Harbor Water Figures | 138 |
| 5.10 Received Power Versus Misalignment of Receiver/Transmitter | 149 |
| 5.10.1 Computing the Distance Misalignment Power | 149 |
| 5.10.2 Misalignment Effects in Harbor Waters | 150 |
| 5.10.3 Misalignment Result Figures | 155 |
| 5.11 Conclusion | 170 |
| 5.11.1 Received Power Conclusion | 170 |
| 5.11.2 Scattering Orders Conclusion | 171 |
| 5.11.3 Temporal Dispersion Conclusion | 172 |
| 5.11.4 Received Power with Receiver Offset Conclusion | 172 |
| Chapter 6 Link Equation for Underwater Optical Communication | 174 |
| 6.1 Received Power | 174 |
| 6.1.1 Diffuse Point Source | 175 |
| 6.1.2 Generalized Lambertian Source | 176 |
| 6.1.3 Gaussian Beam Received Power | 177 |
| 6.1.4 Channel loss | 178 |
| 6.1.5 Ocean water measurements for channel loss | 179 |

| | | |
|-----------------------------|---|------------|
| 6.2 | Receiver Noise | 183 |
| 6.2.1 | Environmental Optical Background Noise | 183 |
| 6.2.2 | Electrical Noise | 185 |
| 6.3 | Signal to Noise Ratio | 186 |
| 6.4 | Modeling Channel Loss | 187 |
| 6.4.1 | Modified b value | 188 |
| 6.4.2 | Defining turbid water loss | 190 |
| 6.4.3 | Model examples | 191 |
| 6.5 | Design Considerations | 194 |
| 6.5.1 | Transmitter Considerations | 194 |
| 6.5.2 | Receiver Considerations | 195 |
| 6.5.3 | Overall Design Considerations | 195 |
| 6.6 | Comparing Various System Performance | 196 |
| 6.7 | Experimental Systems | 198 |
| 6.7.1 | Polarization Modulation using Diode Lasers | 199 |
| 6.7.2 | Using a Modulating Retroreflector for Underwater Optical Communications | 204 |
| 6.7.3 | Using GNURadio and LEDs for Underwater Optical Communication | 215 |
| 6.8 | Conclusion | 220 |
| Chapter 7 | Conclusion and Future Work | 222 |
| 7.1 | Future Work | 223 |
| 7.2 | Conclusion | 224 |
| References | 226 | |
| Appendices | 233 | |
| Appendix A | Errata and Changes | 234 |
| Appendix B | Photonator MCNS Source Code | 235 |

LIST OF TABLES

| | | |
|-----------|--|-----|
| Table 3.1 | Albedo, average cosine for Petzold water types | 15 |
| Table 5.1 | General water types based on measured data. | 63 |
| Table 5.2 | Three different types of Harbor water. | 63 |
| Table 5.3 | List of simulated field-of-view parameters. | 64 |
| Table 5.4 | List of simulated aperture parameters. | 64 |
| Table 5.5 | -3 dB offset distances and angles for various water types at 20 attenuation lengths for a 2 inch aperture with 4 deg. FOV. | 154 |
| Table 6.1 | MAPE values for simulation and model comparison. | 191 |
| Table 6.2 | Table comparing simulation parameters for various detector types | 196 |
| Table 6.3 | Table comparing simulation parameters that are the same for the various detectors | 196 |
| Table 6.4 | Background light constants | 196 |
| Table 6.5 | System parameters for the modulating retroreflector system. | 205 |

LIST OF FIGURES

| | | |
|-------------|---|----|
| Figure 2.1 | Scattering phase functions of various materials..... | 6 |
| Figure 3.1 | Geometry of the inherent optical properties of water | 9 |
| Figure 3.2 | Comparison of various phase functions | 12 |
| Figure 4.1 | MCNS flowchart for the transmitter..... | 20 |
| Figure 4.2 | MCNS flowchart for the receiver..... | 21 |
| Figure 4.3 | Illustration of direction cosines | 21 |
| Figure 4.4 | Photon propagation illustrated. Each successive scattering event causes the trajectory to rotate its local coordinate frame by θ, ϕ , while the global position is updated in reference to the (0,0,0) coordinate. | 24 |
| Figure 4.5 | Illustration showing how the weight is reduced at each optical event. | 25 |
| Figure 4.6 | Illustration showing how the power is integrated over an offset aperture | 31 |
| Figure 4.7 | Illustration showing multiple scattering and temporal dispersion. | 37 |
| Figure 4.8 | Frequency response of various windowing functions..... | 38 |
| Figure 4.9 | 25 attenuation length impulse response. | 39 |
| Figure 4.10 | Experimental on-axis beam profile. | 40 |
| Figure 4.11 | Simulation geometry for the simulations of fixed-size polystyrene spheres ... | 41 |
| Figure 4.12 | Scattering phase function for 1 μm polystyrene spheres suspended in water.. | 42 |
| Figure 4.13 | Photonator compared to published data at an optical depth of 2 - front | 43 |
| Figure 4.14 | Photonator compared to published data at an optical depth of 2 - side | 44 |
| Figure 4.15 | Photonator compared to published data at an optical depth of 5 - front | 45 |
| Figure 4.16 | Photonator compared to published data at an optical depth of 5 - side | 46 |
| Figure 4.17 | Photonator compared to published data at an optical depth of 10 - front..... | 47 |
| Figure 4.18 | Photonator compared to published data at an optical depth of 10 - side | 48 |
| Figure 4.19 | Exp. vs. Sim. for offset power. Normalized to highest power..... | 50 |
| Figure 4.20 | Exp. vs. Sim. for offset power. | 51 |
| Figure 4.21 | Block diagram of experiment in laboratory water tank..... | 52 |
| Figure 4.22 | Gain vs. control voltage for the H6780-20 PMT used in the experiment..... | 53 |
| Figure 4.23 | PMT signal gain vs. control voltage | 54 |
| Figure 4.24 | Experimentally measured optical power v. turbidity of water | 54 |
| Figure 4.25 | Adjusted optical transmitted power | 55 |
| Figure 4.26 | Measured receiver FOV | 57 |
| Figure 4.27 | The CDF of several VSFs are plotted | 58 |
| Figure 4.28 | Experimental data (red) versus several simulations and Beer's Law..... | 59 |
| Figure 5.1 | Petzold VSFs | 63 |
| Figure 5.2 | Offset geometry for receiver/transmitter misalignment | 65 |
| Figure 5.3 | Gaussian beam diverged illustration | 67 |
| Figure 5.4 | Gaussian beam geometric power loss | 69 |
| Figure 5.5 | Results of Fig. 5.4 plotted with a logarithmic y-axis. | 70 |
| Figure 5.6 | Geometric loss from Gaussian beam spreading | 71 |
| Figure 5.7 | Harbor I - 8mm aperture received | 76 |

| | | |
|-------------|--|-----|
| Figure 5.8 | Harbor I - 1 inch aperture received normalized power. | 77 |
| Figure 5.9 | Harbor I - 2 inch aperture received normalized power. | 78 |
| Figure 5.10 | Harbor I - 3 inch aperture received normalized power. | 79 |
| Figure 5.11 | Harbor I - 4 inch aperture received normalized power. | 80 |
| Figure 5.12 | Harbor II - 8mm aperture normalized power. | 81 |
| Figure 5.13 | Harbor II - 1in aperture received normalized power. | 82 |
| Figure 5.14 | Harbor II - 2in aperture received normalized power. | 83 |
| Figure 5.15 | Harbor II - 3in aperture received normalized power. | 84 |
| Figure 5.16 | Harbor II - 4in aperture received normalized power. | 85 |
| Figure 5.17 | Harbor III - 8 mm aperture normalized power. | 86 |
| Figure 5.18 | Harbor III - 1in aperture normalized power. | 87 |
| Figure 5.19 | Harbor III - 2in aperture normalized power. | 88 |
| Figure 5.20 | Harbor III - 3in aperture normalized power. | 89 |
| Figure 5.21 | Harbor III - 4in aperture normalized power. | 90 |
| Figure 5.22 | Harbor I - Normalized, average, received power | 91 |
| Figure 5.23 | Harbor II - Normalized, average, received power | 92 |
| Figure 5.24 | Harbor III - Normalized, average, received power | 93 |
| Figure 5.25 | Harbor I - Power versus FOV - 10 <i>cz</i> | 94 |
| Figure 5.26 | Harbor I - Power versus FOV - 16 <i>cz</i> | 95 |
| Figure 5.27 | Harbor I - Power versus FOV - 20 <i>cz</i> | 96 |
| Figure 5.28 | Harbor I - Power versus FOV - 25 <i>cz</i> | 97 |
| Figure 5.29 | Harbor II - Power versus FOV - 10 <i>cz</i> | 98 |
| Figure 5.30 | Harbor II - Power versus FOV - 16 <i>cz</i> | 99 |
| Figure 5.31 | Harbor II - Power versus FOV - 20 <i>cz</i> | 100 |
| Figure 5.32 | Harbor II - Power versus FOV - 25 <i>cz</i> | 101 |
| Figure 5.33 | Harbor III - power versus FOV at 10AL | 102 |
| Figure 5.34 | Harbor III: 16 attenuation lengths, 3.6 meters - power versus FOV. | 103 |
| Figure 5.35 | Harbor III: 20 attenuation lengths, 4.5 meters - power versus FOV. | 104 |
| Figure 5.36 | Harbor III 25 attenuation lengths, 5.7 meters - power versus FOV | 105 |
| Figure 5.37 | Harbor I received power normalized by the receiver area. | 107 |
| Figure 5.38 | Harbor II received power normalized by the receiver area. | 108 |
| Figure 5.39 | Harbor III received power normalized by the receiver area. | 109 |
| Figure 5.40 | Coastal water, 8mm aperture received power. | 111 |
| Figure 5.41 | Coastal water, 1 in aperture received power. | 112 |
| Figure 5.42 | Coastal water, 2 in aperture received power. | 113 |
| Figure 5.43 | Coastal water, 3 in aperture received power. | 114 |
| Figure 5.44 | Coastal water, 4 in aperture received power. | 115 |
| Figure 5.45 | Clear water, 8 mm aperture received power | 116 |
| Figure 5.46 | Clear water, 1in aperture received power | 117 |
| Figure 5.47 | Clear water, 2in aperture received power | 118 |
| Figure 5.48 | Clear water, 3in aperture received power | 119 |
| Figure 5.49 | Clear water, 4in aperture received power | 120 |
| Figure 5.50 | Scattering orders plotted versus received power | 123 |
| Figure 5.51 | Harbor II - 10 <i>cz</i> Scattering Histogram | 125 |

| | | |
|-------------|---|-----|
| Figure 5.52 | Harbor II - 16 <i>cz</i> Scattering Histogram | 126 |
| Figure 5.53 | Harbor II - 20 <i>cz</i> Scattering Histogram | 127 |
| Figure 5.54 | Scattering histogram of received photons for Harbor II water at 25 <i>cz</i> | 128 |
| Figure 5.55 | Harbor II - 10 <i>cz</i> scattering histogram normalized by max FOV. | 129 |
| Figure 5.56 | Harbor II - 16 <i>cz</i> scattering histogram normalized | 130 |
| Figure 5.57 | Harbor II - 20 <i>cz</i> scattering histogram normalized by max FOV. | 131 |
| Figure 5.58 | Harbor II - 25 <i>cz</i> scattering histogram normalized | 132 |
| Figure 5.59 | Harbor water average scattering histogram - 10 <i>cz</i> | 133 |
| Figure 5.60 | Harbor water average scattering histogram - 16 <i>cz</i> | 134 |
| Figure 5.61 | Harbor water average scattering histogram - 20 <i>cz</i> | 135 |
| Figure 5.62 | Harbor water average scattering histogram - 25 <i>cz</i> | 136 |
| Figure 5.63 | Zoomed view of Fig. 5.59 | 137 |
| Figure 5.64 | Harbor II frequency response, 25 <i>cz</i> | 139 |
| Figure 5.65 | Harbor I water frequency response at 16 attenuation lengths ($d_{rx/tx}$ of 14.5 meters). | 140 |
| Figure 5.66 | Harbor I water frequency response at 20 attenuation lengths ($d_{rx/tx}$ of 18.2 meters). | 141 |
| Figure 5.67 | Harbor I water frequency response at 25 attenuation lengths ($d_{rx/tx}$ of 22.7 meters). | 142 |
| Figure 5.68 | Harbor II water frequency response at 16 attenuation lengths ($d_{rx/tx}$ of 7.3 meters). | 143 |
| Figure 5.69 | Harbor II water frequency response at 20 attenuation lengths ($d_{rx/tx}$ of 9.1 meters). | 144 |
| Figure 5.70 | Harbor II water frequency response at 25 attenuation lengths ($d_{rx/tx}$ of 11.3 meters). | 145 |
| Figure 5.71 | Harbor III water frequency response at 16 attenuation lengths ($d_{rx/tx}$ of 3.6 meters). | 146 |
| Figure 5.72 | Harbor III water frequency response at 20 attenuation lengths ($d_{rx/tx}$ of 4.5 meters). | 147 |
| Figure 5.73 | Harbor III water frequency response at 25 attenuation lengths ($d_{rx/tx}$ of 5.7 meters). | 148 |
| Figure 5.74 | Illustration showing the concept of offset received power. | 150 |
| Figure 5.75 | Radial power calculation illustration | 150 |
| Figure 5.76 | Harbor I misalignment, 10 <i>cz</i> | 155 |
| Figure 5.77 | Harbor I misalignment, 16 <i>cz</i> | 156 |
| Figure 5.78 | Harbor I misalignment, 20 <i>cz</i> | 157 |
| Figure 5.79 | Harbor I misalignment all, 16 <i>cz</i> | 158 |
| Figure 5.80 | Harbor I misalignment all, 20 <i>cz</i> | 159 |
| Figure 5.81 | Harbor II misalignment, 10 <i>cz</i> | 160 |
| Figure 5.82 | Harbor II misalignment, 16 <i>cz</i> | 161 |
| Figure 5.83 | Harbor II misalignment, 20 <i>cz</i> | 162 |
| Figure 5.84 | Harbor II misalignment all, 16 <i>cz</i> | 163 |
| Figure 5.85 | Harbor II misalignment all, 20 <i>cz</i> | 164 |
| Figure 5.86 | Harbor III misalignment, 10 <i>cz</i> | 165 |

| | | |
|-------------|---|-----|
| Figure 5.87 | Harbor III misalignment, 16 <i>cz</i> | 166 |
| Figure 5.88 | Harbor III misalignment, 20 <i>cz</i> | 167 |
| Figure 5.89 | Harbor III misalignment all, 16 <i>cz</i> | 168 |
| Figure 5.90 | Harbor III misalignment, 20 <i>cz</i> | 169 |
| Figure 6.1 | Receiver/transmitter geometry | 177 |
| Figure 6.2 | The ratio of k and c vs. the water albedo | 180 |
| Figure 6.3 | Diffuse attenuation coefficient vs. wavelength | 181 |
| Figure 6.4 | World map showing water conditions. | 182 |
| Figure 6.5 | Solar radiance angular distribution at water depths | 184 |
| Figure 6.6 | Modified <i>b</i> value geometry | 188 |
| Figure 6.7 | Differential modified b value. | 190 |
| Figure 6.8 | Simulated and modeled power loss for Harbor II water. | 192 |
| Figure 6.9 | MAPE for Harbor waters | 193 |
| Figure 6.10 | Simulated power versus distance for PMT and PD link. | 197 |
| Figure 6.11 | Simulated SNR versus Distance | 198 |
| Figure 6.12 | Bit error rate versus distance for PMT and Photodiode based links. | 199 |
| Figure 6.13 | Block diagram of polarization modulation system using two diode laser and two orthogonal detectors. | 200 |
| Figure 6.14 | Bit error rate versus SNR of the received data for both a single laser OOK system, and the PolModSK system. Also shown is the system performance using a UMTS Turbo Code. | 201 |
| Figure 6.15 | Bit error rate versus the attenuation length of the systems (for a fixed distance of 3.66 m). Also shown is the system performance using a UMTS Turbo Code. | 201 |
| Figure 6.16 | Degree of polarization (DOP) versus transmission distance for several different water types. | 203 |
| Figure 6.17 | Degree of polarization (DOP) versus received power for various water types. | 203 |
| Figure 6.18 | Diagram showing the retroreflection process. | 204 |
| Figure 6.19 | Experimental block diagram for MRR communication system. | 206 |
| Figure 6.20 | Block diagram of transmitter for the MRR communication system. | 206 |
| Figure 6.21 | Receiver diagram for MRR system. This was implemented in software in MATLAB. | 206 |
| Figure 6.22 | Cross section diagram of a MEMS modulating retroreflector. The device can be used for ultra-low power underwater optical communication. | 207 |
| Figure 6.23 | MRR optical spectrum. | 207 |
| Figure 6.24 | Top-down picture of the MRR. The small squares surrounding the four central squares are 144 individual modulators. | 208 |
| Figure 6.25 | Mounted view of the MRR with interrogating laser. | 209 |
| Figure 6.26 | View of the MRR interrogating system. | 210 |
| Figure 6.27 | Frequency response of the (green) high-power amplifier, full system (red) and the interrogating laser and detector (blue). | 210 |
| Figure 6.28 | Bit error rate measurements for the MEMS MRR compared with the attenuation length and received optical power. | 211 |
| Figure 6.29 | MRR sending streaming video | 212 |

| | | |
|-------------|--|-----|
| Figure 6.30 | Required transmit power to achieve $5 \mu W$ of received power at the receiver. Plot shows required power at various water conditions, and various distances between the interrogator and the MRR. This assumes perfect alignment and that the MRR is normal to the interrogating beam. | 214 |
| Figure 6.31 | System block diagram for LED-based passband communication system using software defined radio. | 215 |
| Figure 6.32 | Picture of one of the SDR transceivers. Image shows the PD receiver and LED transmitter, along with the USRP digitizer. | 216 |
| Figure 6.33 | Theoretical and experimental BER versus SNR system performance | 217 |
| Figure 6.34 | Experimental BER versus attenuation length system performance | 218 |
| Figure 6.35 | Throughput for the two sets of LED-based network links. | 219 |
| Figure 6.36 | Network latency for the two sets of LED-based network links. | 220 |
| Figure 6.37 | Throughput and latency for laser based optical network link. | 221 |

CHAPTER 1

Introduction

Comprehensive ocean observation is of great interest to the scientific, industrial and military communities. Security concerns, weather monitoring, and ocean commerce all require sensing of the ocean environment. The difficulty is that such measurements can be expensive, dangerous, and quite difficult to make. Any sensor will require some form of communication, and thus underwater communication between mobile ocean systems is of great interest. The limited propagation distance of RF frequencies [1] and low datarate of acoustic communication leave optical communication as a viable alternative for low-latency, high datarate communication in our oceans. By taking advantage of the “blue/green” optical window in ocean water, underwater optical communication systems can utilize low cost optical sources, like diode lasers [2] or LEDs [3].

Previous work has demonstrated the viability of such systems in actual ocean environments [4, 5], along with experimental results at various datarates and turbidities [6, 7, 8, 9]. These systems are all operated in a fixed laboratory environment, or utilize LEDs as transmitters to ease the pointing and tracking requirements inherent in optical communication systems. These systems are also either simplex (one way) communication systems or utilize two sets of transmitters and receivers for duplex communication [10, 11] thereby increasing complexity and system power requirements. Another option for low power optical communication is the use of a modulating retroreflector [12, 13] to eliminate the need for an optical source at one of the endpoints.

With the overarching goal of comprehensive ocean observation, this dissertation will focus on the design and development of underwater freespace optical communication systems, with experimental, theoretical, and simulated performance results for various systems. Specifically, a numerical simulation for computing the underwater lightfield for communication purposes is discussed and

validated. Secondly, various communication scenarios are simulated and analyzed. Thirdly, design considerations for constructing underwater optical communication systems are discussed, and theoretical link budgets are developed to aid in design. Finally, experimental results of various systems are discussed and compared with simulated and theoretical performance metrics.

The goal of this research is to present several tools to the underwater optical communication system designer. These are a validated numerical simulation for computing the received optical signal power, along with theoretical calculations for computing the SNR of the received signal. This helps solve the problem of the difficulty of building and testing actual systems in ocean environments in order to get operational data. This will enable better systems for ocean observation.

The following chapters will first detail the current state of the art of underwater optical communications. Secondly, we will discuss the physical interactions of light and water in the ocean. Third, we will detail the design and validation of the Monte Carlo numerical simulation, Photonator, then use the simulation tool to simulate various communication scenarios. Finally, we will develop a theoretical link budget for a variety of underwater optical links and look at some applications.

CHAPTER 2

Overview of the State-of-the Art

Underwater communication has a lengthy history starting with Leonardo da Vinci observing, “If you cause your ship to stop, and place the head of a long tube in the water and place the outer extremity to your ear, you will hear ships at a great distance from you. [14]”. He wrote this in 1490, but it wasn’t till the proliferation of submarine warfare during World War I that research into sonar systems became necessary, and Paul Langevin created a device for detecting the noise from moving submarines in 1915. The first useful device for communication underwater was the underwater telephone, an acoustic device developed in 1945 [15]. World War II and the Cold War caused great advances in submarine communication due to the creation of the computer [16].

2.0.1 Freespace Optical Communication

Freespace optical communication (FSOC) dates back to the ancient Romans using mirrors for sending optical signals between distant outposts. Alexander Bell also used a free-space optical transmission scheme to encode a voice signal and transmit it to a receiver over six hundred feet away [17]. The creation of the laser in the 1960’s, along with advances in the area of RF communication, fueled a rapid deployment of fiber optic networks and advances in space communication systems. Along this same time, the military proposed systems for freespace communication between submarines [18, 19] or between satellites and submarines [20].

The end of the Cold War saw a reduction in the interest in space-to-submarine communication, while commercial telecommunication needs spurred increased research into terrestrial optical communication systems. While significant difficulties, like fog and clouds, made such systems difficult to implement in practice, the proliferation of high-speed infrared detectors and emitters from the fiber

optic community allowed rapid increases in datarates and communication distances for terrestrial systems [21]. More recently, though, the proliferation of unmanned underwater vehicles, the desire for comprehensive ocean observation, and the need for command and control of these devices have lead to increased research interest into underwater communication systems.

2.0.2 Underwater Freespace Optical Communication

Recent advances in semiconductor light sources, including blue/green LEDs [3] and diode lasers [22], coupled with the need for ocean exploration and environmental sensing, have spurred research into underwater freespace optical communication. Long range satellite-to-submarine communication links [16] have been passed over in favor of shorter range, lower power, low cost systems to be placed on autonomous vehicles or sensor nodes [5, 11]. Practically speaking, using LEDs as a transmitting light source is most often used for deployable systems due to the ease of pointing and tracking. The transmitter bandwidth of these devices is somewhat limited, however, with a maximum implemented datarate of 10 Mbps reported by Farr [5], though for terrestrial applications, datarates as high as 80 Mbps [23] have been reported by utilizing analog filtering to change the pulse shape. Digital filtering can also be used [24]. Simpson demonstrated a 5 Mbps LED link at 7.3 meters, along with forward-error correction capabilities [25]. Doniec demonstrated a deployed system operating at 1.2 Mbps at 30 meters, though the water quality was not quantitatively measured [10, 11]. Anguita demonstrated a LED based receiver/transmitter system operating up to 2 Mbps over short distances (2 meters), and based on the IEEE 802.15.4 standard for wireless personal area networks [7].

Laser-based underwater links have been explored since the 1970's [26, 18, 19], with the measurements of Snow [27] showing the first experimental results with a 7 Mhz square wave propagating over 18 attenuation lengths (-78 dB extinction) at 30 meters distance, and a 100 Mhz signal propagating 45 meters with an attenuation length of 5 m/m (-21 dB extinction). Green wavelengths, between 514 nm and 532 nm were used. Hanson holds the current record for datarate, with a 1 Gbps link established in a 2 meter test tank [6]. The link ran error free up to 8 attenuation lengths and showed no signs of limitation due to inter-symbol interference or pulse spreading due to scattering. Jaruwatanadilok also found, through complex analytical modeling, that the channel was very broadband with over 6 GHz of bandwidth [28]. Mullen also verified experimentally the propagation of >1 Ghz RF modulated signals in the underwater channel [29].

More recently, Mullen et al. at the Patuxent River Naval base have made detailed measurements of the scattering phase function of Maalox [30] and compared them with ocean scattering phase functions. It was found that Maalox closely approximates the scattering phase function of natural waters (though, not as well for small angles, see Fig. 3.2 on page 12). Thus Maalox provides a convenient and suitable material to control the amount of scattering in laboratory experiments. Based on underwater imaging results from Mullen [31], the same techniques for RF subcarrier modulation were applied

to an optical communication system by Cochenour et al. [8] and later expanded [32]. This allowed greater spectral efficiency, since high-order modulation formats could be used. Additionally, links up to 5 Mbps were established at attenuation lengths up to 8 m/m in a short (3.66 meter) tank. The work done by Cochenour et al. [33] compared experimental results to an approximate analytical scattering function with close agreement. The model was then used to predict link performance at large distances, which showed that Beer's Law exponential power loss does not hold for large attenuation lengths as scattered light is captured by the receiver. Experimental results of the power loss versus attenuation length were presented by Cochenour [34], which examined the de-polarization of the light as it propagated. Using nigrosin dye with the Maalox allows the absorption to be controlled independent of the scattering, thus allowing the the albedo of the water to be changed to better match ocean properties.

Some authors have also considered using the scattering nature of ocean water as an advantage by attempting non-line-of-site (NLOS) communications [35]. By using the sea surface as a diffuse reflector, pointing and tracking (P&T) issues could potentially be avoided, though the technical hurdles in such an implementation are many. Light attenuation in seawater is severe, so diffuse reflection would limit the amount of photons at the receiver. Ultraviolet "solar-blind" underwater communication has also been studied in theory by Kedar [36], while transmission lengths are very short (10 meters), operation in shallow water with very wide field-of-view receivers is feasible due to the lack of background solar noise (see Section 6.2.1).

Another area of research is the use of a retro-reflecting modulator for underwater optical communication (see Section 6.7.2 on page 204). This would allow the transmitting device to operate at lower powers since the high power optical beam is generated by the receiving, or interrogating, system. Mullen showed a technique for suppressing backscattering from such a communication device [31], while we experimentally demonstrated that using such a device can be used for communication at several attenuation lengths with a low power laser source (20 mW) [12, 13].

Finally, the propagation of coherent light was explored by Hanson [37] by studying the effects of light propagating over a turbid path and coupling that light into a single-mode fiber. The received optical signal could then be used with modern telecommunications equipment to simplify the design requirements for optical modem technology. Results showed the fiber coupling efficiency was directly related to the beam size versus the coherence length, and the effects of turbulence are reduced as the beam size is reduced.

2.0.3 Monte Carlo Model of Terrestrial Light Transportation

Monte Carlo simulations have been used in modeling terrestrial optical freespace communication links. They have also been used to model the lightfield behavior when propagating through fog [36], dense clouds [38], or dust [39]. The scattering phase function in these cases is similar to the

scattering phase function underwater, in that it is non-isotropic and highly forward peaked. Much can be learned from these techniques. Older implementations used the Henyey-Greenstein scattering function as a good approximation of scattering in clouds. This function is described by,

$$\tilde{\beta}_{HG}(g; \psi) = \frac{1}{4\pi} \frac{1 - g^2}{(1 + g^2 - 2g \cos(\psi))^{3/2}} \quad (2.1)$$

where $\tilde{\beta}$ is the scattering phase function (described below) that is dependent on the scattering angle, ψ and parameter g . This parameter controls the amount of forward versus backward scatter. This parameter fails to account for the significant forward scattering at very small angles in the underwater environment and backscattering at very large angles. Several modifications of this function have been proposed to better match Mie theory. Figure 2.1 below shows an example of several scattering phase functions.

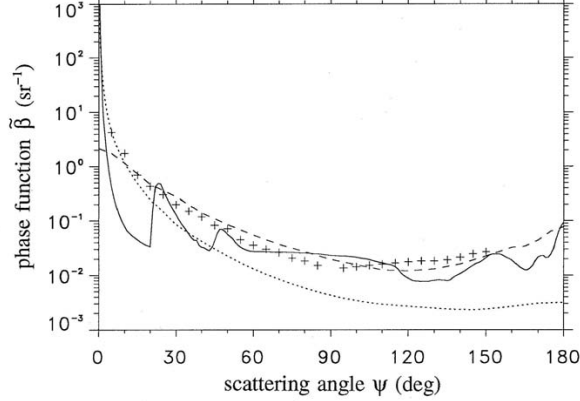


Figure 2.1: The dotted line is the measured phase function from water. The solid line is for cirrostratus cloud at 550 nm. The + signs are human liver tissue at 635 nm and the dashed line is for atmospheric haze at 550 nm [40].

For known particle size distributions, Mie theory can be used to analytically compute the scattering phase function [36, 39]. This calculation usually has to be computed and stored as a look-up table in order to make the simulation computationally efficient [41]. The Mie scattering phase functions can easily be used in atmospheric simulations as the atmospheric constituents are known and well defined. The task is more difficult for the underwater environment where the constituents are widely varied. For example, there can be wildly different scattering from suspended sediment that can depend on the local geology, or the amount of ocean life such as phytoplankton.

2.0.4 Monte Carlo Modeling of Light Underwater

The propagation of light underwater has been traditionally studied for its effects on plant and animal life, not for optical communication. In the former case, the illuminating source is the sun, and the photons are tracked through the air/water interface and as they move downward through the water. As these photons propagate, they are either absorbed or scattered in another direction. To determine the amount of absorption, either to determine heating or photosynthetic reactions, Monte Carlo simulations have been used to track the photon interactions through the water volume. These simulations typically use a “bin” method, where each interaction’s location and angle is recorded so the radiant energy through the whole volume can be determined [42, 43]. These measurements are compared with data taken from instruments that can directly measure the upwelling and downwelling irradiance of the lightfield underwater.

Monte Carlo simulations of directional optical transmitters to optical receivers are not very common due to their computational complexity. Many aspects of downwelling or upwelling irradiance calculations make them easy to compute, however they provide limited information in a communications context, where the field of view and receive aperture are both limited. They can, however, aid in the calculation of background noise, as discussed in Section 6.2.1. A few Monte Carlo models for simulating optical communication have been mentioned in the literature. Laux [30] describes a MC model used to compare against experimental tank data. Hanson [6] utilized a MC model to compare against a high-bandwidth communication experiment, and extrapolate the results to longer distances. Jaruwatanadilok [28] mentions, but does not describe, using a MC model to compare against theoretical calculations of channel bandwidth. More recently, Li [44] developed a semi-analytic MC simulation, which they verified using experimental channel measurement data from Mullen et al [29], and then used to make channel bandwidth estimations. While the methods used have been discussed, to this author’s knowledge, none of the previously mentioned authors have made their source-code available for use or analysis.

2.1 Conclusion

In summary, underwater freespace optical communication draws from a rich history of various disciplines: optical communication, freespace optical, and underwater communication, along with laser development and mathematical modeling. The area has not been as widely explored as terrestrial or space freespace optical communication, but recent advances in low-cost light sources, and more interest in ocean observation, have spurred current research. Much work still needs to be done in the area of modeling and system design, which this research addresses, along with continued efforts to improve the bandwidth of detectors and sources and output power of visible wavelength optical sources.

CHAPTER 3

Light Underwater

The interaction of light and water is quite complicated. Not only does it deal with the complex subject of light interacting with matter, but also deals with the complex nature of the ocean environment. This chapter will try and distill the most important aspects of this interaction as it applies to underwater freespace optical communication. For a more complete view of the subject the works of Mobley [40, 45] and Spinrad [46] are very useful resources.

In general we will address the issues of optical absorption and scattering in the water, as these two factors contribute to power loss between an optical transmitter and a receiver. Other effects, such as photoluminescence, will not be considered.

3.1 Characterizing Light in Water

When considering a differential volume element of water of width Δr , and arbitrarily small height and length, the amount of light entering the volume equals the amount of light leaving the volume, less any absorption loss in the volume. A portion of light leaving the volume will retain the same propagation direction, while the rest will be distributed into other directions. This is illustrated in Fig. 3.1 and based off the work by Mobley [40].

If the the differential volume of water illuminated with a spectral radiant power of Φ_i , Φ_a is the absorbed power, Φ_s is the total scattered power in all directions, and Φ_t is the transmitted power. Note that all of these values are wavelength dependent, but the λ designation has been dropped for convenience. Spectral radiant power is measured as [46]

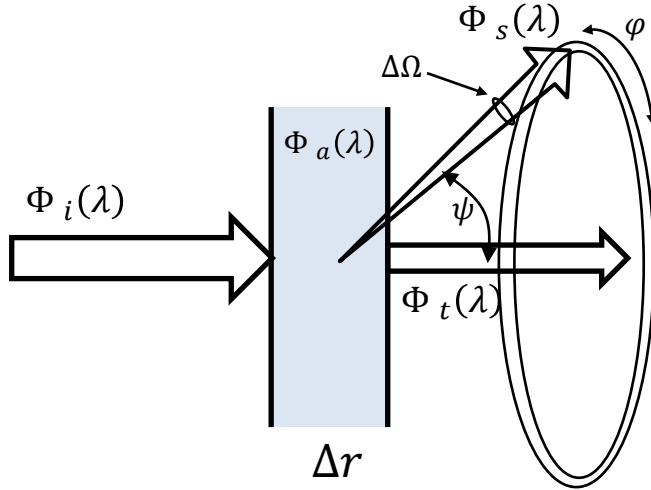


Figure 3.1: Geometry of the inherent optical properties of water, from Mobley [40].

$$\Phi_i(\lambda) = \frac{hc}{\lambda} \frac{N}{\Delta\lambda} \quad (3.1)$$

where hc/λ is the energy of a photon of wavelength λ , N is the number of photons observed per second, and $\Delta\lambda$ is the wavelength range of the observation (or the bandwidth of a filter in a detector). The units of spectral radiant power are W nm^{-1} .

We will define the absorptance as

$$A(\lambda) = \frac{\Phi_a}{\Phi_i} \quad (3.2)$$

the transmittance as

$$T(\lambda) = \frac{\Phi_t}{\Phi_i} \quad (3.3)$$

and the ratio of scattered power as

$$B(\lambda) = \frac{\Phi_s}{\Phi_i}. \quad (3.4)$$

If we divide the quantities above by the distance, Δr , as it approaches zero, then the values above are reduced to coefficients which measure loss per unit distance. These are referred to as the absorption coefficient

$$a(\lambda) = \frac{dA(\lambda)}{dr} \quad (3.5)$$

and the scattering coefficient

$$b(\lambda) = \frac{d B(\lambda)}{dr} \quad (3.6)$$

where both are in units of m^{-1} , since $B(\lambda)$ and $A(\lambda)$ are unit-less ratios. Additionally, the total loss is defined as the *attenuation coefficient*, c , where

$$c = a + b \quad (3.7)$$

which also has units of m^{-1} . An additional helpful value is the single scattering albedo, ω_0 ,

$$\omega_0 = \frac{b}{c} \quad (3.8)$$

which defines are ratio of scattering loss to total loss. This is a helpful term when comparing various water types, as we will see in future chapters. This value is in the range of values from 0 to 1 (expressed as $[0, 1]$), with natural waters having values from around 0.25 for clear ocean water to over 0.8 for turbid harbor waters. A completely scattering medium would have a value of 1, while a medium with no scattering and only absorption loss would have a value of 0.

3.2 Absorption

The absorption in natural waters can be difficult to separate from scattering when taking measurements. Not only does pure water absorb some amount of the optical energy, but the particulate matter in these waters can be even more absorptive. Suspended materials that contribute to absorption include “colored dissolved organic material” (CDOM) and phytoplankton. CDOM absorbs more at shorter wavelengths, while phytoplankton absorbs strongly in the blue and red wavelength regions due to the chlorophyll concentration [47].

3.3 Scattering

Light scattering is due to photon interactions with the water molecules, particulate matter, and other dissolved substances in the water. The beam loss from scattering, shown as Φ_s in Fig. 3.1, is dependent on the angle, ψ , of deviation from the incident beam direction. Since the scatterers in ocean water are randomly distributed the radial angle, φ of scattering is symmetric, shown by the annular ring in Fig. 3.1. The angular distribution of scattering, called the volume scattering phase function, is defined as

$$\beta(\lambda, \psi) = \lim_{\Delta r \rightarrow 0} \lim_{\Delta \Omega \rightarrow 0} \frac{\Phi_s(\psi; \lambda)}{\Phi_i(\lambda) \Delta r \Delta \Omega} \quad (3.9)$$

which is the limit of light scattering out of volume Δr into the solid angle $\Delta\Omega$ in direction ψ , as both go to zero. The units of $\beta(\lambda; \psi)$ are $\text{m}^{-1} \text{ sr}^{-1}$. By integrating β over all angles, we arrive at an expression for $b(\lambda)$, given by

$$b(\lambda) = \int_{4\pi} \beta(\psi; \lambda) d\Omega = 2\pi \int_0^\pi \beta(\psi; \lambda) \sin \psi d\psi \quad (3.10)$$

since the radial scattering angle is symmetric, the integration on that axis reduces to 2π , and the polar scattering angle is in the range $[0, \pi]$.

If the volume scattering phase function, β is normalized by the scattering coefficient, b , then we arrive at the volume scattering phase function, $\tilde{\beta}$, which expresses the angular probability of scattering as a probability density function (PDF)

$$\tilde{\beta}(\lambda; \psi) = \frac{\beta(\lambda; \psi)}{b(\lambda)}. \quad (3.11)$$

The volume scattering phase function is used to choose scattering angles for the numerical MCNS simulation discussed in Chapter 4. In practice, measuring the volume scattering function is very difficult due to the large dynamic range needed for the measurement device.

3.4 Analytical Models

A simple approach to the solution of the scattering problem is available for small spherical particles (radius $< \lambda$). For larger spherical particles the Lorenz-Mie solutions of Maxwell's equations provide a very useful result. However, analytically modeling the scattering phase function is fraught with problems in many real world applications. Not only are the measurements of the volume scattering functions extremely difficult to measure, they also require expensive, time consuming, and dangerous sea voyages to measure actual ocean environments. Many different types of analytical phase functions have been used over the years. The Henyey-Greenstein (HG) function has been popular [41, 50], and was originally based on interstellar dust scattering. In more recent years, the Fournier-Forand (FF) function has been used with good agreement to actual water measurements [51, 52].

The FF model was proposed [53] as an analytic phase function based on the anomalous diffraction approximation of Van de Hulst [54]. While still being a relatively simple, two parameter, equation, it has the benefit of being rooted in the physics of the problem instead of being a purely phenomenological model. The FF phase function assumes that the particle distributions in natural waters follow a hyperbolic (Junge) distribution, which, in practice seems to be appropriate [55, 56], and is based upon the slope of the Junge distribution and the average real index of refraction of the particles. Recently, Mobley et al. [51] was able to re-parameterize the FF function based upon the backscattering fraction, B_p , which represents the probability that a photon will be scattering into a polar angle greater than

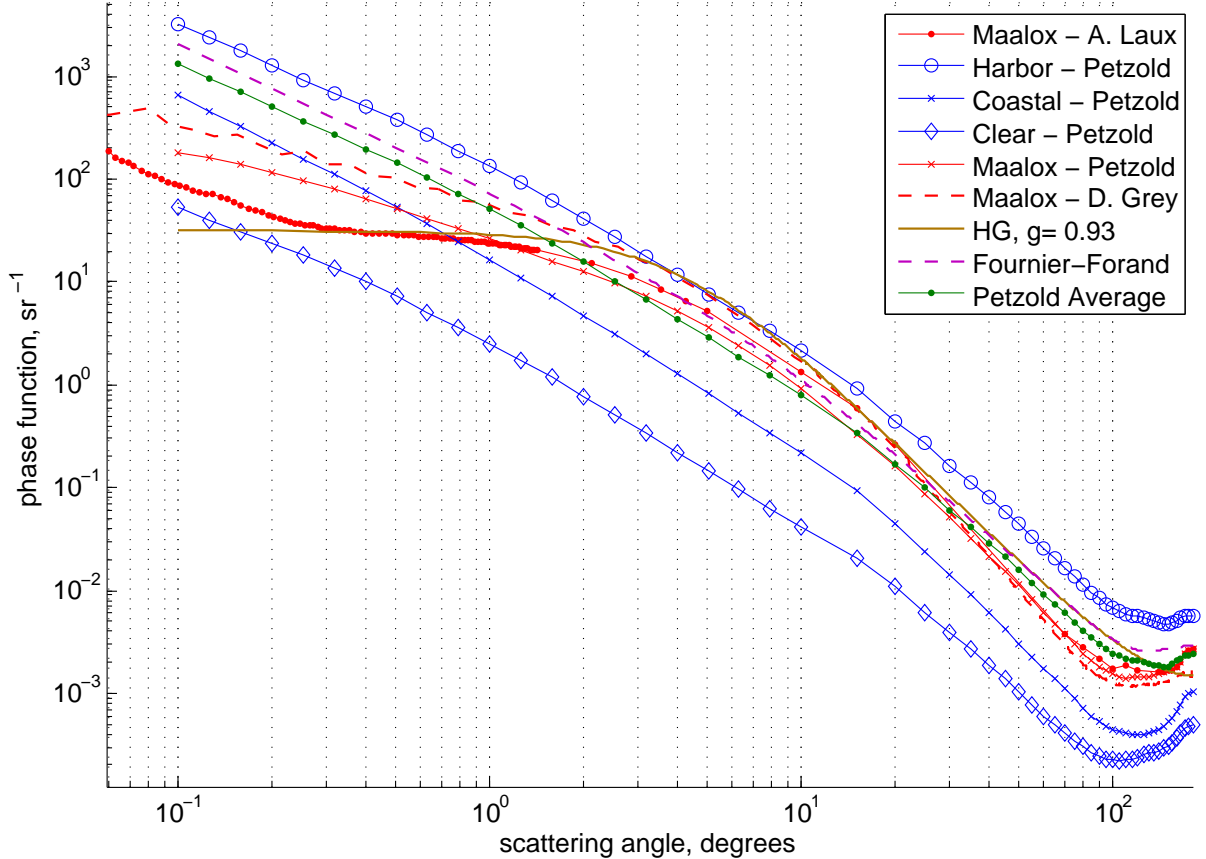


Figure 3.2: Comparison of various phase functions. Shown are measured phase functions from Deric Grey (Maalox) [48], Alan Laux (Maalox) [30], Petzold (Maalox and ocean water) [49], along with a Henyey-Greenstein phase function, and a Fournier-Forand phase function for the Petzold average phase function. These are plotted on a log-log plot to emphasize the effects of small angles.

90° for a single scattering event (for example $B_p = 0.0183$ for the average Petzold scattering phase function). This re-parameterization is very helpful as it is difficult to measure the average index of refraction of the particles in natural waters. Freda and Piskozub [57] compared Mobley's approximation with experimental data from natural waters and proposed an additional set of parameterizations that better match the data.

When just comparing Petzold's measured data with the FF phase function, however, a very good fit can be made by using the parameters $\mu = 3.5835$ and $n = 1.10$. The phase function has the benefit of modeling both the sharply peaked forward scattering and the backscattering peak of natural waters. The FF phase function is therefore appropriate for both modeling the backscattering effects in LIDAR and communication interference and for forward scattering used in communication. However, the simulation results presented later on will use the Petzold scattering phase function. The FF phase

function, along with the average Petzold phase function, is shown in Fig. 3.2.

3.5 Full System View of Light Reception

When considering the loss of light over a path length, r , the attenuation coefficient can be used to describe the total loss. Essentially, the differential path loss is integrated over the distance. If the differential path loss is

$$\frac{dI}{dr} = -cI \quad (3.12)$$

where I is the power incident on the volume of width dr , and c is the attenuation coefficient, $a + b$ with units of m^{-1} . c is negative to show that light is lost over the path. Rearranging this equation and integrating yields

$$\int_{I_0}^I \frac{1}{I} dI = -c \int_0^r dr \Rightarrow \ln(I) - \ln(I_0) = -cr \quad (3.13)$$

which, when simplified, yields the more common expression for Beers Law-type loss:

$$I = I_0 \exp(-cr). \quad (3.14)$$

This equation assumes that all scattered light is lost from the beam and that no multiply scattered light returns to the beam, and as such, does not take into account a receiver of finite aperture. A modification to compensate for this effect is discussed in Section 6.4.1 on page 188. In general, however, a full view of light loss and reception will take into account both the loss due to scattering and the gain due to photons scattering back into the central beam. This total view is considered in the next section on the radiative transfer equation.

The exponent of Eq. 3.5 is a unit-less quantity called the *attenuation length*, and is the multiple of the transmission distance and the attenuation coefficient. This quantity, cz , is often used to compare operation of various systems, since it removes the ambiguity of distance and water conditions.

3.5.1 Radiative Transfer Equation

The radiative transfer equation expresses the conservation of energy of an underwater beam of light. It takes into account losses and gains into the central received beam. The equation is expressed using the definitions above and the radiance of the beam

$$L(z, \lambda, \phi, \theta) = \frac{P(\lambda, z, \phi, \theta)}{\Delta A \Delta \Omega \Delta \lambda} \quad (3.15)$$

where ΔA is the area of the detector, $\Delta\Omega$ is the solid angle in the direction of ϕ, θ , and z is the operating depth in the ocean. The units of radiance are $\text{W m}^{-2} \text{ sr}^{-1} \text{ nm}^{-1}$. Using the radiance, the radiative transfer equation for the simple case of a homogeneous medium, with no inelastic scattering or internal sources like bioluminescence, is

$$\cos \theta \frac{dL(z; \lambda; \theta; \phi)}{dz} = -c(z, \lambda)L(z; \lambda; \theta; \phi) + \int_{4\pi} \beta(z; \lambda; \theta' \rightarrow \theta; \phi' \rightarrow \phi)L(z; \lambda; \theta'; \phi')d\Omega' \quad (3.16)$$

where $L(z; \lambda; \theta; \phi)$ is the radiance at depth z in direction θ, ϕ . The first term on the right, $-c(z, \lambda)L(z; \lambda; \theta; \phi)$ is the Beer's Law loss, and the 2nd term is the gain from light scattering from angle θ', ϕ' into direction θ, ϕ . Even in this simplistic case, this equation is difficult to solve. The Monte Carlo simulation tool in Chapter 5 on page 62 presents a way to solve this equation for an optical transmitter and receiver.

3.5.2 The Diffusion Length

The diffusion length, L_d , introduced by Weisskopf [58] is a useful term when determining whether a system is operating in low to moderate attenuation lengths or at high attenuation lengths. Its equation is

$$L_d = \frac{1}{b(1 - \langle \cos \theta \rangle)} \quad (3.17)$$

where $\langle \cos \theta \rangle$ is the average scattering cosine, g , given as

$$\langle \cos \theta \rangle = 2\pi \int_0^\pi \tilde{\beta}(\theta) \cos \theta \sin \theta d\theta. \quad (3.18)$$

This equation is simply the average of the volume scattering phase function, such that $\langle \cos \theta \rangle$ represents the point where half of the total scattering happens at angles above $\langle \cos \theta \rangle$ and half below.

Eq. 3.17 is derived by calculating the total average length over which a photon propagates along the initial direction, after an infinite number of scattering events. Since b^{-1} describes the average length a photon travels, the distance which a photon moves along the initial direction vector after the first scattering event is $b^{-1} + b^{-1} \cos \theta$, where θ is the azimuthal scattering direction. After the second scattering event, this distance then becomes $b^{-1} + b^{-1} \cos \theta + b^{-1} \cos^2 \theta$, and so forth. On average, each scattering event adds $b^{-1} \langle \cos \theta \rangle$ to the total distance. This equation

$$L_d = b^{-1} + b^{-1} \langle \cos \theta \rangle + b^{-1} \langle \cos \theta \rangle^2 + \dots = b^{-1} \sum_{i=0}^{\infty} \langle \cos \theta \rangle^i \quad (3.19)$$

is a geometric sum, which, since $\langle \cos \theta \rangle$ is < 1 , reduces to the result in Eq. 3.17.

Lerner and Summers [59] call mediums which are thicker than the diffusion length, "optically

Table 3.1: Albedo, average cosine, and diffusion attenuation length for the three Petzold water types.

| | Turbid | Coastal | Clear |
|-------------------------------|--------|---------|-------|
| ω_0 | 0.83 | 0.55 | 0.25 |
| $\langle \cos \theta \rangle$ | 0.92 | 0.94 | 0.87 |
| cL_D | 15.1 | 30.3 | 30.7 |

thick". If the medium is isotropic, then the diffusion length will simply be b^{-1} . However, as the scattering phase function, $\tilde{\beta}(\theta)$ becomes more peaked in the small angles, the diffusion length increases. Essentially, it takes longer before the number of photons scattering backwards, equals those scattering forward. While photons still continue to move along the incident direction, *on average* the forward motion has stopped by distance L_d .

By looking at the diffusion length in terms of the number of attenuation lengths, as developed by Cochenour and Mullen [60], the following equation is derived

$$cL_D = \omega_o^{-1} \frac{1}{1 - \langle \cos \theta \rangle} \quad (3.20)$$

where ω_o is the albedo of the water. This number ranges from 0.25 for clear ocean waters to 0.83 for turbid harbor waters. The average scattering cosine, $\langle \cos \theta \rangle$, for Petzold's harbor water scattering phase function ranges from 0.87 to 94. This number is typically greater than 0.90 for natural waters, and is 0.924 for the average Petzold scattering phase function. For the three Petzold water types, the diffusion length is presented in Table 3.1.

Based on Table 3.1 it is clear that Coastal and Clear water types maintain their forward scattering motion over a very long distance when compared to harbor water. At 30 attenuation lengths, the optical source will be attenuated by more than thirteen orders of magnitude. This makes it very difficult to experimentally measure this type of waters at the point they begin to significantly diverge from Beer's Law, and similarly difficult to simulate this behavior. In this sense, harbor water types prove to be much more "interesting" from a scattering perspective. Thus, most of the work in this thesis is focused on various Harbor water conditions, though results are presented for Clear and Coastal waters to illustrate their differences.

3.6 Conclusion

In conclusion, the interaction of light and water is quite complicated, and depends highly upon both the wavelength of the light and the constituents of the water. Decades of research have been devoted to understanding these interactions, especially in regards to biological effects and underwater imagining, such as LIDAR. While point-to-point communication is a relatively small aspect of this area of study, the effects of the water are appropriate for most applications.

Light loss between the transmitter and receiver is governed both by absorption of the photons by the water molecules, suspended particulate matter, and dissolved materials and scattering. Chlorophyll in phytoplankton, along with CDOM are two chief absorbers of visible wavelengths in the under-water channel. These depend highly on the location and depth an underwater optical communication system is operating. Scattering affects also play a large part in underwater optical communication, as they contribute to temporal dispersion (elongation of the path length that photons travel) and to power loss as photons are scattered away from the receiver aperture. Scattering is also highly dependent on suspended particulate matter and the water itself, and is difficult to model due to the variability of the scattering phase functions chiefly at small angles. Both theoretical and phenomenological models can be used in simulations and analytical calculations of power loss in communication systems. Additionally, looking at the scattering characteristics of the water can tell us important aspects of the power loss models, as past a certain distance, the diffusion length, the propagation of the light is no longer predominantly collimated and forward scattering. As we will see in later chapters, the diffusion length can be a useful indicator for a change in the shape of the power loss curves in highly scattering environments, such as Harbor water. Finally, for many waters types the Beer's Law loss model works well to characterize the loss of signal power over a given distance. This model is useful as a baseline calculation for the channel loss, and will be compared to simulated outputs in future chapters.

CHAPTER 4

Simulation of the Underwater Lightfield

Since field testing is both costly and time consuming, an important aspect of system design is the ability to predict the system's performance prior to construction and testing. While various approximations and analytical models of the underwater light-field exist, these often do not take into account the specific needs for optical communication or can be inadequate for determining optimal system performance. For example, while Beer's Law (see Eq. 3.5 on page 13) provides a convenient equation for determining the channel loss, it can severely underestimate the power of the light-field in highly turbid environments, thereby underestimating the system's performance in such an environment. Another example would be analytical models which employ the small angle approximation. While these models are very convenient for rapid calculation of the light-field power, they cannot yield correct answers for extreme pointing angles or non-line of sight communication. Additionally, typically these models do not take into account time resolution and thereby make it difficult to determine the channel bandwidth of the underwater optical communication channel.

In order to fill some of the gaps left by other kinds of channel models, a Monte Carlo numerical simulation (MCNS), "Photonator", is presented for calculating the underwater light-field, specially for optical communication systems. The simulation is useful both in terms of the underlying simplicity of the simulation and the public presentation and availability of the software for general use.

4.1 Overview of Monte Carlo Numerical Simulation

Monte Carlo numerical simulation (MCNS) uses random sampling to arrive at an approximate answer to an exact problem, as opposed to an analytical model, which is an exact answer to an approximate

problem. Put another way, a MCNS approximates a complex probability distribution function (PDF) through random sampling of known, exact, simpler PDFs. For our particular problem, the underwater light-field, a solution to the PDF of the light-field on the receiver is desired. This can be computed using approximate formulas to arrive at an exact solution to these formulas, or a large number of photon trajectories can be computed, each using known PDFs for scattering lengths and volume scattering functions. These photon trajectories can be summed to approximate the light-field at the receiver. In the area of computer graphics, this method is generally termed “ray tracing”, due to the tracing of individual rays of light from source to receiver. Mobley [40] describes the Monte Carlo method as knowing, “the probability of occurrence of each separate event in a sequence of events, then we can determine the probability that the entire sequence of events will occur.”

While MCNS requires a great deal of computational power, the Moore’s Law-type increase in computation power makes the method more and more feasible as time progresses. Additionally, the conceptually simple methodology makes it accessible to students and researchers who do not possess a background in mathematics, required for many of the analytical models. The simulation is constructed according to common methods described in many publications [61, 62, 63, 64, 65, 66, 67, 68, 43, 40, 30]. Especially helpful references include that of Mobley [40], Leathers [62], and Wang [65].

4.2 Simulation Assumptions and Approximations

While the number of assumptions about the behavior of the MCNS were kept to a minimum, there are still several assumptions that were made and need to be noted. These are listed below, along with explanation:

- Homogeneous medium - Photonator MCNS assumes that the simulation medium is homogeneous, meaning that scattering and absorption are uniform throughout the volume of the environment.
- Elastic scattering (no Raman, etc.) - All scattering is assumed to be elastic, meaning there are no shifts in wavelength, only direction.
- Random number generator produces sufficiently independent uniform random numbers - No computational random number generator is perfect, and will eventually repeat the random string of numbers. In the MCNS the random number generator is seeded with a new seed for each time the simulation is run.
- Simulation boundaries are perfectly absorbing - For open water simulations, photons that propagate backwards past the transmitter plane are terminated.
- No photons propagate past the receiver plane, back, and then across it again (no 3x backscattering) - Any photon that crosses the receiver plane is logged and terminated.

- Sufficient number of photon packets are collected to form an accurate estimation of the total probability from transmitter to receiver - by randomly sampling a discrete distribution to approximate a continuous distribution, it is assumed that after a certain point the discrete approximation begins to approach the continuous approximation. This assumption can be tested using the Central Limit Theorem.

Other assumptions, when made, are noted. Any assumptions that were made were usually chosen not from convenience but from necessity - whether this was computational complexity necessity or simply based on the numerical method chosen.

4.3 Mechanics of the Photonator Simulation

The simulation is divided into three major parts: initial conditions, photon propagation, and photon reception. Each part will be discussed below. The three sections correspond to three aspects of the source code in Appendix B on page 235. The two major processes, transmission and reception, are illustrated via a flowchart in Fig. 4.1 and Fig. 4.2. Photons that are propagated in the transmission process are passed to the receiver process, once all photons have been terminated or received, for processing into irradiance and power measurements on the receiver plane.

4.3.1 Initial Conditions

The simulation initial conditions determine the type of environment, the type of light source, and the receivers that will be simulated. The simulation geometry uses a cartesian coordinate system where the receiver plane is situated on the x/y-plane at a fixed point along the z-axis. Any photons that cross the x/y-receiver plane are marked as received and their x/y location, and arrival angle are recorded. While the receiver(s) is always on the x/y plane, the initial location and incident angles of the light source is not limited.

Light source definition

Each photon packet is determined by its x, y , and z location and the projection of a unit vector, in the direction of propagation, projected on the x, y , and z axes. These projections, commonly called “direction cosines” determine the direction of propagation of the photon and reduce the need for time consuming and complex trigonometric calculations. The photon direction vector is projected onto the x, y and z axis of the Cartesian coordinate frame. These projections, are illustrated in Fig. 4.3 and are defined by,

$$\mu_x = \cos(\theta_x) \quad (4.1)$$

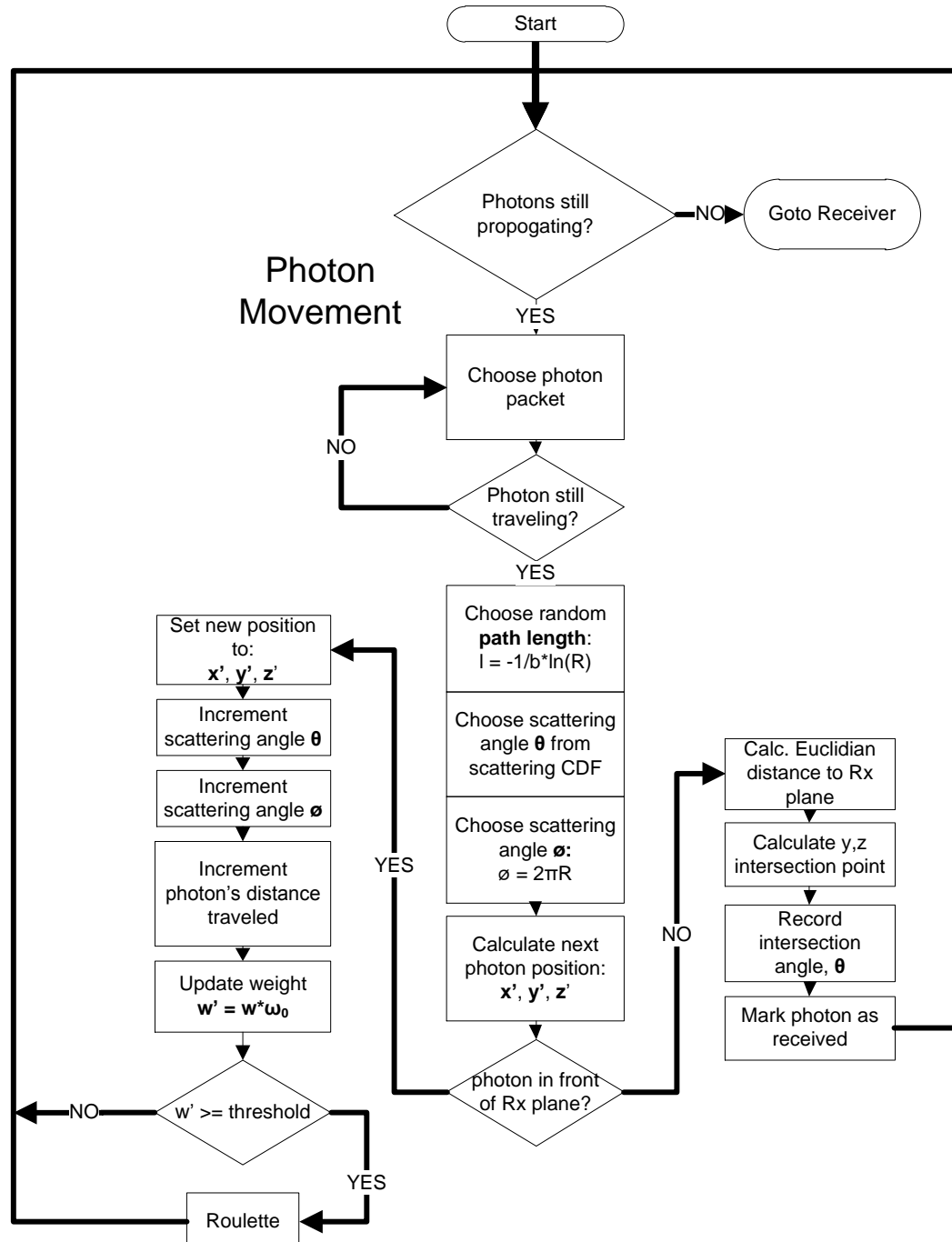


Figure 4.1: Flowchart showing basic process for transmitting photons from the transmitter to receiver. The flowchart starts at the top and moves downward. Once all the photons have been terminated, the process is passed to the receiver, illustrated in Fig. 4.2

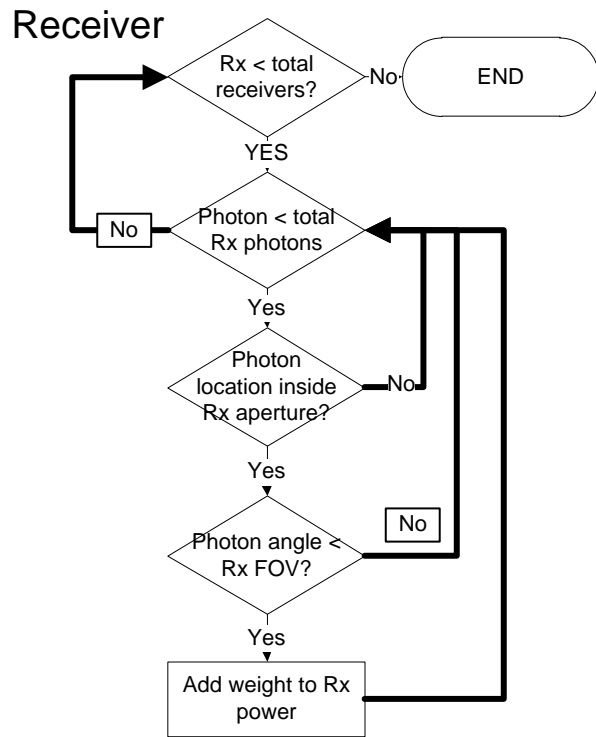


Figure 4.2: MCNS flowchart for the receiver process. Photons are passed from the transmitter, shown in Fig. 4.1, to the receiver to be processed.

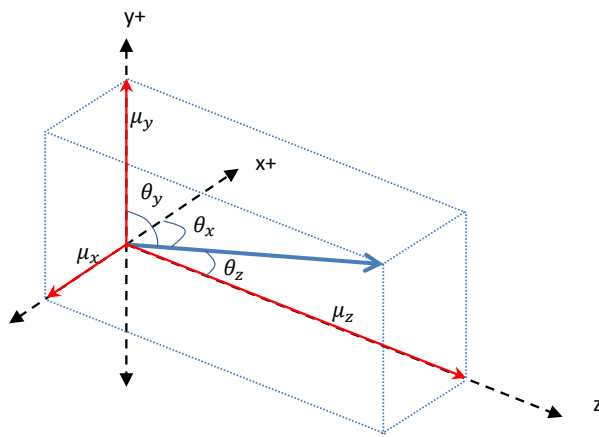


Figure 4.3: Illustration of direction cosines. The blue vector is the photon trajectory direction vector, the red vectors, μ_x , μ_y , μ_z , are the projections of the photon's direction vector onto the x , y , and z axes. Photon trajectories are tracked using the direction cosine vectors.

$$\mu_y = \cos(\theta_y) \quad (4.2)$$

$$\mu_z = \cos(\theta_z) \quad (4.3)$$

where θ_x , θ_y , and θ_z are the angles between the direction vector and the x, y, and z axis, respectively. These three values must also satisfy the normalization

$$\mu_x^2 + \mu_y^2 + \mu_z^2 = 1 \quad (4.4)$$

which assures that the direction vector is a unit vector.

The angular representation of a source depends on the source function [62], given by $\Psi_0(\theta, \phi)$ and normalized such that

$$\int_0^{2\pi} \int_0^{\pi/2} \Psi_0(\theta, \phi) \sin(\theta) d\theta d\phi = 1 \quad (4.5)$$

where θ is the polar angle and ϕ is the azimuthal angle. For most sources, ϕ will be symmetric, and thus the normalization is reduced to

$$2\pi \int_0^{\pi/2} \Psi_0(\theta, \phi) \sin(\theta) d\theta = 1. \quad (4.6)$$

In this situation, the azimuthal transmission angle is simply

$$\phi = 2\pi \mathbb{R} \quad (4.7)$$

where \mathbb{R} is a uniform random number in the interval $[0, 1]$. The polar transmission angle, θ is then chosen from the Cumulative Distribution Function (CDF) of the source function

$$P(\theta) = 2\pi \int_0^{\theta_0} \Psi_0(\theta) \sin(\theta) d\theta = \mathbb{R} \quad (4.8)$$

where \mathbb{R} is a uniform random number taken from the interval $[0, 1]$. A function used to describe a generalized Lambertian transmitter that could be appropriate for a LED source is discussed in Section 6.1 on page 174.

Additionally, the initial location can be chosen to approximate the initial power density function, and the starting direction cosines can be chosen to simulate beam divergence. For instance, to simulate a Gaussian beam, the initial photon locations can be randomly chosen to match the gaussian distribution defined by

$$p(r) = \exp(-r^2)/(2\sigma^2) \quad (4.9)$$

where $p(r)$ is probability of the photon being distance r from the beam center and σ is the standard deviation of the beam (or beam width). In this case, the beam is uniform along fixed radius from the beam center, and the x and y locations are defined by

$$x_0 = r \cos(\phi) \quad (4.10)$$

$$y_0 = r \sin(\phi) \quad (4.11)$$

where ϕ is randomly chosen to lie on the interval $[0, 2\pi]$. Example source-code can be found in Appendix B on page 235. A diffuse point-source, liked an LED, can be similarly defined using manufacturer's data-sheets or measurements. Section 5.2.2 on page 66 details the initial condition setup for simulated results using a Gaussian beam with 1.5 mrad of divergence. Another potential method would be to simulate an infinitely small beam, and use the output as a point-spread-function which would be convolved with the source function. Wang et al [65] details an approach for this method.

Environmental definition

The simulated environment is defined by the attenuation coefficients, c , the albedo, ω , and the volume scattering function, $\tilde{\beta}$. The albedo defines how scattering contributes to loss, as $\omega = b/c$, where b is the scattering coefficient in m^{-1} . For each photon interaction with the medium, the albedo determines the ratio of scattering to total loss, or alternately, what percentage of the photons "weight" (see 4.3.2) is reduced due to absorption, since the remaining scattered portion is redirected and continues to propagate.

The MCNS computes the underwater light-field for a homogeneous medium. While this assumption limits the applicability to all environments, this assumption is simplifying and reduces the simulation time and complexity. The simulator can, however, be used to simulate a non-homogeneous, stratified, environment, by taking the output of propagation and using it as the initial conditions for another simulation using the next stratified water conditions.

4.3.2 Photon Propagation

Photon propagation is governed by its photon pathlength, the distance over which it travels before being scattered or absorbed, and its scattering angles, which are determined from the beam scattering function, described later.

Photon Path Length

An photon path length, or distance over which the photon travels in a homogeneous medium, is chosen from the cumulative probability distribution [40]

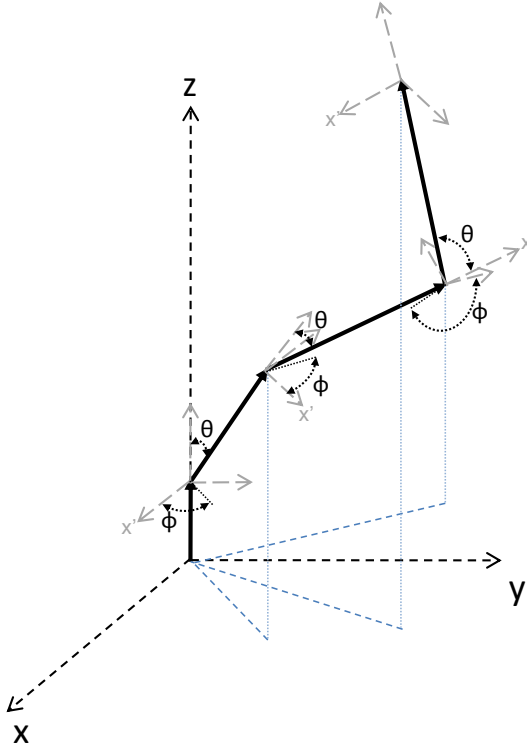


Figure 4.4: Photon propagation illustrated. Each successive scattering event causes the trajectory to rotate its local coordinate frame by θ, ϕ , while the global position is updated in reference to the $(0,0,0)$ coordinate.

$$P_l(l) = 1 - e^{-l} \quad (4.12)$$

where $P_l(l)$ is the probability of travel over an optical scattering pathlength of l . Solving for l , this becomes

$$l = -\log(1 - P_l(l)). \quad (4.13)$$

Since $P_l(l)$ is uniformly distributed over the interval 0 to 1 (l then becomes exponentially distributed), $P_l(l)$ can be substituted for $1 - P_l(l)$, and since the optical pathlength is defined as

$$l = cr \quad (4.14)$$

where c is the attenuation coefficient and r is the geometric distance between optical events (defined as either scattering or absorption), we can solve for geometric distance between optical events using the equation

$$r = -\frac{1}{c} \log P_l(l) \quad (4.15)$$

where $P_l(l)$ is a uniform random number between 0 and 1. This distance is the distance the photon packet travels before being scattered or absorbed.

Photon Weight

Once a photon's pathlength before an optical event has been randomly chosen, a naive approach would be to again draw from a uniform random distribution to determine whether the optical event was absorption or scattering. Some percentage of the photons (ω_0 100%) will be scattered, and the remaining percentage will be absorbed. Since it is computationally wasteful to terminate a photon before it reaches the receiver plane or any boundary, we instead view each photon as a packet, or group, of photons and reduce the group weight by the percentage absorbed in the event. Initially starting at a weight of 1, the new photon weight is calculated as

$$w_{n+1} = w_n \omega_0 \quad (4.16)$$

where w_{n+1} is the new weight and w_n is the previous weight before the optical event ($w_{n+1} < w_n$). Fig. 4.5 illustrates how the photon packet weight changes at each optical event.

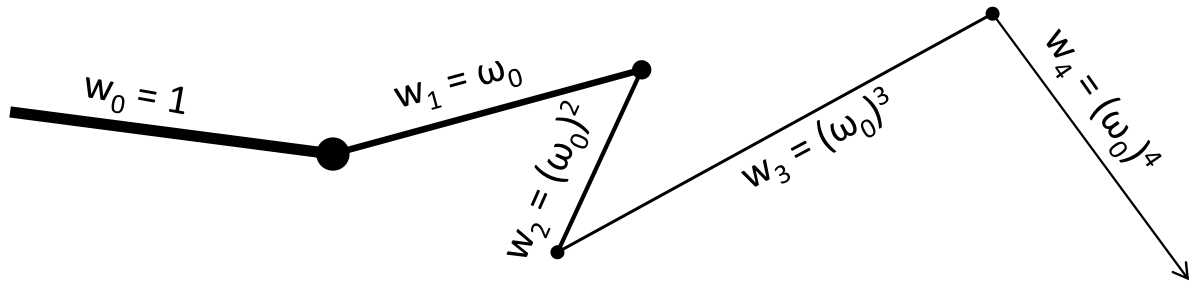


Figure 4.5: Illustration showing how the weight is reduced at each optical event, to compensate for the absorption. A percentage of the weight is lost by absorption and the rest of the photon packet is redirected along another scattering path.

Another way to consider this model is to think of the simulation as randomly choosing statistically probable paths from transmitter to receiver and iteratively computing the probability that a photon would move along that path from transmitter to receiver. At each optical event the probability of a photon traversing past that point is reduced. This reduction in probability is the albedo, ω_0 , which is the ratio of scattering to total loss at each optical event. Consequently, $1 - \omega_0$ is the ratio of absorption

to total loss, since $c = a + b$. In essence, *instead of computing a continuous probability distribution of paths from transmitter to receiver, we are computing the total probability of the path from transmitter to receiver by randomly sampling from the discrete distribution of probable paths*. By simulating a large number of these paths, and then considering the total probability in aggregate, we can approximate the true probability of a photon moving from the transmitter to the receiver.

When we refer to the “photon weight” we are, in essence, referring to the probability of a photon traversing the path from transmitter to the current position of the photon path at that moment. This probability is iteratively calculated until the path intersects the receiver plane or is terminated, as discussed below.

Rouletting

After a photon packet has scattered many times its weight can drop to levels where it will no longer make a significant impact on the final value of the simulation if it were to be received. Instead of simply terminating the photon packet, which would violate the conservation of energy in the simulation, a common method, termed “rouletting”, is employed. An arbitrary lower limit is set on packet weights, which is a function of the water’s albedo, and determines a maximum threshold for scattering events.

In other words, by setting a lower limit on the photon weight, or path probability, we are choosing the point at which a path probability is so low that it is no longer computationally beneficial to continue to compute the path probability to the receiver. For example, if a photon weight, that has moved from the transmitter to the receiver is 0.1, that means 1 in 10 photons taking that path will survive. If, however, the path weight is 0.001 that means 1 in 1000 photons taking that path will survive. At some point, the weight, or probability, becomes so low as to not be useful. In essence we are choosing the discrete limit to how probable a path needs to be in order to be considered in the simulation. This limit is the rouletting threshold. In practice this is somewhat arbitrarily set to limit computation time and balance with accuracy at very high scattering events. The figures shown in Section 5.8 show the affects of rouletting in high turbidity waters, as the probability of seeing photons scattered more than 60 times is dramatically reduced due to the rouletting threshold chosen. However, at 60 scattering events, the photon path probability is more than four orders of magnitude lower than the most probable path, and it was judged that this was sufficient for the information presented. The MCNS allows for flexibility based on what aspect of the light-field the system designer wishes to analyze.

Once this threshold has been reached, and for each subsequent optical event, a uniform random variable is compared against an arbitrary rouletting threshold, $1/\alpha$ ($1/\alpha = 0.1$ in Photonator) and the photons weight is set according to Eq. 4.17.

$$w' = \begin{cases} 0 & \text{if } \mathbb{X} > \frac{1}{\alpha} \\ \alpha w & \text{if } \mathbb{X} \leq \frac{1}{\alpha} \end{cases} \quad (4.17)$$

where w' is the new weight, w is the old weight, \mathbb{X} is a random number chosen from a uniform distribution on $[0, 1]$, and α is the roulette threshold. Effectively, for $\alpha = 10$, this means that 90% of the time, once the packet has reached a minimum weight, it will be terminated. However, 10% of the time, the weight will be boosted by a factor 10, thereby preserving the total system energy. This method reduces the amount of unnecessary calculations that the system has to perform. Essentially, when an improbable path is terminated, its weight is combined with another equiprobable path, thereby preserving the total probability, but reducing the computational burden.

Scattering

After choosing an appropriate distance to move, a new direction angle is chosen for the photon. This angle is chosen according to a volume scattering function (VSF), discussed in Section 3.3 on page 10. Various VSFs can be used, including the Henyey-Greenstein analytic function, shown in Fig. 2.1 or the ocean water VSF taken by Petzold [49], shown in Fig. 5.1.

The scattering angle is chosen from the VSF via the equation

$$\mathbb{R} = \int_0^{\theta'} \tilde{\beta}(\theta) \sin \theta \, d\theta \quad (4.18)$$

where \mathbb{R} is a random number chosen on the interval $[0, 1]$, and θ' is the chosen polar scattering angle. This equation depends on the integration of the VSF to form a cumulative distribution function (CDF). Several of these are pictured in Fig. 4.27. Since there is no analytic expressions for the ocean water VSFs, this equation is numerically evaluated. Several analytical or empirical solutions for the VSF that come close to modeling the natural water VSF are presented by Haltrin [69].

Due to the symmetric nature of radial scattering underwater, caused by the random orientation of scatterers, the radial scattering angle, ϕ' is chosen from the distribution

$$\mathbb{R} = \frac{1}{2\pi} \phi' \quad (4.19)$$

yielding $\phi' = 2\pi\mathbb{R}$, where \mathbb{R} is a random number chosen on the interval $[0, 1]$. Note that the random number used to choose θ' should be different from the random number used to choose ϕ' in order that they both be independent random variables.

Once the new scattering direction, based on θ' and ϕ' is chosen, the direction cosines must be updated in order to give the photons global direction of travel, as the scattering angles ϕ and θ describe the scattering direction *based on the current direction of travel*. The conversion between the

local and global coordinate frame involves a rotation matrix.

4.3.3 Moving the photons

After choosing a scattering length and scattering angles, the position and direction cosines of the photon group must be updated.

Update position

The photons new position is defined as

$$x' = r\mu_x \quad (4.20)$$

$$y' = r\mu_y \quad (4.21)$$

$$z' = r\mu_z \quad (4.22)$$

where μ_x, μ_y , and μ_z are the current direction cosines, which define the direction vector based on the current direction of propagation, and r is the randomly chosen propagation distance.

Updating the direction cosines

After the new position, x', y', z' , is chosen, the direction cosines need to be updated with the newly chosen pointing angles, ϕ' and θ' .

Given a vector, $[\mu_x, \mu_y, \mu_z]$, defining the photons current direction of motion, also defined by θ, ϕ , the new direction vector when rotated by ϕ', θ' is defined as [62]

$$\begin{bmatrix} \mu'_x \\ \mu'_y \\ \mu'_z \end{bmatrix} = \begin{bmatrix} \mu_x \mu_z / \sqrt{1 - \mu_z^2} & -\mu_y / \sqrt{1 - \mu_z^2} & \mu_x \\ \mu_y \mu_z / \sqrt{1 - \mu_z^2} & \mu_x / \sqrt{1 - \mu_z^2} & \mu_y \\ -\sqrt{1 - \mu_z^2} & 0 & \mu_z \end{bmatrix} \begin{bmatrix} \sqrt{1 - \mu_s^2} \cos \phi' \\ \sqrt{1 - \mu_s^2} \sin \phi' \\ \mu_s \end{bmatrix}, \mu_z^2 < 1 \quad (4.23)$$

where μ_s is defined as $\cos \theta'$, to make use of the convenient relationship, $\sin \theta' = \sqrt{1 - \mu_s^2}$, as that computation is generally faster than using the equation, $\sin \theta' = \sin \cos^{-1} \theta'$. This relationship is also used extensively in Eq. 4.3.3 to compute $\sin \theta$, as $\mu_z = \cos \theta$. This equation comes from using two basic rotation matrices to rotate the direction cosines into the new direction. This form looks like

$$\begin{bmatrix} \mu'_x \\ \mu'_y \\ \mu'_z \end{bmatrix} = R_z(\phi') R_x(\theta') \begin{bmatrix} \mu_x \\ \mu_y \\ \mu_z \end{bmatrix} \quad (4.24)$$

where $R_z(\phi)$ and $R_x(\theta)$ are the standard rotation matrices about the z and x global coordinate frames.

When μ_z is very close to 1, meaning the direction vector is nearly pointing straight down the z-axis, Eq. 4.3.3 reduces to

$$\begin{bmatrix} \mu'_x \\ \mu'_y \\ \mu'_z \end{bmatrix} = \begin{bmatrix} \sin \theta' \cos \phi' \\ \sin \theta' \sin \phi' \\ \frac{\cos \theta}{|\cos \theta|} \cos \theta' \end{bmatrix} = \text{sign}(\mu_z) \begin{bmatrix} \sqrt{1 - \mu_s^2} \cos \phi' \\ \sqrt{1 - \mu_s^2} \sin \phi' \\ \mu_s \end{bmatrix}, \mu_z^2 \approx 1. \quad (4.25)$$

Notes

Since μ_x, μ_y , and μ_z define a unit vector pointing in the direction of photon travel, it is important to make sure that they are normalized. Due to rounding errors in computation, they can begin to drift which would distort the movement. A simple check is to verify that

$$\sqrt{\mu_x^2 + \mu_y^2 + \mu_z^2} \approx 1. \quad (4.26)$$

If this check fails, the vectors can be normalized by dividing each value by $\sqrt{\mu_x^2 + \mu_y^2 + \mu_z^2}$.

4.3.4 Photon Reception

Receiver definition

Photon packets that propagate to the receiver plane are terminated and their data is recorded: location, angle of arrival, weight and distance traveled. The number of scattering events can be inferred from the weight by the equation

$$\frac{\log(w)}{\log(\omega_0)} = N_s \quad (4.27)$$

where w is the photon packet weight, ω_0 is the albedo of the environment, and N_s is the number of scattering events. Note that Eq. 4.3.4 only applies when wall or surface interactions are not present, as they reduce the photon weight. In this case, individual scattering events have to be tracked separately from the photon packet weight.

The photons that intersect the receiver plane can either be processed in real-time, along with the rest of the simulation, or the data can be stored for later processing. The latter method allows for much more flexibility, as the entire light-field on the receiver plane is defined and can be processed separately for various receiver configurations.

Each “receiver” is defined by its location, aperture, and field of view (FOV). Each photon packet is parsed to determine if its location is within the radius of the aperture and whether its azimuthal angle of arrival is less than the FOV of the receiver. The photon reception is independent of the polar angle of arrival. Multiple receivers can be defined and processed concurrently to decrease total simulation

time. For a more accurate representation of the receiver FOV, an equation can be defined to express the FOV and the following equation used to decrease the photon weight based on its angle of arrival

$$w'_i = F(\cos^{-1}(\mu_{zi}))w_i \quad (4.28)$$

where w'_i is the new photon weight, $F(\theta)$ is the receiver FOV function in degrees, μ_{zi} is the incident photons angle of arrival, and w_i is the incident photons weight.

Additionally, for more accurate simulations the interactions with the receiver window can be simulated. Photons which are not within the critical angle of the window are discarded. To simulate a physical separation between the window and the actual receiver optics, the photons incident angles are taken into account, along with the refractive index of the window, window thickness, and the distance from the window to the receiver optics. The final photon position and angle are then corrected before determining whether they fall into a specific receiver.

As with surface interactions, the Fresnell Equations and Snell's Law can be used to adjust the photons weight and incident angle as it moves through the window. The Fresnell transmission equation is given by

$$R_s = \left(\frac{n_{water} \cos \theta_i - n_{window} \cos \theta_t}{n_{water} \cos \theta_i + n_{window} \cos \theta_t} \right)^2 \quad (4.29)$$

$$R_p = \left(\frac{n_{water} \cos \theta_t - n_{window} \cos \theta_i}{n_{water} \cos \theta_t + n_{window} \cos \theta_i} \right)^2 \quad (4.30)$$

$$T_{unpolarized} = 1 - (R_s + R_p)/2 \quad (4.31)$$

where n_{window} and n_{water} is the index of refractions for the optical window and the water respectively, θ_i is the incident angle the light makes with the window normal, θ_t is the transmission angle, and $T_{unpolarized}$ 100% is the percentage of light transmitted into the window. The angle at which the light is transmitted is given by Snell's Law:

$$n_{water} \sin \theta_i = n_{window} \sin \theta_t \quad (4.32)$$

where θ_i is the angle the light makes incident to the window normal, and θ_t is the transmitted angle. The value of $T_{unpolarized}$ would be used to reduce the photon path weight for the path through the window.

Circular Integration of the Lightfield

For the simulation results presented in Section 5.10 on page 149 radial irradiance of the light-field is calculated from the center of the beam outwards in the receiver plane. This produces a vector of

irradiance vs. distance from the beam center. Using this information, the power in an aperture of given radius and position can be calculated based on the formula

$$P(d; r) = \sum_{R=d-r+\Delta r}^{d+r} I(R) \Delta A(R) \quad (4.33)$$

where $P(d; r)$ is the power in a circle of radius r at a radial distance d from the beam center, Δr is the radial bin width, $I(R)$ is the irradiance at distance R from the beam center, $A(R)$ is the area circular segment overlap between the receiver aperture at $(d, 0)$ and the circle of radius R at location $(0, 0)$. This is best illustrated in Fig. 4.6.

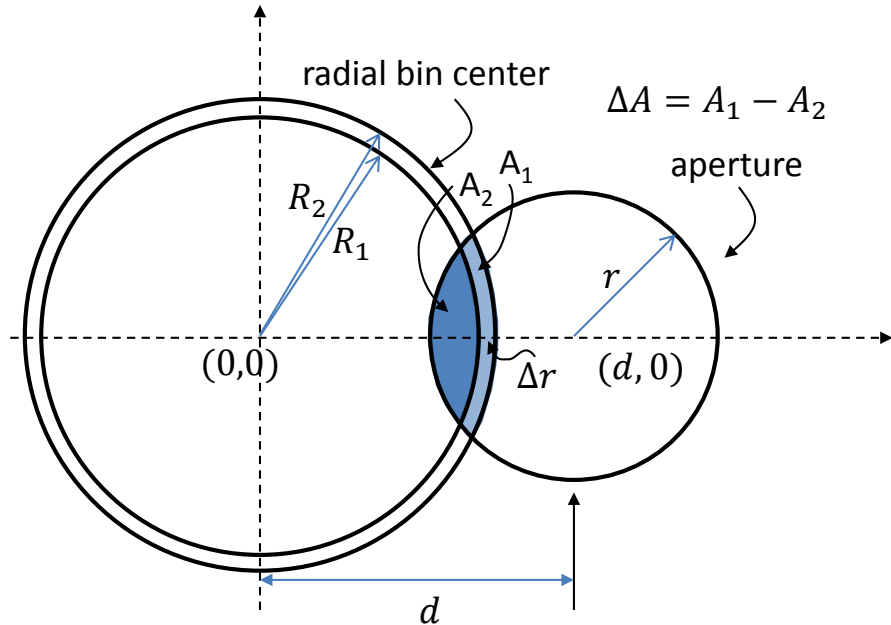


Figure 4.6: Illustration showing how the power is integrated over an aperture that is offset from the beam center.

The equation for calculating $A(R)$ is given by [70]

$$A(R; d; r) = r^2 \cos^{-1} \frac{d^2 + r^2 - R^2}{2dr} + R^2 \cos^{-1} \frac{d^2 + R^2 - r^2}{2dR} - \quad (4.34)$$

$$\frac{\sqrt{(-d+r+R)(d+r-R)(d-r+R)(d+r+R)}}{2}, \quad \text{if } R > r - d. \quad (4.35)$$

If, however, the bin center, $R < (r - d)$, then $A(R)$ is simply the area of a circle of radius R or, πR^2 .

4.3.5 Determining Accuracy of the Simulation Output

At its simplest form, the MCNS simulation is used to determine the expected, or mean, value of the underwater light-field at the receiver plane, under various conditions. It can also be considered as computing the probability of photons moving from the transmitter to the receiver. This expected value is determined by complex interactions of photons with the underwater environment, and be considered as a random variable X . The MCNS simulation takes independent, identically distributed (i.i.d), random samples, x_n from this random variable, and the sample mean is calculated as

$$\hat{x} = \frac{1}{N} \sum_{i=1}^N x_i \quad (4.36)$$

where \hat{x} is an unbiased estimator of the population mean, μ , and x_i are the individual observations in the sample. The observations can be any measured quantity, such as photon weight, position, angle of arrival, etc.

As stated above,

$$\mu = E[X] \quad (4.37)$$

also,

$$VAR[X] = \sigma^2 \quad (4.38)$$

where σ^2 is the variance of the population. Both $E[X]$ and $VAR[X]$ are unknown and the MCNS is being used to determine them via random sampling. By the central limit theorem (CLT) [71] we know,

$$P\left\{-z \leq \frac{\sqrt{N}}{\sigma}(\bar{x} - \mu) \leq z\right\} \rightarrow P_{N \rightarrow \infty}\{-z \leq \mathcal{N}(0, 1) \leq z\} \quad (4.39)$$

where $\mathcal{N}(0, 1)$ is the standard Normal distribution, and \bar{x} is an arbitrarily chosen interval. In other words, the distribution of the sample means, $p(\bar{x})$, tends towards a Normal distribution, regardless of the distribution of the samples. By setting Eq. 4.39 equal to $1 - \delta$ and rearranging, we arrive at

$$P\left\{\mu \in \left[\bar{x} - \frac{z\sigma}{\sqrt{N}}, \bar{x} + \frac{z\sigma}{\sqrt{N}}\right]\right\} = 1 - \delta \quad (4.40)$$

where δ and z are chosen based on the desired confidence interval and using standard Normal tables (found in most statistics textbooks. Example [72]) and the equation

$$P\{|\mathcal{N}(0, 1)| \leq z\} = 1 - \delta. \quad (4.41)$$

Based on the result in Eq. 4.40 we are able to determine when the population mean, μ lies within

the confidence interval determined from Eq. 4.41 from the sample mean, \bar{x} . The following equation is used to describe whether μ lies within one standard deviation from \bar{x} .

$$\bar{x} \pm \frac{\sigma}{\sqrt{N}}. \quad (4.42)$$

The confidence interval is inversely proportional to the square root of the number of samples, N . In order to decrease the size of the confidence interval by a factor of two, the number of samples would have to be increased by a factor of four. It should also be noted that since σ is not known *a priori* an unbiased estimator of σ must be used instead.

$$S_N^2 = \frac{1}{N-1} \sum_{i=1}^N (x_i - \bar{x})^2 \quad (4.43)$$

where x_i are the individual sample observations. Substituting Eq. 4.43 into Eq. 4.42 yields the following equation for determining a one standard deviation confidence interval for the population mean.

$$\bar{x} \pm \frac{S_N}{\sqrt{N}}. \quad (4.44)$$

For further information, readers are referred to the “Error Estimates” section of [73] and the “Estimation” section of [72].

Binomial Confidence Interval Bound

One difficulty with this approach is that the central limit theorem in Eq. 4.40 does not hold very well for when the population mean is very close to 1 or 0. Since the population mean that is being calculated with the MCNS simulation is usually a very small number, close to 0, a more appropriate method to determine the confidence interval is to bound the confidence interval using the Binomial confidence interval.

The binomial distribution is the sum of n Bernoulli trials, each of which has one of two outcomes, for instance, ‘1’ or ‘0’. For n trials with the probability of success, or ‘1’, being p , the Binomial distribution can be approximated with a Normal distribution

$$\mathcal{N}(np, np(1-p)) \quad (4.45)$$

with the provision that n and p meet the criteria that np and $n(1-p)$ be greater than 5, which yields a 95% confidence interval of approximately $(2p, 0.5p)$. In other words, the receiver must observe at least 5 photons in order to make an estimate of the mean value and its confidence interval. In the simulations in Chapter 5 the MATLAB function `berconfint()` is used to compute the confidence interval for each simulation given $n_{photons}$ observations out of $n_{transmitted}$ simulated photon paths. For more details on this method see [74].

Since each photon path has a weight on the range of $[0, 1]$ the Binomial confidence interval will be overestimating the interval, since it assumes that each trial only takes the values of either ‘1’ or ‘0’. If we call our unknown random variable X , then since $0 \leq X \leq 1$, we know $X^2 \leq X$ and $E[X^2] \leq E[X]$. Therefore,

$$Var(X) = E[X^2] - E[X]^2 \leq Var_{bin}(X) = E[X] - E[X]^2 \quad (4.46)$$

with $Var_{bin}(X)$ being the variance of a Binomial RV. This equal has equality when $E[X^2] = E[X]$, which only happens when $X = 1$ or 0 as in a Binomial distribution. This only holds when $E[X] < 1/2$, which is true for nearly all of the useful simulated channels. This shows that the variance of our unknown random variable is less than the variance of the Binomial distribution having the same number of non-zero values. The reduction in variance yields a reduction in the size of the confidence interval.

4.3.6 On-line Computation of Mean and Variance Statistics

In order to reduce the memory requirements of the simulation, it is important to determine the important statistics of the simulation, like mean and variance, in an “on-line” method, or concurrent with the running simulation. This avoids the problem of saving large amounts of data in order to determine the statistics in bulk. While the on-line mean calculation is straightforward, the variance calculations are not, and require individual treatment depending on which quantity is being measured.

Online Mean Calculation

The total photon weight in each receiver is averaged to obtain the mean photon weight per receiver, non-receiver photons are also factored into the mean to produce a normalized intensity value. The mean weight is calculated by

$$\bar{w}_{rx} = \frac{1}{N_{tot}} \sum_{i=1}^{N_{rx}} w_i \quad (4.47)$$

where \bar{w}_{rx} is the average weight at the receiver, w_i is the individual received photon packet weights, and N_{tot} and N_{rx} are the number of transmitted and received photon packets, respectively. Non received photons are assumed to have a zero weight.

Online Weighted Mean Calculation

When looking at certain statistics at the receiver, such as angle of arrival, it is important to weight each element by the path weight. This causes the need for calculating the weighted mean in an online manner. For this, the following two equations can be used

$$\bar{x}_{n+1} = \bar{x}_n + \frac{w_{n+1}(x_{n+1} - \bar{x}_n)}{\sum_{i=1}^n w_i + \bar{x}_n} \quad (4.48)$$

For finding the total mean of a separate partitions of a sample of weighted values, the following expression can be used

$$\mu = \frac{S_1\bar{x}_1 + S_2\bar{x}_2 + \dots + S_n\bar{x}_n}{\sum_{i=1}^n S_i} \quad (4.49)$$

where S_n is the sum of all the weights in that partition.

Online Variance Calculation

When processing the received data an online method is used to calculate the variance, as this reduces the complexity of having to processes the data twice - once to get the mean and once to calculate the variation from the mean. This method, as proposed by Welford [75] and further elaborated on by Knuth [76], can be used to incrementally calculate the variance of a population based on samples.

Given a new element, x_{new} , an existing sample mean of \bar{x}_n , and a sample variance of σ_n^2 , the following sets of equations can be used to iteratively compute the variance of the sample and population:

$$\Delta = x_{new} - \bar{x}_{n-1} \quad (4.50)$$

$$\bar{x}_n = \bar{x}_{n-1} + \Delta/n \quad (4.51)$$

$$M_{2,n} = M_{2,n-1} + \Delta(x_{new} - \bar{x}_n) \quad (4.52)$$

$$\sigma^2 = \frac{M_{2,n}}{n} \quad (4.53)$$

and the implementation can be seen in the code in Appendix B.

Variance Calculation for Two Partitions

Since when computing the mean and variance of the photon path weights, a significant majority of the paths have weights of zero, it is not necessary to perform an online calculation for each of these. Instead, the sample is partitioned into two sets - one set of all non-zero weights and one set of zero weights. The method for computing the variance in this case is provided by Chan et al [77] for a partition of a sample into sets X_a and X_b

$$\delta = \bar{x}_a - \bar{x}_b \quad (4.54)$$

$$\bar{x}_X = \bar{x}_a + \delta \frac{n_b}{n_X} \quad (4.55)$$

$$M_{2,X} = M_{2,a} + M_{2,b} + \delta^2 \frac{n_a n_b}{n_X} \quad (4.56)$$

where n_a , n_b , and n_X are the number of elements in each of the sets.

Variance Calculation for Unequal Partitions

In order to speed up the simulation results, often the simulation is run in parallel, generating many different light-field sets that need to be combined together. Each set will have its own variance and size. When this is the case the following equation can be used to determine the total sample variance based on the variance of partitions

$$\text{Var}(X_1, \dots, X_n) = \frac{1}{n-1} \left(\sum_{j=1}^g [(k_j - 1)\text{Var}(X_j) + k_j(\bar{x}_j - \bar{x})^2] \right) \quad (4.57)$$

where X_n are the g partitions, each with k_j elements, yielding n elements in total. \bar{X} is the weighted average of all the means.

4.4 Determining Channel Bandwidth from Simulation

Since the Photonator simulation assumes a homogeneous medium, the speed of photon propagation is directly proportional to the time-of-flight (TOF) of the photon, which is given by

$$t_{\text{photon}} = \frac{d_{\text{photon}} n_{\text{water}}}{c} \frac{m}{m/s} \quad (4.58)$$

where t_{photon} is the TOF, d_{photon} is the distance traveled by the photon, n_{water} is the index of refraction for water, and c is the speed of light in a vacuum. To remove the affects of ballistic TOF or latency, the time delay is normalized by the direct distance from transmitter to receiver using the equation,

$$\Delta t_{\text{photon}} = t_{\text{photon}} - t_0 \quad (4.59)$$

where t_0 is the ballistic TOF, gives the extra time that the photon takes to arrive at the receiver due to scattering in the environment. The equation for t_0 is given by

$$t_0 = \frac{d_{rx/tx} n_{\text{water}}}{c} \quad (4.60)$$

where $d_{rx/tx}$ is the straight line distance between the receiver and transmitter.

Using the TOA information, the temporal response of the channel can be estimated. Since the simulation input is an impulse response, which has all photon packets originating at the same moment in time, the PDF of the TOA at the receiver represents the impulse response of the combined channel

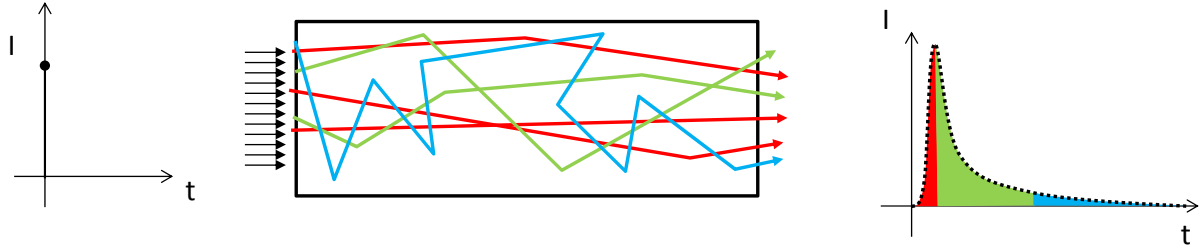


Figure 4.7: Illustration showing how the multiple scattering in water affects the temporal dispersion of an impulse of light propagating through the water.

and receiver. This is illustrated in Fig. 4.7. This impulse response PDF is approximated by a discrete histogram of the time of arrival, where the bin size, T_{bin} determines the maximum frequency that can be approximated due to Nyquist's sampling theorem,

$$f_{max} = \frac{f_s}{2} = \frac{1}{2T_{bin}} \quad (4.61)$$

where f_{max} is the maximum frequency that can be represented with the bin width, T_{bin} in seconds. For example, when choosing a bin size of 60 mm, the maximum frequency that can be represented in the channel dispersion estimation is given by

$$f_{max} \{D_{bin} = 0.06m\} = \frac{c}{2D_{bin}n_{water}} = 1.88GHz. \quad (4.62)$$

To transform the impulse response to a frequency response, the discrete Fourier transform (DFT) of the data can be taken. The MATLAB command, `freqz()` can be used to easily compute this value. The transform is computed using the following expression

$$H(z)|_{z=e^{j\omega}} = \frac{\sum_{k=0}^{M-1} b(k)e^{-j\omega k}}{\sum_{l=0}^{N-1} a(l)e^{-j\omega l}} \quad (4.63)$$

where, in our case, $M = 0$ since the output is defined based on the time-delayed input only, N is the number of bins in the impulse response measurement, $a(l)$ is the power at bin l , and $\omega = 2\pi f_s$. This is the basic DFT form, where the system impulse response is taken to be a digital filter response.

A plot showing the frequency response of various number of bins is shown in Fig. 4.8. Since this function will be convolved with the true frequency response, the function that is closest to a delta function at 0 Hz will provide the best representation of the true frequency response. It is evident from the figure that as the number of bins grows, the spread of power over various frequencies decreases.

The larger the number of bins used to estimate the temporal dispersion, the less ripple is imposed upon the estimated frequency response. This is due to the fact that the number of bins can be considered a windowing function (maximum time limit) on the actual PDF of time-of-arrival. When

the maximum measured TOA is limited in time, this equivalent to multiplying the time function by a square window extending from $t = 0$ to $t = N_{bins} T_{bin}$. This square shape in time is represented by a sync function in frequency, which is convolved with the true frequency response. A reduction in the window size will result in more ripples in the frequency response, however this must be balanced against computational and memory constraints when calculating the histogram of the TOA. Additionally, if very small bin sizes are chosen, the random nature of the simulated photons will cause some bins to have no value. For the results presented in Chapter 5 Section 5.9 on page 138, N_{bins} was chosen to be 200, which represents a maximum excess travel distance for the photon of 12 meters.

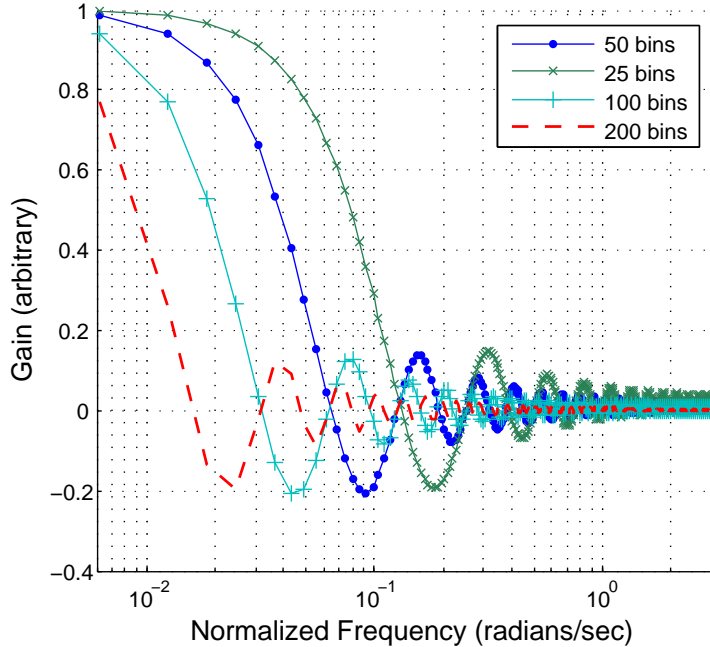


Figure 4.8: The frequency response of various sizes for the number of histogram bins. The limit on the number of bins represents a window function in time, and a sinc function in frequency. The more bins are used in the histogram, the less effect the window has on the true frequency response.

Each photon packet that arrives at the receiver has its packet weight placed into the appropriate bin, based on its total distance traveled. Once the total histogram is computed, it is normalized by the total histogram weight in order to produce a PDF, or similarly, a discrete-time impulse response. *In essence, the impulse response shows the distribution of power over time at the receiver. By taking the z-transform of this impulse response, we can arrive at a frequency response.* Fig. 4.9 shows an example impulse response for a 4" receiver of various FOV's operating at 25 attenuation lengths from the transmitter. The data is shown on a semi-log plot to emphasize how the initial power is very high

and the power at longer times is much lower. The smaller FOV's demonstrate a more peaked impulse response at the lower times.

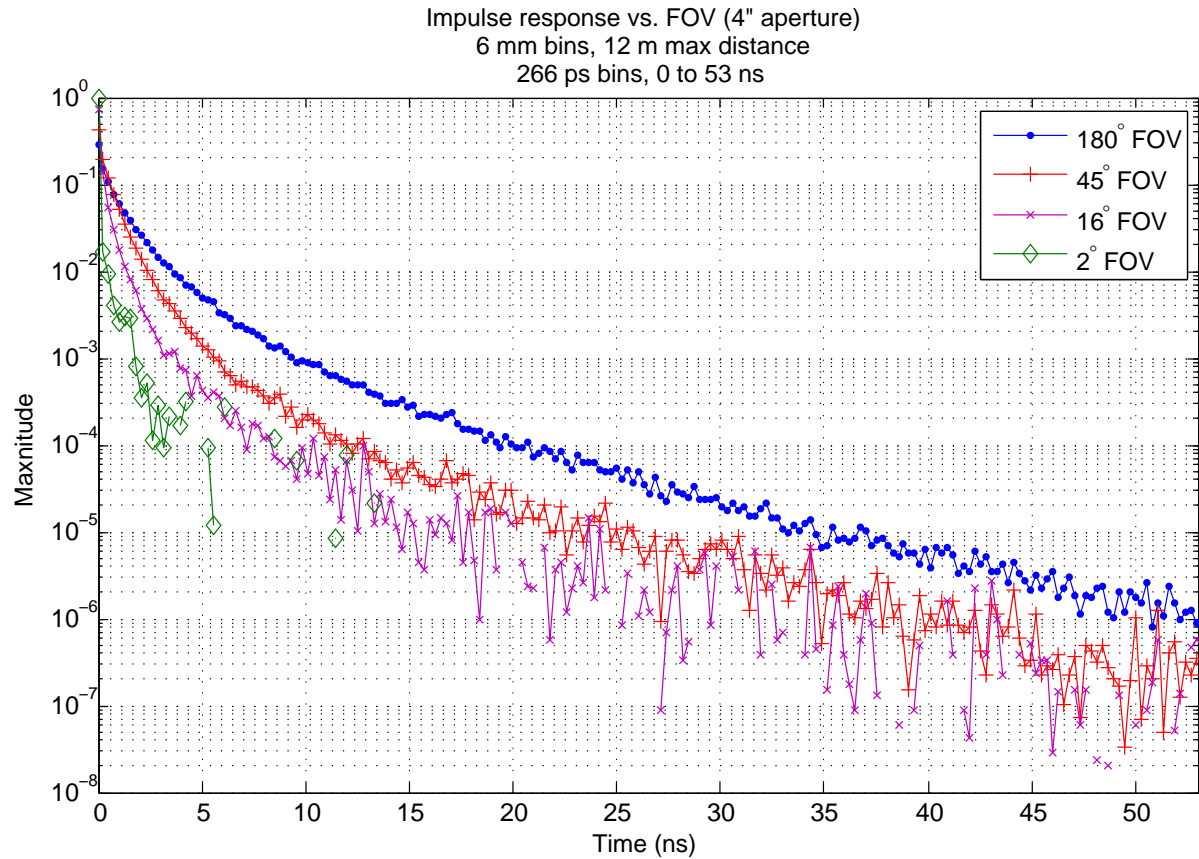


Figure 4.9: Figure showing impulse response of transmission at 25 attenuation lengths into a 4 inch receiver of various FOVs. The higher the FOV the larger the tail of the impulse response is. For smaller FOV's, less photons are collected, which increases the variance of the plotted data.

4.5 Validating the Simulation Model

Careful validation of the simulation model is necessary to have any confidence in the output data. By validating the model with published experimental data, other models, and laboratory experiments we can then use the model to make predictions about system performance in a variety of situations.

Aspects of the model that should be validated include the initial conditions, such as beam width and divergence, the propagation and motion of the individual photon packets, the scattering of each packet, and the reception of the photon packets to form an aggregate value of power or intensity on the receiver plane.

4.5.1 Validation Against Mie Scattering from Fixed-Size Polystyrene Spheres

The MC model was validated against experimental data for multiple scattering from a aqueous solution of polystyrene spheres. The experimental data was taken by E. Barrocal [78]. To simulate these results, the initial conditions of the beam were taken from the initial beam intensity profile in [78], shown in Fig. 4.10. Photon starting positions were randomly sampled to match this distribution and propagated through the medium. Boundary conditions were identical to the experiment (10 mm cube, see Fig. 4.11) and the scattering phase function was calculated via Mie scattering theory for the appropriately sized spheres. The scattering phase function is shown in Fig. 4.12.

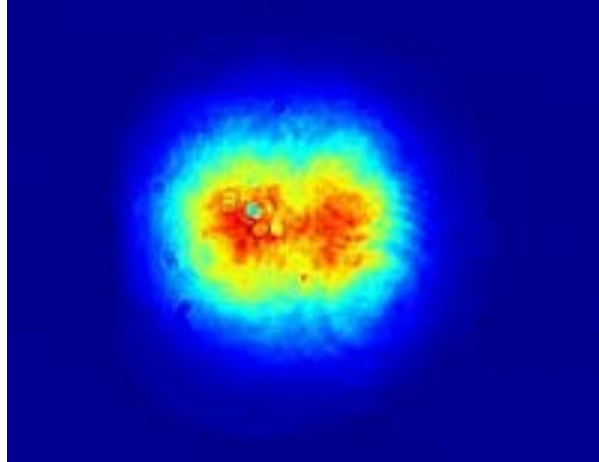


Figure 4.10: Experimental on-axis beam profile from [78].

Three different optical depths, or attenuation lengths, were tested, 2, 5, and 10, corresponding to c values of 200 m^{-1} , 500 m^{-1} , and 1000 m^{-1} , since the path length was only 10 mm. For each attenuation length, the receiver was positioned on-axis and 90° off axis. The simulated results were

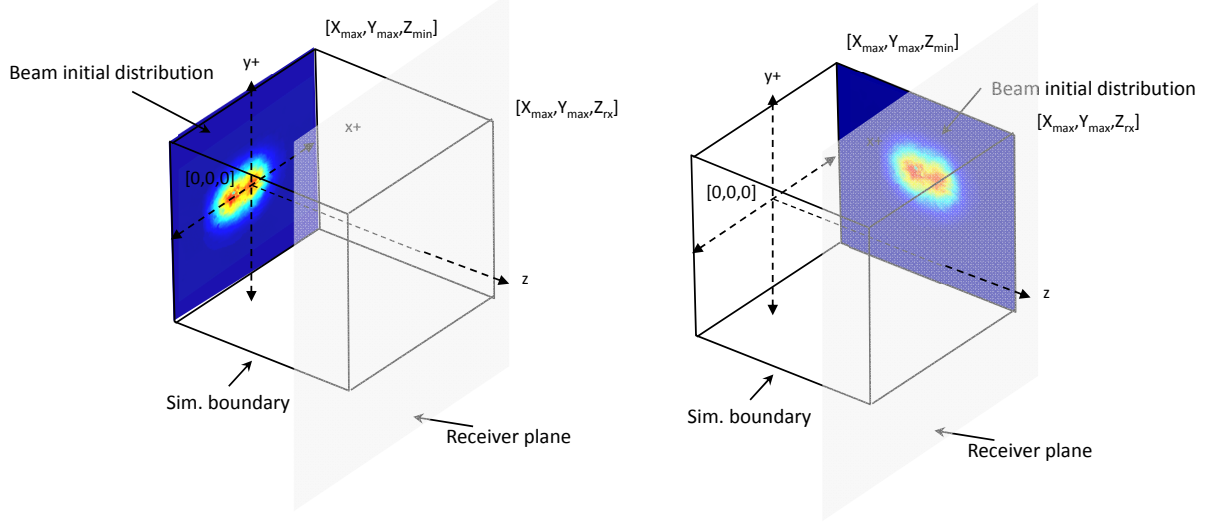


Figure 4.11: Simulation geometry for the simulations of fixed-size polystyrene spheres. Left geometry is on-axis, right is off-axis.

compared to the simulated results from [78] to validate the simulations method of propagating photons. For the simulation, the boundaries were taken to be perfectly absorbing and the refractive affects of the receiver window were not taken into account. The receiver field-of-view was chosen to match the imaging system employed in [78], with a FOV of 8.5° . Fig. 4.11 shows the geometry of the simulations, with the beam source being placed to the right of the receiver to simulate looking at the beam off-axis.

The results are presented in Fig. 4.13, Fig. 4.14, Fig. 4.15, Fig. 4.16, Fig. 4.17, Fig. 4.18.

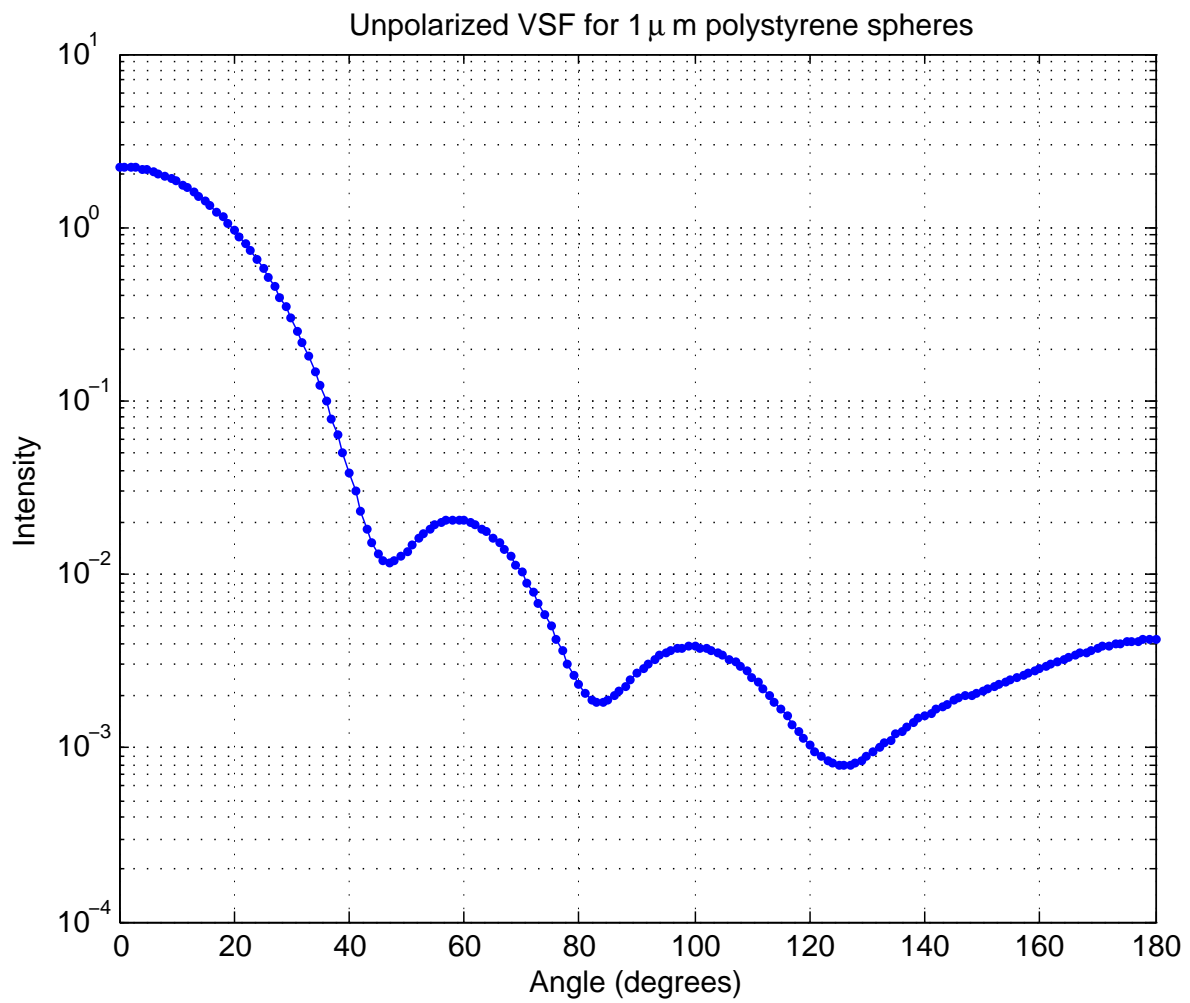


Figure 4.12: Scattering phase function for $1 \mu\text{m}$ polystyrene spheres suspended in water. Calculated using web based program [79]

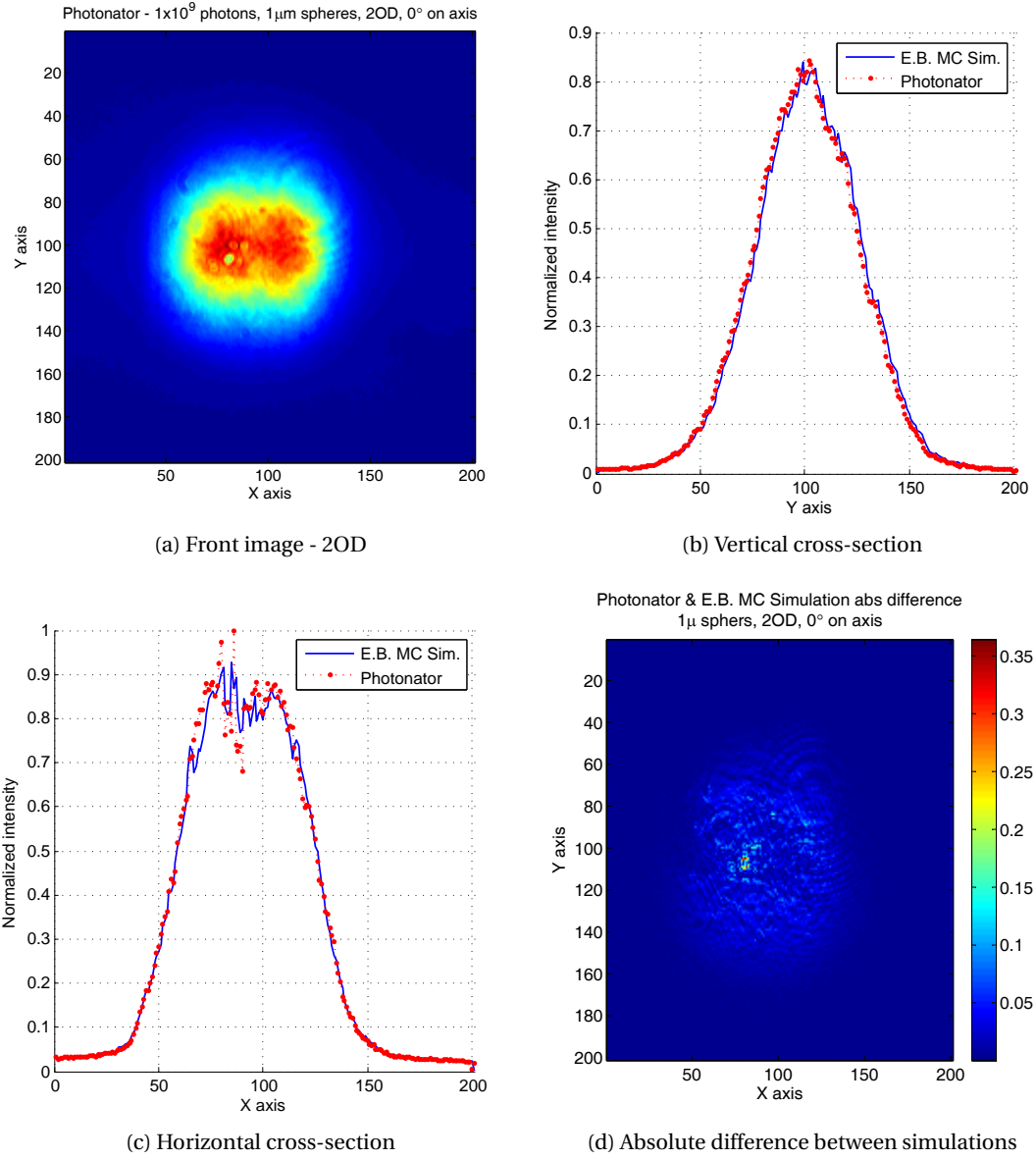


Figure 4.13: Photonator on-axis comparison to published data from [78] at an optical depth of 2 and 1×10^9 photons simulated. Images show the absolute difference between the two, along with cross-section comparisons. Notice the “hole” in the beam profile in Fig. 4.13a is not distinct due to the limited number of photons in the simulation.

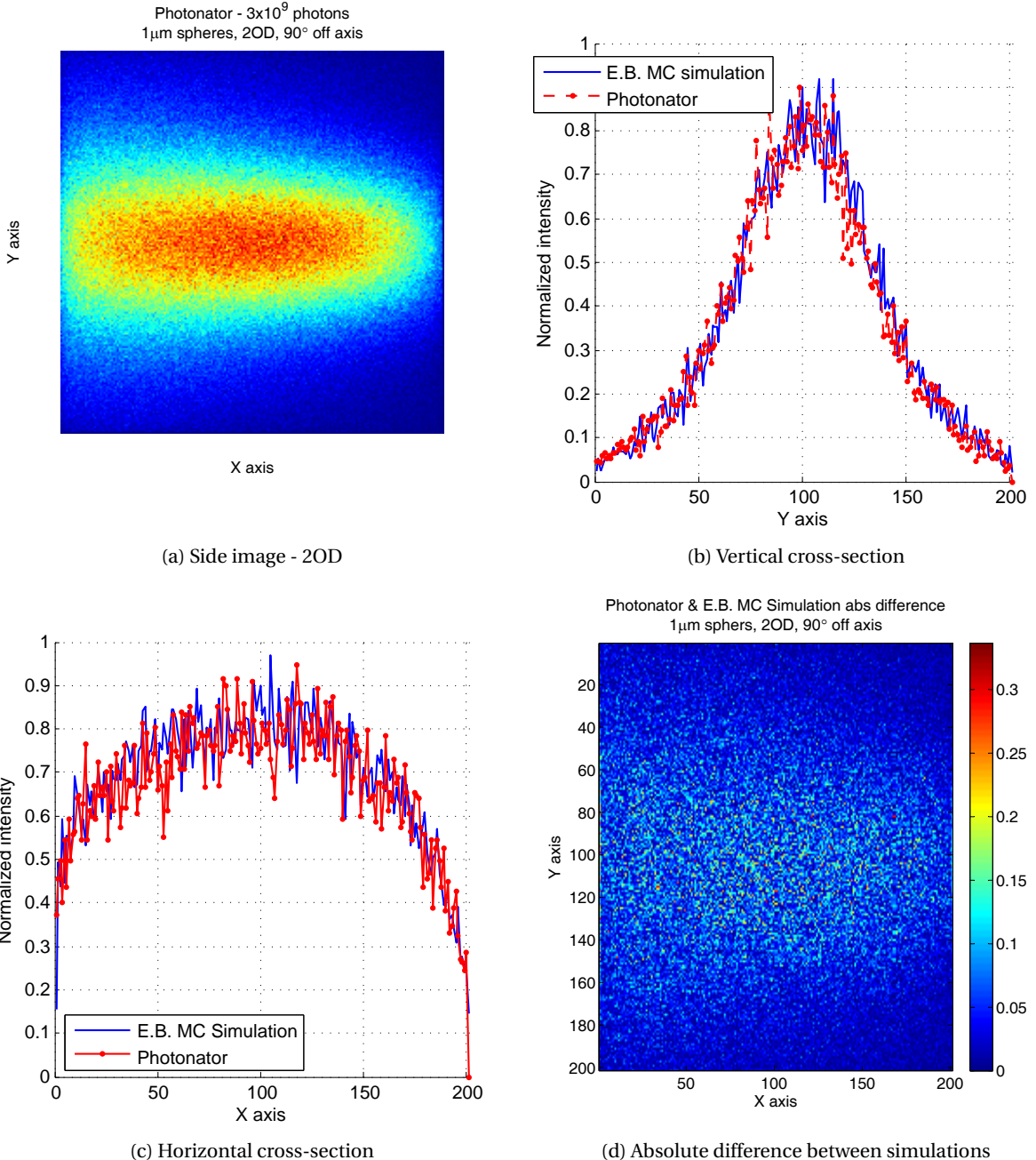


Figure 4.14: Photonator 90° off-axis comparison to published data from [78] at an optical depth of 2 and 3×10^9 photons simulated. Images show the absolute difference between the two, along with cross-section comparisons. The absolute differences shown in Fig. 4.14d are quite noisy, due to the limited number of photons.

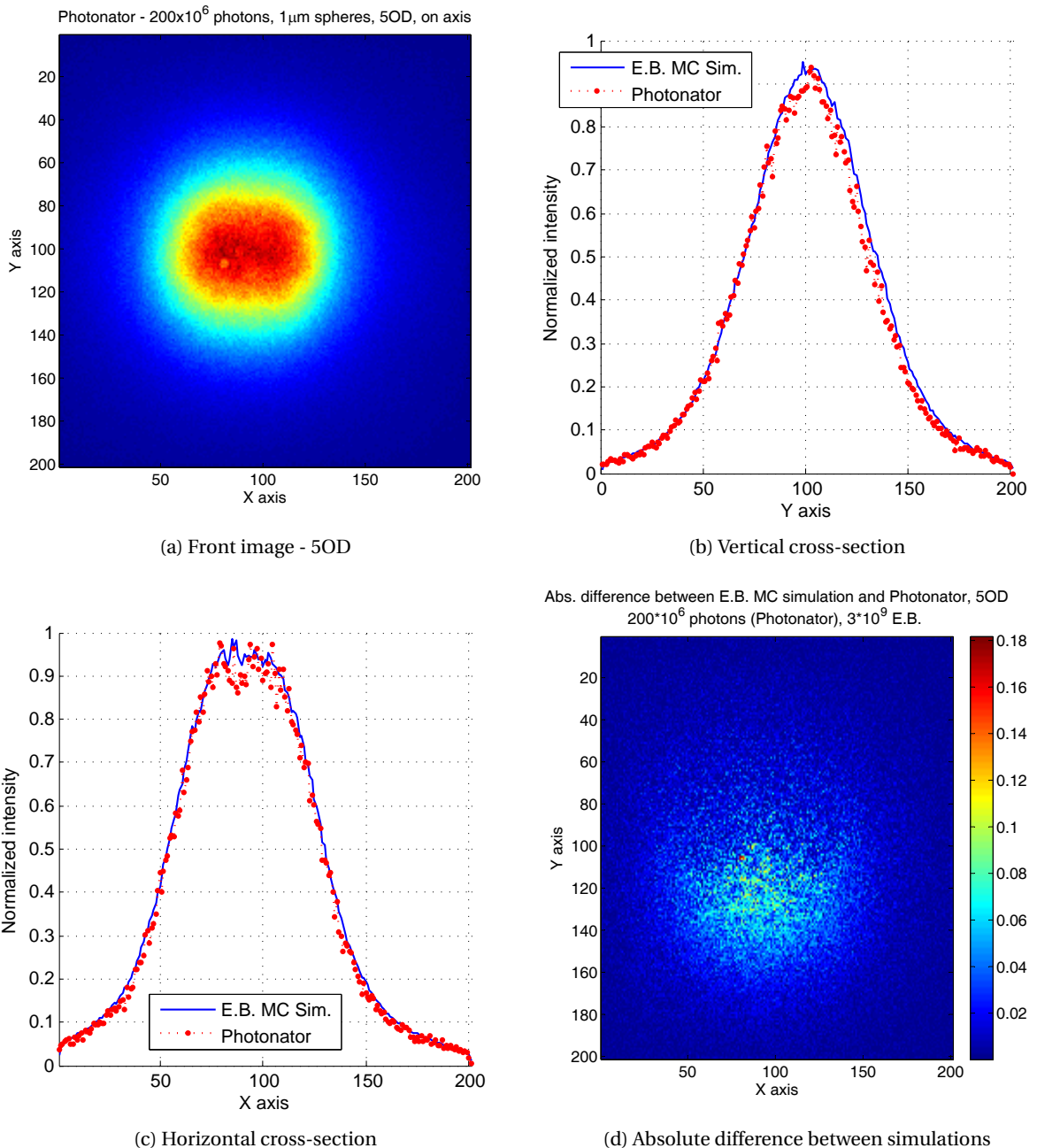
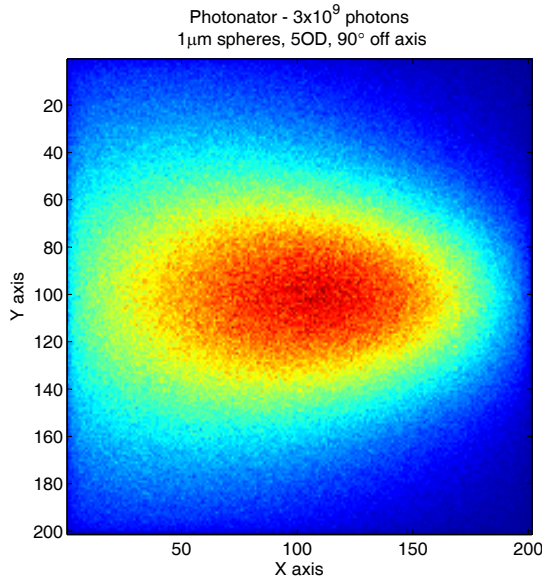
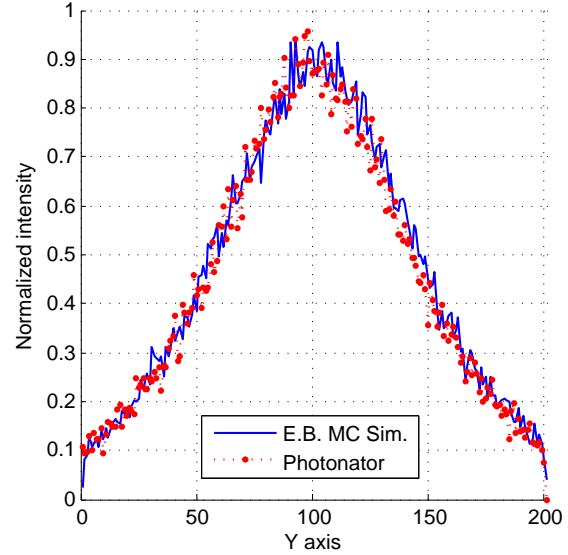


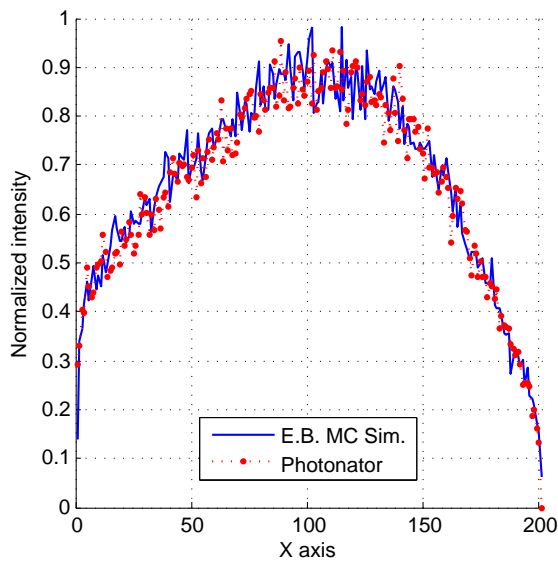
Figure 4.15: Photonator on-axis comparison to published data from [78] at an optical depth of 5 and 200×10^6 photons simulated. Images show the absolute difference between the two, along with cross-section comparisons. Better agreement could be achieved by simulating more photons. However the 1/15th reduction in simulated photons (as compared to the 3×10^9 of the original) still yields good results.



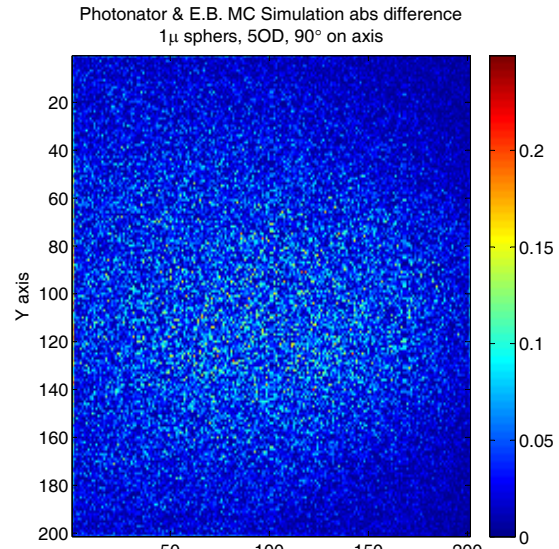
(a) Side image - 5OD



(b) Vertical cross-section



(c) Horizontal cross-section



(d) Absolute difference between simulations

Figure 4.16: Photonator 90° off-axis comparison to published data from [78] at an optical depth of 5 and 3×10^9 photons simulated. Images show the absolute difference between the two, along with cross-section comparisons.

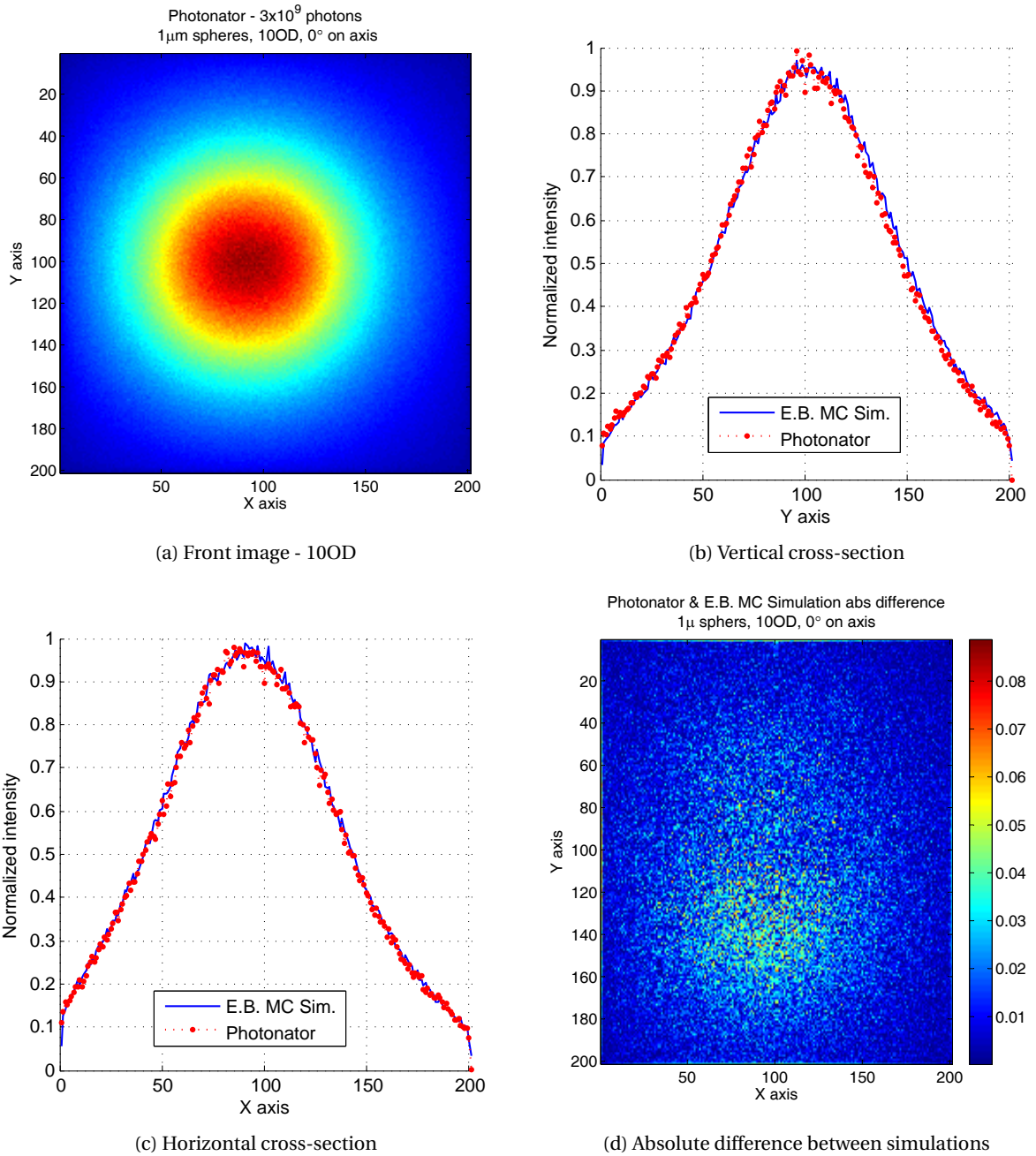


Figure 4.17: Photonator on-axis comparison to published data from [78] at an optical depth of 10 and 3×10^9 photons simulated. Images show the absolute difference between the two, along with cross-section comparisons.

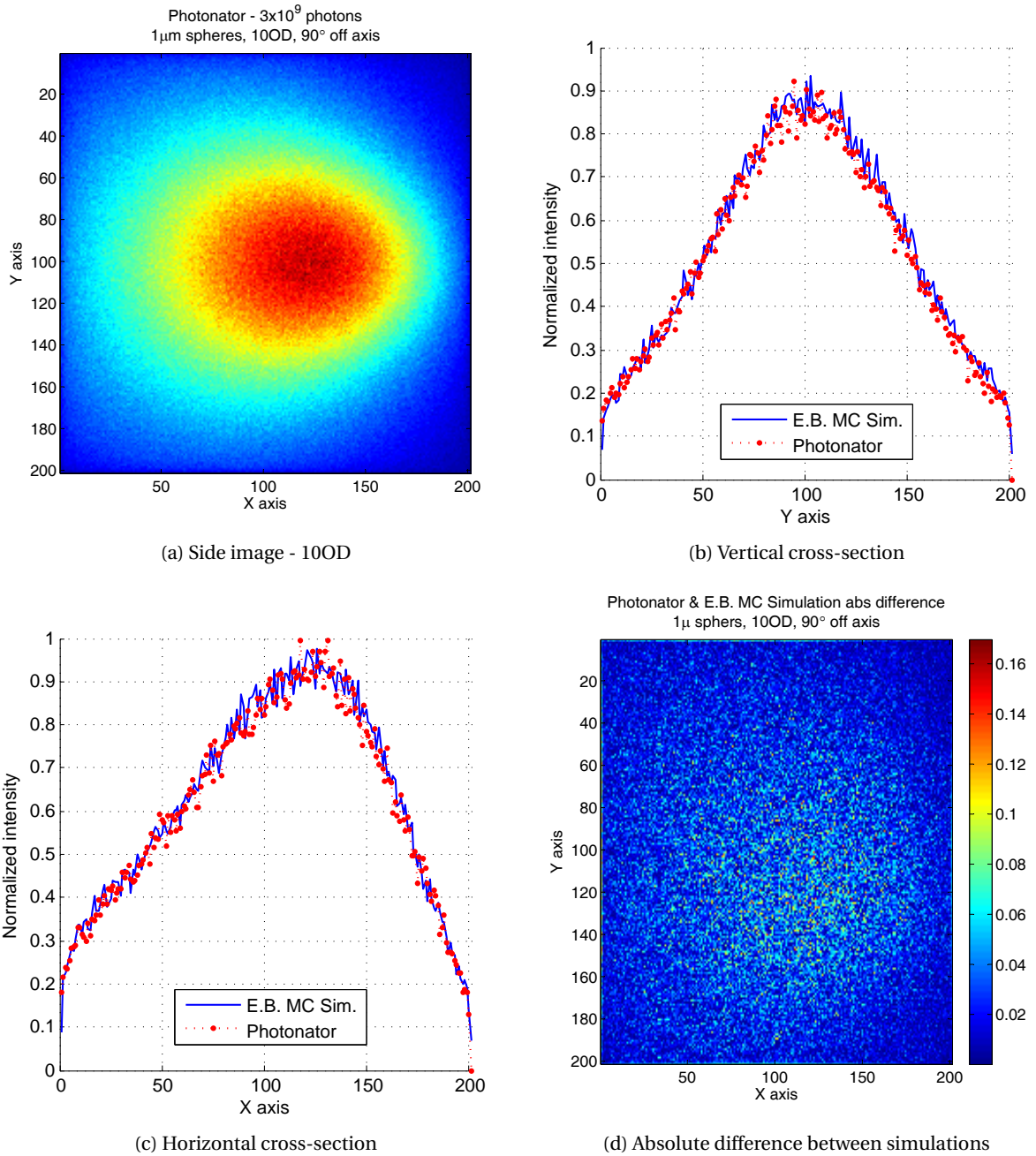


Figure 4.18: Photonator 90° off-axis comparison to published data from [78] at an optical depth of 10 and 3×10^9 photons simulated. Images show the absolute difference between the two, along with cross-section comparisons.

4.5.2 Validation Against Off-Axis Power Measurements with Maalox as the Scattering Agent

The MC model was validated against the off-axis power measurements presented by Cochenour [33]. The data presented in this study was from measurements made in a 3.66 meter water tank with a Maalox solution used as the scattering agent. A wide FOV PMT-based receiver was used to detect the light-field with a 1mm aperture. The detector was scanned horizontally along the receiver plane from the center of the on-axis beam, to 40 cm off-axis. The shape of the field on the receiver plane was measured for various water conditions.

For the MC simulation, the water conditions and physical constraints of the system were modeled. The tank was taken to be 1.2 meters by 1.2 meters on the end and 3.66 meters long with perfectly absorbing interfaces. The simulated FOV was 180° . In order to increase the accuracy of the simulated measurements, the intensity was measured along annular rings surrounding the on-axis beam and normalized to the area of the physical detector, or $\pi D^2/4 \text{ m}^2$. The radius of each annular ring was set to the measurements distances of the experiment, and the width of each ring was 1 mm. This closely approximates the actual experimental measurement made.

The phase function presented in the paper, measured by Alan Laux [30], along with the phase function measured by Deric Grey [48], both presented in Chapter 3, were used in the MC simulation. It was found that the VSF from Grey matched the results better and was consequently used to present the data shown in Fig. 4.19 and Fig. 4.20.

The initial conditions of the beam and VSF had a large affect on the offset between the initial on-axis value and the power in the “tail” of the data - the off-axis portion. Since the initial beam conditions were not discussed by Cochenour [33], it was found that a initial beam with a Gaussian profile and 0.8 mm standard deviation yielded the best agreement to the measured data. It should be noted that the size of the incident beam in the measured data was not explicitly measured. However, in spite of the change in relative position of the curves due to initial conditions, the shape of the curves remained relatively constant and in good agreement with the measured data.

4.5.3 Validation Against Experimental Measurement of On-Axis Power vs. Water Turbidity

The final method of validation for the Monte Carlo simulation was to compare against data taken in the laboratory test environment, which is a 3.66 m long water tank. The tank holds approximately 1,000 gallons of water, and is 1.2 m by 1.2 m square on the ends. It is equipped with polycarbonate windows on each end for transmission and reception. A pool pump circulates and filters the water. The water tank was filled with municipal water and maalox was added to the water to create a turbid environment. The submerged pump was left running to circulate the water and maalox mixture. A fixed amount of maalox was added to the water for each experimental data point and the attenuation

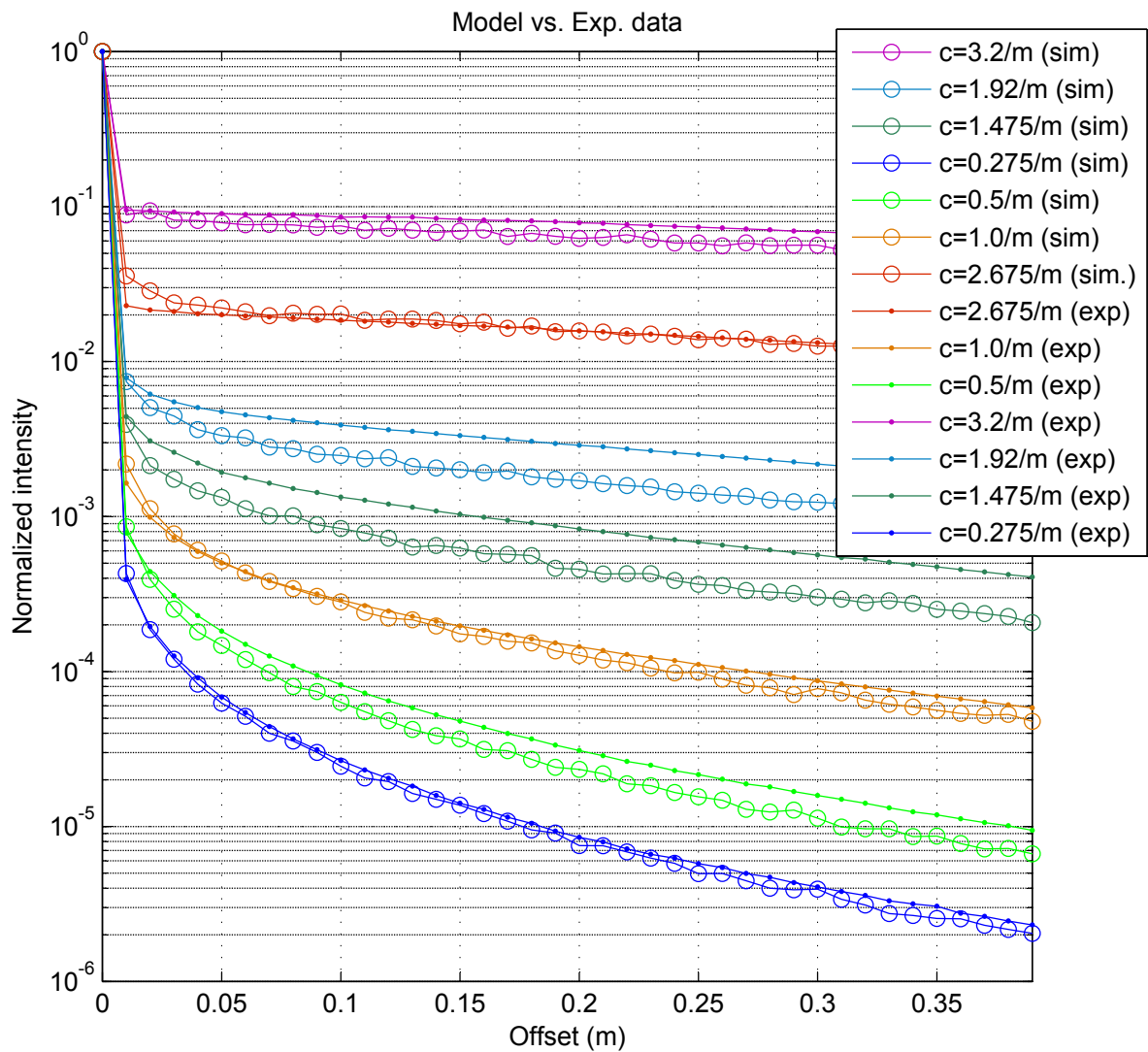


Figure 4.19: Simulation output versus experimental data for measured power at a distance offset from the central beam. The data here is normalized to the maximum value.

Curve shapes - Simulation versus Experiment

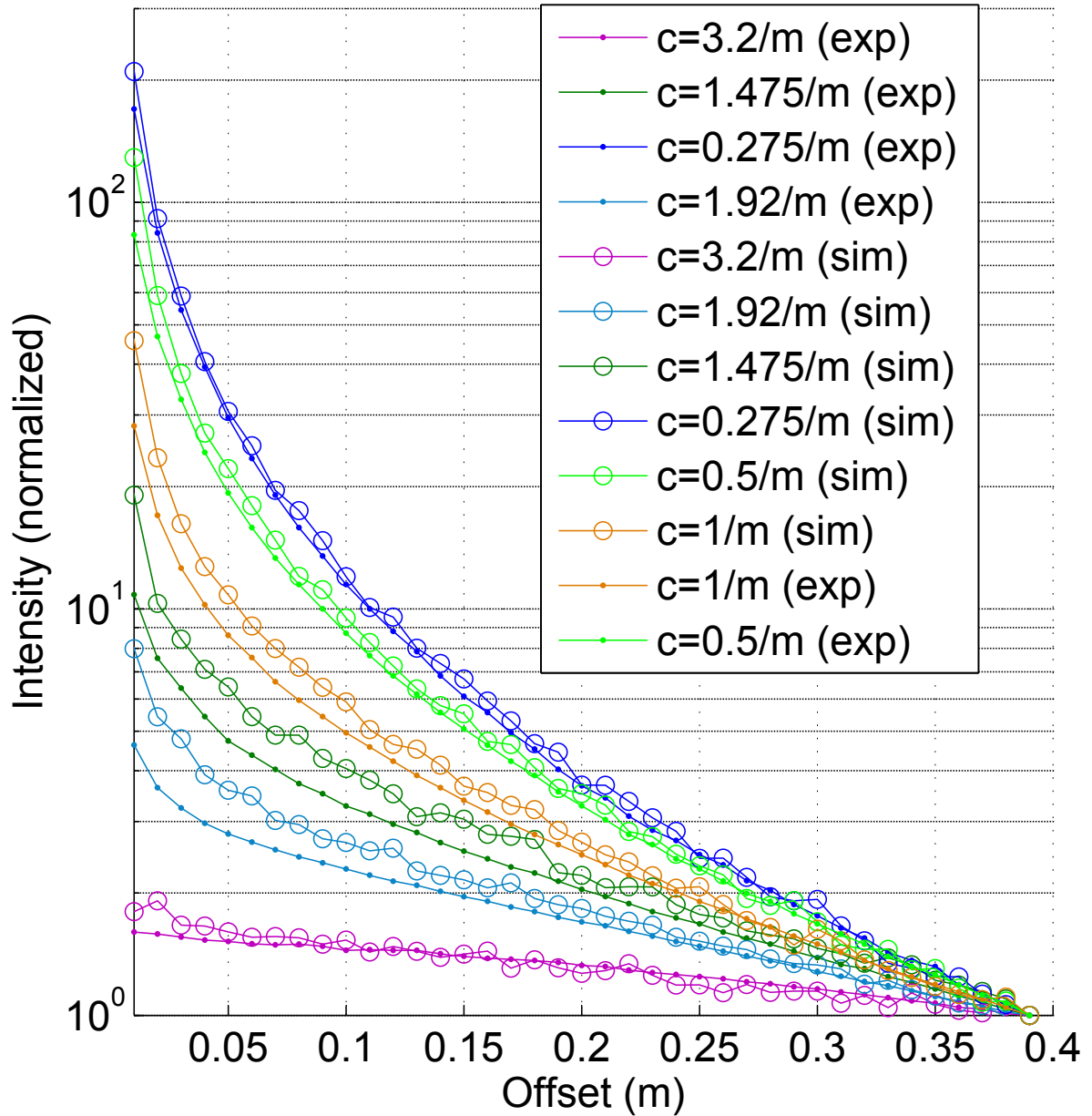


Figure 4.20: Simulation output versus experimental data for measured power at a distance offset from the central beam. The data presented here is normalized to the lowest value.

coefficient was measured using the Wet Labs C-Star transmissometer at 532 nm. The attenuation coefficient values were allowed to settle to a steady-state before taking a measurement. This usually was only a few minutes.

The transmit beam was from a 532 nm diode pumped solid state (DPSS) laser operating at 450 mW optical power. The transmit beam had a 2 mm beam diameter and sub-1.5 mrad divergence. The beam was passed through a 2.0 optical density (OD) neutral density (ND) filter before being sent through the tank transmit window. The full laser power was not sent through the tank window as some heat induced lensing affects were observed.

The receiver, consisting of a 25.4 mm diameter, 532 nm, optical filter with a 25.4 mm achromatic biconvex lens with a 75 mm focal length, was placed on axis with the transmit beam and positioned such that the front face was normal to the transmit beam and as close as possible to the receiver window to eliminate any stray light from outside the tank from entering the receiver optics. The lens was focused on a Hamamatsu H6780-20 packaged PMT unit with a 8 mm active area. The block diagram is shown in Fig. 4.21.

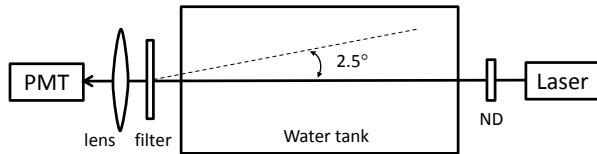


Figure 4.21: Block diagram of experiment in laboratory water tank.

The output of the PMT was connected to a 50k ohm load and the signal voltage was measured using a Fluke 87 V multimeter. The bias voltage on the PMT was adjusted to keep the signal in the observable and linear region. Fig. 4.23 shows measurements of the PMT at various control voltages. The device exhibits good linearity between different control voltages and generally matches the datasheet values for gain versus control voltage. Fig. 4.22 shows the datasheet values for gain versus control voltage. Using an estimated fit line for this plot yields the following equation for gain versus control voltage

$$G = 2E^6(V_c^{6.85}) \quad (4.64)$$

where G is the unitless signal gain and V_c is the control voltage, which ranges from 0.25 ν to 1 ν . The exponent of this equation matches the experimental results shown in Fig. 4.23. The differences in values can be attributed to the experimental setup, where stray light collection could have been better managed. The experimental results show the PMT has slightly less gain than in the datasheet.

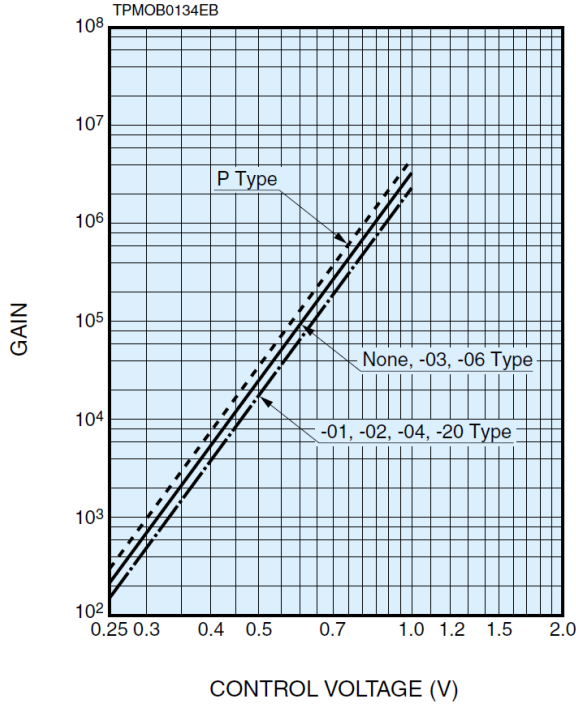


Figure 4.22: Gain vs. control voltage for the H6780-20 PMT used in the experiment.

For each different water quality, two measurements were made of the PMT signal, one with the laser on and one with the transmit beam blocked, to determine what, if any, the dark current of the PMT was. The collected data was converted from observed voltages to optical power via the equation

$$P_{optical} = \frac{V_{exp}/R_L}{G\eta\tau_{window}\tau_{rx}} \quad (4.65)$$

where $P_{optical}$ is the estimated received optical power, V_{exp} is the experimental measured voltage, R_L is the PMT load resistance, G is the PMT signal gain, η is the quantum efficiency of the PMT, and τ_{window} and τ_{rx} are the optical losses from the receiver optics and tank windows, respectively.

Fig. 4.24 shows the experimental results starting at six attenuation lengths due to the maximum received power limit of the PMT. The curve was normalized to an optical power of 1 to match the simulation output. An arbitrary offset factor was multiplied with the signal to bring the low turbidity values in line with the Beer's Law curve. The first four data points were used to create an exponential trendline. The estimated slope was approximately 2.5-4.5% more shallow than the Beer's Law curve (depending on the fitting algorithm and program). The offset factor was adjusted such that the trend line went to 1 at an attenuation length of 0. Fig. 4.25 shows the adjusted curve plotted against Beer's Law ($\exp(-cr)$) for reference.

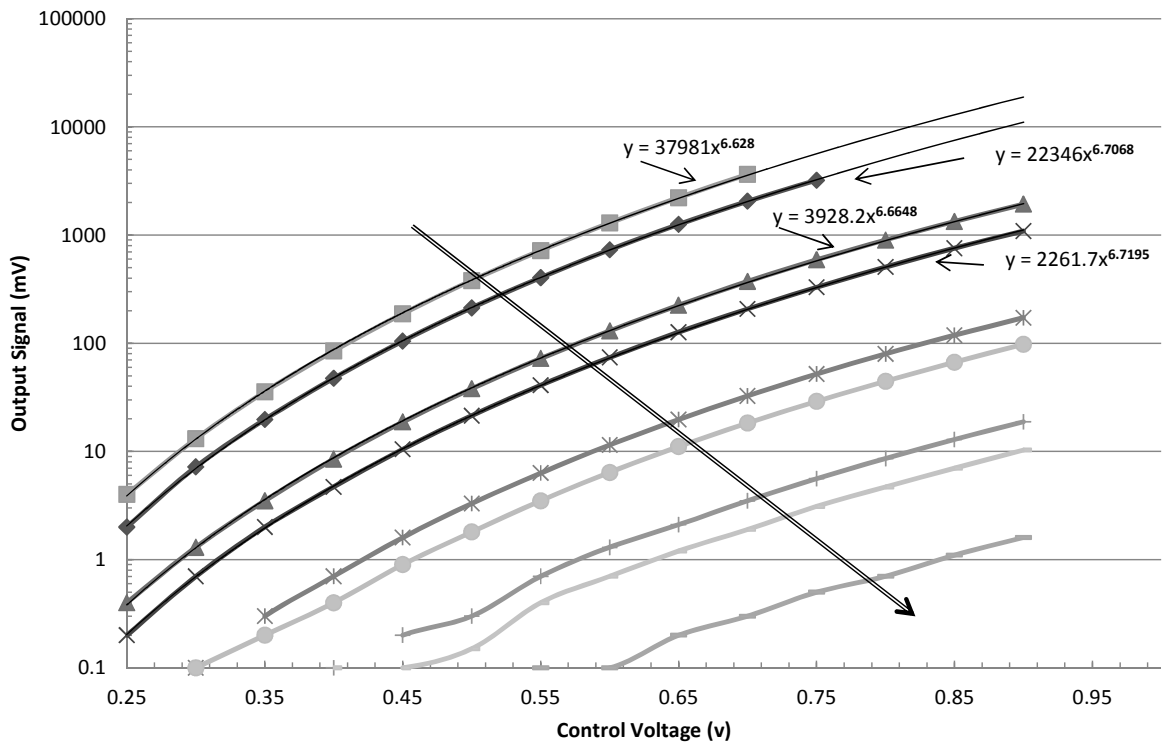


Figure 4.23: PMT signal gain vs. control voltage. The nine curves represent nine different levels of optical attenuation before the detector. The fit lines show that the curves are relatively consistent across several orders of magnitude.

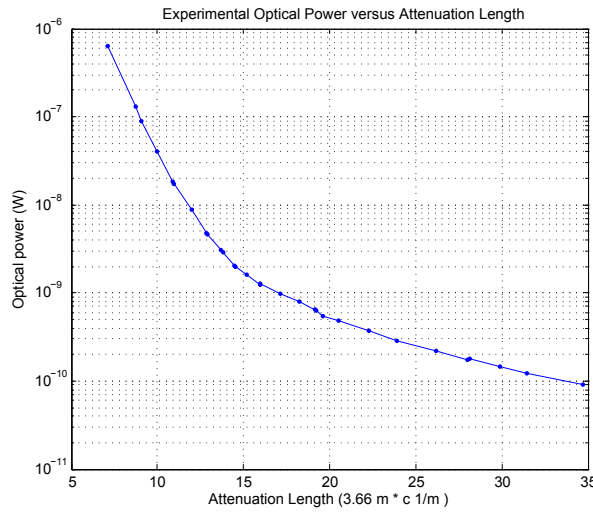


Figure 4.24: Experimentally measured optical power vs. the turbidity of the water in the 3.66 m water tank.

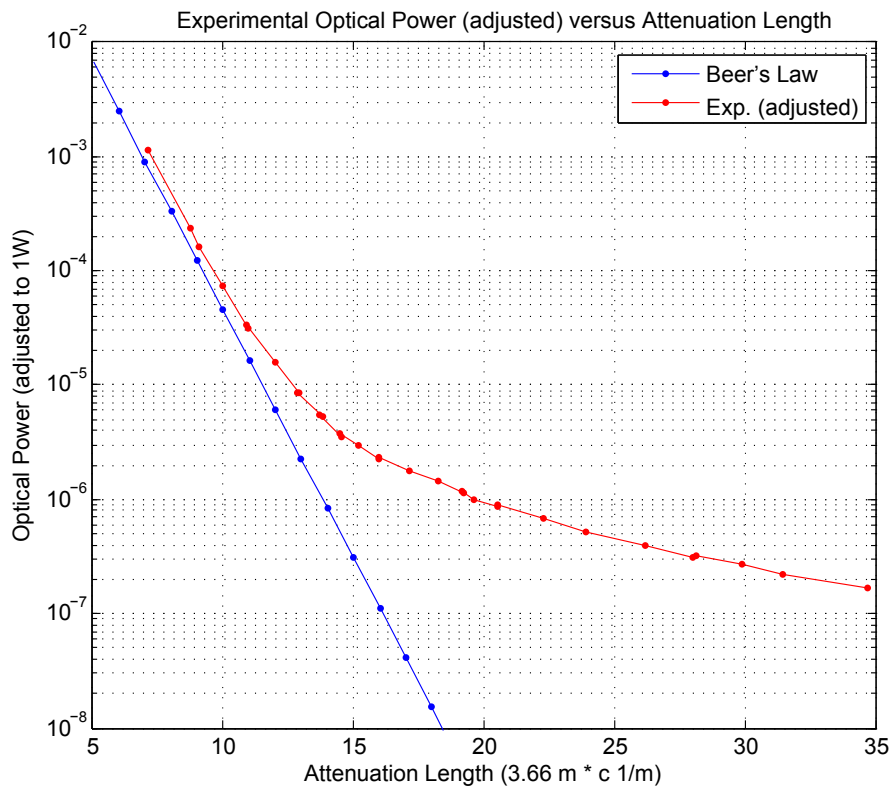


Figure 4.25: Adjusted optical power to correspond to a transmitted power of 1W. The curve was scaled such that the first four experimental points form an exponential trend towards 1 at an attenuation length of 0.

Differences between simulation and experiment

Several differences between the simulation and experiment are recognized. All of these can contribute to the differences between the two. For making quantitative comparisons between simulated and real-world data, these must be carefully evaluated. However, when comparing simulated outputs directly, system specific effects (e.g. specific receiver window losses, or the wall effects) are nullified. In other words, while the MCNS can be made to model actual experiments, it is better suited to comparing channel effects that ignore some of the more tedious system design aspects.

Below are listed several items that are either differences between the simulation and experiment or are unknowns between the two.

- Wall scattering function - The scattering function for the tank walls is unknown. The material is glossy epoxy resin covered by a single coat of black matte paint. The surface is specularly reflective while being somewhat absorptive.
- Wall absorption - The amount of absorption from the coat of black paint is unknown.
- Tank window lensing/bowing - Slight bowing of the windows happens due to water pressure in the tank. The exact amount is unknown and causes slight lensing effects of the light-field passing through the window.
- Surface waves - Waves on the tank surface are caused by the circulating pump that is used to keep the scattering material in suspension. The reflective effects of these waves are not quantified.
- Water albedo and VSF - The exact water albedo and VSF is unknown. Other published results can be used, however any manufacturing differences in the Maalox are unaccounted.
- Exact FOV of receiver - The FOV of the receiver was measured by taking a wide-area collimated light source and measuring the response of the detector as it was rotated in this field. This provides an aggregate response of the detector, but does not yield an area-specific FOV response. i.e. The FOV is only known for the full detector surface, not individual areas of the surface.
- Initial beam conditions - The initial beam conditions are dependent on the quality of the laser beam source. Since a salvaged diode laser was used, there are no published specifications on the beam quality or shape. Additionally, the beam first passes through the tank window before entering the water, which can cause aberrations of the beam.

All of these items can prove difficult to measure, and would only be necessary if it was crucial to exactly match an experiment to the simulated results. However, when using the simulation to make comparisons between system parameters, general or standard values can be used for the

parameters above. For instance, most simulations will not involve wall or surface interactions and instead simulate open water.

Simulating the Experiment

The experiment was simulated using the MCNS. Many aspects of the experiment had to be assumed, as there was no simple way to measure them. Reasonable values were assumed for the albedo of the water, scattering phase function, wall scattering, etc. Changes to these values were made and the simulation output was compared to the experimental results. Specific areas of difference between the simulation and experiment were discussed in Section 4.5.3.

For the simulation, the physical aspects of the water tank were emulated, including the beam placement in the water tank, which was approximately in the center of the tank side. A 2 mm diameter Gaussian beam was simulated propagating through the water towards a 52.4 mm aperture. The FOV acceptance was modeled from the measured FOV of the receiver, shown in Fig. 4.26. The receiver FOV was measured with an incident, collimated, optical source that covered the entire aperture. The receiver was then rotated off the beam axis and the received signal power was measured. This was normalized by $\cos(\theta)^{-1}$ to remove the geometric offset from the data. A two term Gaussian was used to fit the experimental data. Photons incident in the receiver area had their weights multiplied by the FOV function to emulate the effects of a limited FOV.

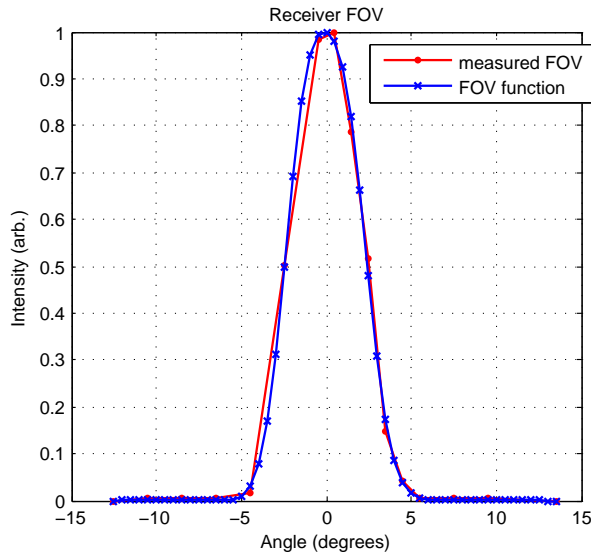


Figure 4.26: Receiver FOV measured and fit with a two-term Gaussian. Receiver was a 52.4 mm lens in front of a PMT with an 8 mm aperture. This was used as a weighting function for incident photons, based on angle of arrival.

Surface and wall reflections were shown to have an affect on the slope of the curve at high turbidities. The surface reflections were modeled as an air/water interface, with indices of refraction of $n_{air} = 1$ and $n_{water} = 1.33$. Surface waves, which were present in the experiment from the running submerged pump, were not modeled in the simulation. The surface was assumed to be perfectly flat when reflecting. The tank walls were modeled as specular reflectors with a variable absorption. While the walls certain exhibited some diffuse reflection, the specular reflection was assumed to be reasonable as the physical surface was highly reflective polyurethane epoxy with a layer of black spray paint. A diffuse wall reflection was not simulated due to the added complexity. The transmission characteristics of the receiver window were also modeled as an air/water interface, as the polycarbonate window would not affect the exit angles. The slight translation in photon entrance and exit points from the receiver window (due to the path length travel in the polycarbonate window) were not modeled.

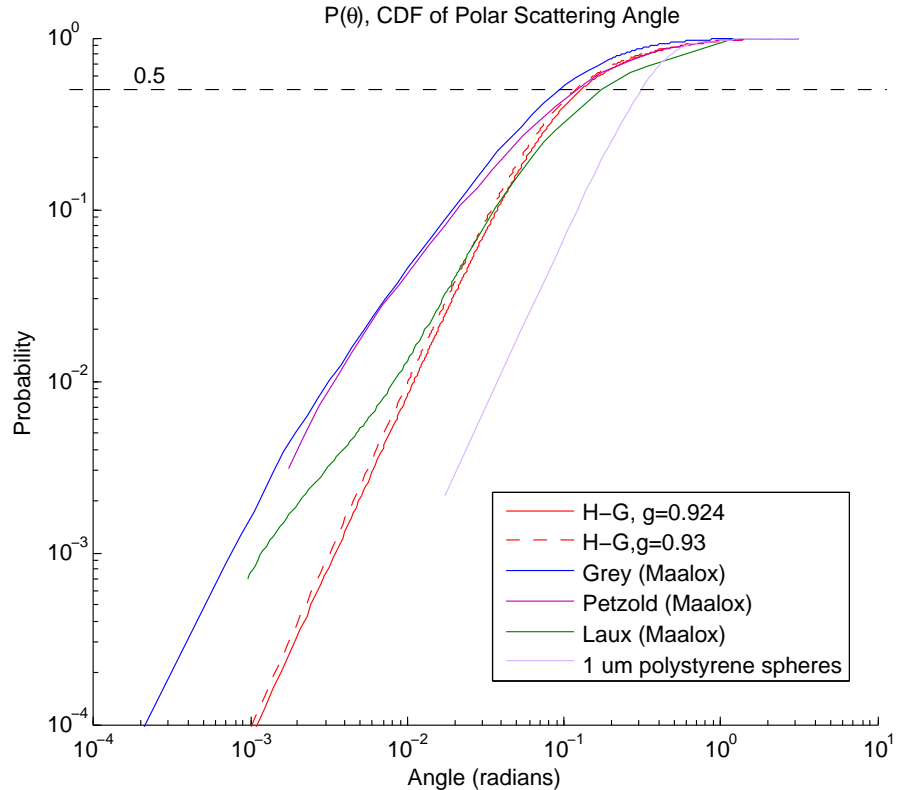


Figure 4.27: The CDF of several VSFs are plotted. The VSFs are integrated using a trapezoidal integration and normalized to a maximum value of one. The dashed line indicates the 1/2 probability mark.

Through running various simulations, it was found that the scattering phase function plays a large part in the behavior of the attenuation curve, specifically on the slope at high turbidities. Simulations were conducted with both the measured Maalox scattering phase functions of Alan Laux [30] and Deric Grey [48], as discussed in Chapter 3. Fig. 4.27 shows several cumulative distribution functions for the polar scattering angle of various volume scattering functions. Due to the differences at very small scattering angles, the VSF from Grey overestimated the slope at high turbidites and the VSF from Laux underestimated the slope at high turbidities. Ultimately the Henyey-Greenstein (HG) VSF was used as an approximation and the g parameter was tuned to achieve a good fit with the experimental data. The data in Fig. 4.27 shows that the HG function better matches the data from Deric Grey than the data from Alan Laux, though the HG function still underestimates the “peak” at small angles in both of the other datasets. It is unclear whether the differences in measured VSFs of Maalox are due to experimental differences or differences in the actual Maalox product purchased.

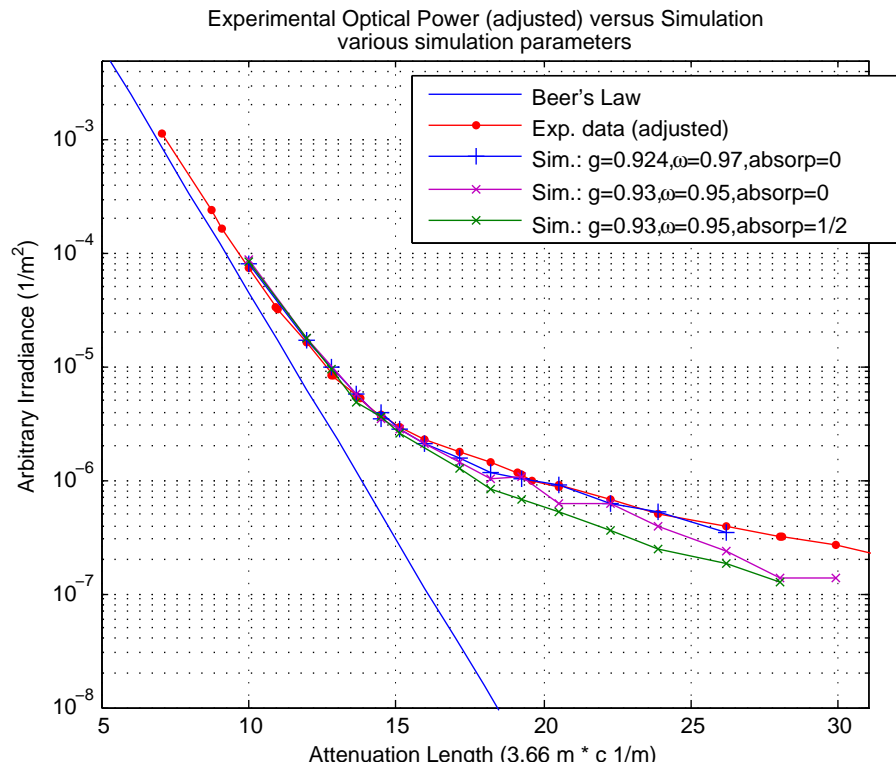


Figure 4.28: Experimental data (red) versus several simulations and Beer's Law.

Fig. 4.28 shows three different simulated datasets compared to the experimental data. The closest match, shown in the blue curve, results from a g of 0.924, and albedo of 0.97, and specular reflection

from the walls, with no absorption. The purple curve is using a g value of 0.93 and an albedo of 0.95. Finally, the green curve shows specular wall reflection with an absorption of 50%. The curves match well at low turbidites to the measured data. The simulation that included wall absorption exhibits a more steep slope at very high turbidites than the experimental data. The reason for this is not entirely clear, but the VSF and particulars of the wall scattering and absorption are certainly factors. The slope at the very high turbidities seems to depend quite a bit on the nature of the scattered light from the tank surfaces.

While there exist some differences between the experimental and simulated data, it is judged that reasonable system parameters can be attributed to this. Additionally, while great effort can be made to match the two exactly, it is judged that such an effort is not entirely useful due to several unknowns about the experimental data.

4.5.4 Concluding the Validation

Based on three separate lines of experimental and simulated data, it is concluded that the MCNS adequately simulates the effects of the underwater light-field for the needs of most underwater optical system designers. It was shown in Section 4.5.1 that the simulation could match the experimental and simulated results from light scattering from $1 \mu\text{m}$ polystyrene spheres. The results showed the simulated output for side and front views of the scattered light-field with agreement to within 5%. Section 4.5.2 showed that the simulation was able to match experimental data for light scattering underwater from a maalox suspension and correctly show the off-axis power attenuation. Finally, Section 4.5.3 shows that the simulation was able to match experimental data taken in the lab for on-axis light attenuation from scattering and absorption underwater due to Maalox. These three validations cover both the mechanics of the model, along with the proper application of the various volume scattering functions. It also shows that the simulated receiver model works properly.

4.6 Conclusion

In this chapter we have discussed the design and validation of a Monte Carlo numerical simulation (MCNS) of the underwater light-field for the purpose of simulation optical communication. In Sections 4.1 through 4.4 the design of the simulation was discussed, along with methods for determining the simulation accuracy and how to use the simulation outputs to answer questions about the channel and received power. For example, Section 4.4 discusses the use of the MCNS to determine the channel bandwidth. Chapter 5 presents results using the simulation tool discussed in this chapter to generate results for a variety of underwater communication channels and receiver characteristics.

Secondly, Section 4.5, discussed validating the simulation to verify that the outputs matched both experimental outputs and other models. The validation consisted of three parts: validation

against another MC model of light scattering, validation against experimental 3rd party results of the underwater light-field, and validation against results taken at NCSU of the underwater light-field. These three separate validation points verified the geometrical structure of the program, the processing of the light-field, and the final simulation outputs of received signal power. The MCNS was verified both with experimental results for a fixed size particle scattering phase function, and with measured scattering phase functions for Maalox suspension in water. All three validations show good agreement between the MCNS and the validation datasets. The experimental data measured at NCSU showed slight disagreement with simulation at high turbidities for some possible simulation parameters. This is expected since at high turbidities the scattering phase function has a large influence on the received power, along with the specific scattering function of the water-tank walls. Both are difficult to measure and general functions were used. Additionally, it is shown that the simulation parameters can be tuned in order to achieve greater agreement, and therefore the question is not in the validity of the simulation, but in the precision by which the actual system parameters can be determined.

In conclusion, the Photonator MCNS was shown to be a valid tool for simulation the underwater light-field, specifically as it relates to optical point-to-point communication. This tool will then be used to predict channel characteristics of optical links operating in environments that are difficult to experimentally verify, thereby enabling a system designer to make better design decisions prior to fielding a system.

CHAPTER 5

Simulating Various Scenarios for Underwater Optical Communication

Chapter 4 described the mechanics and validation of the Photonator simulation. Results generated from the simulation, for various water conditions, source conditions and receiver conditions, are discussed in this chapter. The three main aspects of the simulation are the source, channel and receiver. Each play a large part in the overall measured quantity, which, for optical communication, is usually the total received optical power or the temporal spread of the data pulses. Both of these measured quantities directly affect the ability to reliably communicate data from the transmitter to the receiver.

5.1 Partitioning the Simulation Variable Space

The effects of the source, channel and transmitter are all closely tied together and are therefore difficult to logically separate for the purposes of presentation. The method chosen here is to separate the data and simulations into several use-cases, which provide a logical separation in order to analyze the data. One such separation is to divide the data into operations in one of three water types: clear water, coastal water, and harbor water. These distinctions are somewhat arbitrary as ocean waters exhibit a wide degree of variability, but the distinction has nonetheless persisted in literature.

Detailed discussion of light in the ocean, along with descriptions and discussion of the water types used below are given in Chapter 3. Table 5.1 lists the important parameters for these water types. Fig. 5.1 shows the scattering phase functions, which are taken from the work done by Petzold [49].

In addition to the three water types listed in Table 5.1, the Harbor water type is divided into three separate types, all with the same albedo but varying the attenuation coefficient, c . These types are

Table 5.1: Three general water types based on measured data from Petzold [49]

| Water Type | c Value | Albedo |
|------------|-----------------------|--------|
| Harbor | 2.19 m^{-1} | 0.83 |
| Coastal | 0.4 m^{-1} | 0.55 |
| Clear | 0.15 m^{-1} | 0.25 |

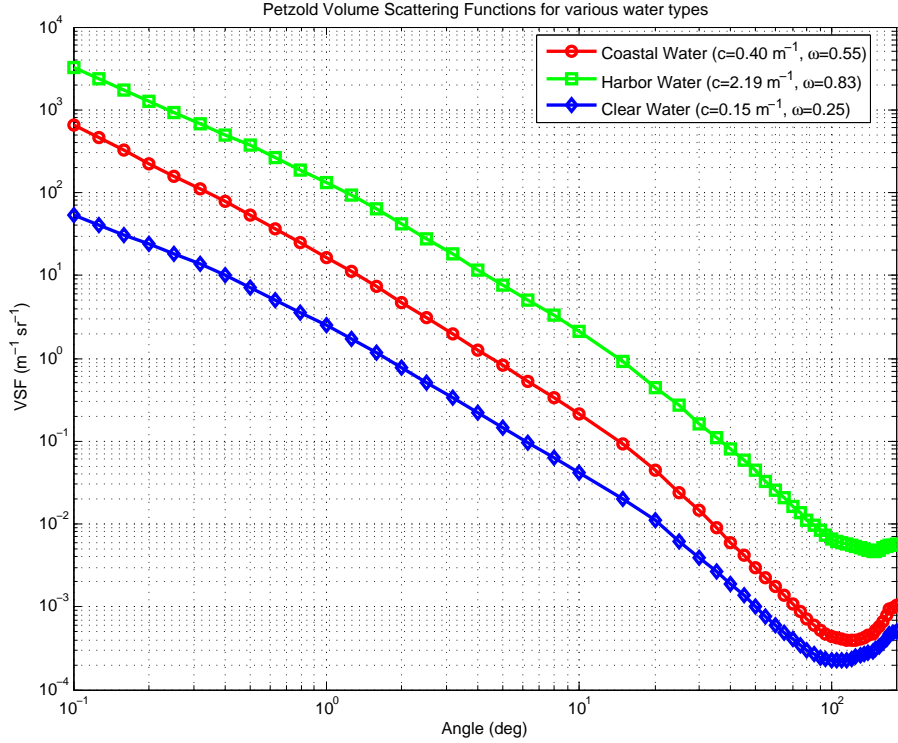


Figure 5.1: Three volume scattering functions as measured by Petzold [49], which show the VSF used for Clear, Coastal and Harbor water types.

classified Harbor I, Harbor II, and Harbor III. Their features are listed in Table 5.2. The three different harbor water types correspond to equally scattering water, hence the same albedo, but with varying degrees of attenuation per unit distance, with Harbor III-type water being the most turbid and Harbor I water the least.

Table 5.2: Three different types of Harbor water.

| Water Type | c value | Albedo |
|------------|----------------------|--------|
| Harbor I | 1.1 m^{-1} | 0.83 |
| Harbor II | 2.2 m^{-1} | 0.83 |
| Harbor III | 4.4 m^{-1} | 0.83 |

5.1.1 Receiver Aperture and Field of View

In addition to several different water types, simulation results are also produced for a range of receiver apertures and FOVs. This enables us to make predictions about various link performances over a range of receiver configurations. When choosing which receiver variables to simulate it is important to choose useful numbers that can be implemented in the real world. The minimum receiver size was chosen to be 8 mm to correspond to the active area of a Hamamatsu RU7400 PMT, while the maximum size was chosen to be 4 inches to correspond to the upper limits for feasible optical systems. These units are deliberately mixed to provide the most convenient information for system designers, as the RU7400 PMT is commonly used for many optical systems, and lenses are typically purchased with imperial measurements. While larger lenses could be produced, they would be cost and weight prohibitive for small communication systems. The Photonator simulation allows for any size receiver, but larger apertures will not be considered in this study.

The system full-angle FOV was simulated over a range from 1 degree to 180 degrees. The minimum value was chosen to provide a small FOV while still allowing for some pointing offset in the link and the maximum value was chosen to correspond to a bare detector substrate. In practice, the full FOV would only be achievable with a specialized lens system or a curved PMT detector. The full set of receiver FOV's and apertures are listed in Table 5.3 and Table 5.4.

Table 5.3: List of simulated field-of-view parameters.

| Field of View | 1° | 2° | 4° | 8° | 16° | 45° | 90° | 180° |
|---------------|----|----|----|----|-----|-----|-----|------|
| | | | | | | | | |

Table 5.4: List of simulated aperture parameters.

| Aperture | 8 mm | 1 inch | 2 inch | 3 inch | 4 inch |
|----------|------|--------|--------|--------|--------|
| | | | | | |

The receiver structure can be simulated for aligned receivers, where the transmit source and the receiver are collinear, or for receivers with a position offset from the center of the transmit source. This would represent a receiver that has been offset due to pointing and tracking errors or movement on the part of the receiver or transmitter.

5.2 Source Effects

The simulated transmitter source can broadly be partitioned into three areas: collimated, diffuse and semi-collimated. We consider the former to be a collimated laser beam with a very low divergence, on the order of milliradians. A diffuse source would be similar to an LED that transmits its energy over a large spherical section. Finally, a semi-collimated source would either be a laser that has been purposefully diffused or a LED that is focused.

The simulated transmitter can also be off-axis to the receiver plane, thereby simulating various pointing and tracking issues, such as angular misalignment.

5.2.1 Transmitter/Receiver Misalignment

The MCNS simulation requires that the receiver plane be on the global x/y plane. In order to simulate angular offsets of the receiver and transmitter the position and transmit angle of the transmitter must be adjusted. This geometry is illustrated in Fig. 5.2, where γ_{rx} is the angular offset of the receiver, and ϕ_{tx} is the angular offset of the transmitter. Any angular transmitter offset will also contribute to a distance offset on the receiver plane of d_{offset} . This is calculated by

$$d_{offset} = \frac{d \sin(\phi_{tx})}{\cos(\phi_{tx} + \gamma_{rx})} \quad (5.1)$$

by the Law of Cosines. The transmitter offset on the transmitter plane, h_{tx} is defined by

$$h_{tx} = d \sin(\gamma_{rx}). \quad (5.2)$$

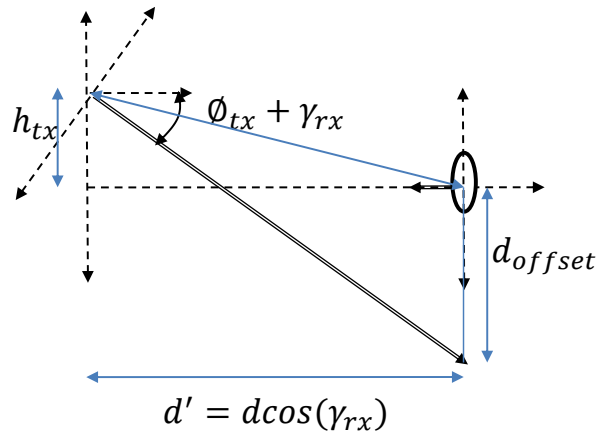


Figure 5.2: Illustration showing the geometry for how transmitter/receiver misalignment is simulated. This shows both angular and distance misalignment.

The transmitter should be moved to a new position, x' , based on the old position

$$x' = x + h_{tx} \quad (5.3)$$

and the receiver's new z-axis position z' should be

$$z' = d \cos(\gamma_{rx}). \quad (5.4)$$

Since the simulation is radially symmetric, there isn't a need to translate in the y-axis, but the principles discussed above would apply. The pointing vectors of the transit beam, μ_x, μ_y, μ_z would be rotated using a rotation matrix on the y-axis, $R_y(\theta_r)$

$$R_y(\theta_r) = \begin{bmatrix} \cos \theta_r & 0 & \sin \theta_r \\ 0 & 1 & 0 \\ -\sin \theta_r & 0 & \cos \theta_r \end{bmatrix} \quad (5.5)$$

where $\theta_r = \phi_{tx} + \gamma_{rx}$ and which assumes that the illustration in Fig. 5.2 shows the y-axis pointing towards the viewer (out of the page). This yields the following expressions for the new pointing vectors

$$\mu'_x = \mu_x \cos \theta_r + \mu_z \sin \theta_r \quad (5.6)$$

$$\mu'_y = \mu_y \quad (5.7)$$

$$\mu'_z = -\mu_x \sin \theta_r + \mu_z \cos \theta_r. \quad (5.8)$$

5.2.2 Initial Conditions

The initial conditions for a Gaussian beam transmission consist of creating a Gaussian distribution on the transmit plane and then choosing the proper initial starting angles to produce a divergent beam. A simple method for doing this is to approximate the beam as a collimated source that is diverged with a lens (Milsom [80] has a more rigorous method for doing this). Fig. 5.3 illustrates how the beam is diverged and the starting angles are chosen. The divergence angle is chosen based on the desired light source (1.5 mrad in our case), and the distance for this divergence angle is chosen to be the beam waist (1 mm in our case). In order to produce a divergence half-angle of 0.75 mrad at the beam waist, a focal length is chosen based on the equation

$$f_l = -\frac{w_0}{\phi_{div}} \quad (5.9)$$

where f_l is the focal length, w_0 is the beam waist radius (1mm), and ϕ_{div} is the divergence half angle (0.75 mrad). For each randomly generated photon radial distance (chosen based on a Gaussian

distribution), the polar angle chosen is

$$\theta_0 = -\frac{r_0}{f_l} \quad (5.10)$$

which is based on the common Thin Lens Equation [81] and the geometric simplification that $\tan(r_0/f_l) = r_0/f_l$.

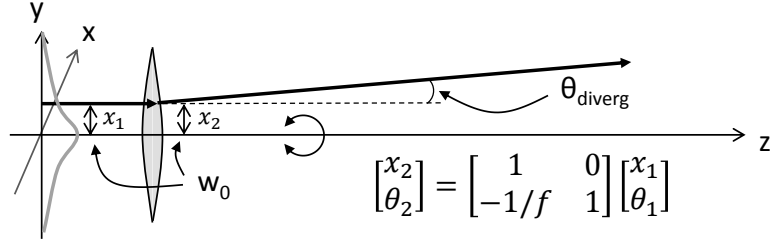


Figure 5.3: Illustration showing how the initial conditions of a Gaussian beam with a fixed divergence is simulated.

Since the beam is symmetric radially, the radial angle, ϕ_0 , is chosen randomly on the uniform interval $[0, 2\pi]$.

The starting radius of the photons on the transmit plane from the beam center is chosen from the Gaussian distribution, such that

$$r_0 = w_0 \sqrt{-\ln(1 - \mathbb{R})} \quad (5.11)$$

where r_0 is the initial radius, w_0 is the beam waist and \mathbb{R} is a uniform randomly chosen value on the interval $[0, 1]$.

The x/y starting location on the transmit plane is defined by

$$x_0 = r_0 \cos \phi_0 \quad (5.12)$$

$$y_0 = r_0 \sin \phi_0 \quad (5.13)$$

and the starting direction cosines are chosen to be

$$\mu_x = \sin \theta_0 \cos \phi_0 \quad (5.14)$$

$$\mu_y = \sin \theta_0 \sin \phi_0 \quad (5.15)$$

$$\mu_z = \cos \theta_0. \quad (5.16)$$

5.3 Geometric Loss

Many existing Monte Carlo simulations assume that the transmit source is an infinitely thin beam. This has the advantage of removing the effects of source choices, such as the type of laser, from the final result, however it makes it difficult to understand how a real system will perform. In the simulation outputs discussed in the following sections, the source is simulated as a Gaussian beam with 1.5 mrad of divergence. This divergence plays an important part in the total received power, especially at longer link distances, such as are simulated in Section 5.5 and 5.6. In order to understand how big of a role the geometric losses represent, Fig. 5.4 shows the received power at various distances for a Gaussian beam transmitting through a vacuum. Each of the apertures featured in the following simulation outputs are shown in Fig. 5.4. As discussed by Salah [82], the power ratio over a circular area of radius r is the following simple expression for a Gaussian beam

$$\frac{P_{rx}}{P_{tx}} = 1 - \exp\left(-\frac{2r^2}{W(z)^2}\right) \quad (5.17)$$

where $W(z)$ is the beam width (distance from center to edge) at a distance z , which is approximated as $\phi_{diverg}z$ due to the beam divergence angle, ϕ_{diverg} .

A plot of the power ratio for various apertures is shown in Fig. 5.4. The vertical dashed lines show the 30 attenuation length point for various water conditions. Since the attenuation coefficient, c , is different for each water type, the distance which represents 30 attenuation lengths is different for each water type. The losses at larger distances are better shown in Fig. 5.5 which shows the same data as Fig. 5.4 plotted with a logarithmic y-axis.

It is clear that at larger distances the loss from beam spreading is significant. For a 4" diameter receiver at 200 meters, 90% of the power is lost, while with an 8 mm aperture the power is reduced by a factor of nearly 10^{-3} .

When analyzing the results in the following sections, it is important to note that the observed losses are a combination of both channel losses from absorption and scattering and from geometric beam spreading. These factors are especially noticed at large distances, such as those featured in Sections 5.5 and 5.6.

5.4 Harbor Water - Absolute Received Power Versus Distance

The results presented below are for Harbor Waters of type I, II and III. Each plot shows the received power versus attenuation length over a range of FOVs. Several different apertures are also simulated, along with data showing the average received power over all FOVs for each aperture size.

When looking at the data presented below, several aspects should be noted. First, the overall shape of each curve should be observed. This shows the overall loss of signal power as the receiver

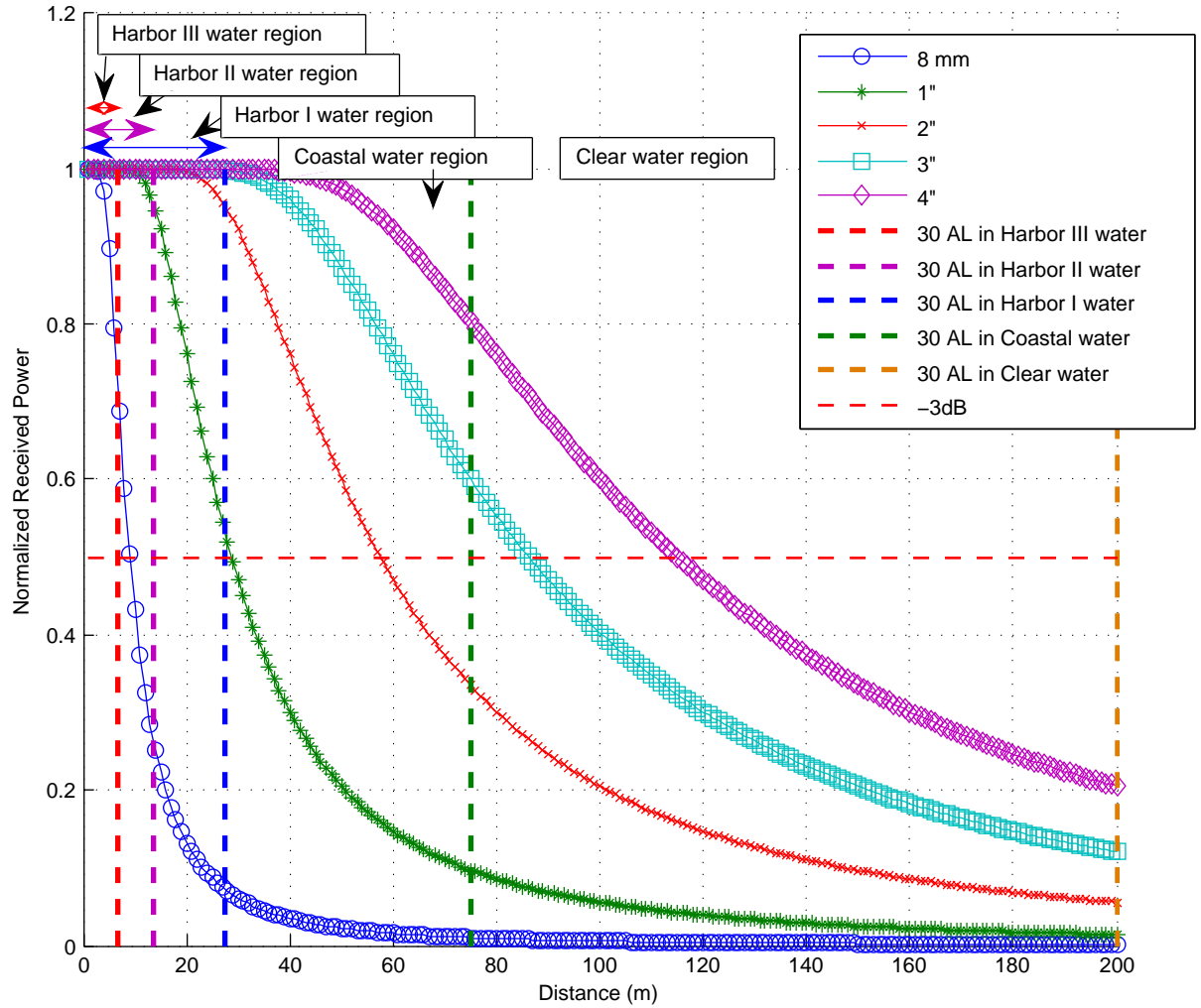


Figure 5.4: Power loss from beam spreading for a Gaussian beam integrated over various aperture sizes at various distances.

is moved further along the x-axis away from the transmitter. This loss of power loosely follows Beer's Law, but diverges at a certain point. This divergence from Beer's Law is more pronounced for the smaller apertures and bigger FOVs. When looking at the scattering order histogram, presented in Section 5.8, it is clear that as the scattered photons transition from a low number of scattering orders (<10), to a high number of scattering orders the curves begin to diverge. This is intuitive, as multiply scattered photons have a greater probability of intersecting the receiver aperture, once having scattered out of the incident beam. As noted in Chapter 3, Beer's Law only accounts for non-scattered, non-absorbed photons, and therefore is a poor approximation when multiple scattering accounts for the predominate loss of photons.

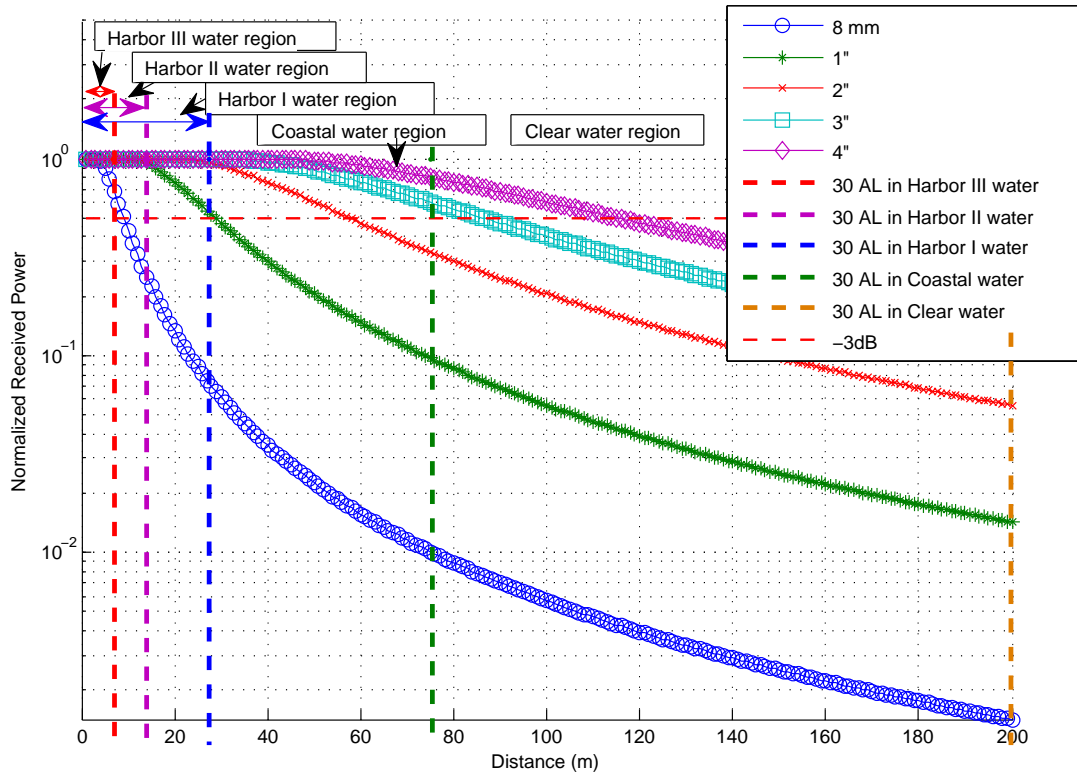


Figure 5.5: Results of Fig. 5.4 plotted with a logarithmic y-axis.

The second aspect of the figures below is that an increase in receiver aperture controls the degree to which the curves follow Beer's Law at attenuation lengths less than 15. As the aperture increases, the loss of power versus attenuation length also decreases. This effect is attributed to the larger aperture collecting a larger percentage of photons that are scattered into small angles. This small angle scattering capture effect is accentuated for larger attenuation coefficients (compare Harbor I Fig. 5.7 - 5.11 to Harbor III Fig. 5.17 - 5.21 waters, starting on page 76). While the attenuation coefficient may scale the scattering versus distance, the scattering angle profile does not scale. As the physical distance between receiver and transmitter is increased, the offset distance radially away from the transmit path is also increased.

5.4.1 Geometric Loss in the Simulation

It should be noted that not only do the curves show the loss from the channel's absorption and scattering, but they also show losses from geometric spreading of the Gaussian beam. While these effects are small for the short distances featured in Harbor waters, they can play a part in deviations

from Beer's Law-type losses. Fig. 5.6 shows these geometric losses for the distances associated with Harbor waters. This plot is the same as the plots in Fig. 5.4 and Fig. 5.5, but only shows distances up to 27 meters (~ 30 attenuation lengths in Harbor I water).

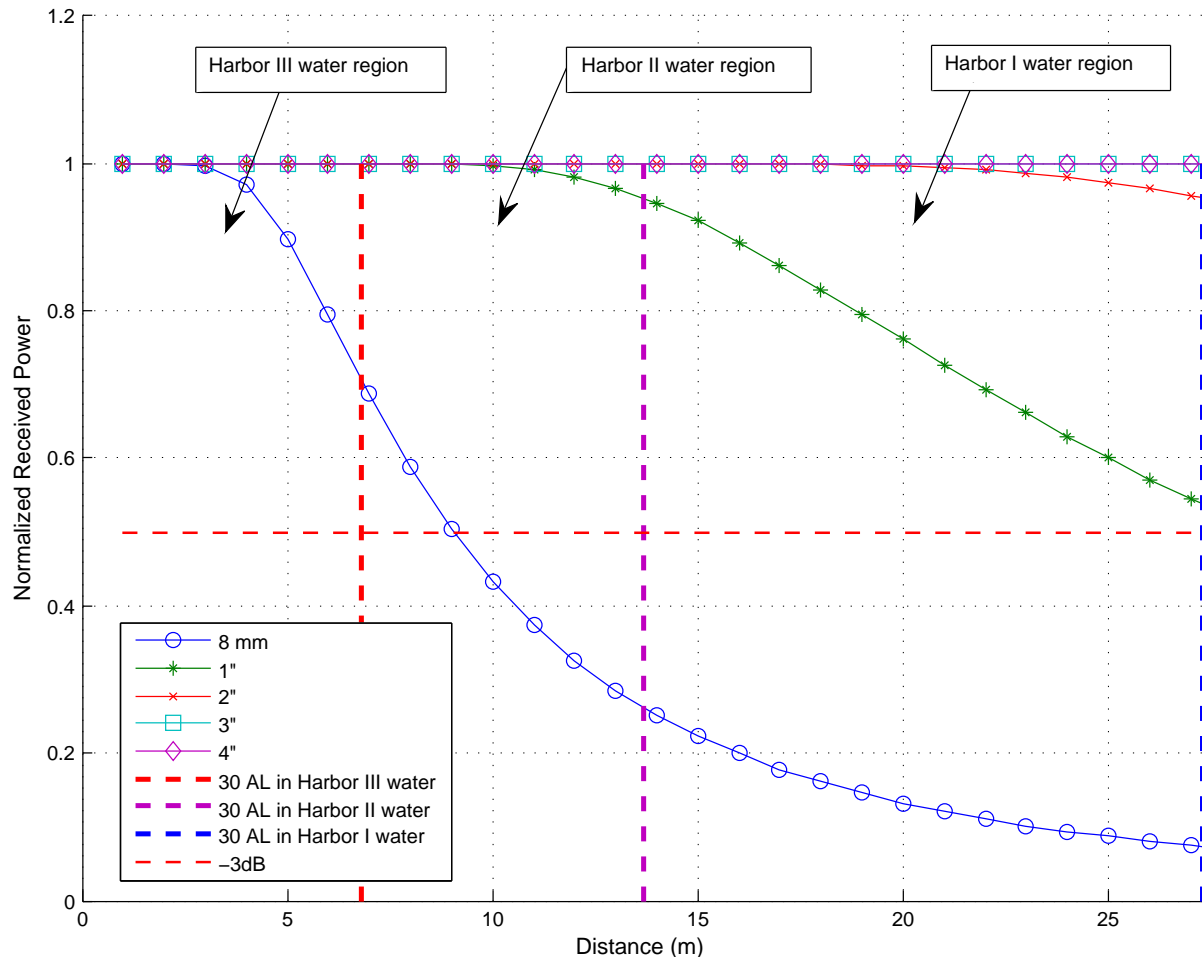


Figure 5.6: Geometric loss from Gaussian beam spreading. Results show power loss for various apertures at various distances.

5.4.2 Harbor I-type Water Power Loss

The results presented in Fig. 5.7 - Fig. 5.11 (starting on page 76) show the simulated power versus attenuation length plots for Harbor I-type waters. These waters have a c value of 1.1 m^{-1} and an albedo of 0.83. The diffusion length in this type of water is approximately 15 m/m, as discussed in

Section 3.5.2 on page 14. They would represent the clearest type of harbor water. The results presented are for a range of FOVs and apertures, as discussed in Section 5.1.

In Fig. 5.7 we see the power versus cz plot for the smallest simulated aperture, 8 mm. This could represent a small PMT, or a larger area photodiode. The power closely follows Beer's Law, presented in green, up to around the diffusion length, 15 attenuation lengths, where they begin to diverge. Prior to that point, it should be noted that the power actually dips below the Beer's Law curve. This, as observed in Fig. 5.6 for the 8 mm aperture, is due to geometric losses. By 20 attenuation lengths, the curves showing the smaller FOVs no longer have enough datapoints to be statistically relevant and are thus not plotted. However, at 25 attenuation lengths, the 180° FOV line shows receiving a power that is approximately ten times the power predicted by Beer's Law. The curves begin to flatten out towards the limit of absorption loss only, shown in red at the top of the plots. This curve represents a receiver that receives all scattered photons and the only losses are due to absorption.

The other apertures shown in Fig. 5.7 - Fig. 5.11 continue a trend of an increasing slope in the smaller attenuation lengths, due to the increased aperture receiving more single scattered photons. By Fig. 5.11 every curve is well above the Beer's Law limit, and most curves, except for the smallest FOVs show significant power gains at high attenuation lengths due to scattering. At 25 attenuation lengths for Fig. 5.11 the power gain between the smallest and largest FOV is over one order of magnitude. At 18 attenuation lengths, the deviation between Beer's Law and the 180° FOV is nearly 10 dB.

5.4.3 Harbor II-type Water Power Loss

The results shown in Fig. 5.12 - Fig. 5.16 (starting on page 81) show the received power versus attenuation length for Harbor II-type waters. These waters have a c value of $2.2 m^{-1}$, an albedo of 0.83, and a diffusion length of 15. These correspond to the "Harbor water" as defined by Petzold (see Section 3 or Table 5.1). The results are similar to those shown in Fig. 5.7 - 5.11 but show an increased gain due to the shorter physical distance between receiver and transmitter (since we have a fixed attenuation length and the c value increases, the distance decreases). This corresponds to less geometric loss, as shown in Fig. 5.6. The 8 mm aperture results in Fig. 5.12 show that until about 15 attenuation lengths (the diffusion length for this water type) the results are nearly identical to the Beer's Law limit. By 25 attenuation lengths the 8 mm aperture received power is 10 dB higher than predicted by Beer's Law, and in Fig. 5.16 the power gain for 180° FOV is over 20 dB.

5.4.4 Harbor III-type water power loss

The results shown in Fig. 5.17 - Fig. 5.21 (starting on page 86) show the received power versus attenuation length for Harbor III-type waters. This water type has a c value of $4.4 m^{-1}$, an albedo of 0.83, and a diffusion length of 15 m/m. It represents extremely turbid water, and the link distances, as shown in the top horizontal axis of the plots, are for short distances, reflecting the high c value.

The results show a significant gain over Beer's Law losses for all apertures greater than 8 mm. The 8 mm aperture, shown in Fig. 5.17 closely follow Beer's Law until about 15 attenuation lengths and then begins to diverge. For the larger apertures the gain is more pronounced than in the other water types. This is both due to very little geometric losses, and due to the fact that the links are operating at very short distances, and thus prevent the scattered light from moving too far away from the central beam. In Fig. 5.19 we see that even with a 2" aperture, the gain over Beer's Law at 15 attenuation lengths is nearly 10 dB, with that gain increasing to over 20 dB by 25 attenuation lengths. By using a 4" aperture, shown in Fig. 5.21, the 180° FOV power is about 25 dB greater than predicted by Beer's Law at 25 attenuation lengths. This is a significant gain to be considered as a system designer, when designing a communications link for very turbid waters. It should also be noted that at 25 attenuation lengths, the 4" aperture power is reduced by about 10^{-6} , while this power loss happens by only 15 attenuation lengths when using an 8 mm aperture.

5.4.5 Average Power Loss for Harbor Waters

The results shown in Fig. 5.22 - Fig. 5.24 (starting on page 91) show the average power loss for each aperture size, for each Harbor water type. Essentially, the results presented in the three sections above are averaged over each aperture size. The figure simplifies the results above, but has the downside of obscuring the large difference between the small and large FOVs. Fig. 5.22 - Fig. 5.24 can be used to gauge the differences between the three Harbor water types.

5.4.6 Received power versus FOV for various Harbor water types

The results presented in Fig. 5.25 - Fig. 5.36 (starting on page 94) show the same results as presented in the sections above, except they are presented at a fixed attenuation length, and show the FOV and aperture response of the received power. This provides a better visual picture of the impact of increasing the aperture or FOV of the receiver at a fixed distance. The results are presented at 10, 16, 20, and 25 attenuation lengths. 10 $c z$ being before the diffusion length, 16 being right at the diffusion length transition and 20 and 25 being well past the diffusion length.

Fig. 5.25 shows the FOV and aperture response of Harbor I waters at 10 attenuation lengths. For the smallest aperture, 8 mm, the FOV response is negligible, with some gain from the larger apertures. This result shows that most of the energy is concentrated into a central beam at small angles, however the geometric spreading of the beam spreads some of the energy over the receiver plane, hence the increased power from increasing the aperture. Fig. 5.26 shows the response at 16 attenuation lengths, which shows again that the 8 mm aperture experiences very little gain from increasing the FOV, as most of the beam energy in that area is confined to a central, small angle beam. Some of the beam energy has spread however, which is shown from the increased power associated with increasing the aperture. Fig. 5.27 and Fig. 5.28 show the FOV and aperture response at 20 and 25 attenuation lengths.

These demonstrated both a strong FOV and aperture gain, demonstrating that both the beam has spread in area on the receiver plane, hence the gain from increasing the area, and the angular spread of the beam is significant, hence the gain from increasing the FOV of the receiver. It should also be noted that the FOV gain rolls off for FOVs greater than 45°. This shows that the lightfield still has a degree of directionality to it, and the energy is not equally propagating in all directions.

The results shown in Fig. 5.29 - Fig. 5.32 show the aperture and FOV response in Harbor II-type waters. These have a larger c value than the Harbor I-type waters, and therefore show communication over a shorter distance. This produces less geometric spreading, which shows in Fig. 5.25 as less response to increasing the aperture. Between the Harbor I and Harbor II-type waters, the curves look very similar.

Finally, Fig. 5.33 - Fig. 5.36 shows the aperture and FOV response at various attenuation lengths in Harbor III-type waters. This water type has the largest c value, and the smallest distance between receiver and transmitter. The 10 attenuation length plot in Fig. 5.25 shows that at small FOVs, the response of all of the receivers is nearly identical. The beam at this point is nearly fully collimated into an area less than 8 mm. This is due to the short transmission distance, which yields very little geometric beam spreading. For the larger attenuation length plots the response curves are very similar to the Harbor I and Harbor II-type water plots.

5.4.7 Received power, normalized by receiver area versus FOV for various Harbor water types

While the Figures 5.25 - 5.36 show the FOV and aperture response at specific attenuation lengths, another useful picture of system performance can be gained by normalizing the received power by the area of the receiver. It is to be expected that the received power will increase as the system's aperture increases, but it is useful to see how much it increases in relation to other aperture sizes. This allows a system designer to look at the power per area of the receiver, along with the gain from increasing the FOV.

The results in Fig. 5.37 show the received power at four different attenuation lengths: 10, 16, 20, and 25. Each received power value is normalized by the the area of the receiver aperture, yielding an intensity value with units of mm^{-2} . Each color represents an aperture size, and the four groupings of data represents each attenuation length. If there is equal power per area, each curve should be aligned with each other, as the curves at 20 and 25 attenuation lengths are. However, as the receiver and transmitter are moved closer to each other, and the attenuation length is lowered, the larger receivers exhibit less power per area than the smaller receiver. This is intuitive, since at the smaller cz 's, the beam is more collimated, as the light is less spread over the receiver plane. In other words, since the photons are traveling over a physically shorter distance, they spread less radially on the receiver plane. For Fig. 5.38, the trend is similar, however the spread between the various apertures is accentuated

at small FOVs. Again, this is intuitive because the smaller FOVs effectively prevent the reception of photons coming from extreme angles due to scattering. Finally, Fig. 5.39 shows the normalized power and FOV response to receivers in Harbor III-type waters. In all three figures, the lightfield at 25 attenuation lengths shows equal power versus area for the various aperture areas simulated.

5.4.8 Figures

Harbor I

The figures below are for the results discussed in Sections 5.4.2 through 5.4.7 on the previous pages 71 through 74.

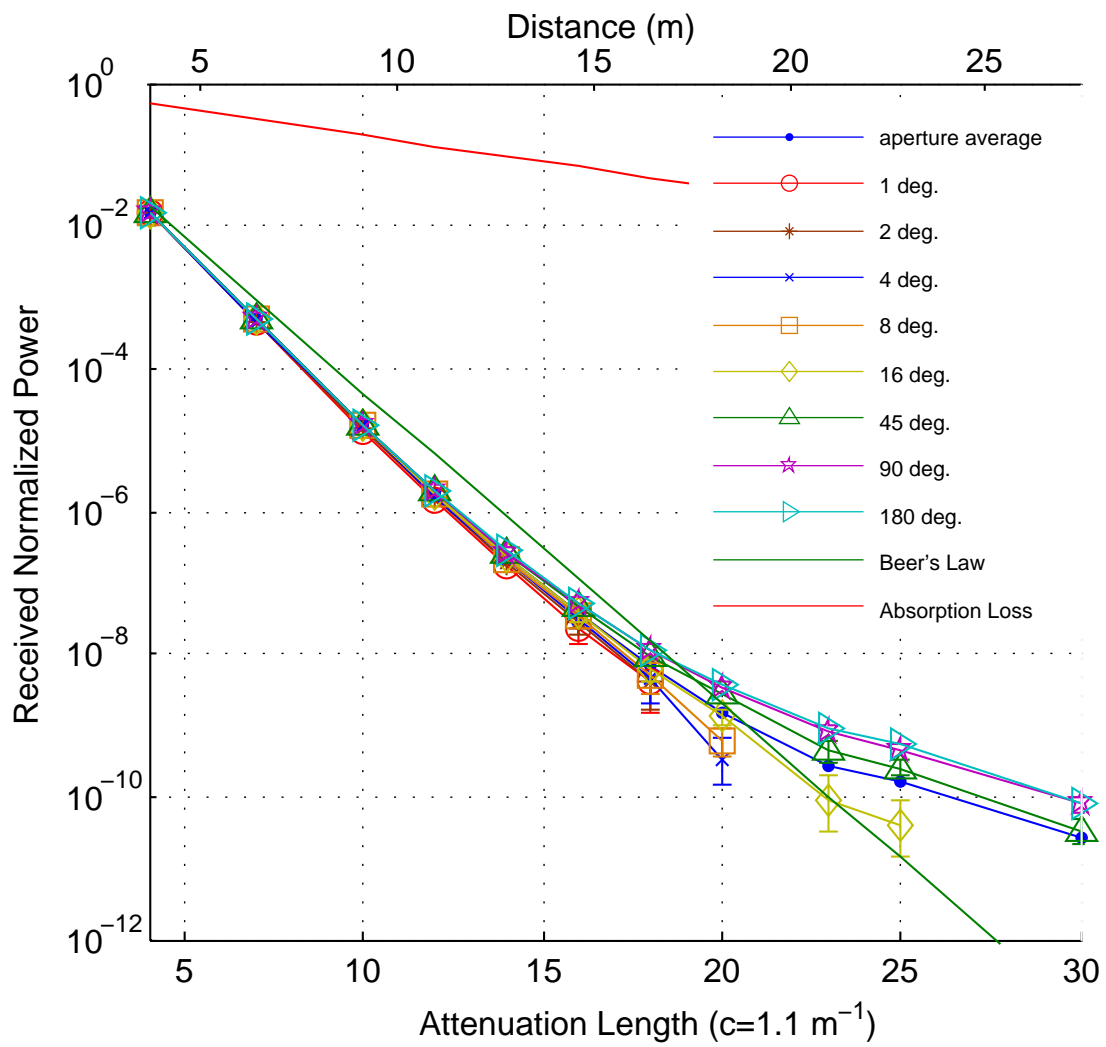


Figure 5.7: Harbor I - 8mm Aperture: Received power normalized by transmit power, plotted versus receiver attenuation length. The c value is fixed and the distance is scaled. Error bars are plotted when the estimated error is greater than $\pm 25\%$. Error bars represent 95% confidence for a binomial distribution, which should be slightly greater than the actual photon weight distribution.

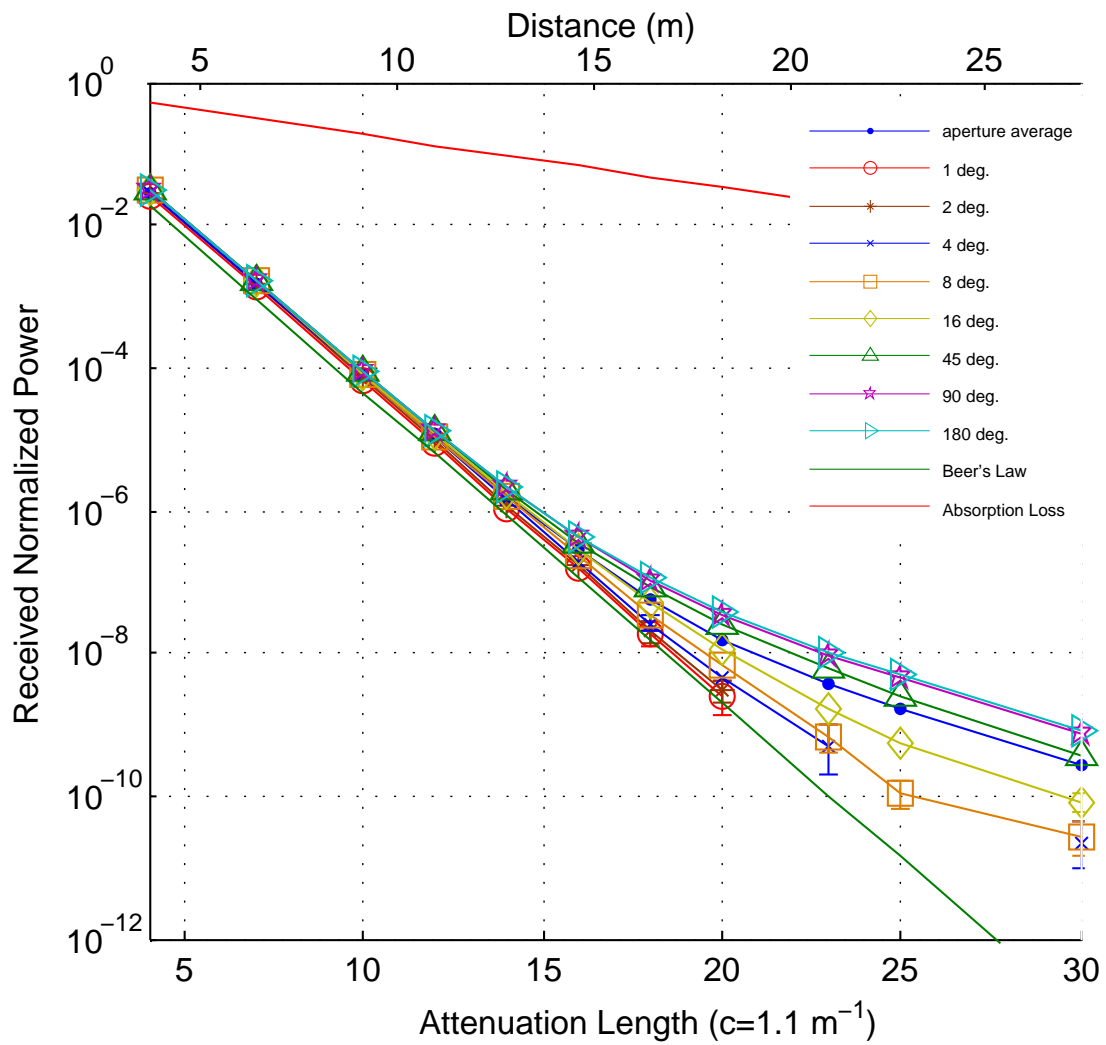


Figure 5.8: Harbor I - 1 inch aperture received normalized power.

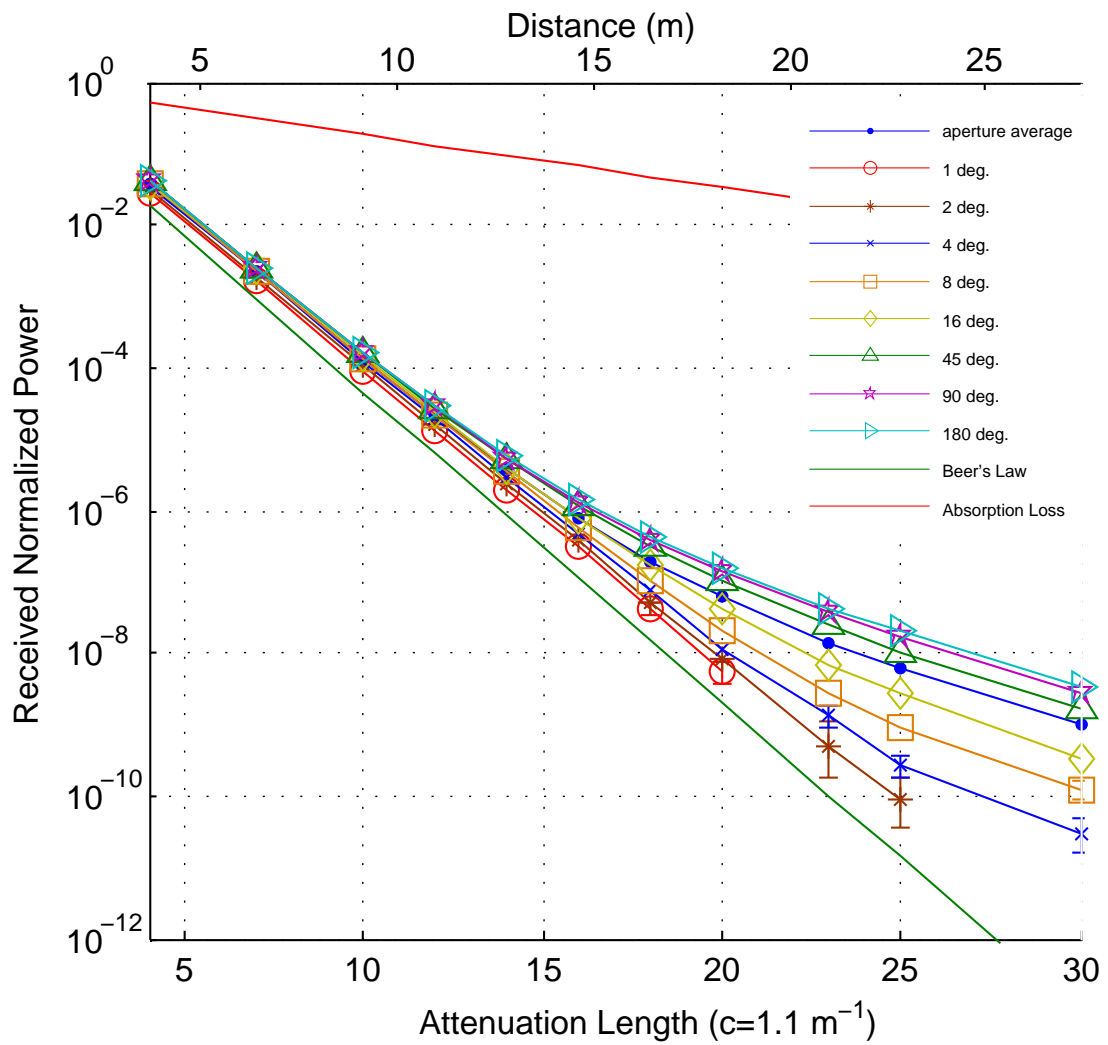


Figure 5.9: Harbor I - 2 inch aperture received normalized power.

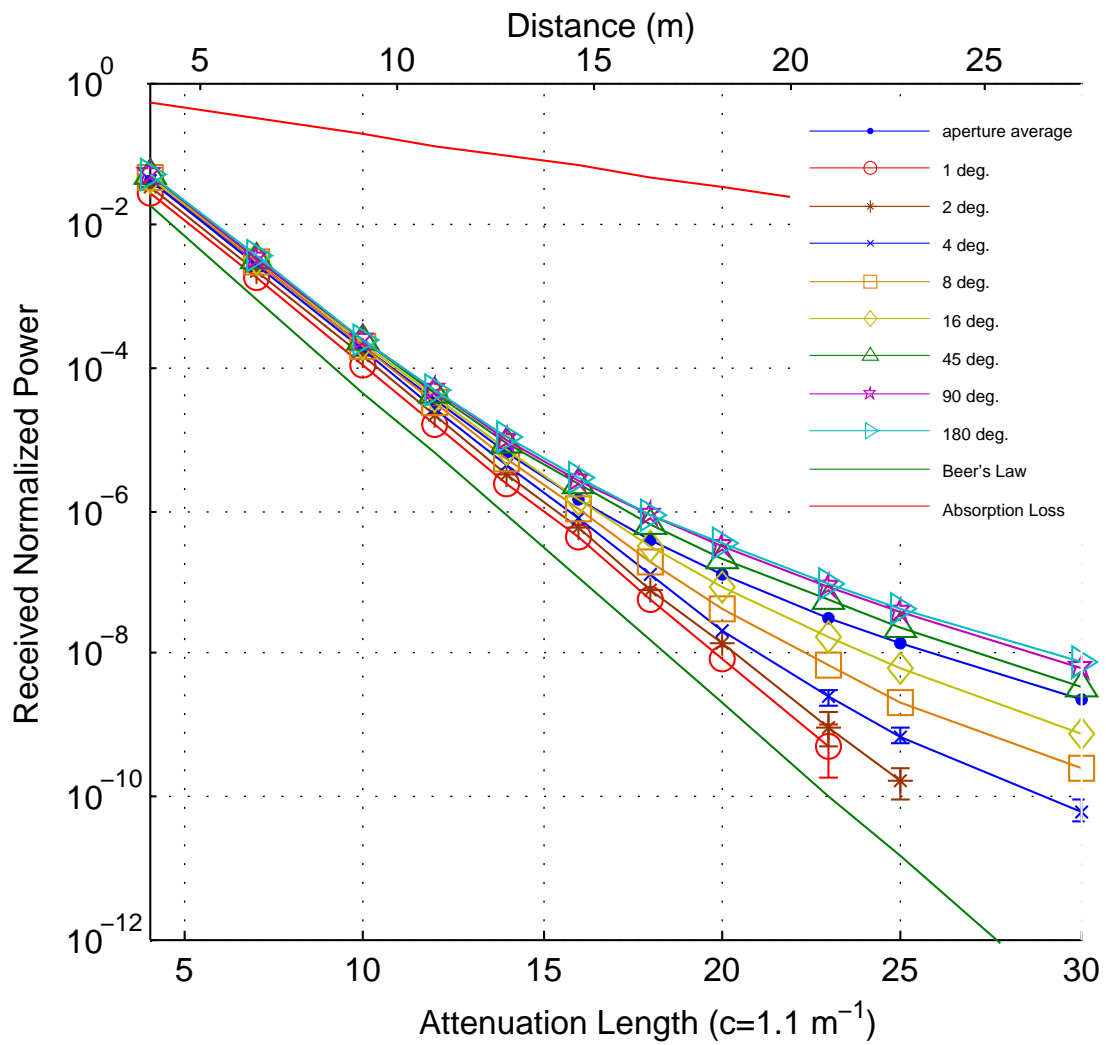


Figure 5.10: Harbor I - 3 inch aperture received normalized power.

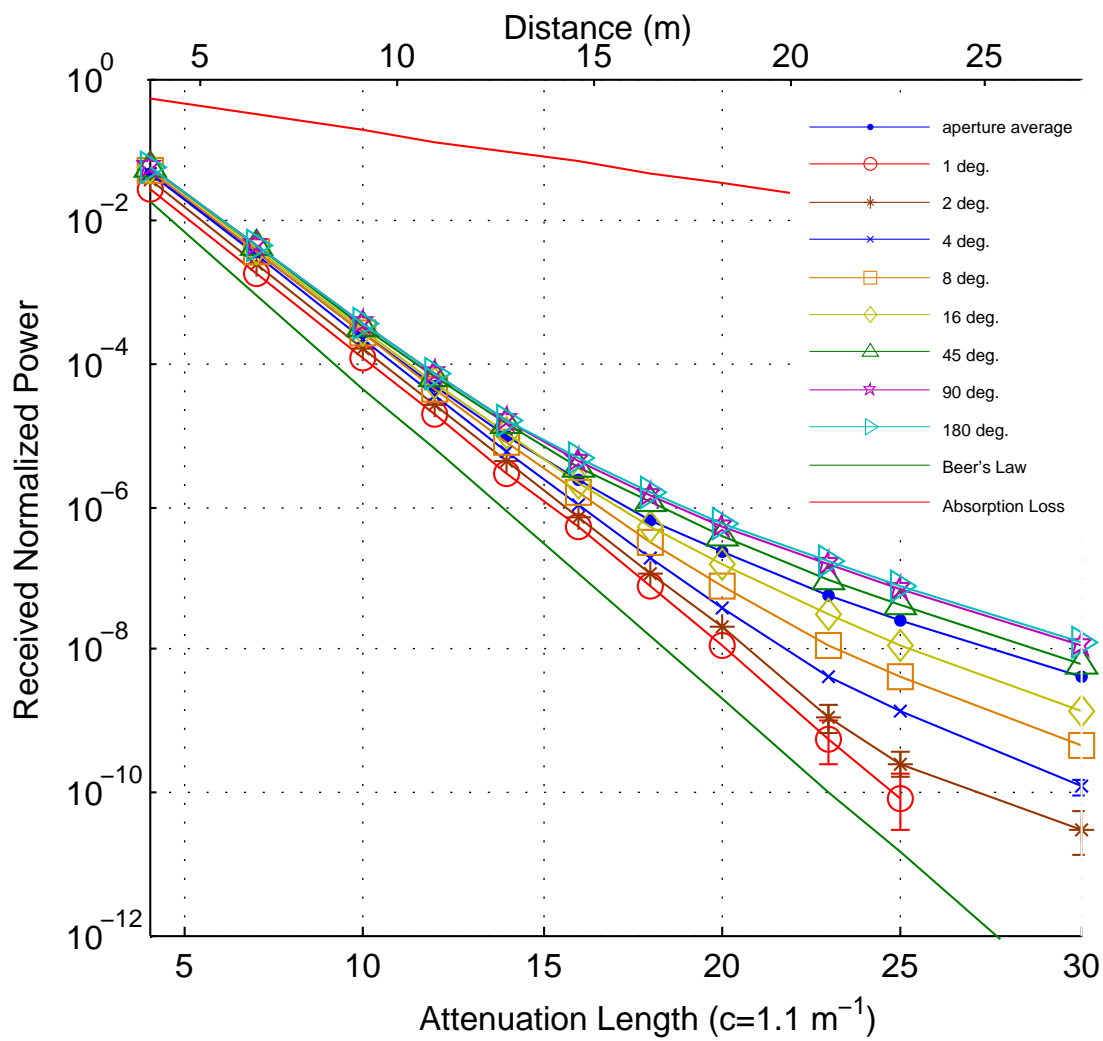


Figure 5.11: Harbor I - 4 inch aperture received normalized power.

Harbor II

Figures for Harbor II-type waters are presented next.

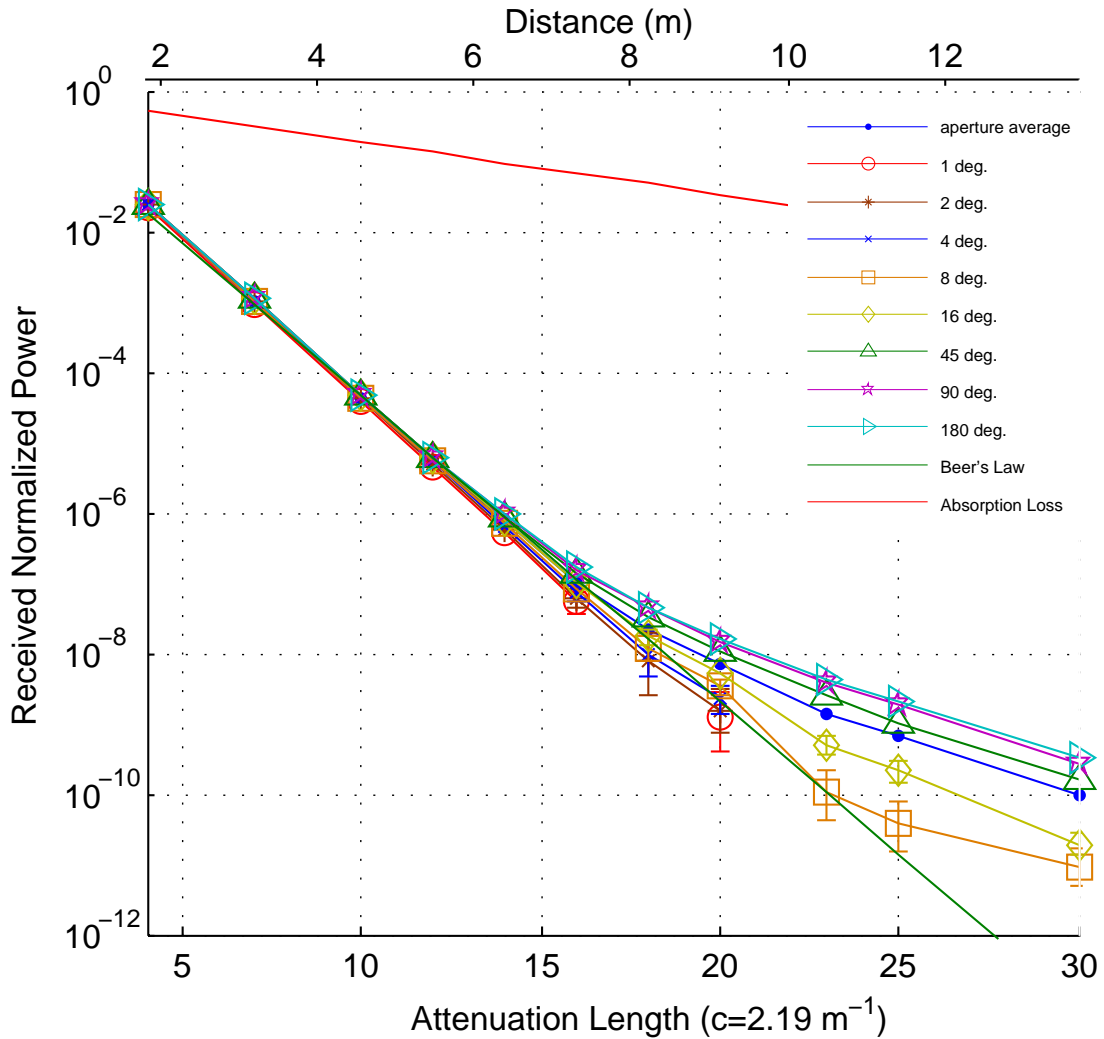


Figure 5.12: Harbor II - 8mm aperture: Received power normalized by transmit power, plotted versus receiver attenuation length. The c value is fixed and the distance is scaled. Error bars are plotted when the estimated error is greater than $\pm 25\%$. Error bars represent 95% confidence for a binomial distribution, which should be slightly greater than the actual photon weight distribution.

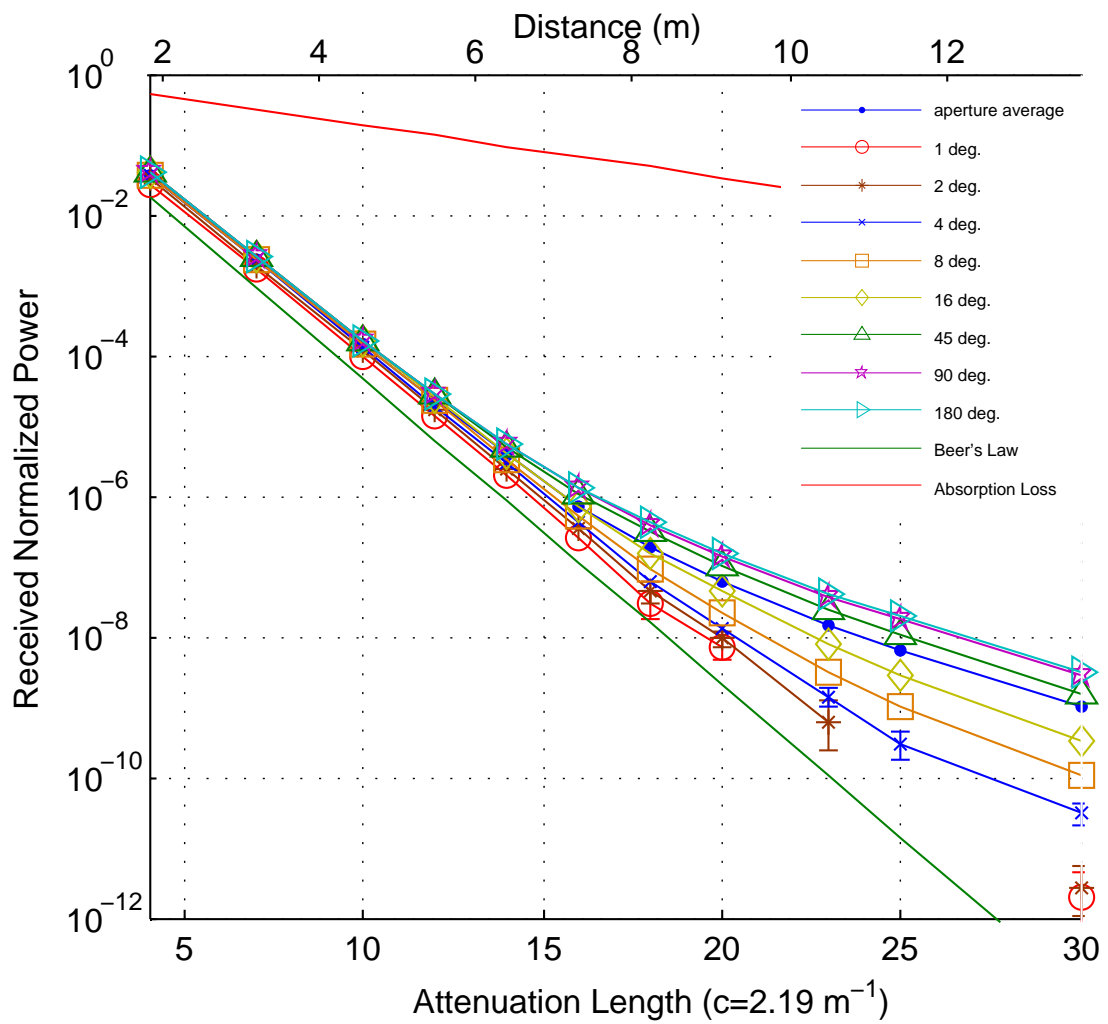


Figure 5.13: Harbor II - 1in aperture received normalized power.

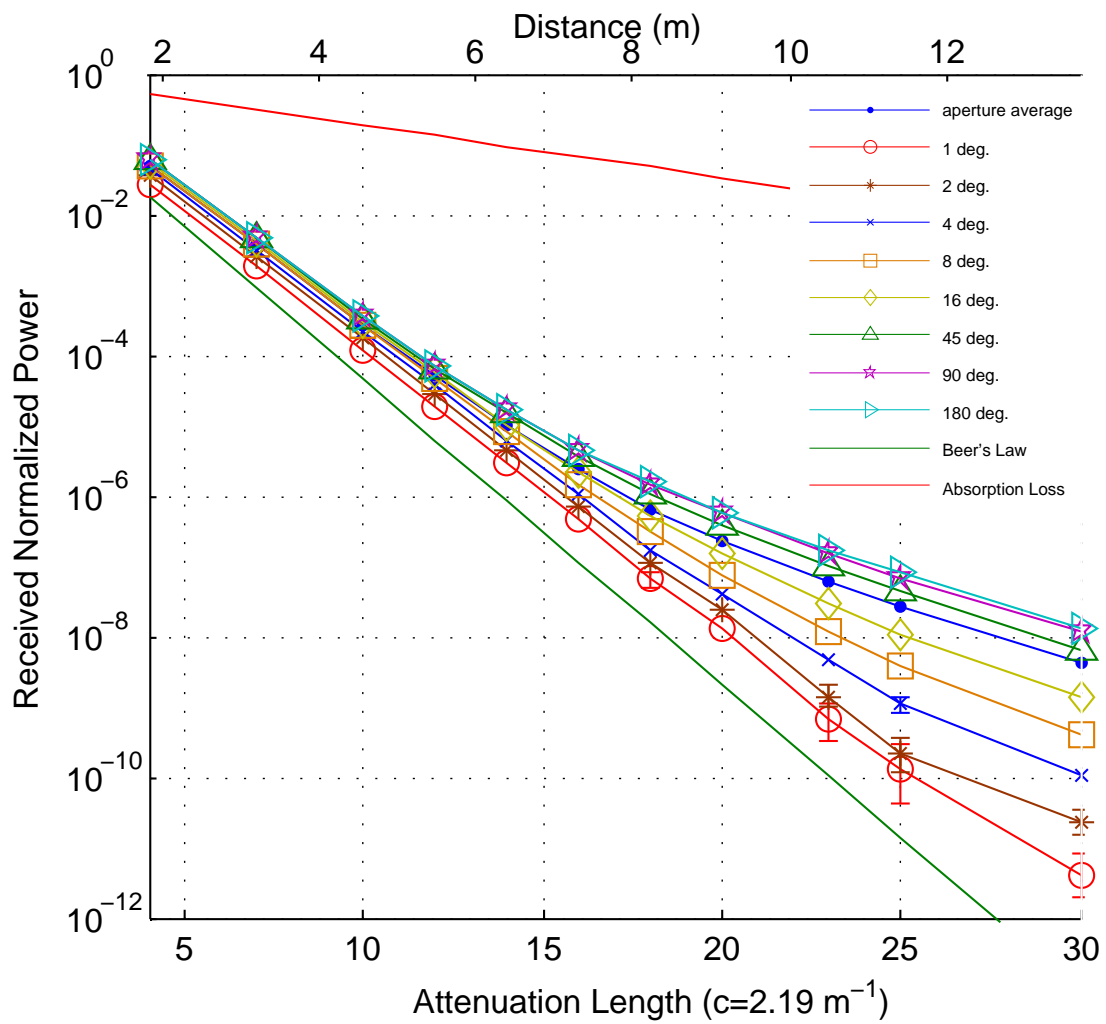


Figure 5.14: Harbor II - 2in aperture received normalized power.

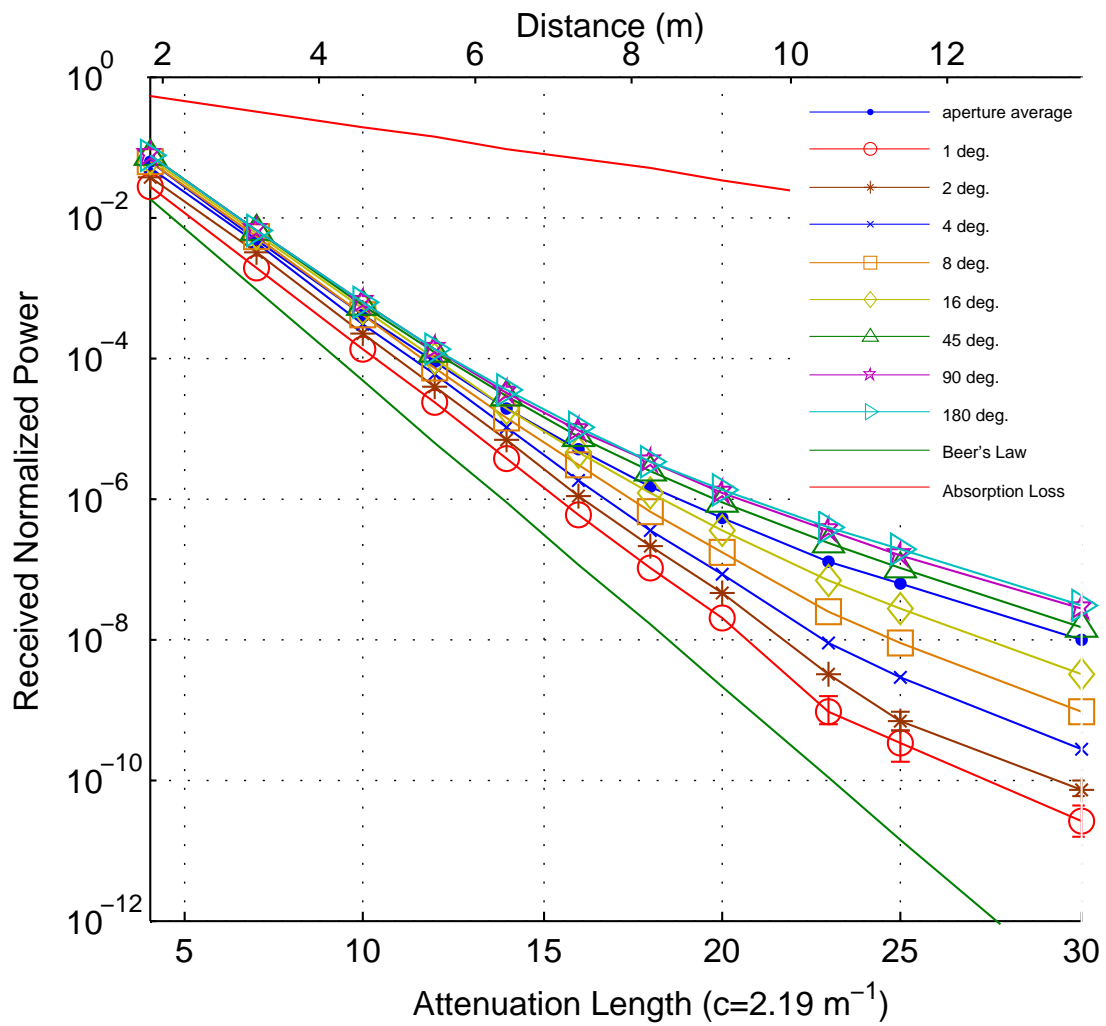


Figure 5.15: Harbor II - 3in aperture received normalized power.

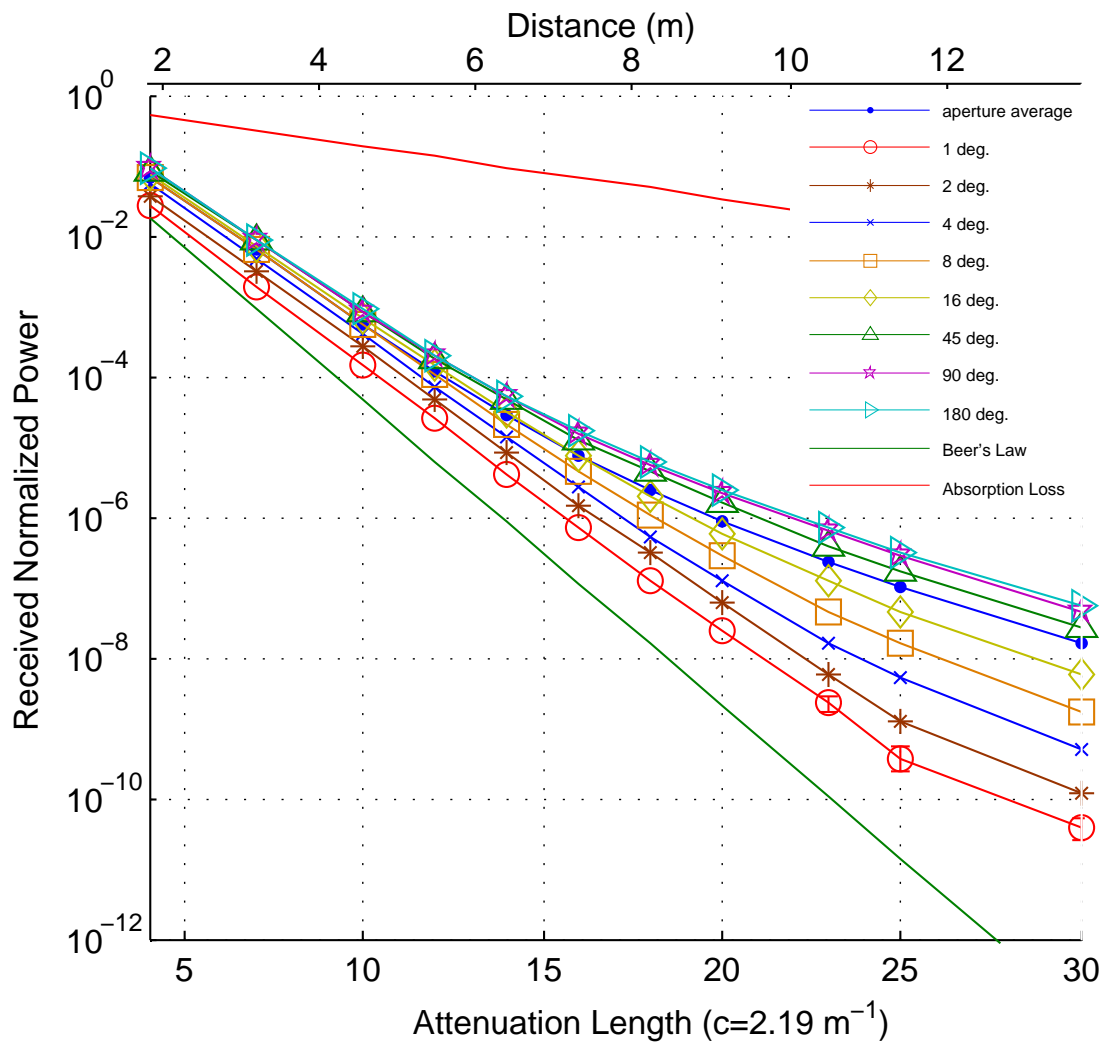


Figure 5.16: Harbor II - 4in aperture received normalized power.

Harbor III

Figures for Harbor III-type waters are presented next.

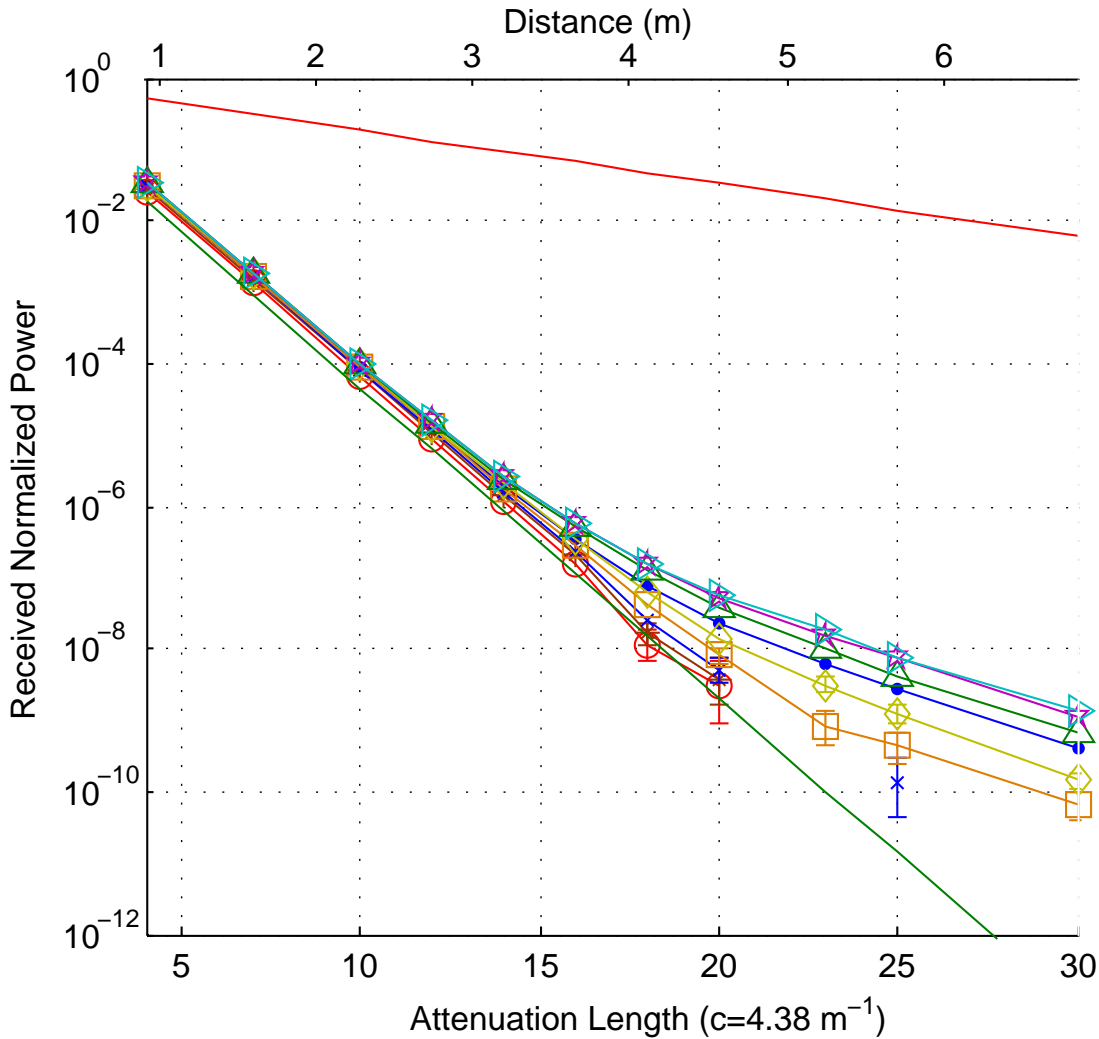


Figure 5.17: Harbor III - 8mm aperture: Received power normalized by transmit power, plotted versus receiver attenuation length. The c value is fixed and the distance is scaled. Error bars are plotted when the estimated error is greater than $\pm 25\%$. Error bars represent 95% confidence for a binomial distribution, which should be slightly greater than the actual photon weight distribution.

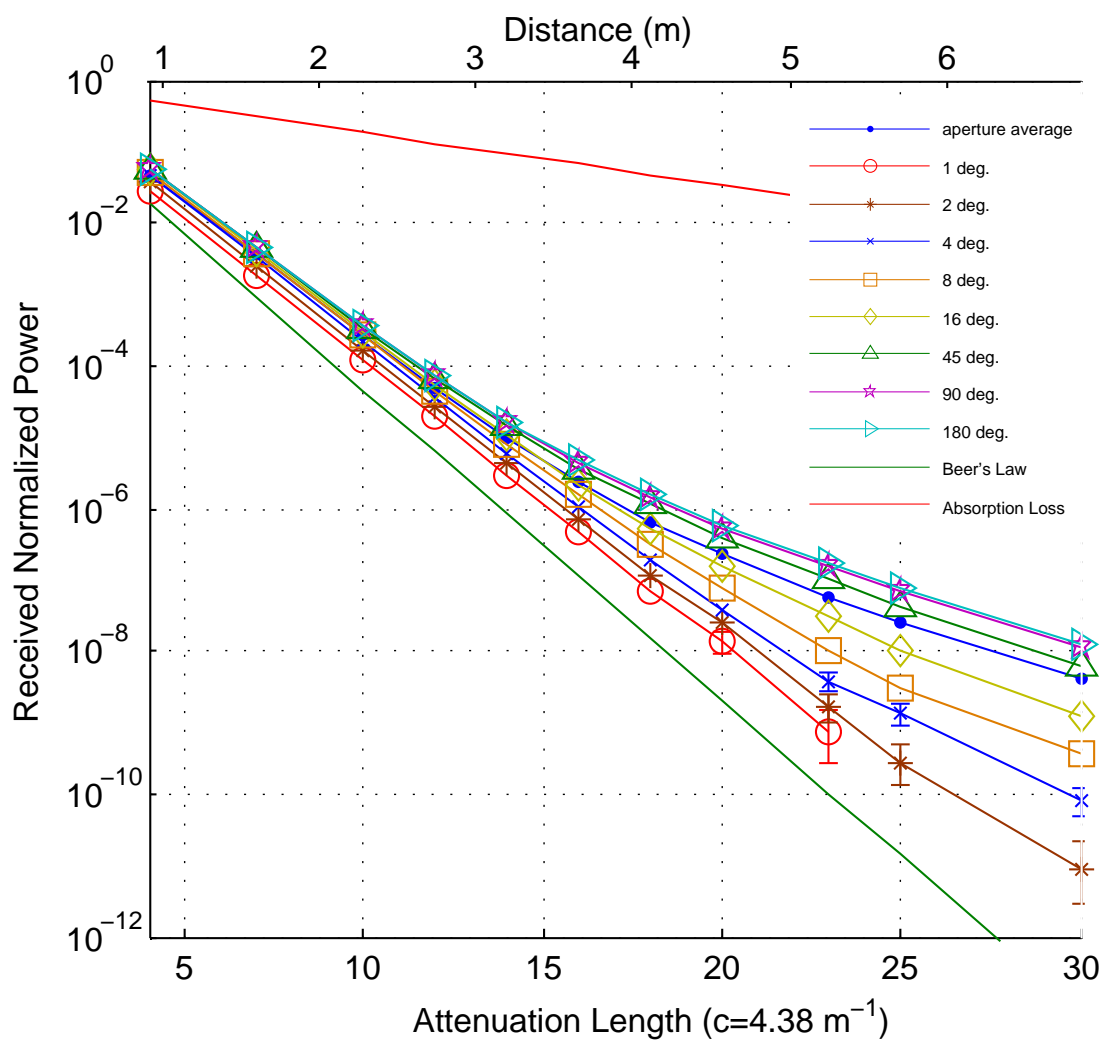


Figure 5.18: Harbor III - 1in aperture normalized power.

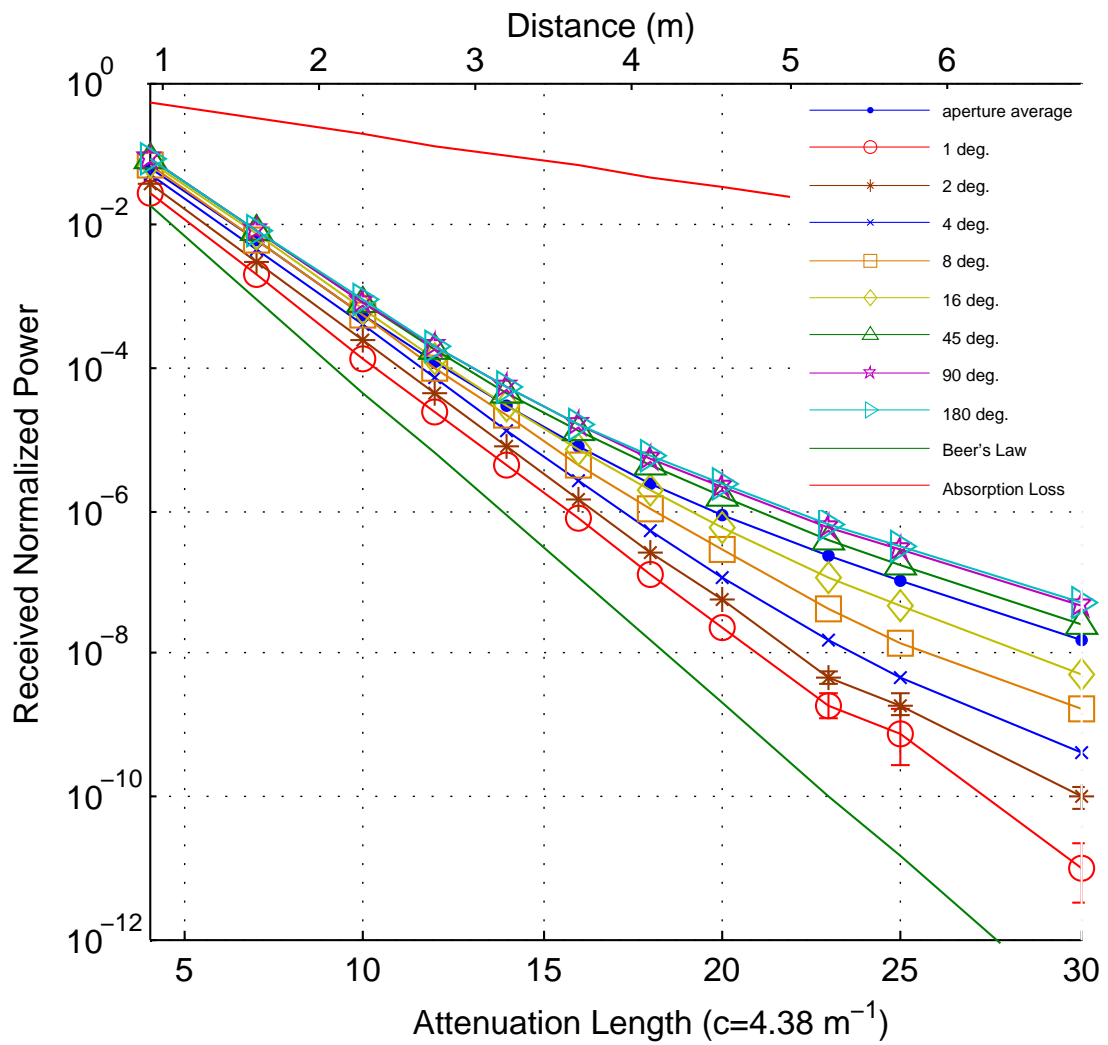


Figure 5.19: Harbor III - 2in aperture normalized power.

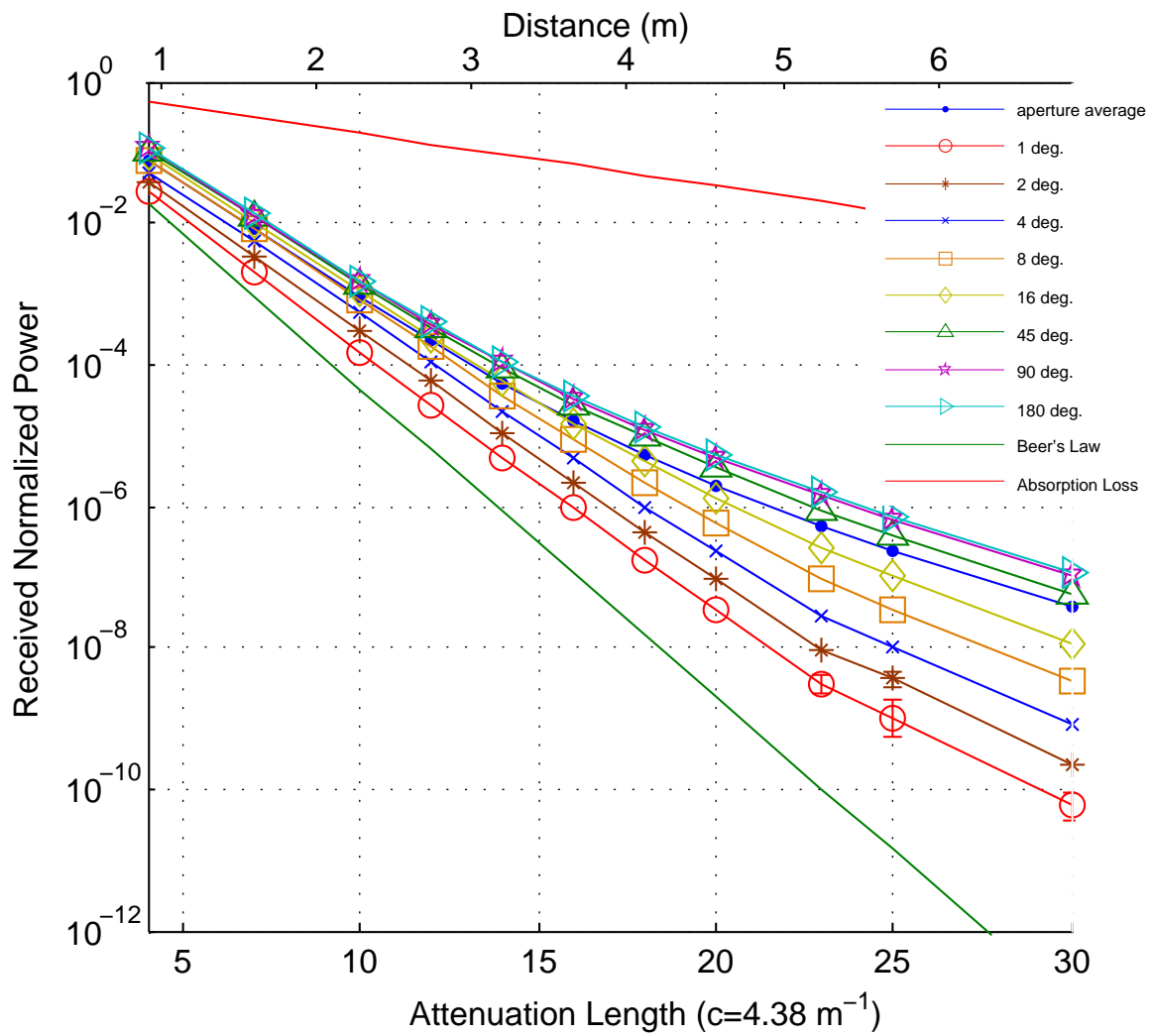


Figure 5.20: Harbor III - 3in aperture normalized power.

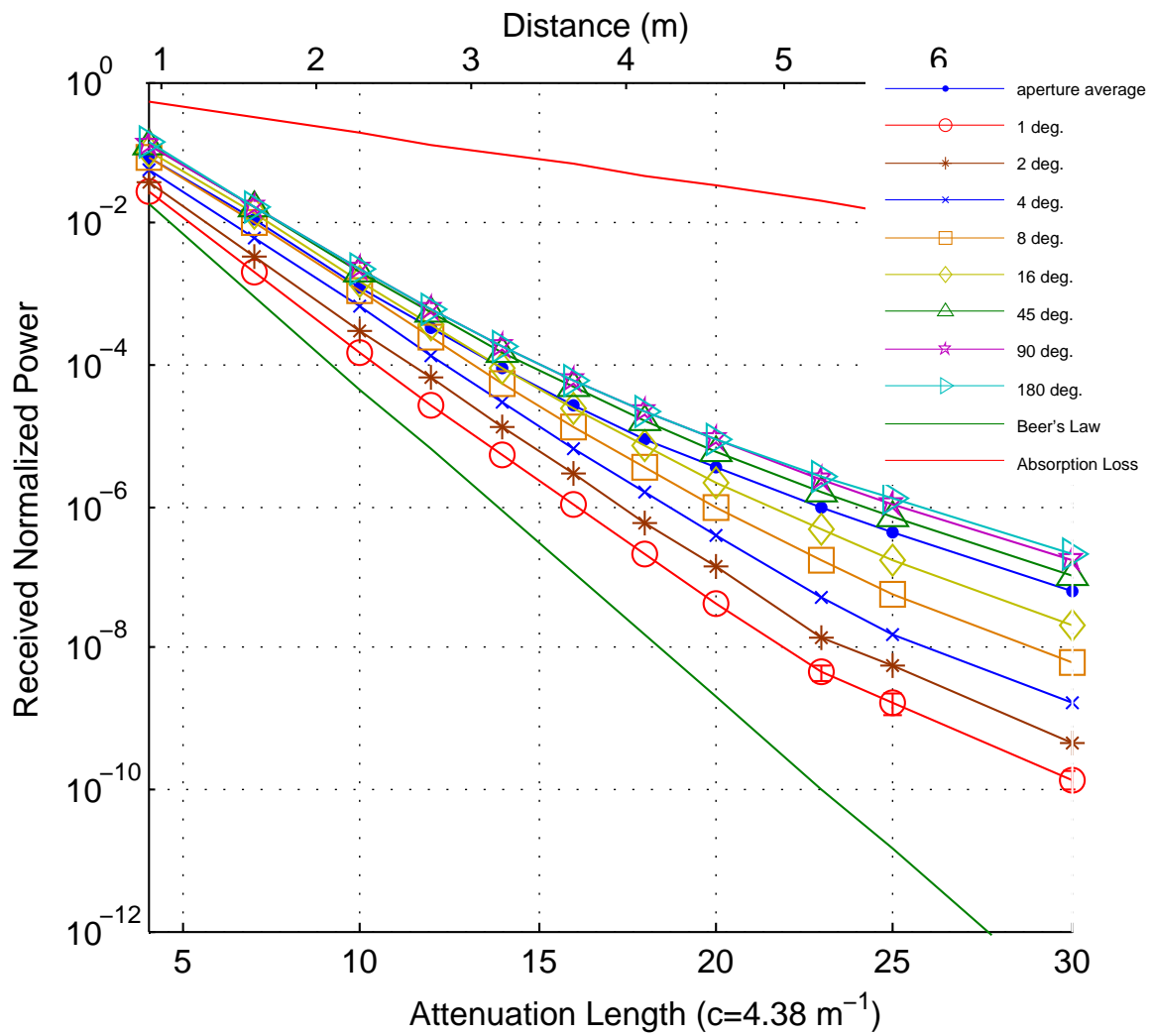


Figure 5.21: Harbor III - 4in aperture normalized power.

Average Power

The average received power for various apertures is presented next.

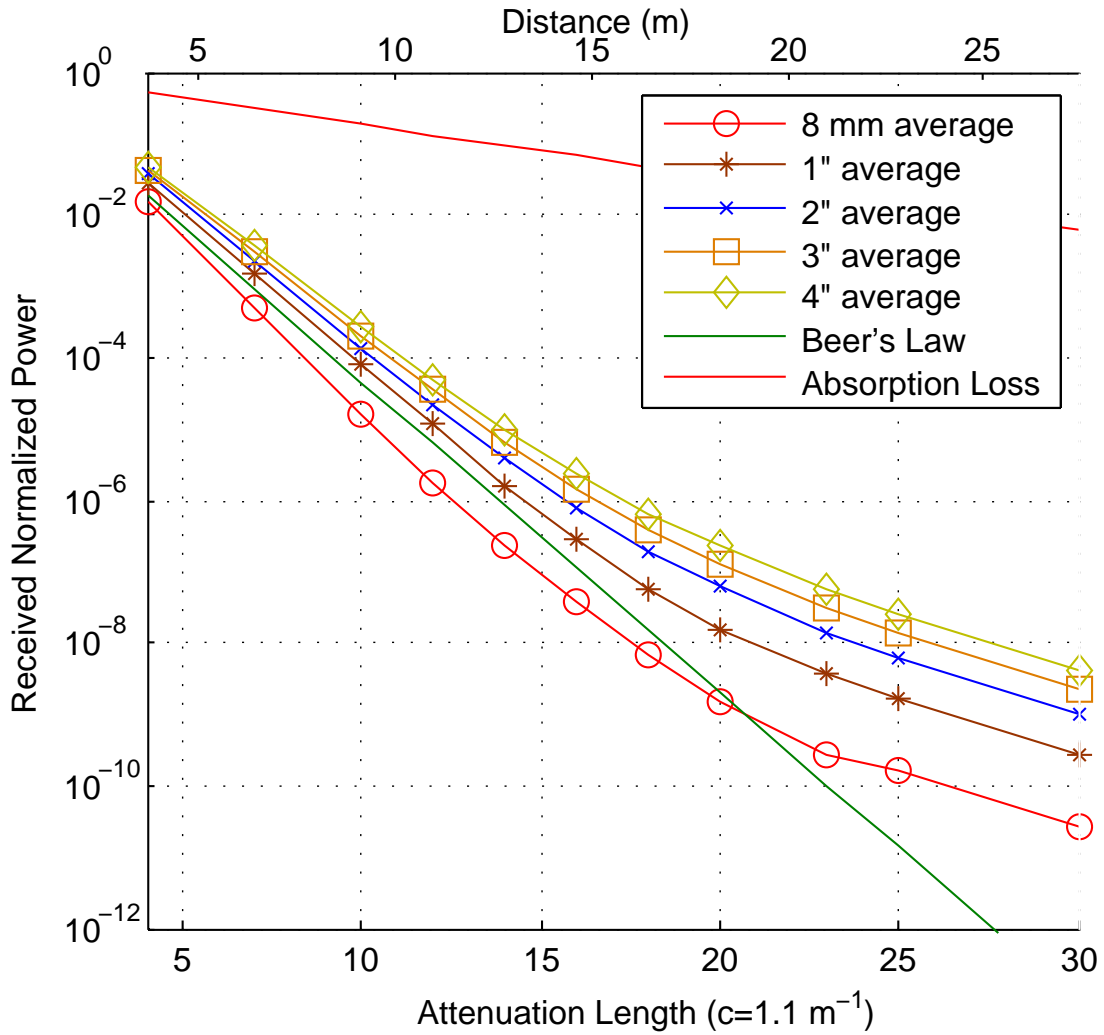


Figure 5.22: Harbor I - Normalized received power for various apertures, averaged over their FOVs.

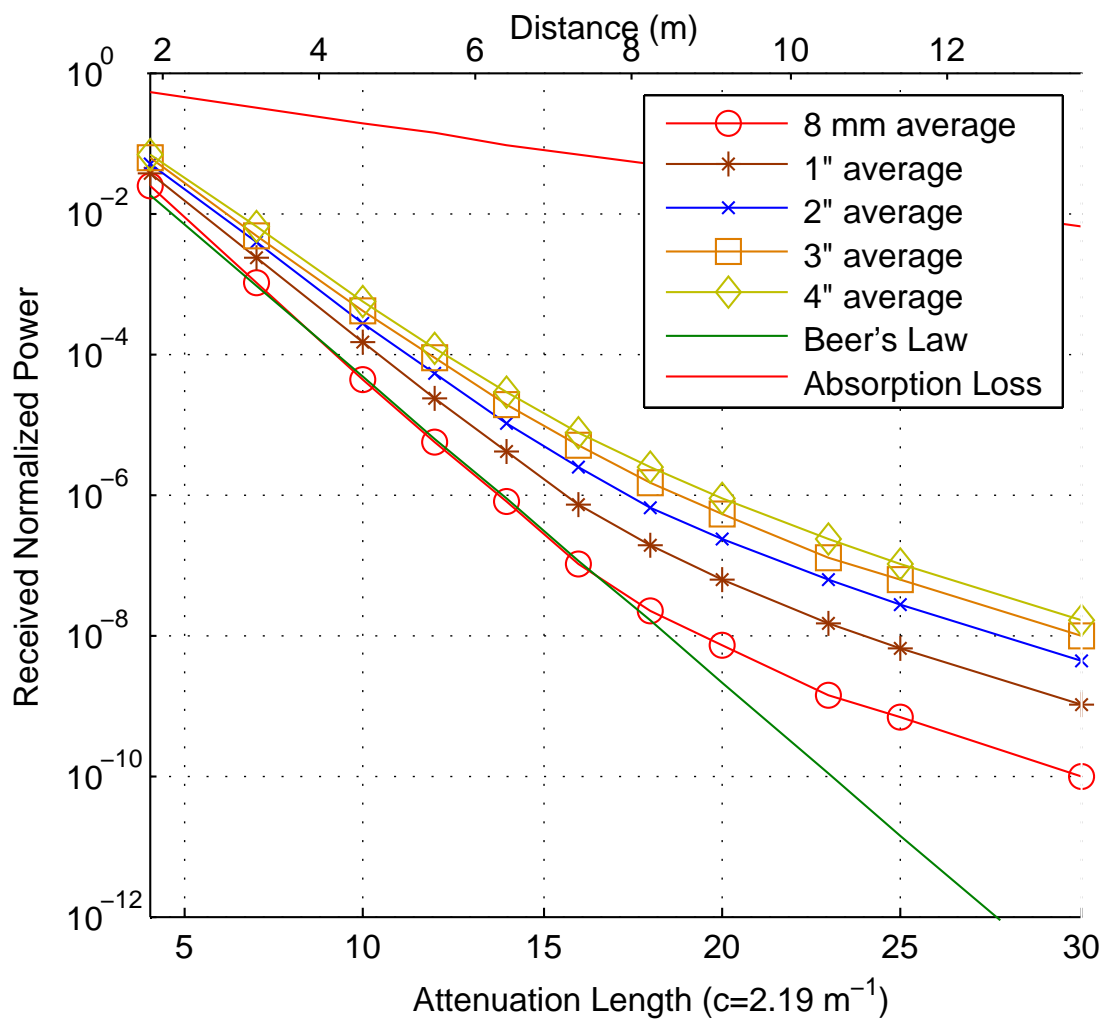


Figure 5.23: Harbor II - Normalized received power for various apertures, averaged over their FOVs.

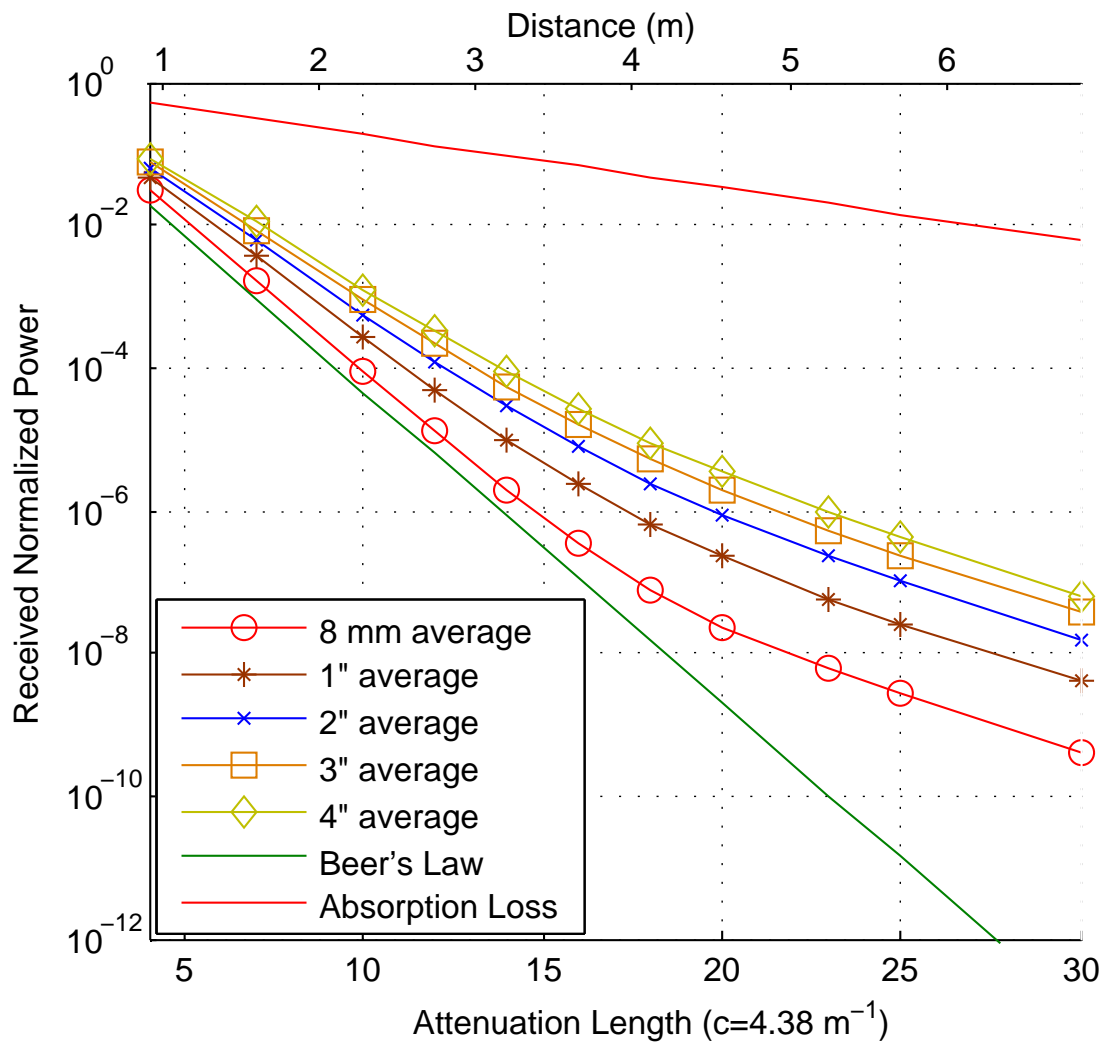


Figure 5.24: Harbor III - Normalized received power for various apertures, averaged over their FOVs.

Power versus FOV

Figures showing the power versus the field of view (FOV) are presented next.

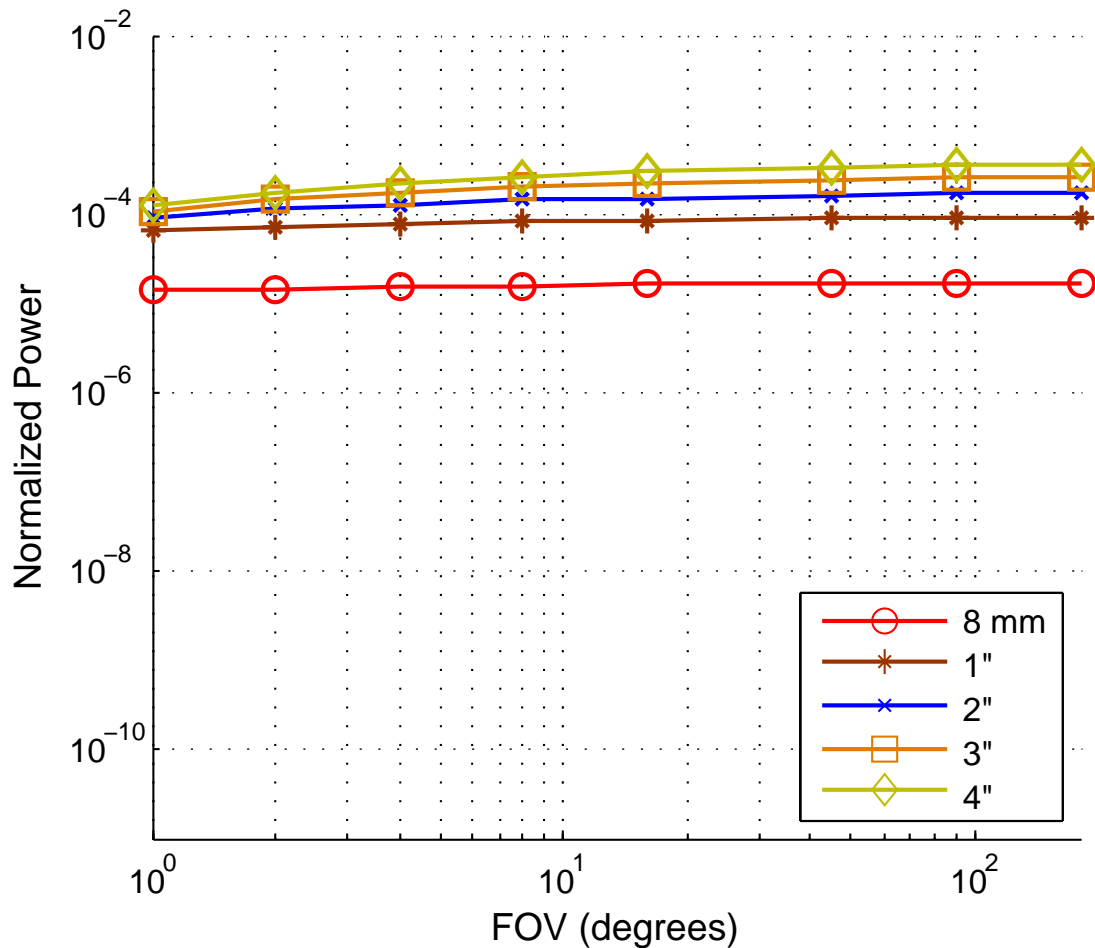


Figure 5.25: Harbor I: Received power normalized by transmit power at 10 attenuation lengths (9.1 m), plotted versus receiver FOV. Error bars are presented with binomial 95% confidence interval is greater than 25% of the value.

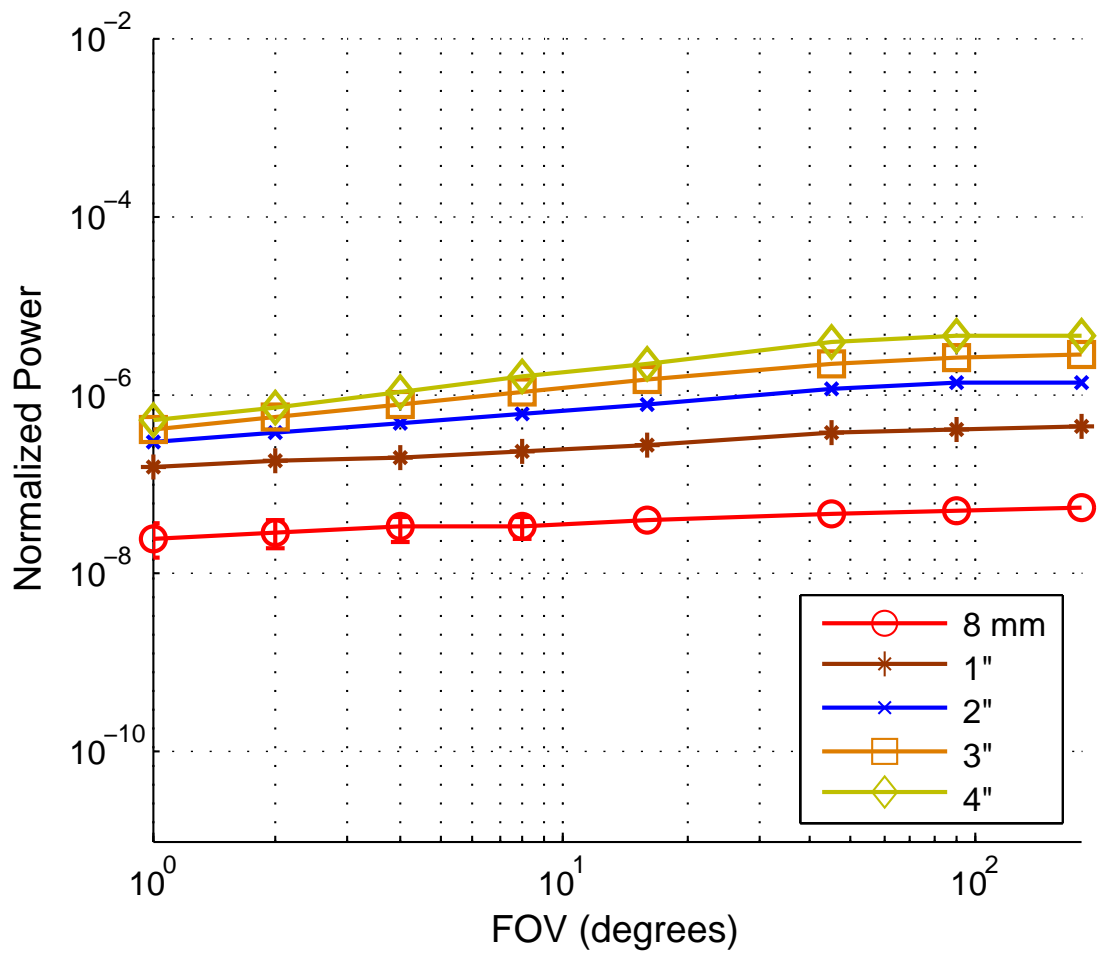


Figure 5.26: Harbor I - Received power at 16 attenuation lengths (14.5 m).

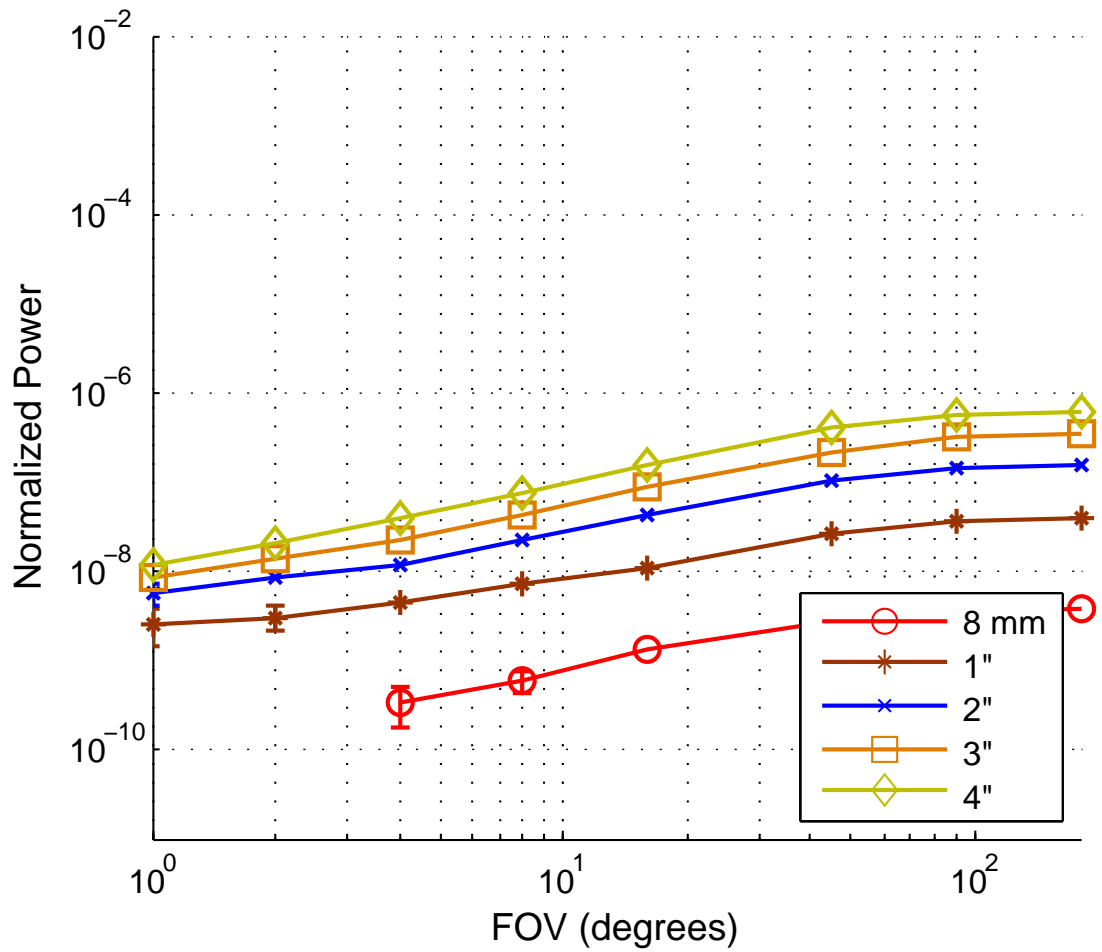


Figure 5.27: Harbor I - Received power at 20 attenuation lengths (18.2 m).

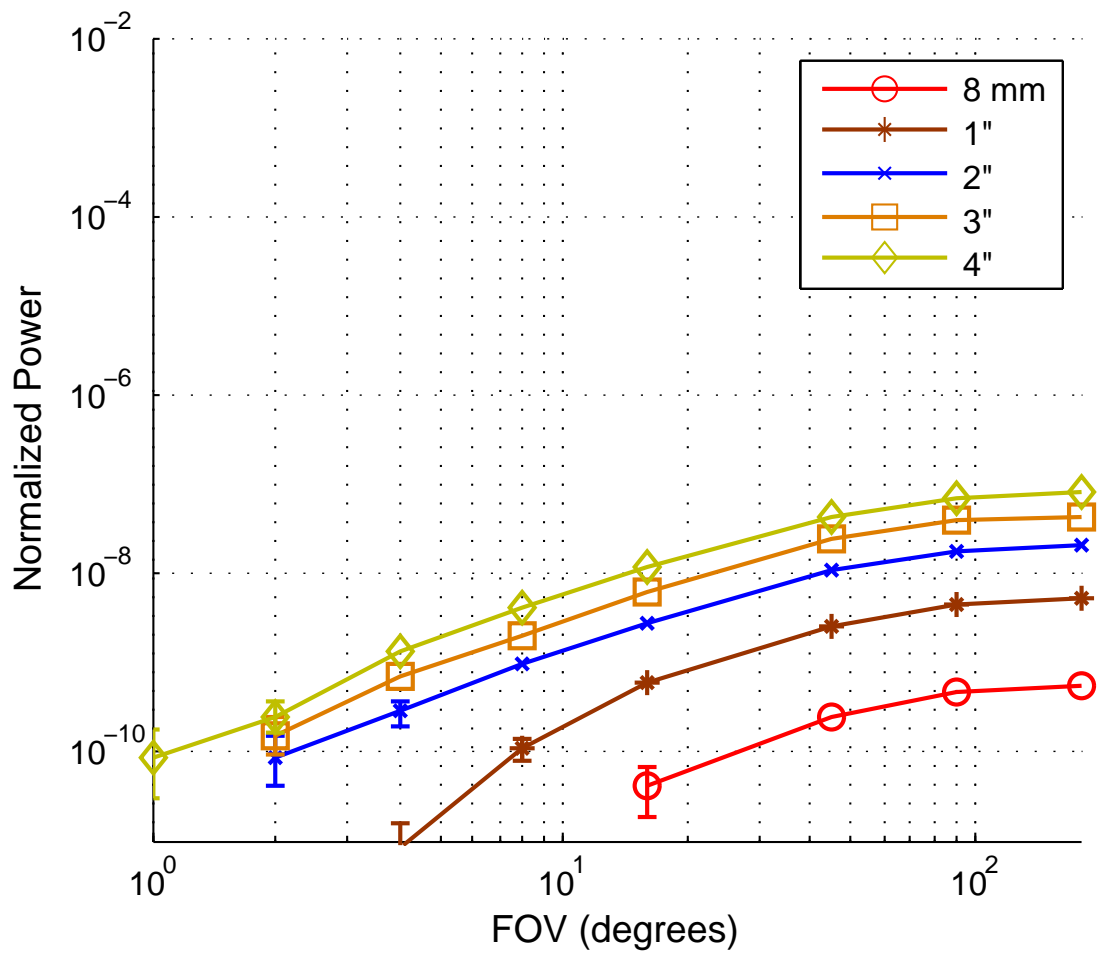


Figure 5.28: Harbor I - Received power at 25 attenuation lengths (22.7 m).

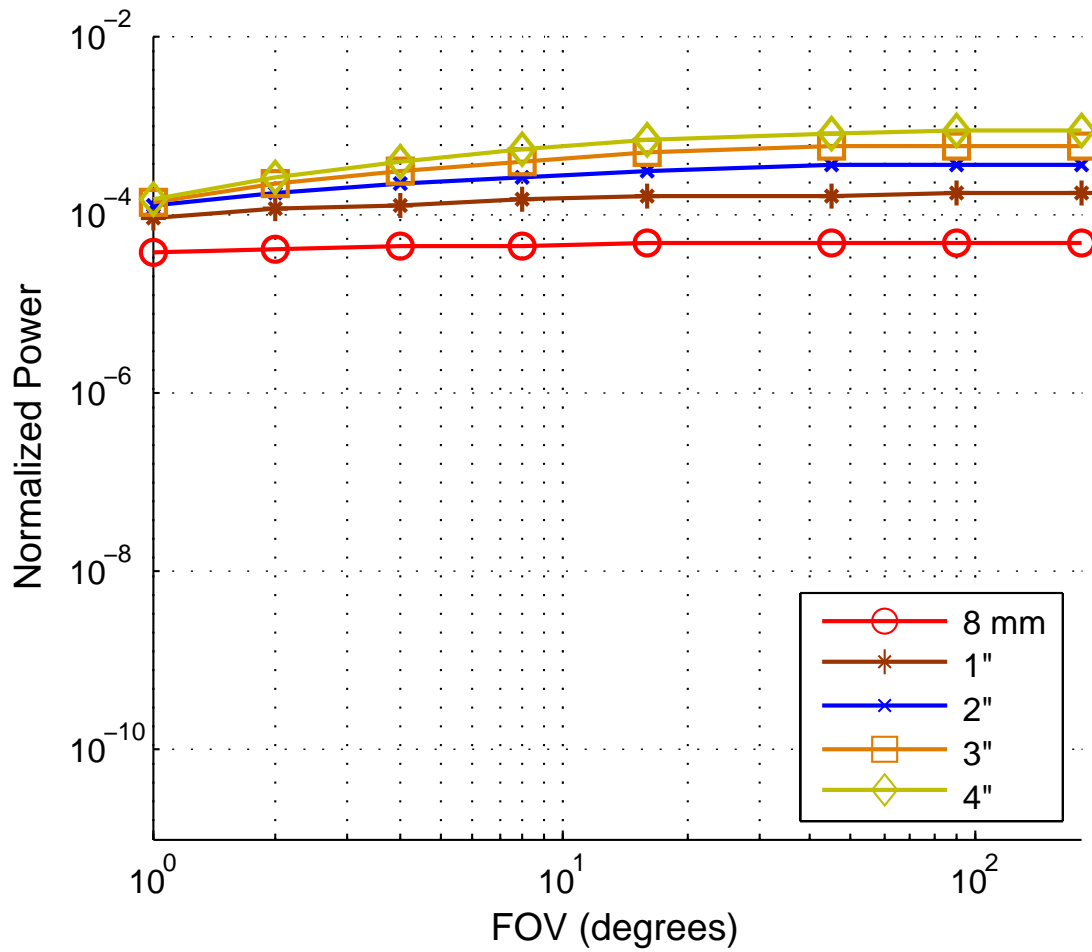


Figure 5.29: Harbor II: Received power normalized by transmit power at 10 attenuation lengths (4.5 m), plotted versus receiver FOV. Error bars are presented with binomial 95% confidence interval is greater than 25% of the value.

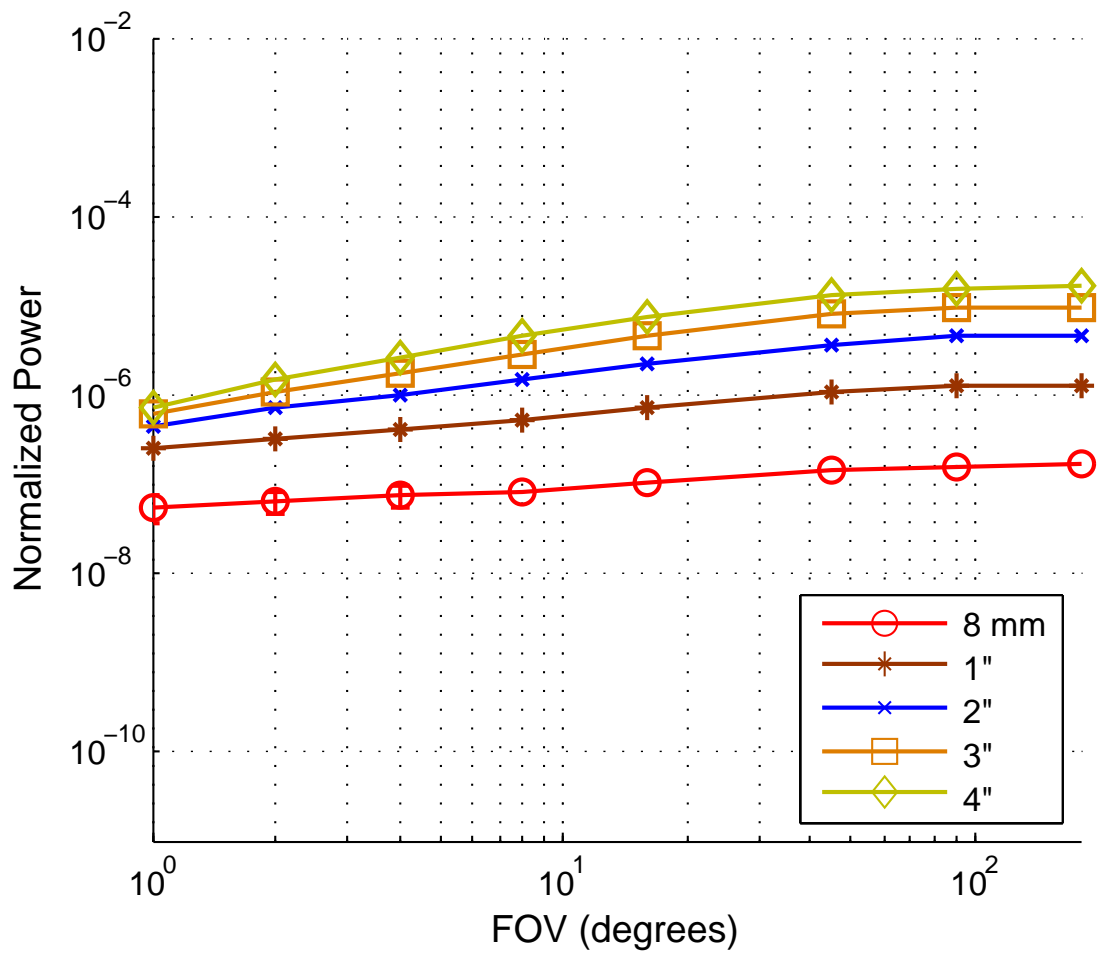


Figure 5.30: Harbor II - Received power at 16 attenuation lengths (7.3 m).

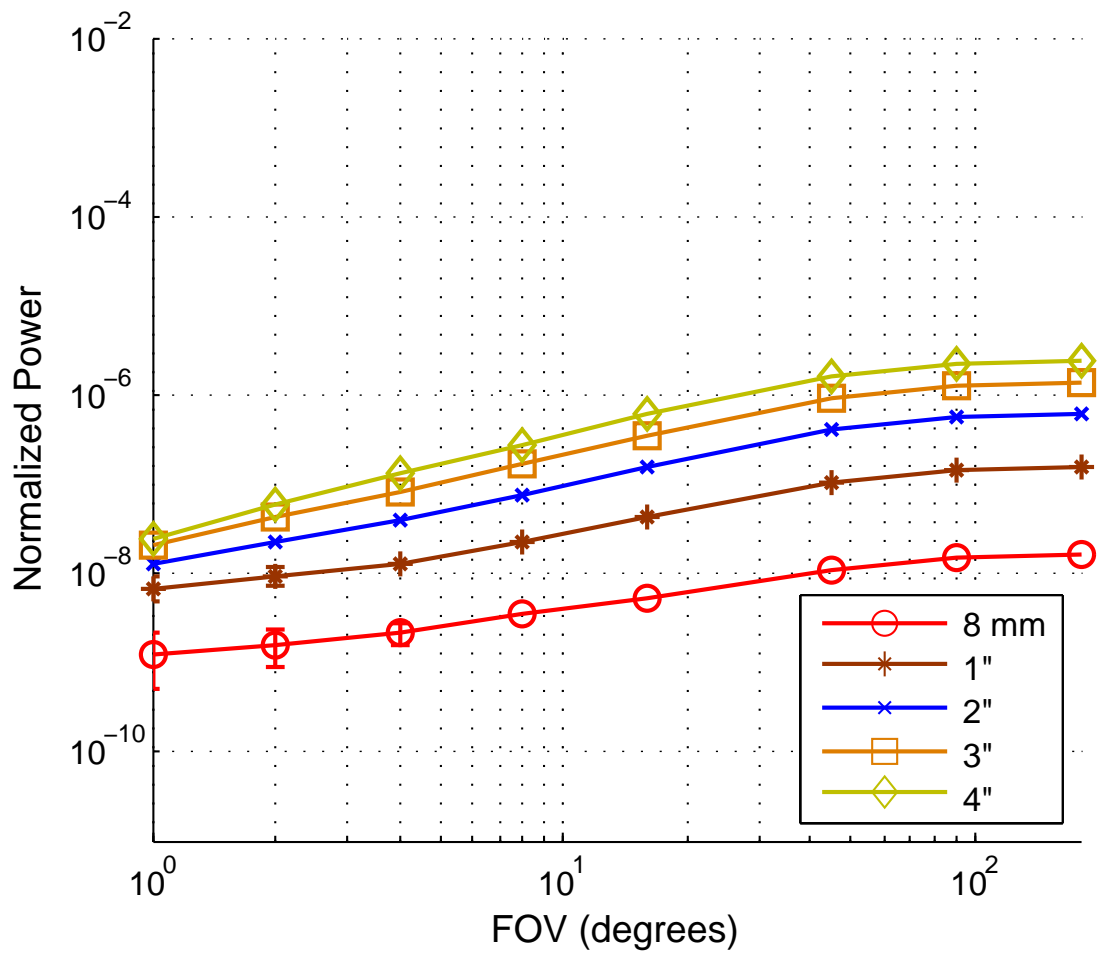


Figure 5.31: Harbor II - Received power at 20 attenuation lengths (9.1 m).

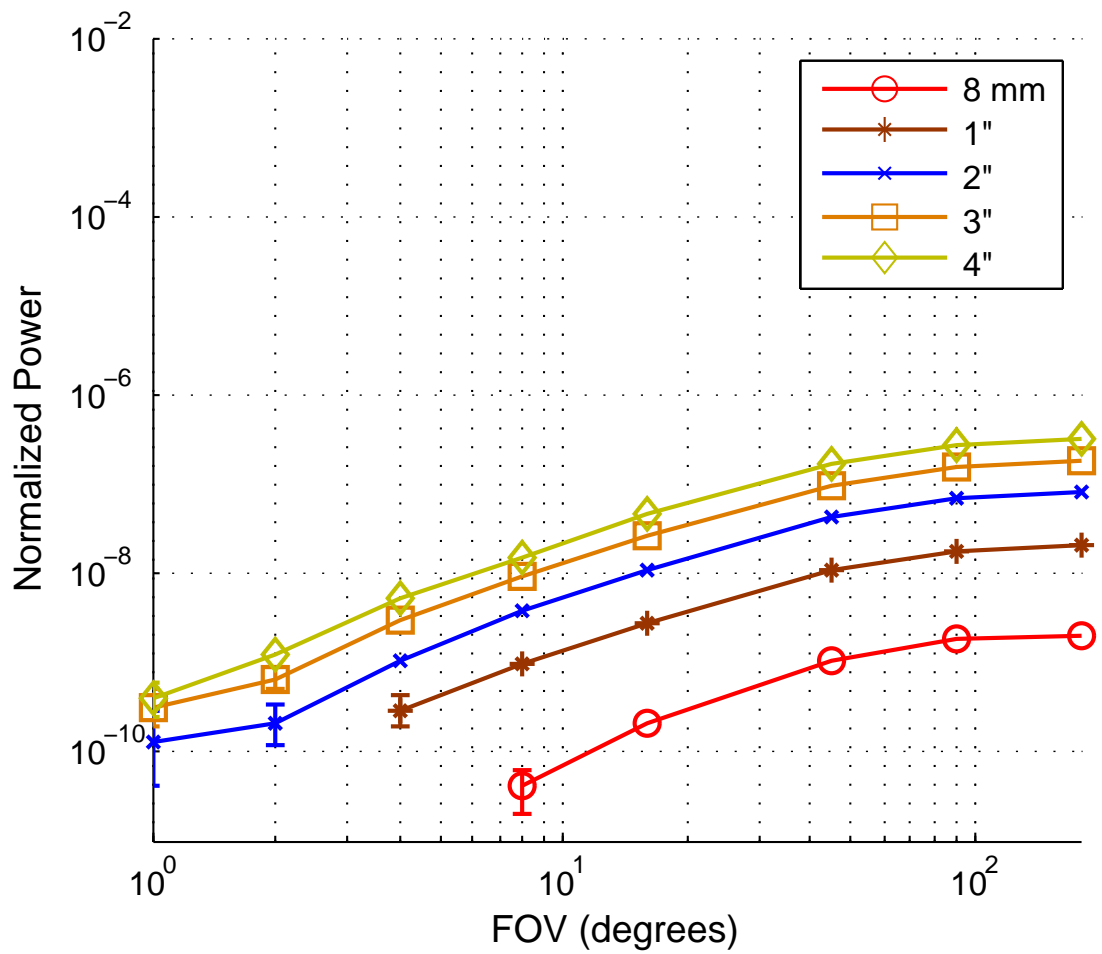


Figure 5.32: Harbor II - Received power at 25 attenuation lengths (11.3 m).

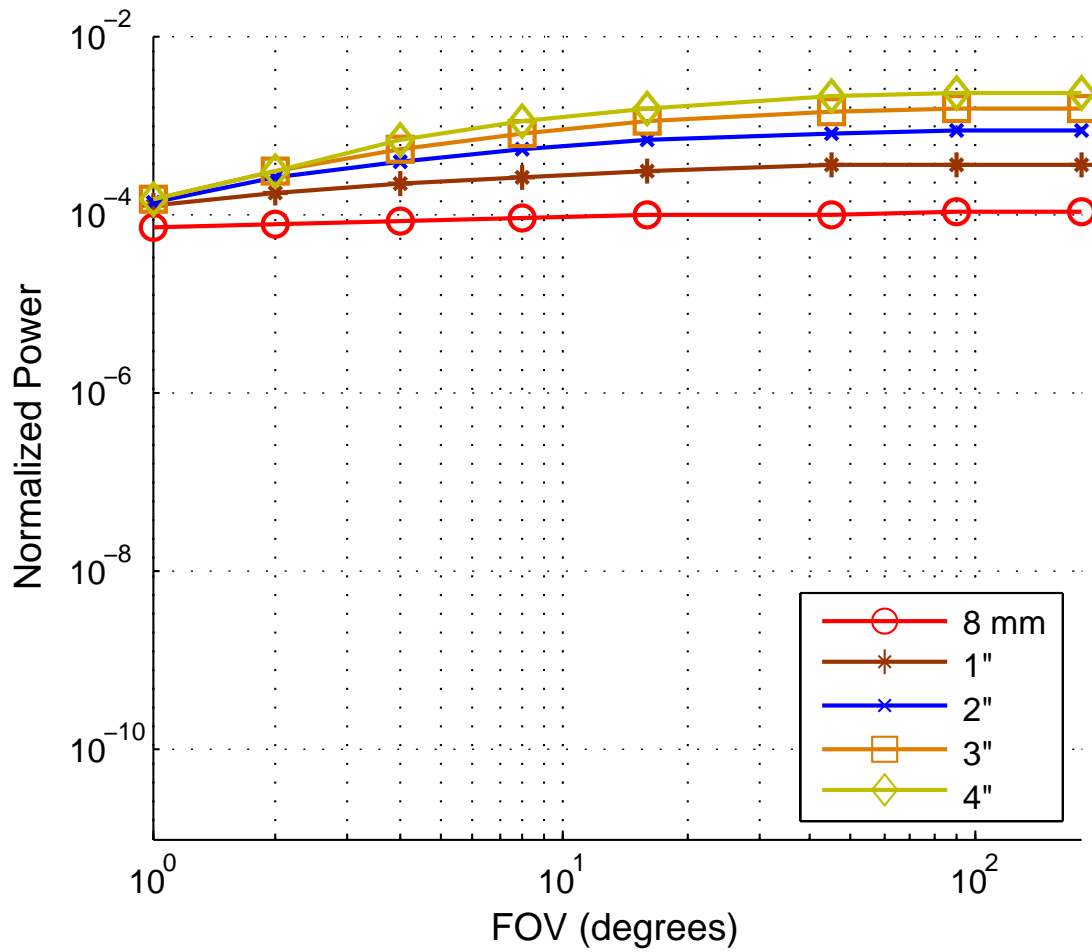


Figure 5.33: Harbor III: 10 attenuation lengths, 2.3 meters. Received power normalized by transmit power, plotted versus receiver FOV. Error bars are presented with binomial 95% confidence interval is greater than 25% of the value.

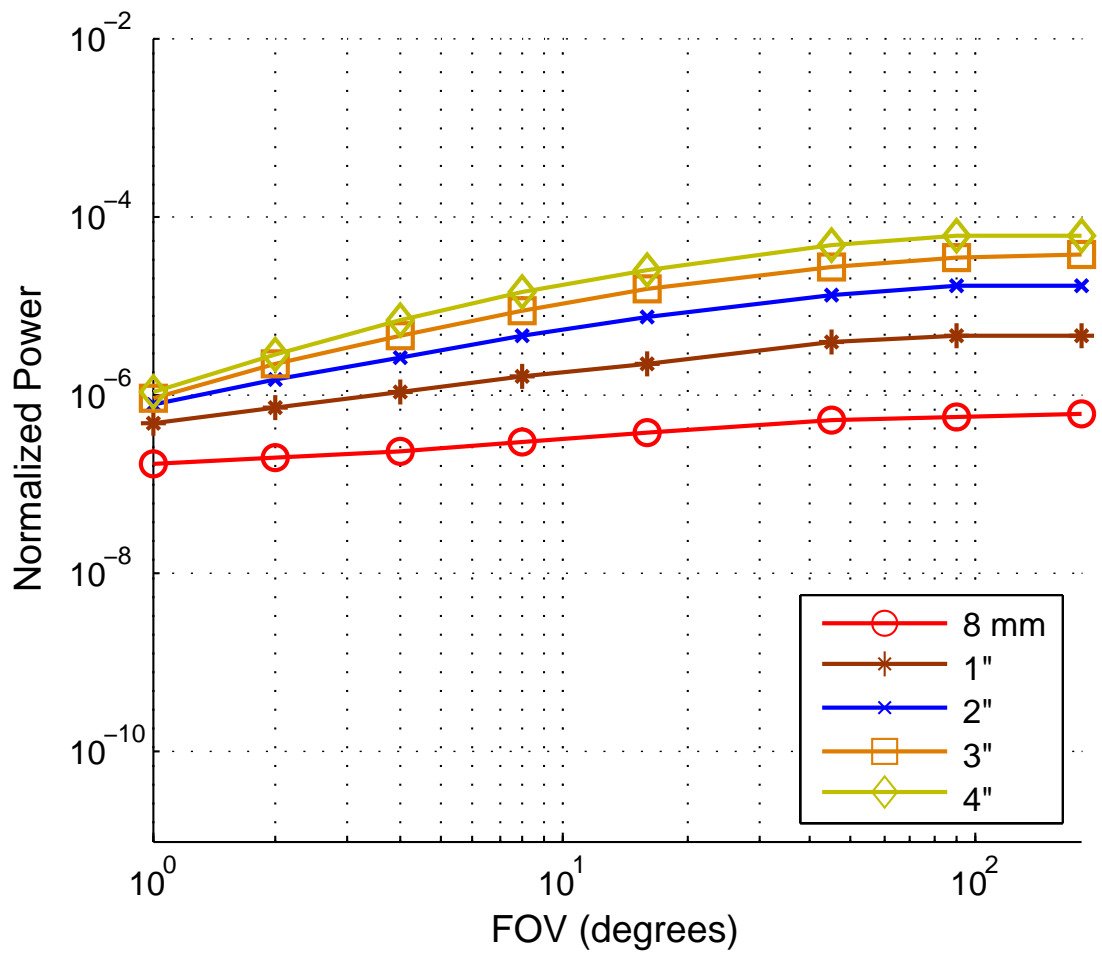


Figure 5.34: Harbor III: 16 attenuation lengths, 3.6 meters - power versus FOV

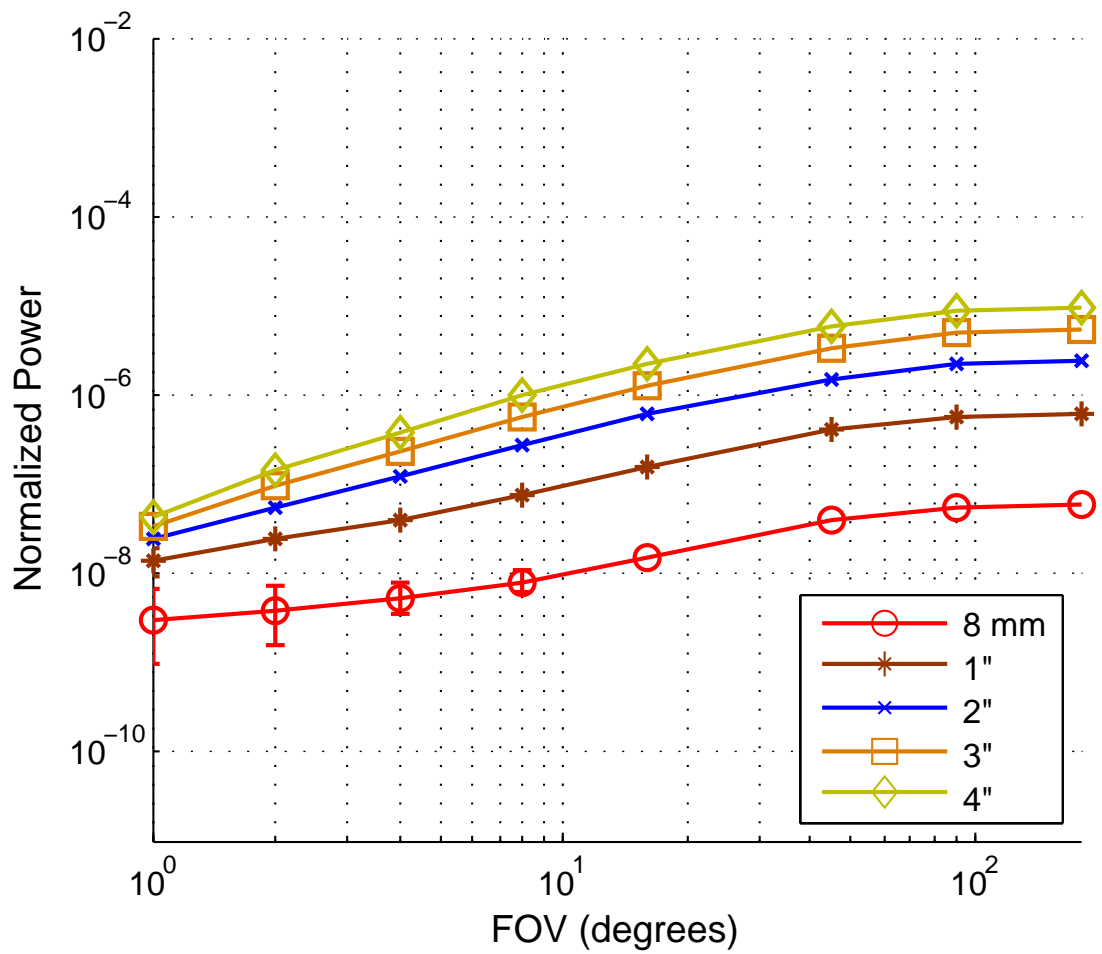


Figure 5.35: Harbor III: 20 attenuation lengths, 4.5 meters - power versus FOV

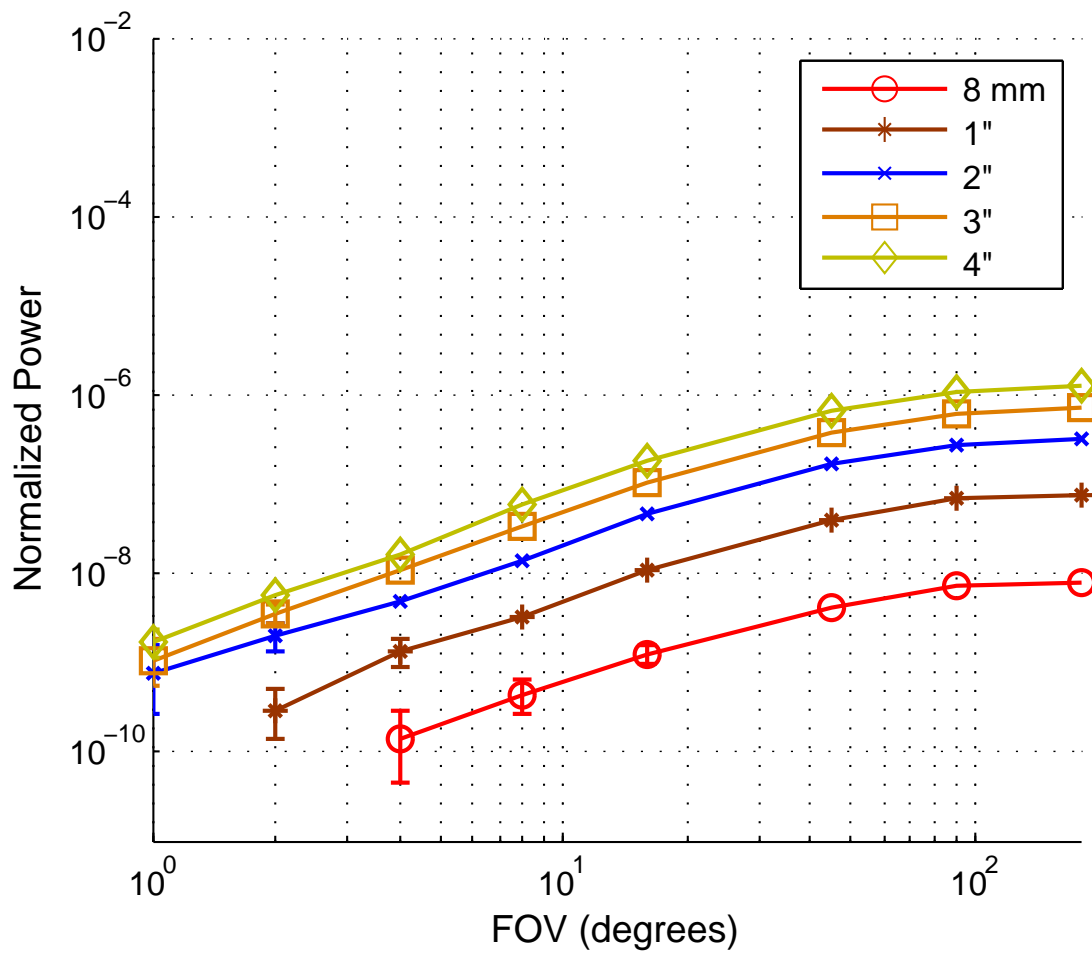


Figure 5.36: Harbor III 25 attenuation lengths, 5.7 meters - power versus FOV

Area normalized power versus FOV

Figures showing received power normalized by the receiver aperture versus FOV are presented next. These figures are discussed in Section 5.4.7 on page 74.

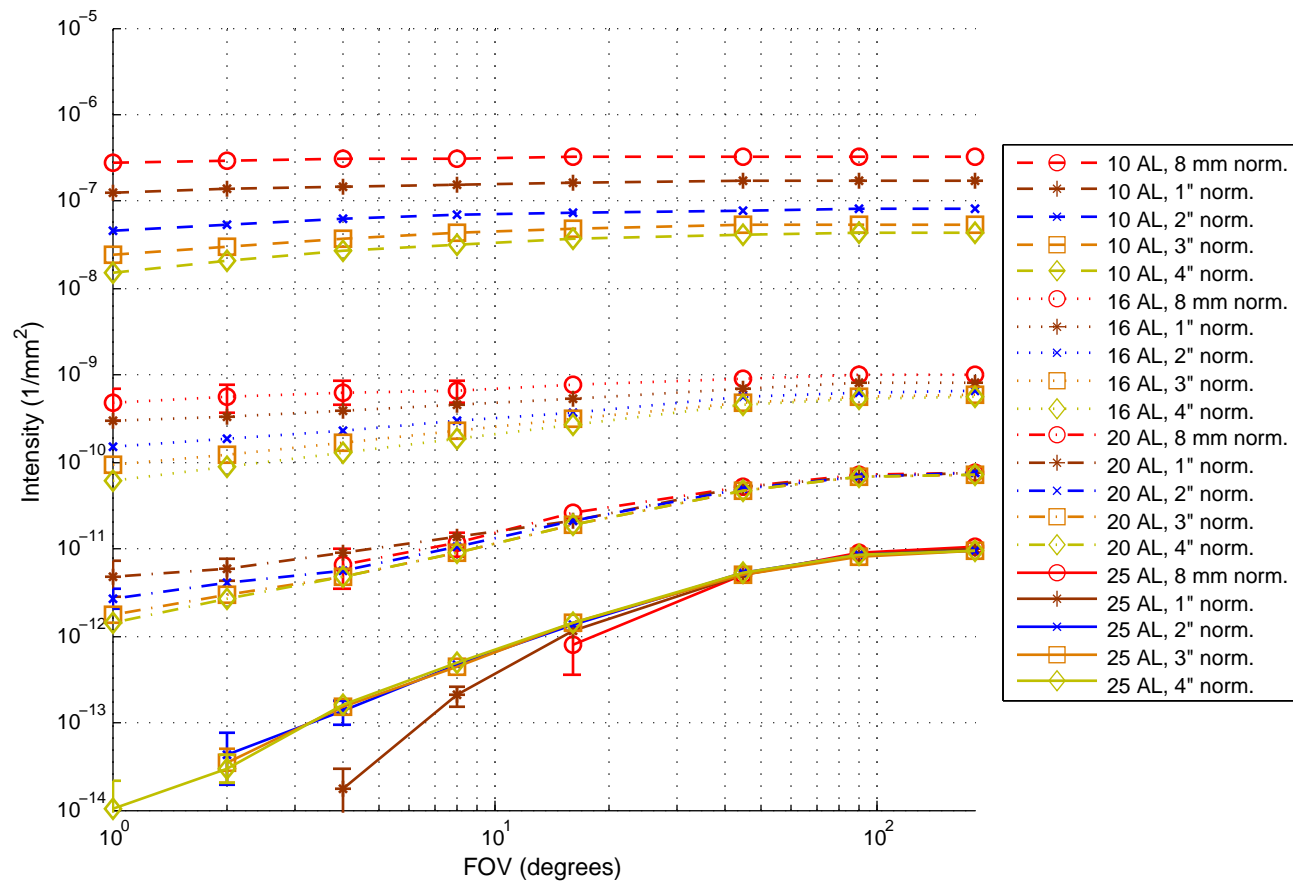


Figure 5.37: Harbor I received power normalized by the receiver area.

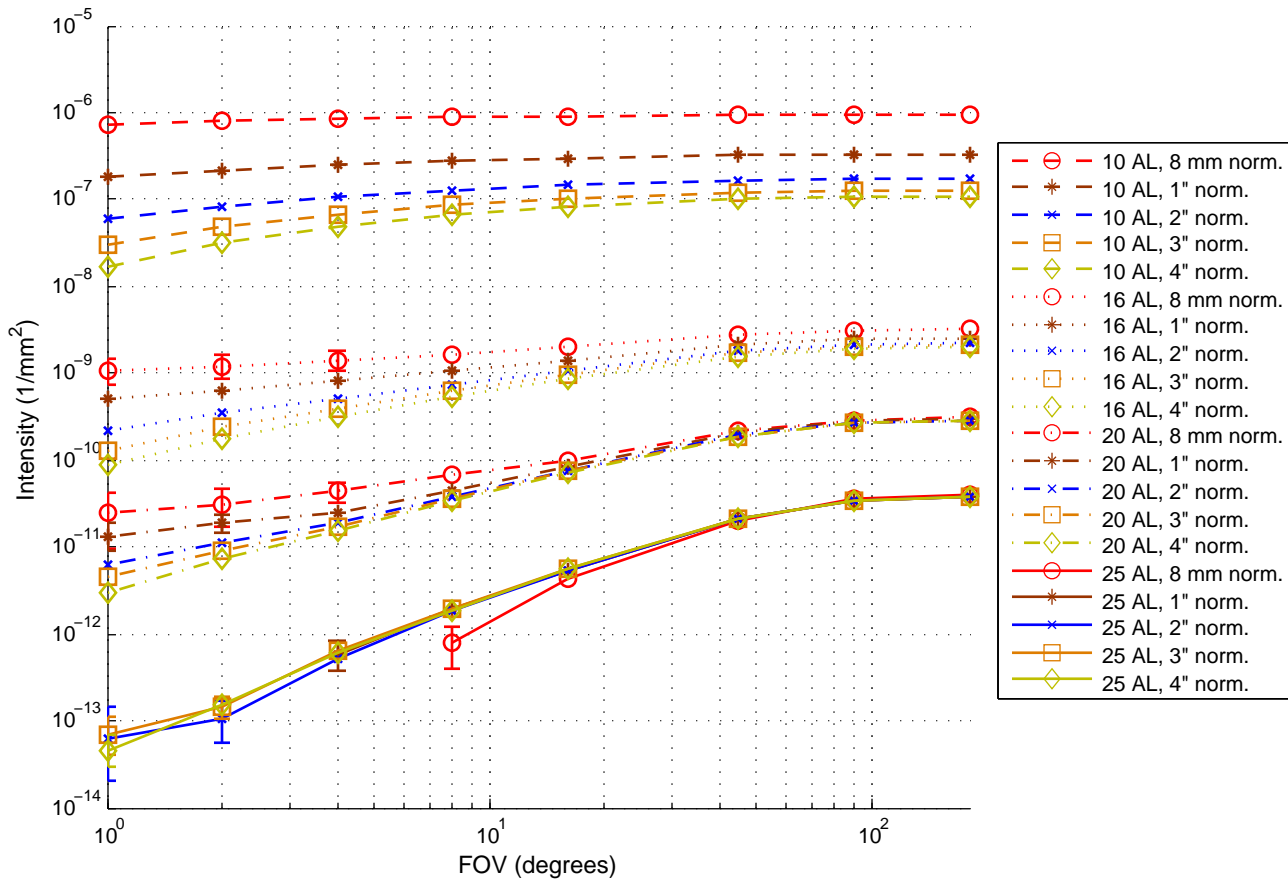


Figure 5.38: Harbor II received power normalized by the receiver area.

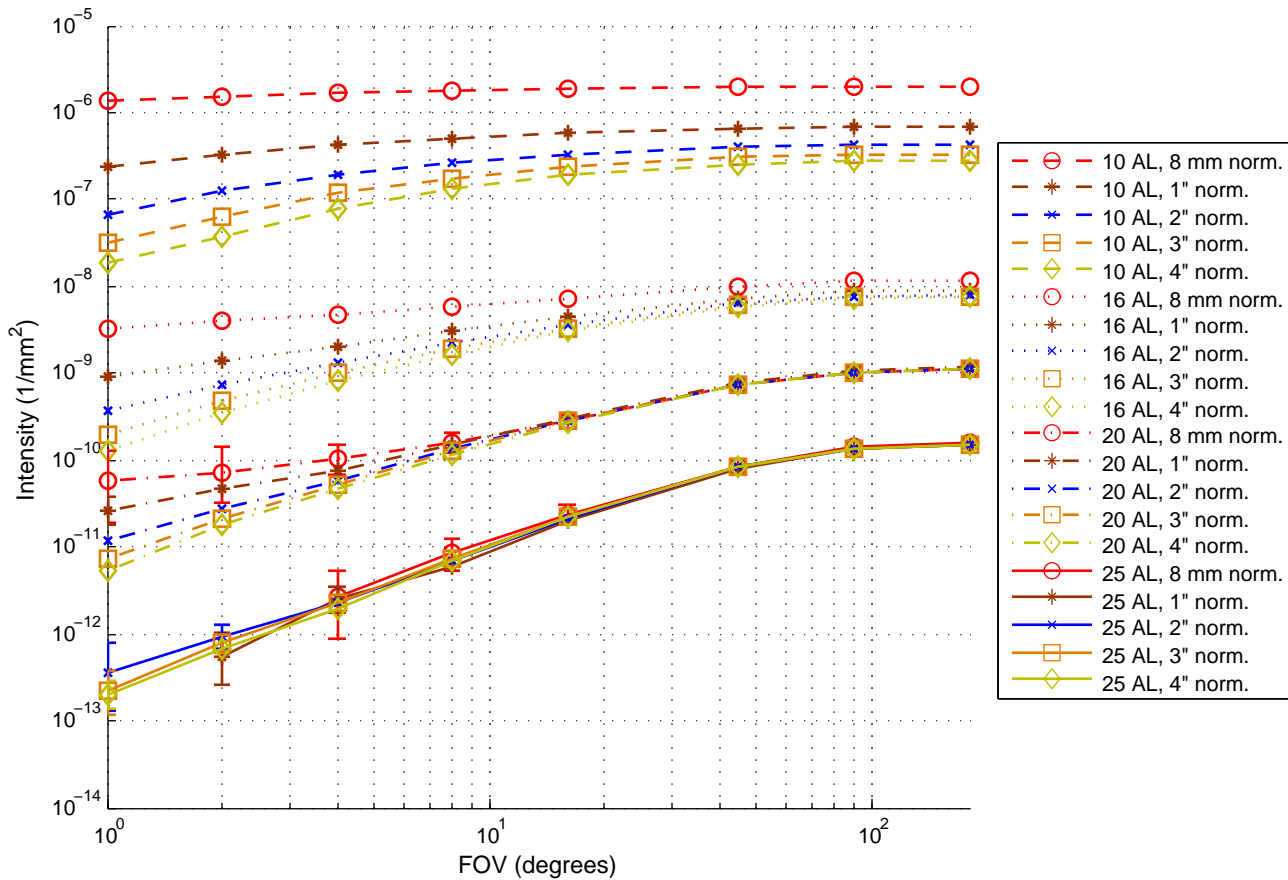


Figure 5.39: Harbor III received power normalized by the receiver area.

5.5 Coastal Water - Absolute Received Power versus Distance

Coastal waters are simulated with a c value of 0.4 m^{-1} and an albedo of 0.55. The simulated results for various apertures and FOVs over a range of distances is presented below in Fig. 5.40 - 5.44 (starting on page 111). The lower horizontal axis shows the distance in units of attenuation lengths (a unitless quantity) and the upper horizontal axis shows the distance in units of meters. The results are simulated for the same source function as the results presented for Harbor waters (Section 5.4) and Clear waters (section 5.6), a laser with a 1 mm beam radius and a 1.5 mrad full angle divergence.

The simulated apertures that are less than 2" in diameter exhibit loss that is greater than Beer's Law loss (plotted in green). This is due to the geometric loss associated with the beam spreading over the larger distance. This effect is not as noticeable for shorter link distances, such as those in Harbor-type waters. To mitigate these effects, a more tightly collimated beam could be used.

As discussed in Section 3.5.2, the diffusion length for Coastal-type waters is greater than 30 attenuation lengths. The simulated results for this section only show powers simulated out to 20 attenuation lengths. Since the light beam still has a predominate forward scattering behavior at distances less than the diffusion length, the behavior will be very close to Beer's Law. Consequently, in order to observe any large deviation from Beer's Law, a very large number of photons would need to be simulated, on the order of $1/\exp(-30)$ or greater than 10^{13} photon trajectories. This is not practical for the current simulation model, and furthermore designing a system to operate with optical losses greater than 10^{-13} would be very difficult.

5.6 Clear Water - Absolute Received Power versus Distance

Clear ocean waters are simulated for an albedo of 0.25 and a c value of 0.15 m^{-1} . This corresponds to a diffusion length of approximately 31 attenuation lengths, as discussed in Section 3.5.2. The data presented in Fig. 5.45 - 5.49 on page 116 shows the normalized power loss versus attenuation length for a link operating in clear ocean waters. The actual transmission distance is plotted on the top x-axis. The total loss from scattering and absorption is plotted in red (Beer's Law), while absorption loss is plotted in green. This represents the minimum and maximum for channel loss. The results, however, show that the overall loss is lower than the Beer's Law line. The reason for this is the addition of geometric loss from the beam spreading. Since the link is operating at a very long distance (up to 130 meters) and the simulated beam has 1.5 mrad of divergence, the geometric size of the beam spot at this long of a distance is quite large. The half-power beam diameter will be approximately 20 cm at a distance of 130 meters.

The large beam size at long distances have both benefit and cost. The downside to this effect is the loss of power, but the benefit is that pointing loss will be lessened due to the spread of power over a larger area. Since the link is operating at such large distances, pointing accuracy needs to be much

greater in order to maintain the accuracy of the transmit beam's position on the receiver plane.

5.7 Clear and Coastal Water Received Power Figures

Figures showing the received power for various apertures in Clear and Coastal-type waters is presented next. These correspond with the discussion in Sections 5.5 through 5.6 on previous pages.

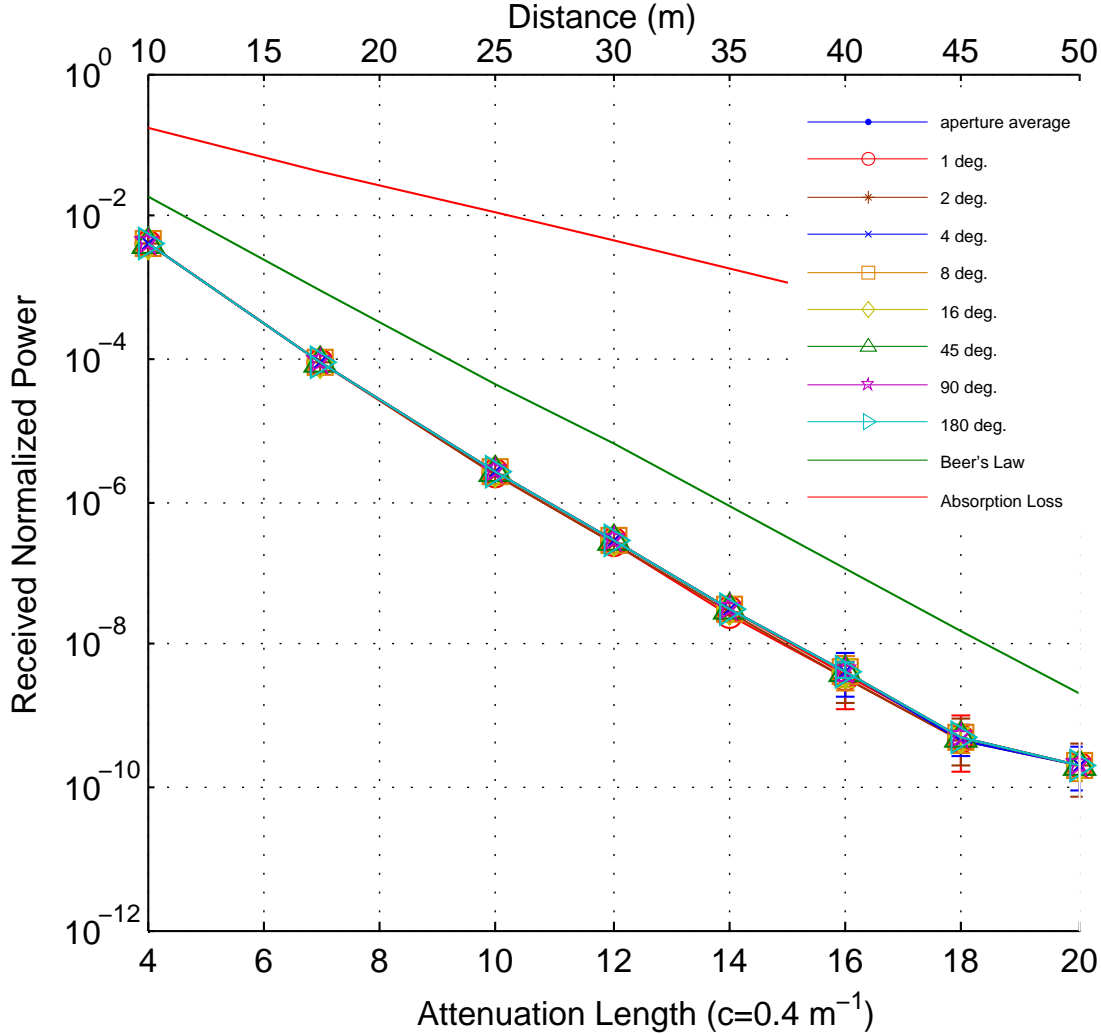


Figure 5.40: Coastal 8 mm: Received power normalized by transmit power, plotted versus receiver attenuation length. The c value is fixed and the distance is scaled. Error bars are plotted when the estimated error is greater than $\pm 25\%$. Error bars represent 95% confidence for a binomial distribution, which should be slightly greater than the actual photon weight distribution.

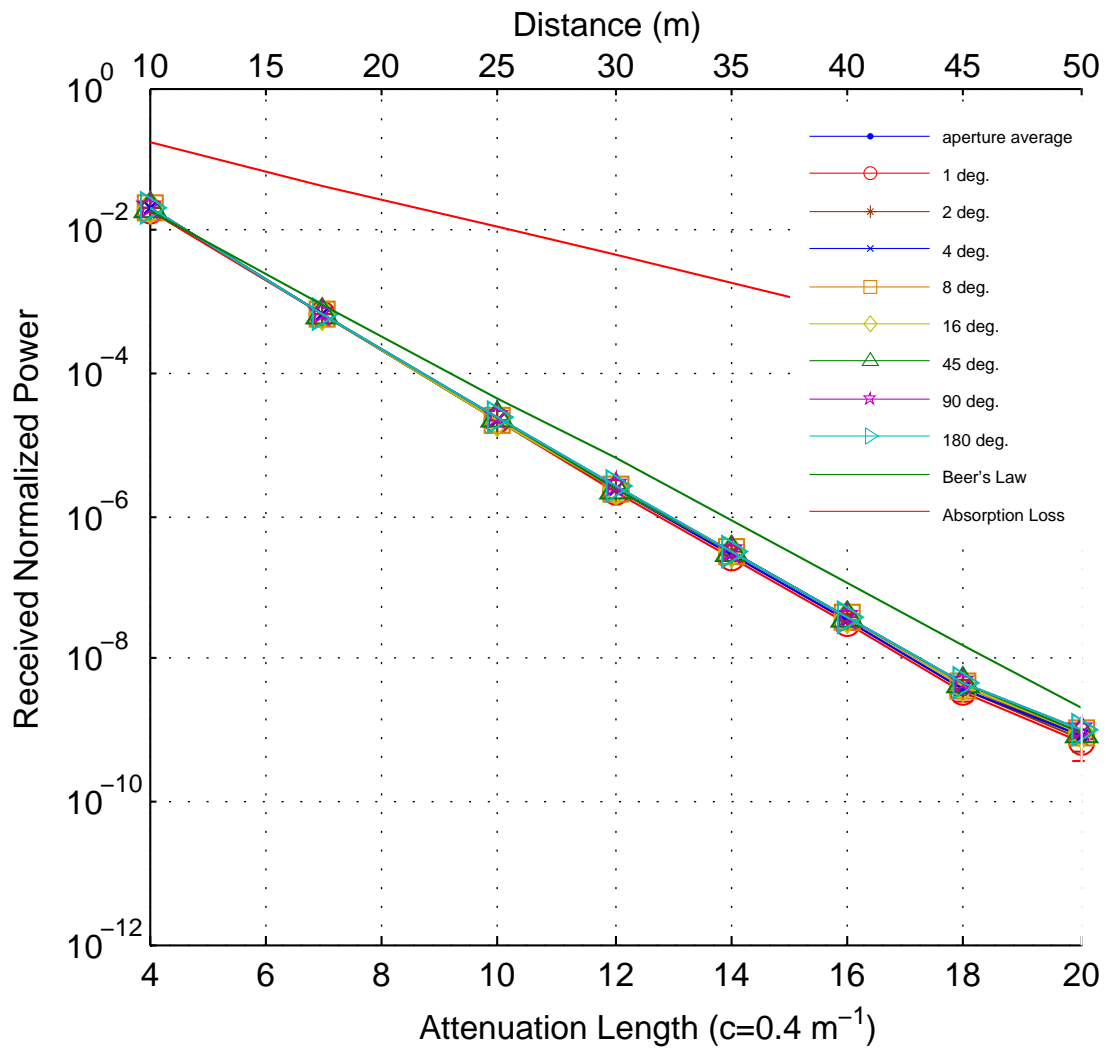


Figure 5.41: Coastal water, 1 in aperture received power.

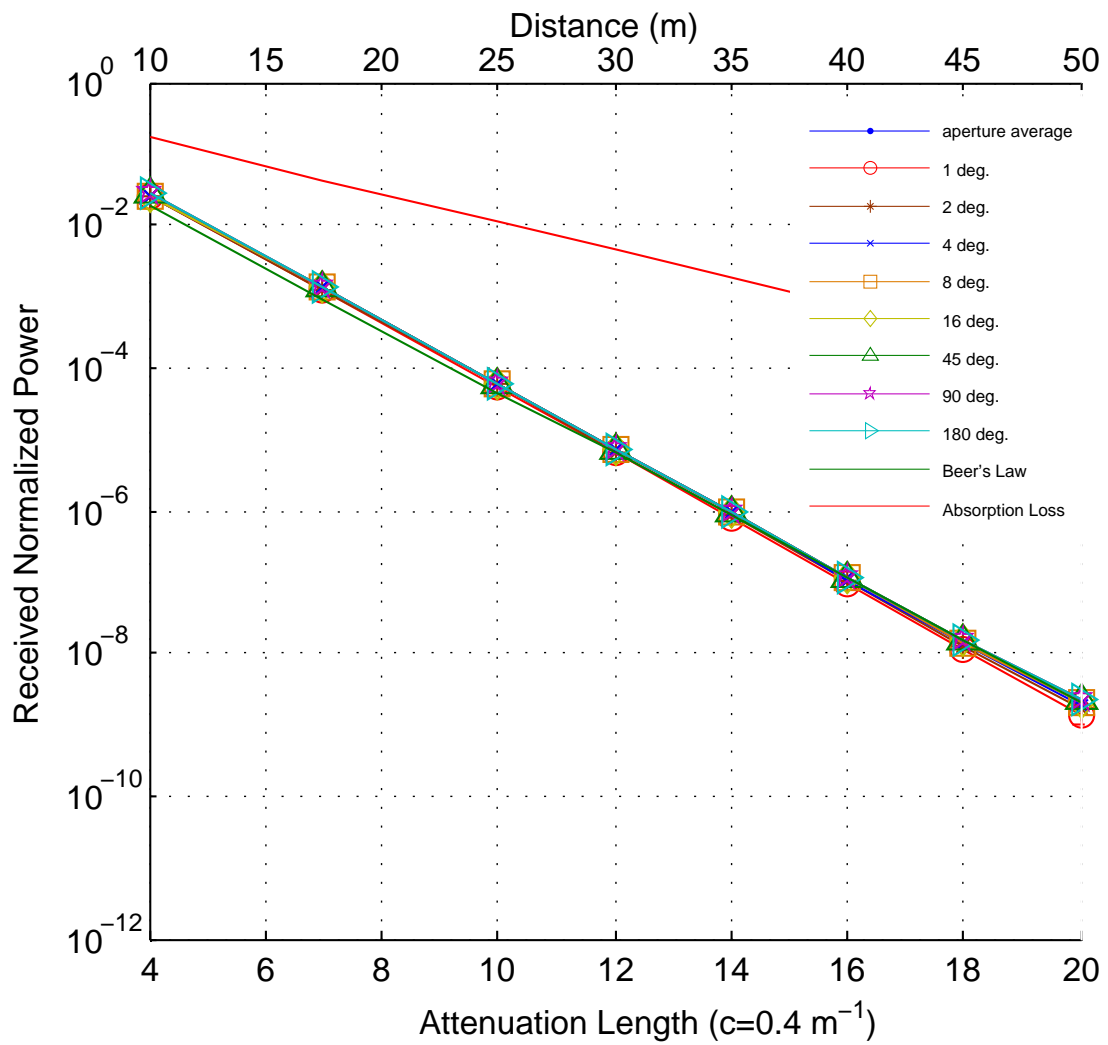


Figure 5.42: Coastal water, 2 in aperture received power.

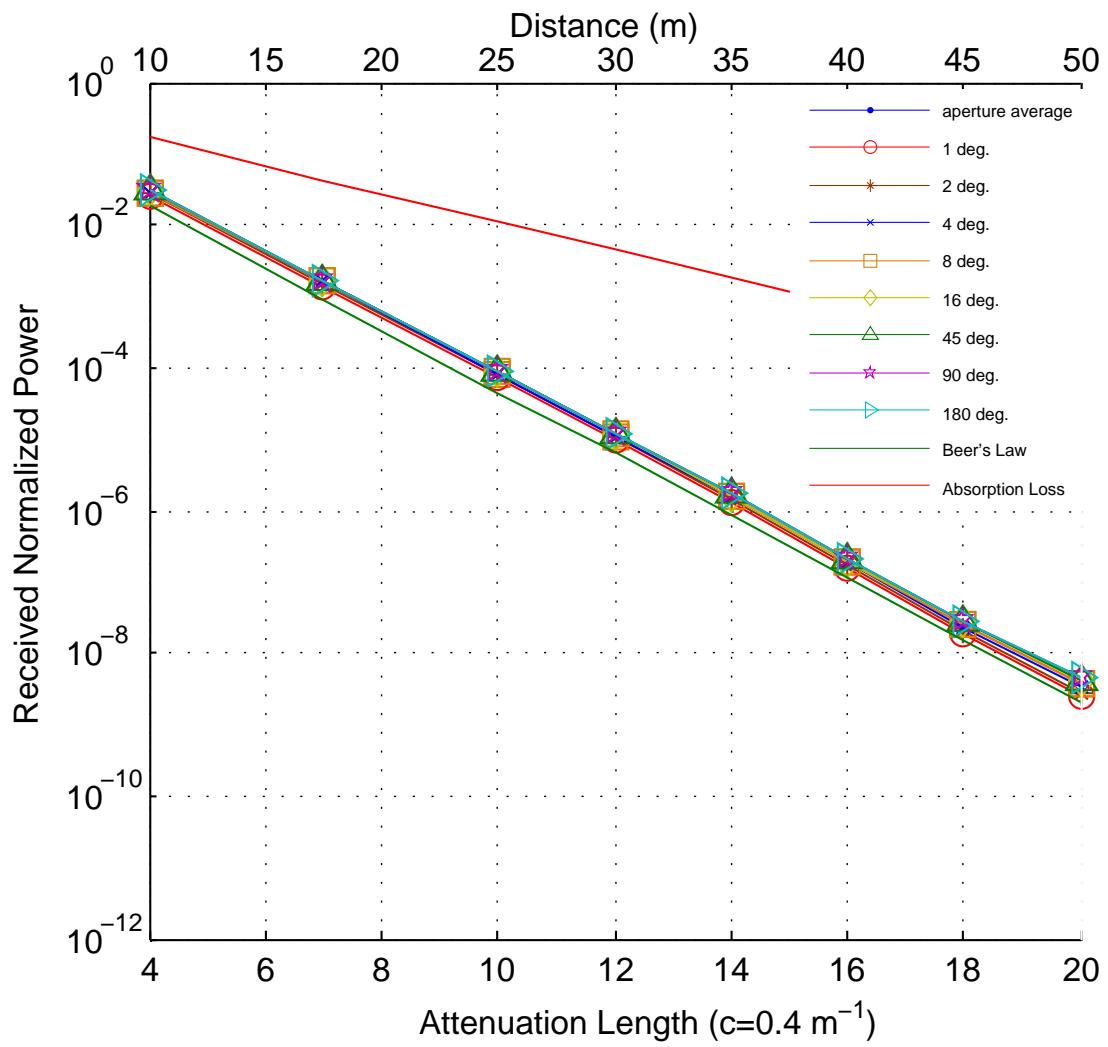


Figure 5.43: Coastal water, 3 in aperture received power.

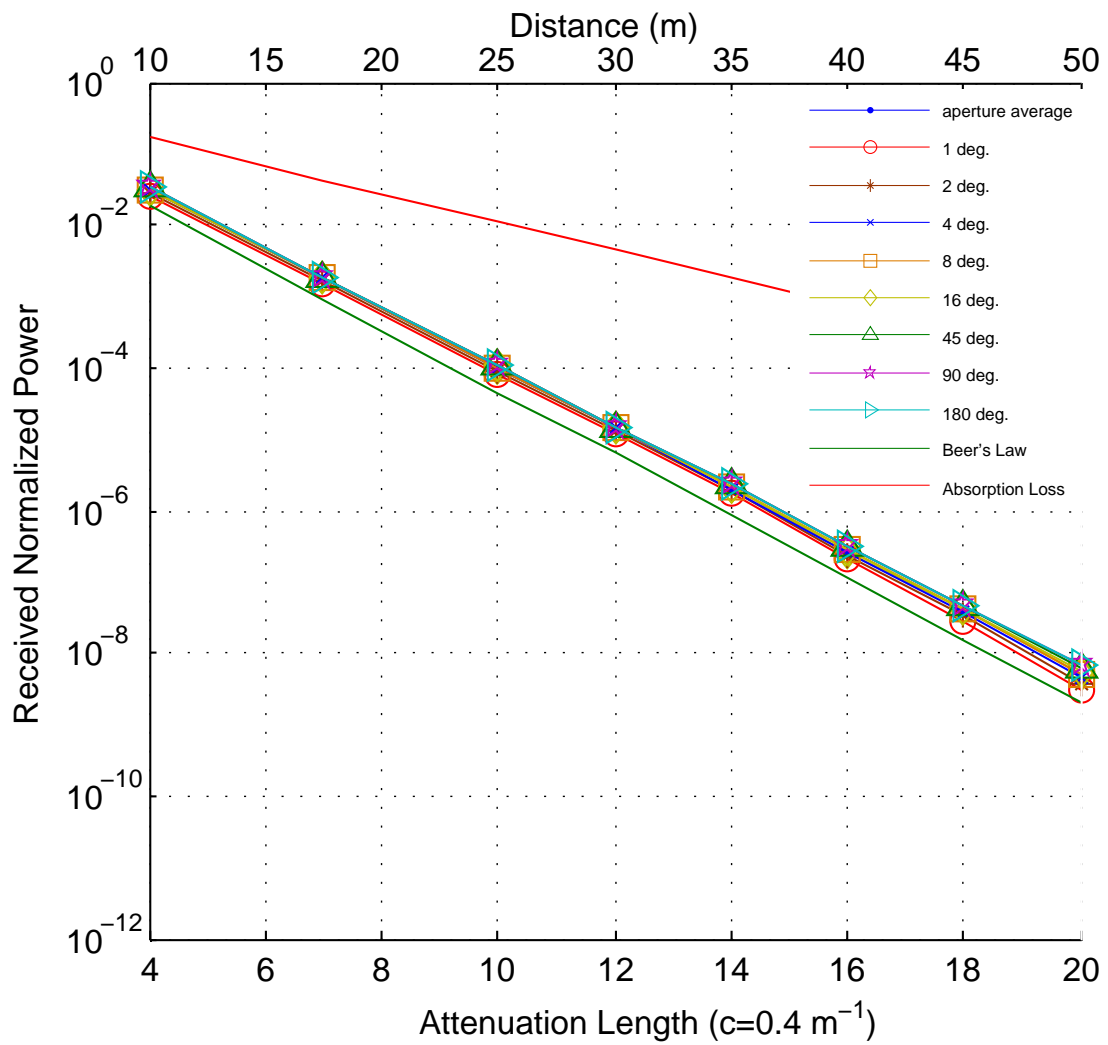


Figure 5.44: Coastal water, 4 in aperture received power.

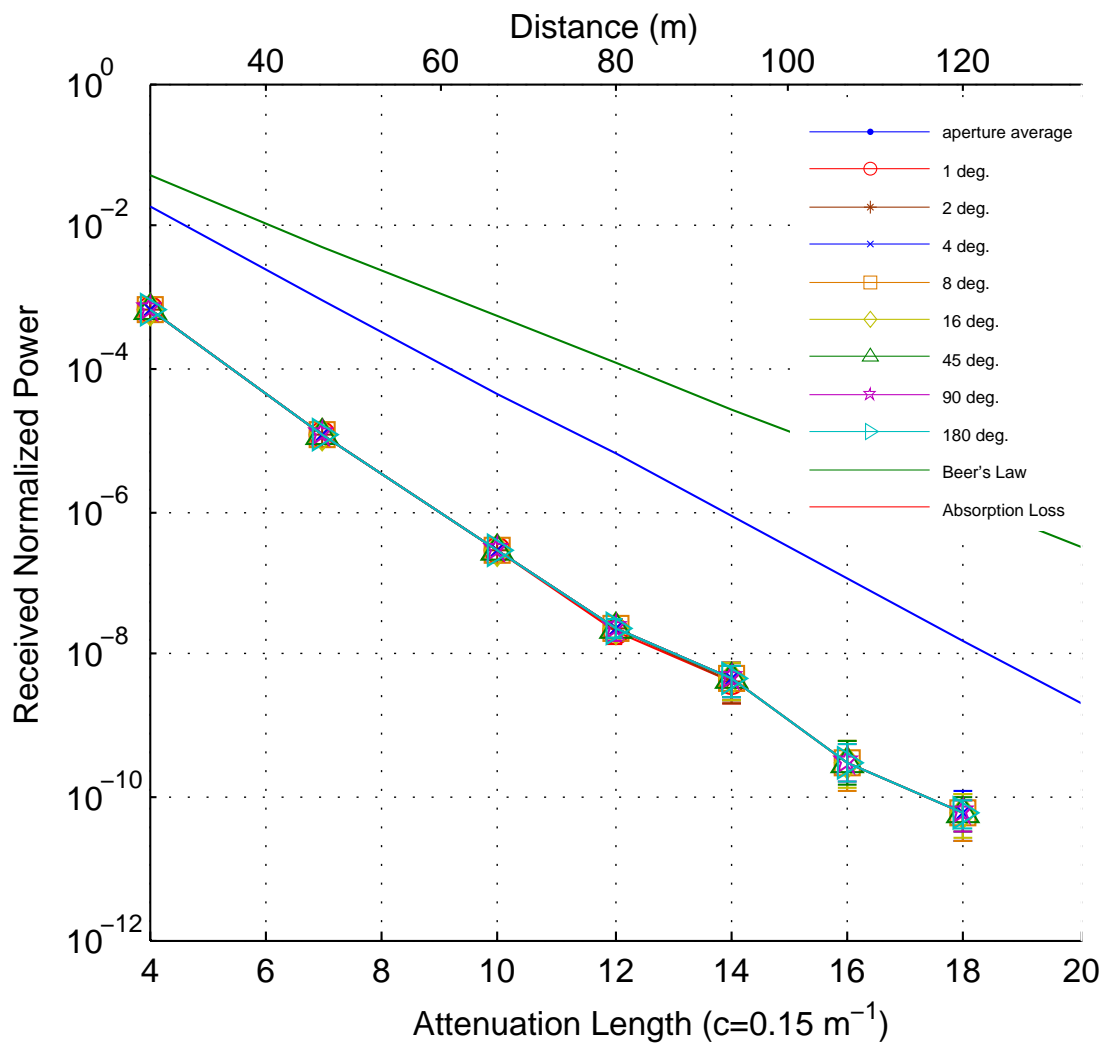


Figure 5.45: Clear 8mm aperture: Received power normalized by transmit power, plotted versus receiver attenuation length. The c value is fixed and the distance is scaled. Error bars are plotted when the estimated error is greater than $\pm 25\%$. Error bars represent 95% confidence for a binomial distribution, which should be slightly greater than the actual photon weight distribution.

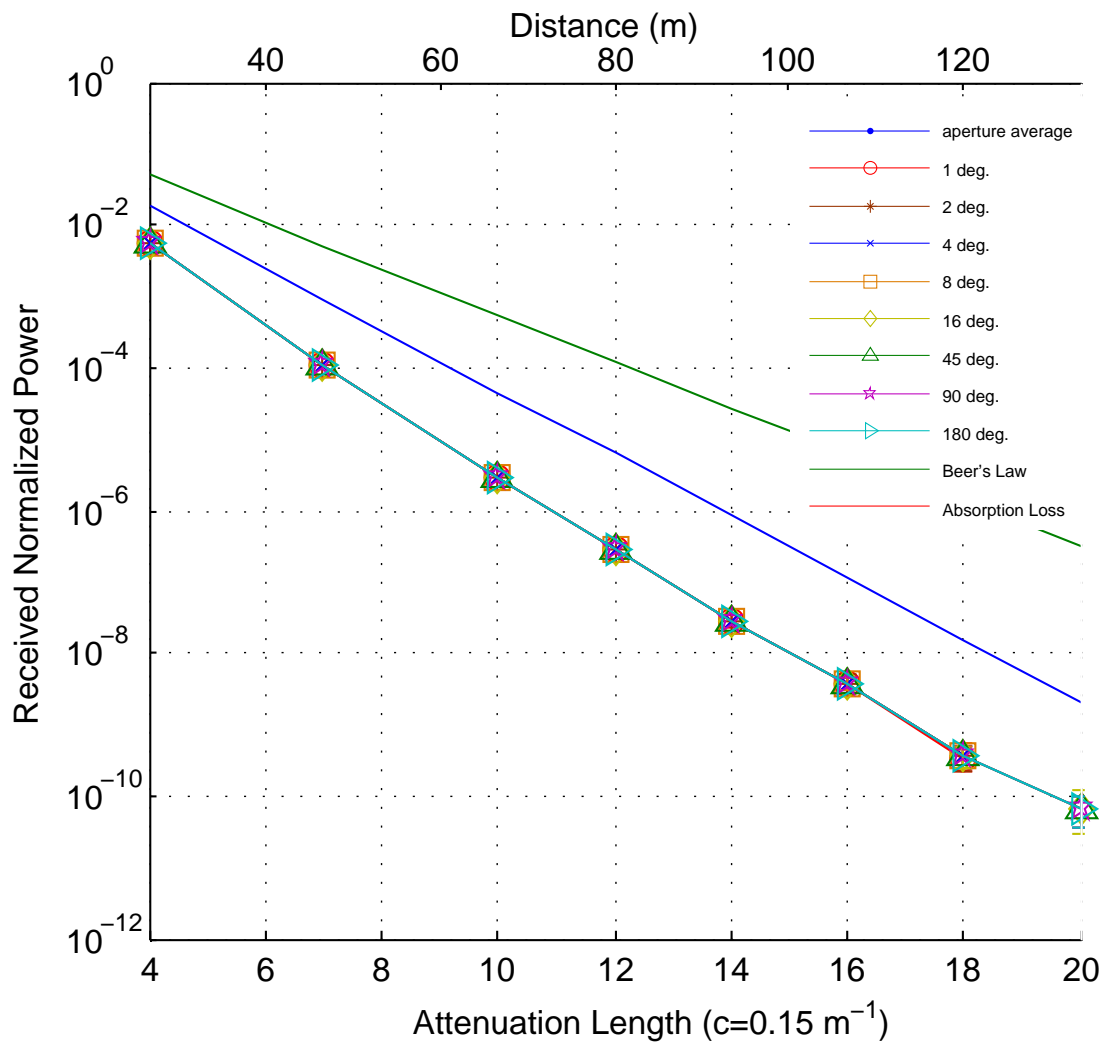


Figure 5.46: Clear water, 1in aperture received power

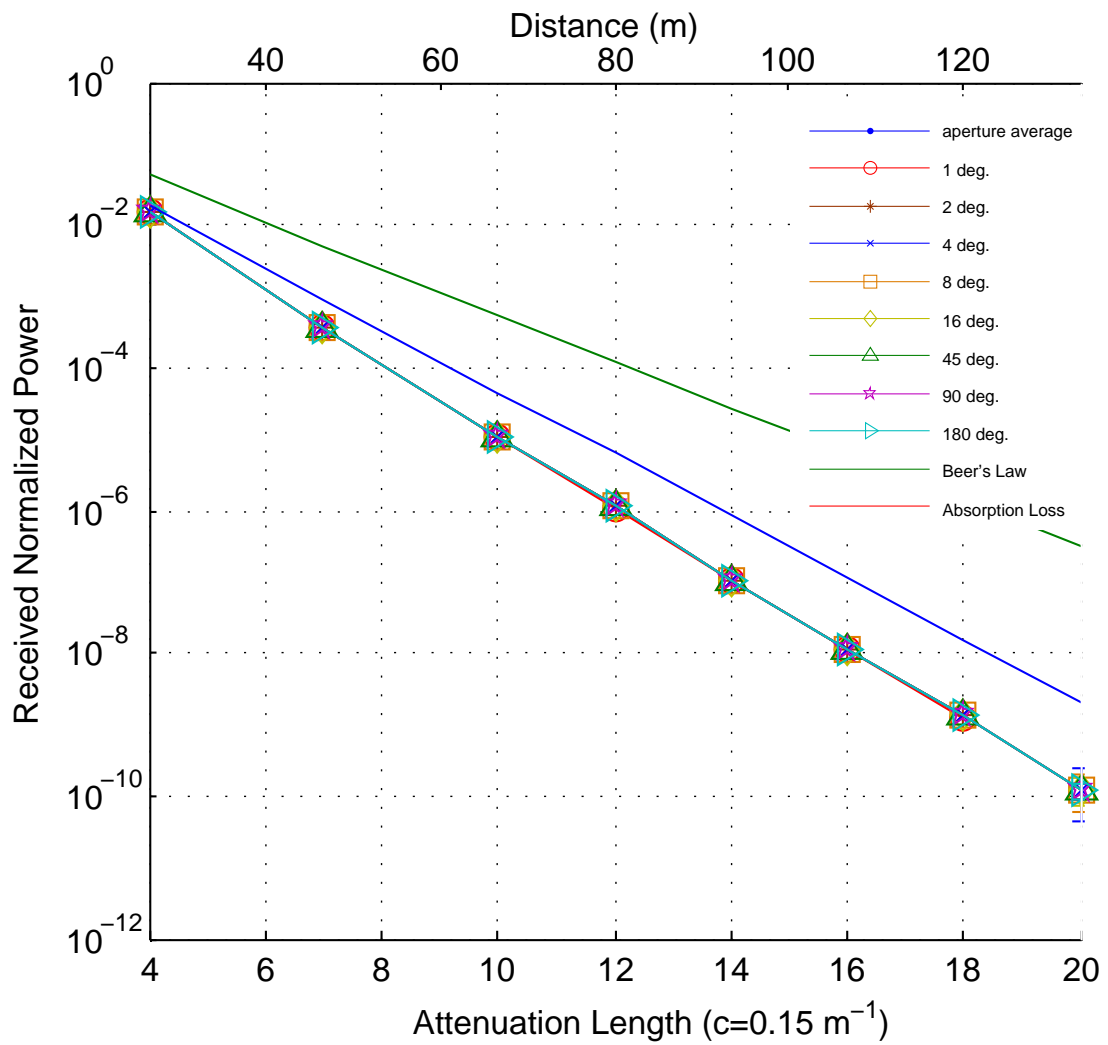


Figure 5.47: Clear water, 2in aperture received power

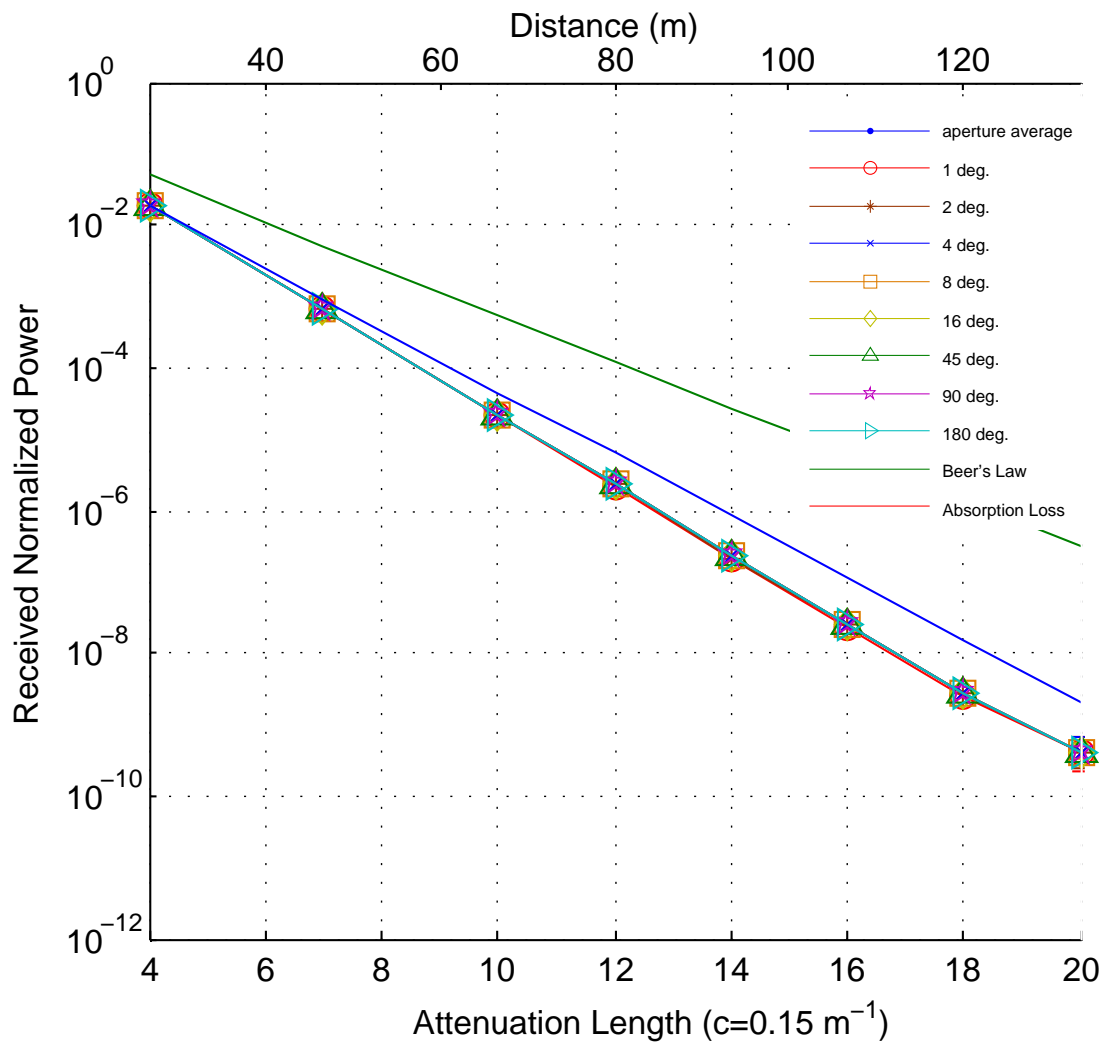


Figure 5.48: Clear water, 3in aperture received power

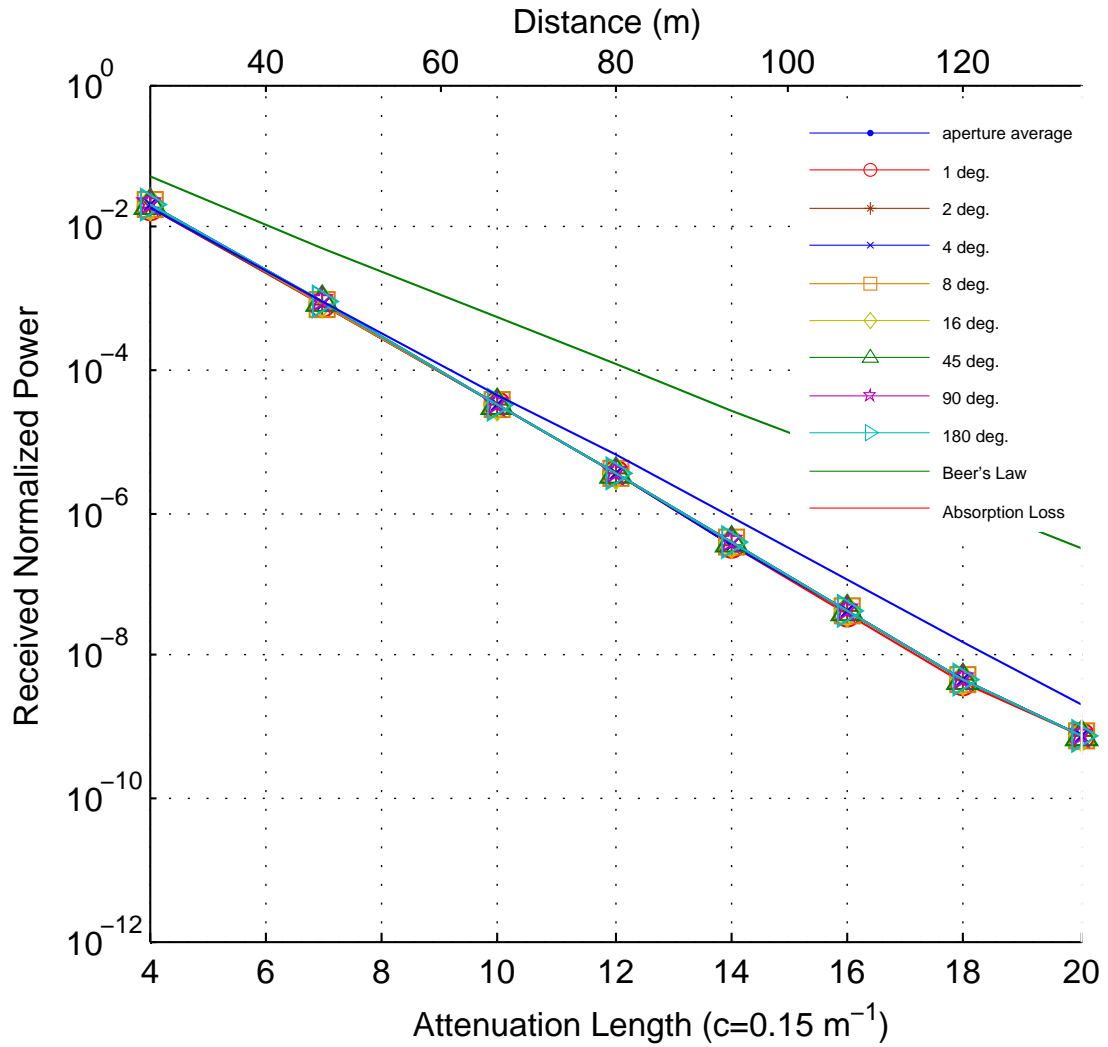


Figure 5.49: Clear water, 4in aperture received power

5.8 Harbor Water - Scattering Orders at the Receiver

The Photonator simulation allows us to look at a number of aspects of the received photons. One of these aspects is how many times received photons have been scattered on their path to the receiver. As discussed in Section 4.3.2 and shown in Fig. 4.5, the photon packet weight (path probability) can be used as a measure of scattering, since, for infinite mediums, the photon weight is reduced at, and only at, each scattering event. Essentially the packet weight describes the probability of a single photon, that takes that specific path, making it from transmitter to receiver. For simulations without perfectly absorbing boundaries (essentially, boundaries that reduce the photon packet weight), the number of times a photon has scattered on its path to the receiver can be calculated as

$$N_{scatter} = \log(w_{packet})/\log(\omega) \quad (5.18)$$

which comes from the equation for photon packet weight,

$$w_{packet} = \omega^{N_{scatter}} \quad (5.19)$$

since at each scattering event (where $N_{scatter}$ is the total), the packet weight, w_{packet} , is reduced by the albedo, ω . We will call this number, $N_{scatter}$, the “scattering order” of the received photon.

A weighted histogram of the scattering orders of received photons provides an interesting way to look at the receiver data. Each scattering order bin, usually consecutive integers starting at 0, are weighted by the path probability of that number of scattering events. For example, for a direct path from transmitter to receiver, any photon taking that path will arrive at the receiver 100% of the time. However, for a specific path involving x scattering events, a photon taking that path has a probability of ω^x of making it to the receiver. The equation to describe each bin value is

$$y(n) = x(n)\omega^n \quad (5.20)$$

where $y(n)$ is the value of scattering order bin n , $x(n)$ is the number of received photon packets that have scattered n times, and ω is the albedo of the water. It should be noted that

$$\frac{1}{N_{tx}} \sum_{n=0}^{\infty} y(n) = P_{rx} \quad (5.21)$$

which simply states that summing all of the received photon weights, at each scattering order, is the total power at the receiver and dividing by the number of transmitted photon packets results in the mean power estimate for that particular receiver.

5.8.1 Unnormalized Histogram of Scattering Orders

The scattering orders at the receiver can be presented in several ways: normalized by transmitted power, normalized by received power, and un-normalized. Each provides different benefits. The results presented in this section show the unnormalized scattering order histogram. Results presented at 10 attenuation lengths (cz) will have a much larger value than results at 25 attenuation lengths, as much less photons are captured at 25 cz than at 10 cz . It is helpful, however, to view the total change that happens as the receiver is moved further away (increasing the cz), and as the aperture size and FOV change.

Fig. 5.50 shows the scattering order histograms for Harbor II type water inset on a figure showing the normalized power at various attenuation lengths. At a cz of 10, there is a significant amount of power received at very low scattering orders, while at 25 cz , there is no power received at scattering orders less than about 5. In essence, this shows that at 25 cz , no ballistic photons are received (for this simulation) and all observed photons have been multiply scattered.

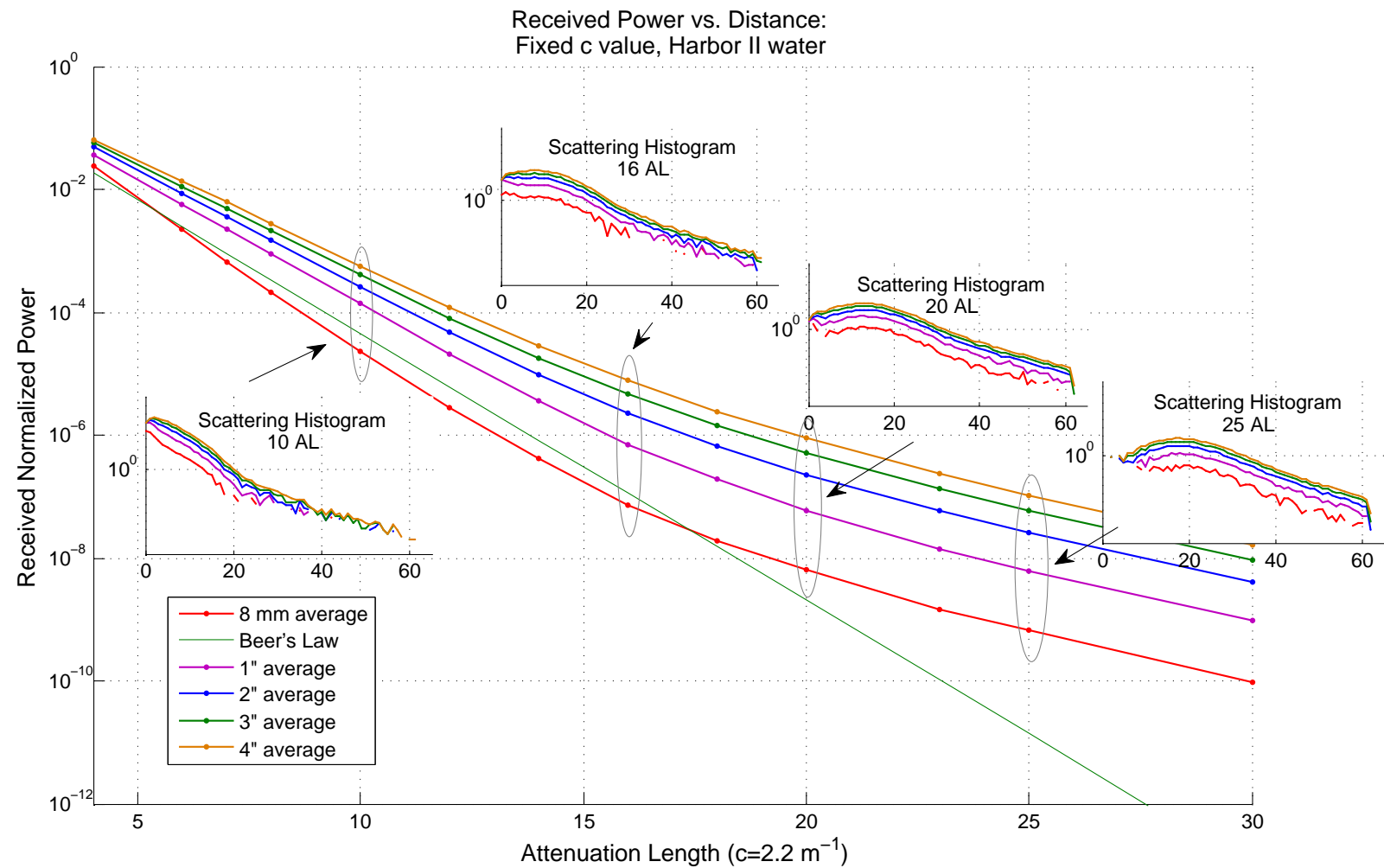


Figure 5.50: Harbor II type water received power versus attenuation length, with inset histograms of the received scattering orders. Scattering order histogram presented with a logarithmic y-axis showing the weighted received count at each scattering order.

5.8.2 Normalized Histogram of Scattering Orders

The data presented in Fig. 5.51 through Fig. 5.54 (page 125 to page 128) show the scattering order histograms for several different attenuation lengths without normalizing for the amount of received power. While it is evident that the scattering order histogram will have much larger numbers at $10\text{ }cz$ than at $25\text{ }cz$, it's also helpful to look at the shape of the distribution, while ignoring the relative amounts of received power. To do this, we can normalize each curve by the total amount of received power.

The data presented in Fig. 5.55 through Fig. 5.58 (page 129 to page 132) show the same data as in Fig. 5.51 through Fig. 5.54, but this time each curve has been normalized by the received power at a 180° FOV for each aperture size. This does two things: it presents the 180° FOV curves as a true PDF of scattering order, and shows the relative loss of power as the FOV decreases. In this case, we present the max FOV, 180° , the average value over all FOVs (normalized by the 180° FOV power) and the minimum FOV, 1° .

It can be seen from the curves in Fig. 5.56, Fig. 5.57, Fig. 5.58 that at higher attenuation lengths the scattering order probability is roughly the same for all apertures and field-of-views. However, as the attenuation length begins to decrease, for instance at $10\text{ }cz$, Fig. 5.55 shows that the FOV and aperture size do affect the PDF of scattering orders.

5.8.3 Scattering Order Probability Versus Water Type

To compare the scattering order probability between various water types, for each Harbor water-type, Harbor I, II and III the average probability of scattering order was calculated for each aperture size. Essentially, for each water type, for each aperture, the average histogram of scattering orders was computed for all the simulated FOVs. This curve was then normalized by the total power to produce a probability density function. Fig. 5.59 through Fig. 5.62 show the average PDF of scattering orders for all three waters types, and all 5 aperture sizes.

While the curves in Fig. 5.60, Fig. 5.61, and Fig. 5.62, are similar, it's evident that for Fig. 5.59 the different water types and aperture sizes do demonstrate different scattering order PDFs. Fig. 5.63 shows a closer view of the $10\text{ }cz$ plot for better clarity.

At this low attenuation length, the spatial and angular distribution of incident photons is much less homogeneous, which contributes to the difference between various aperture sizes. A significant portion of the transmitted beam is still ballistic and central to the aperture. For all of the water types, a small aperture size, 8 mm, produces nearly identical curves (shown in red in Fig. 5.63). As the aperture sizes increases to 4" the curve shape changes dramatically between the three water types. Harbor III water, with its larger scattering coefficient, b captures more scattered light with the 4" aperture, while Harbor I water still is peaked at the very low scattering orders (the 4" curve overlaps the Harbor III water 1" aperture curve).

5.8.4 Harbor Water Scattering Orders Figures

The figures for the previous discussion of Section 5.8 are presented below for readability.

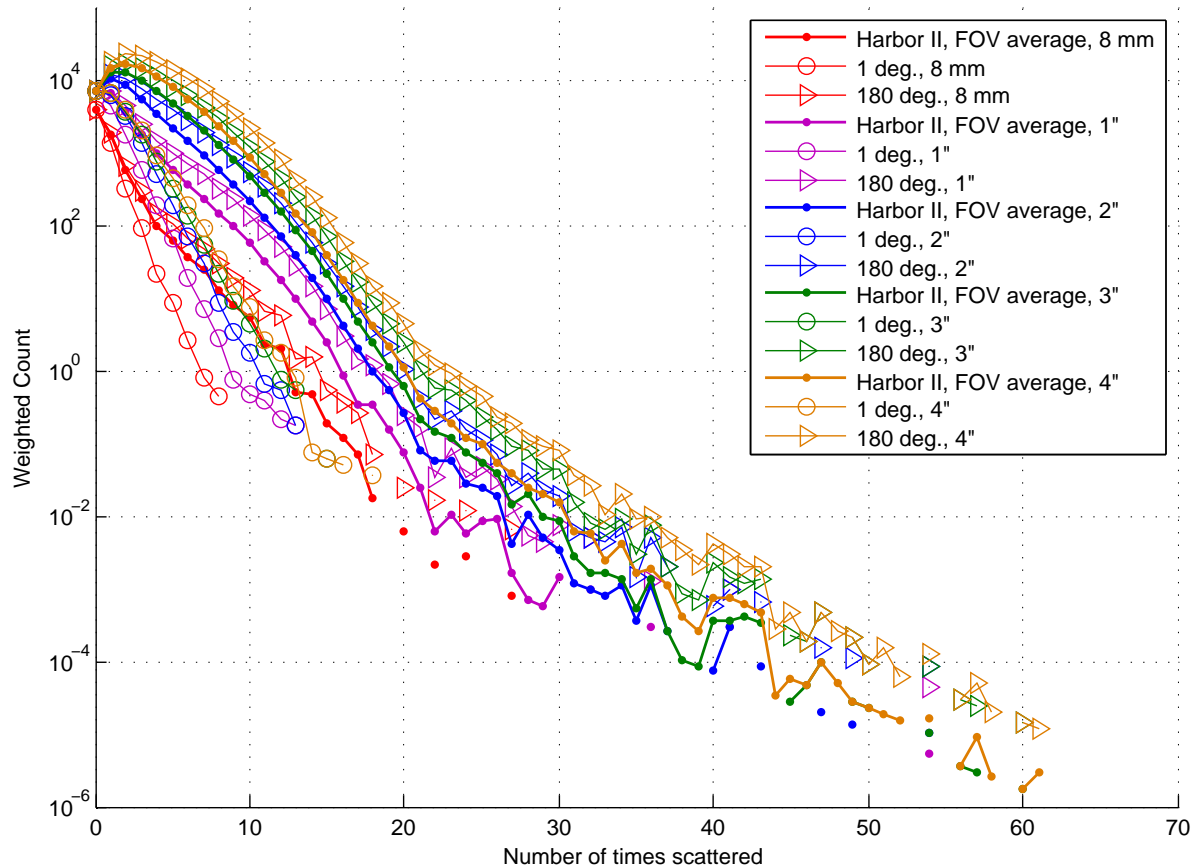


Figure 5.51: Harbor II - $10 \text{ } cz$ Scattering Histogram

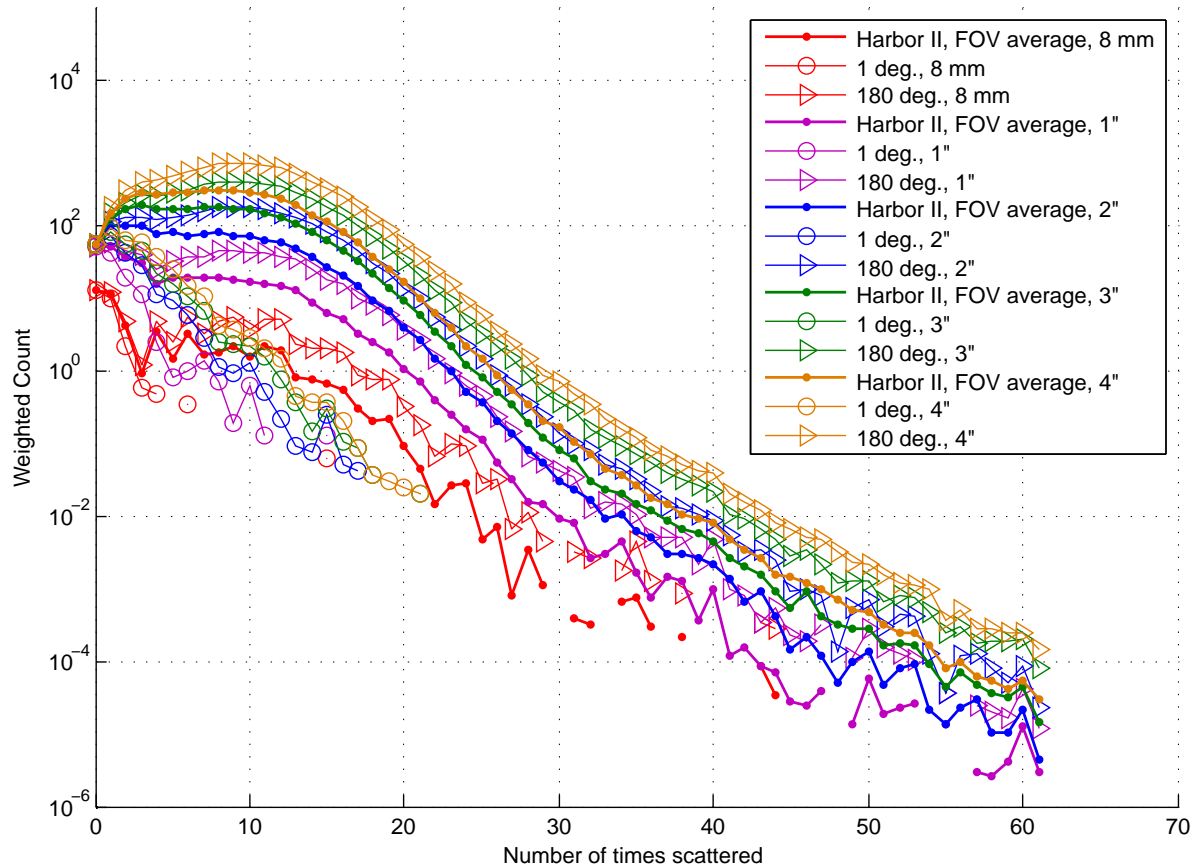


Figure 5.52: Scattering histogram of received photons for Harbor II water at 16 cz . Various aperture sizes plotted with min, max, and average value over the FOV.

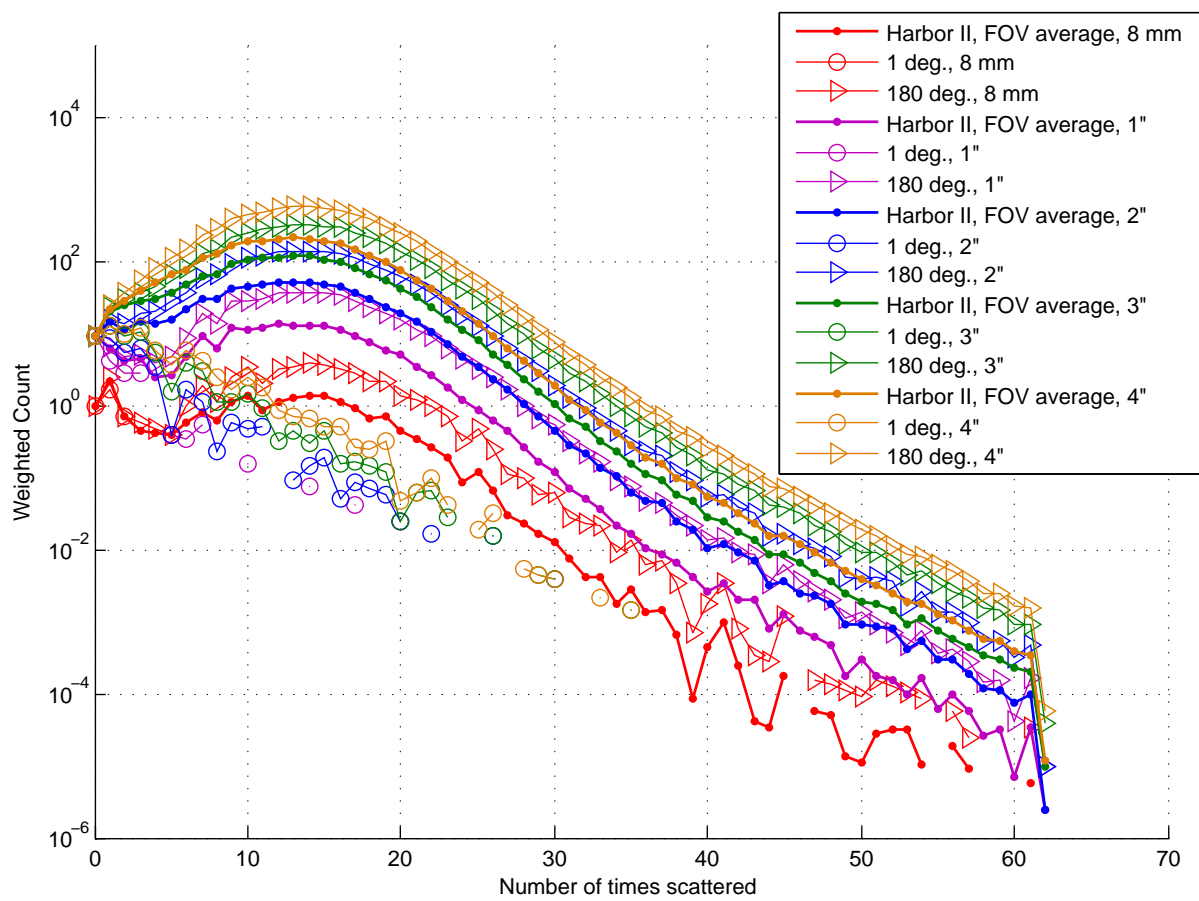


Figure 5.53: Harbor II - $20 \text{ c}/z$ Scattering Histogram

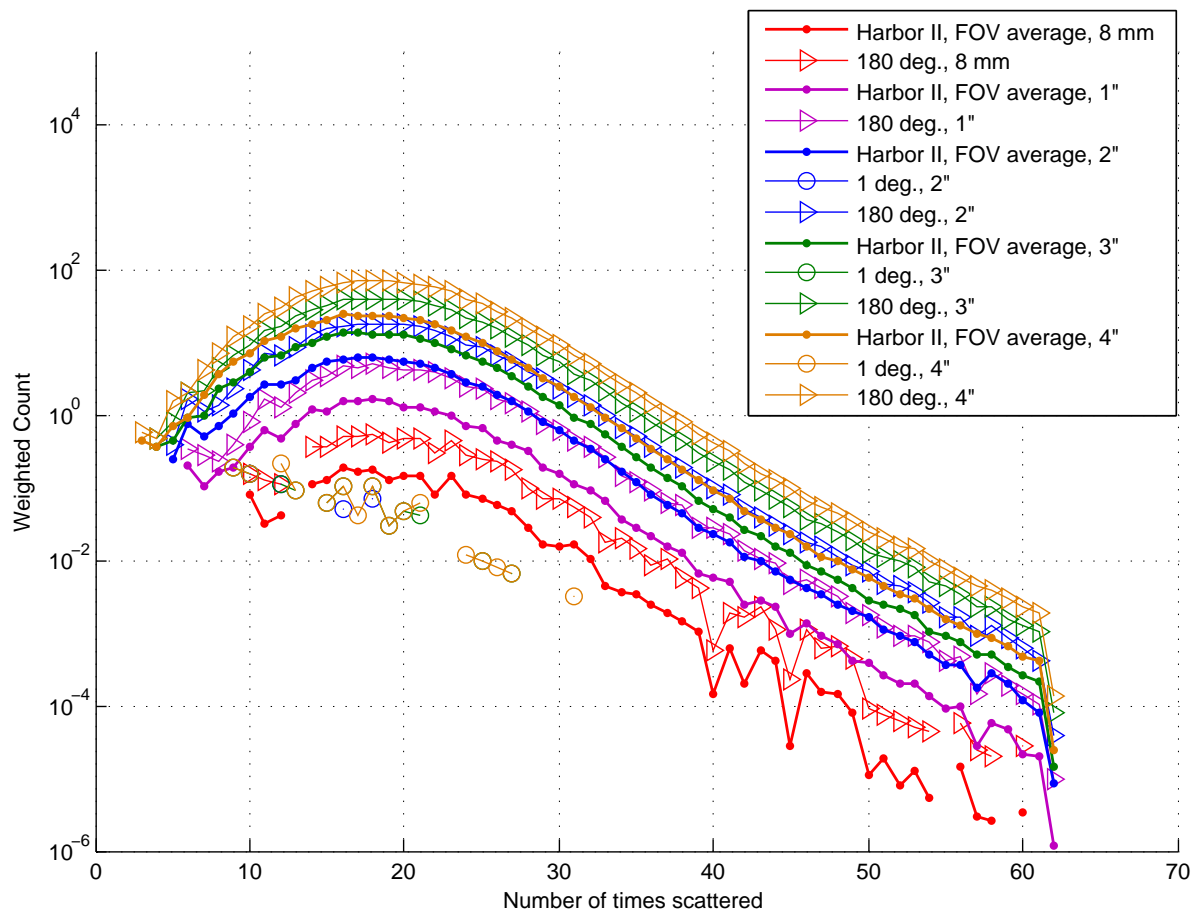


Figure 5.54: Scattering histogram of received photons for Harbor II water at 25 cz.

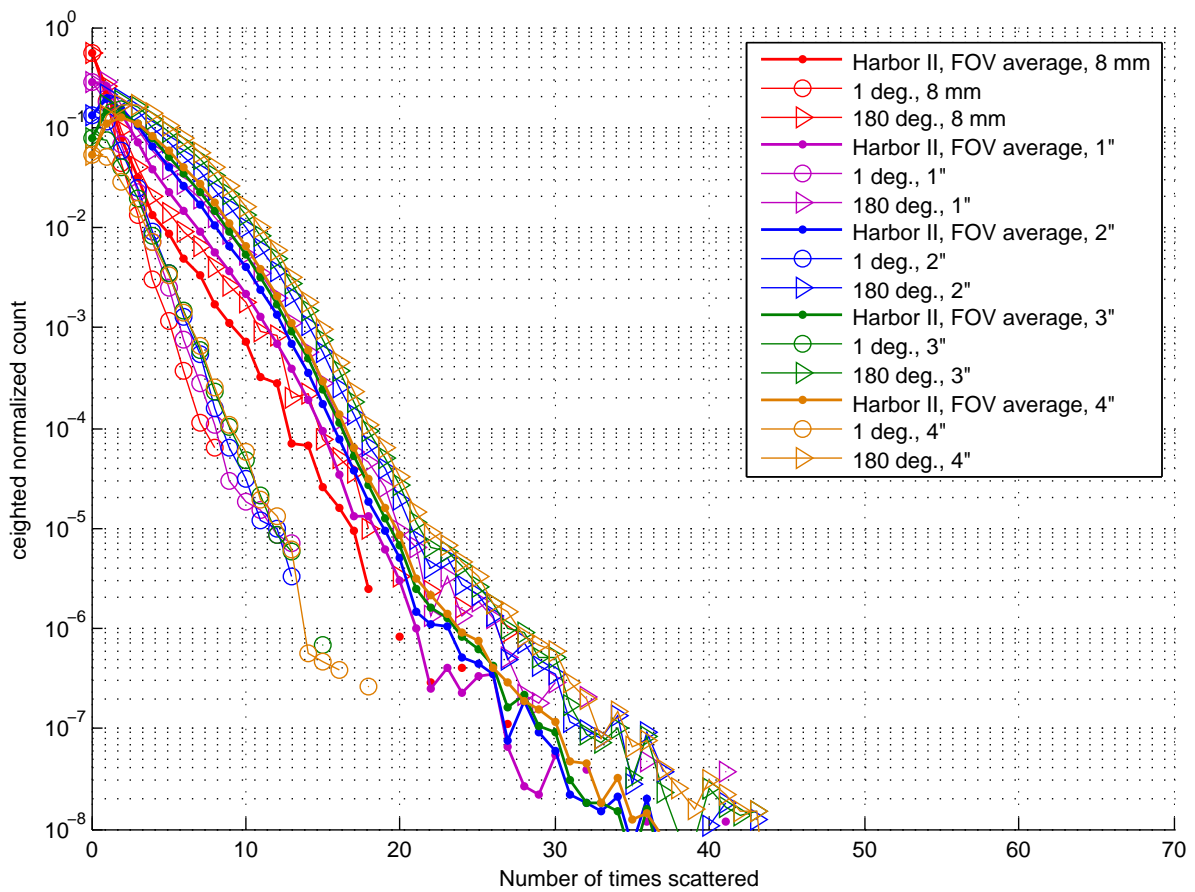


Figure 5.55: Harbor II - 10 cz scattering histogram normalized by max FOV.

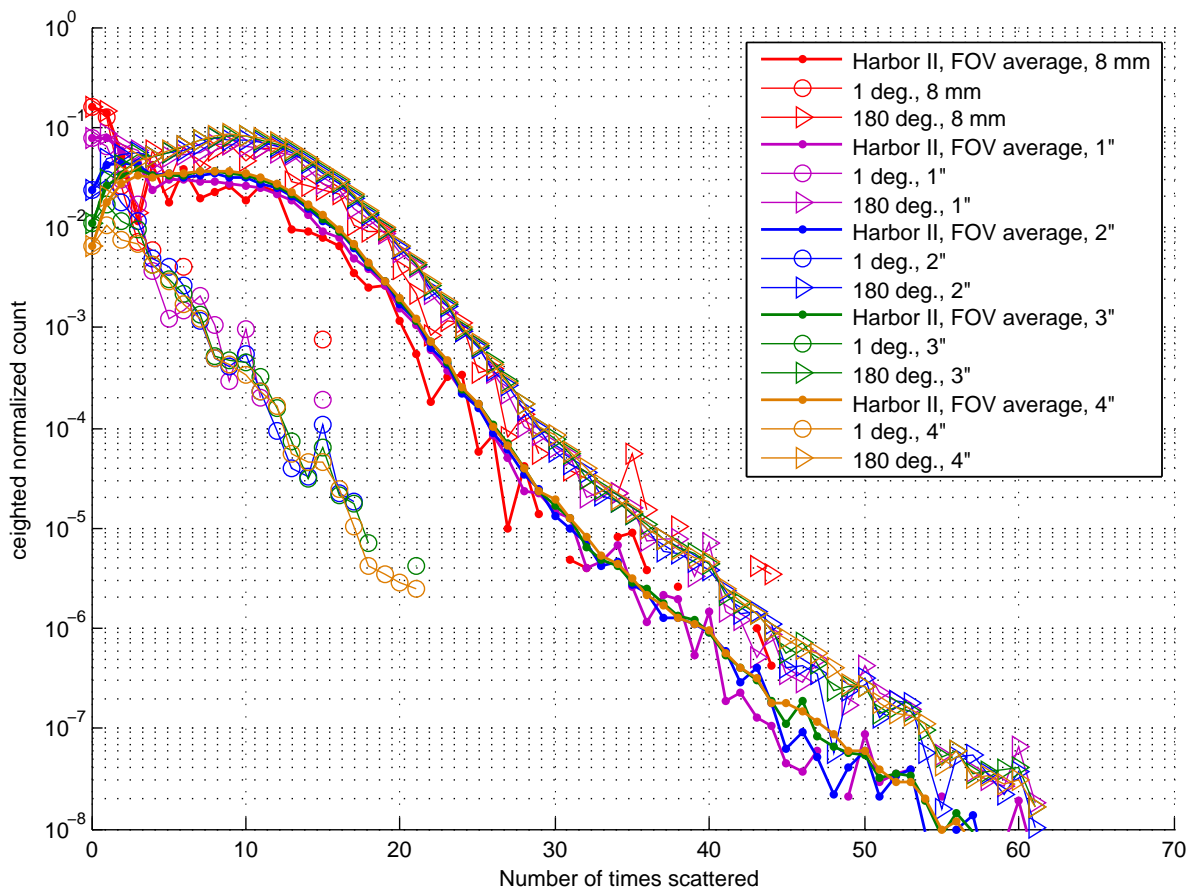


Figure 5.56: Scattering histogram of received photons for Harbor II water at 16 attenuation lengths. Each curve is normalized by the power at a 180° FOV for that aperture size. 180°, 1°, and FOV average is plotted.

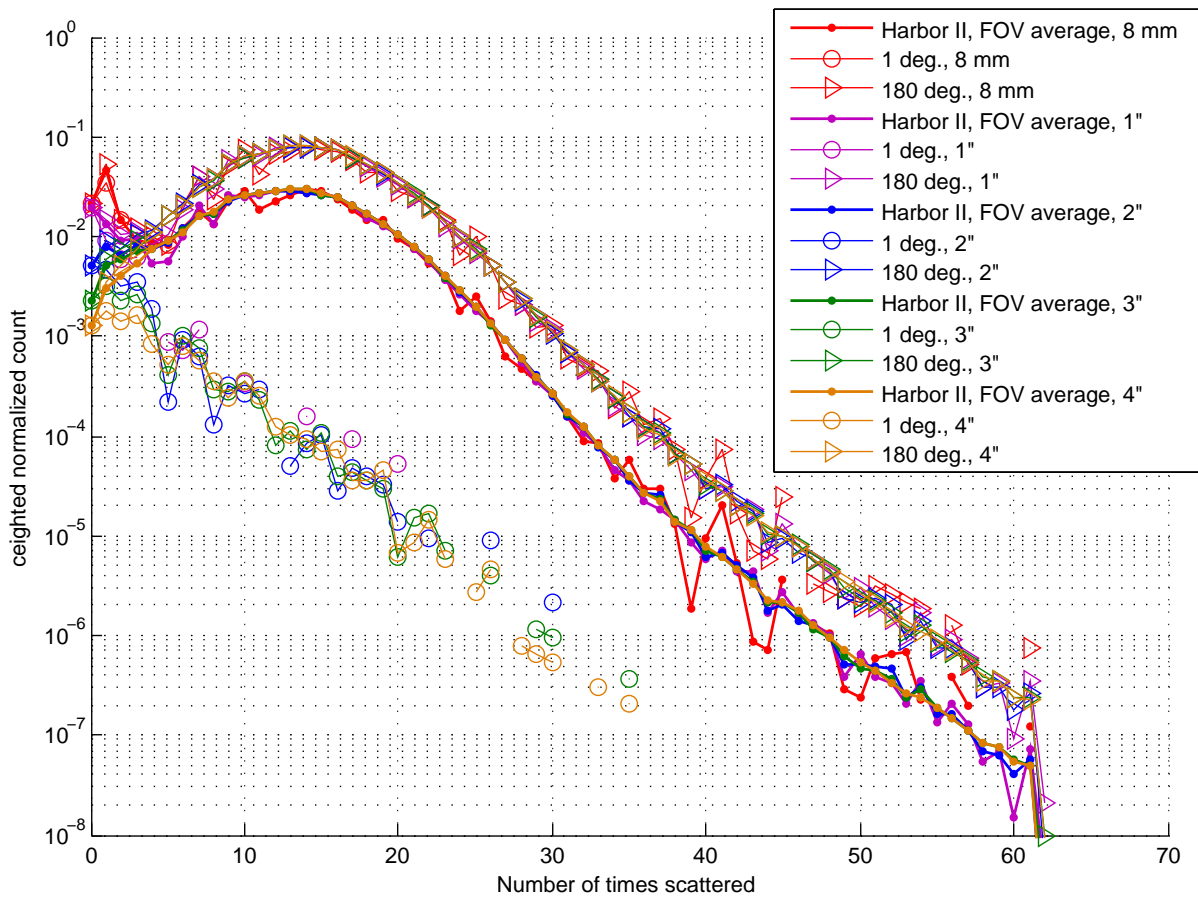


Figure 5.57: Harbor II - 20 cz scattering histogram normalized by max FOV.

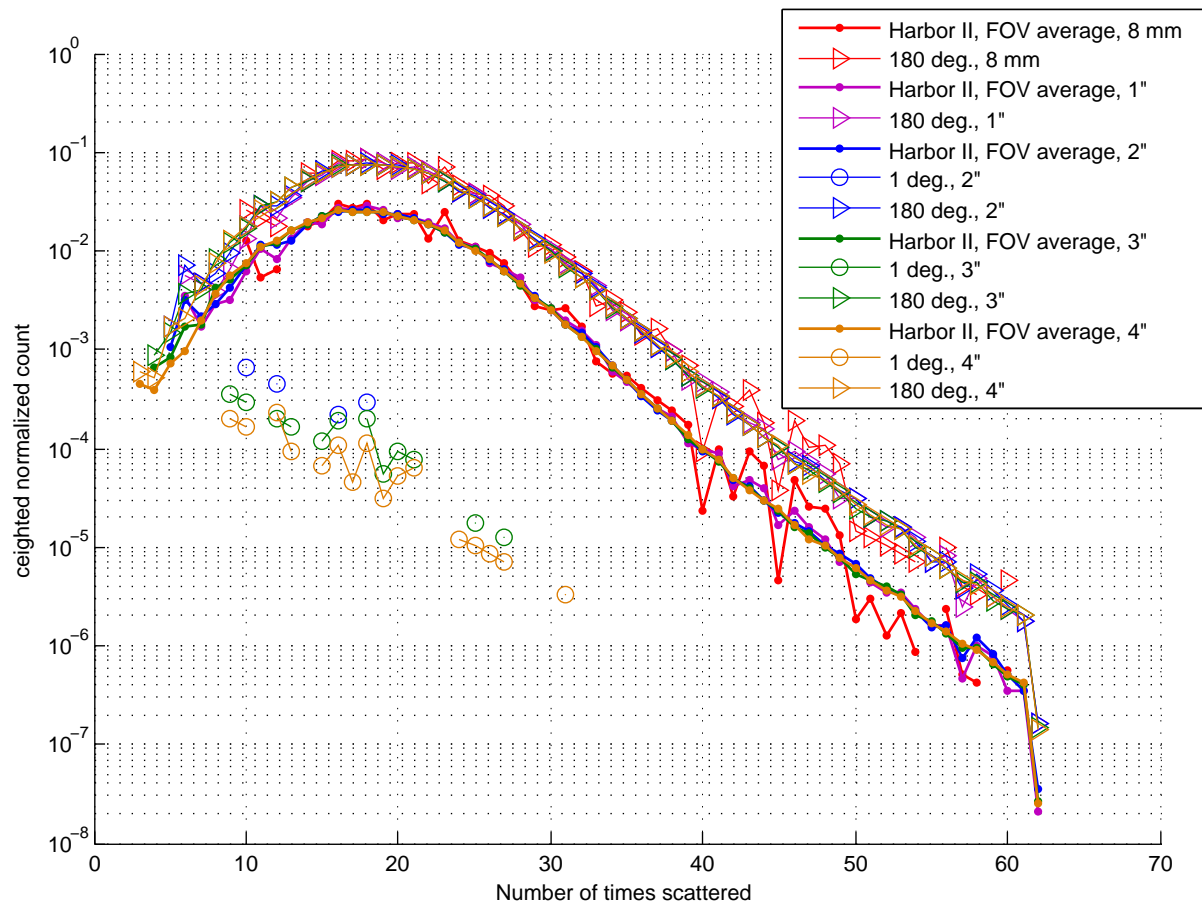


Figure 5.58: Scattering histogram of received photons for Harbor II water at 25 attenuation lengths. Each curve is normalized by the power at a 180° FOV for that aperture size. 180°, 1°, and FOV average is plotted.

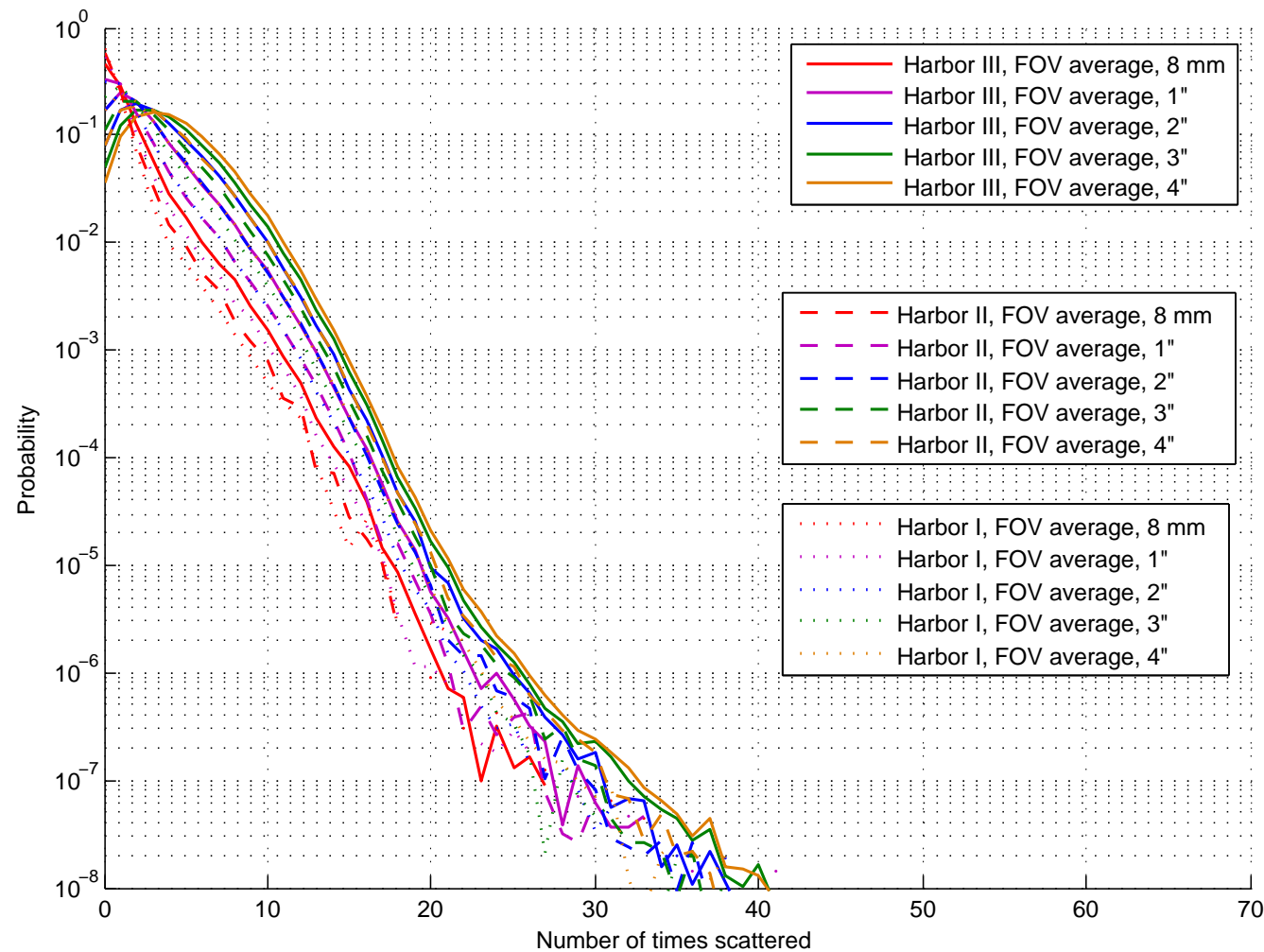


Figure 5.59: Harbor water average scattering histogram - 10 cz

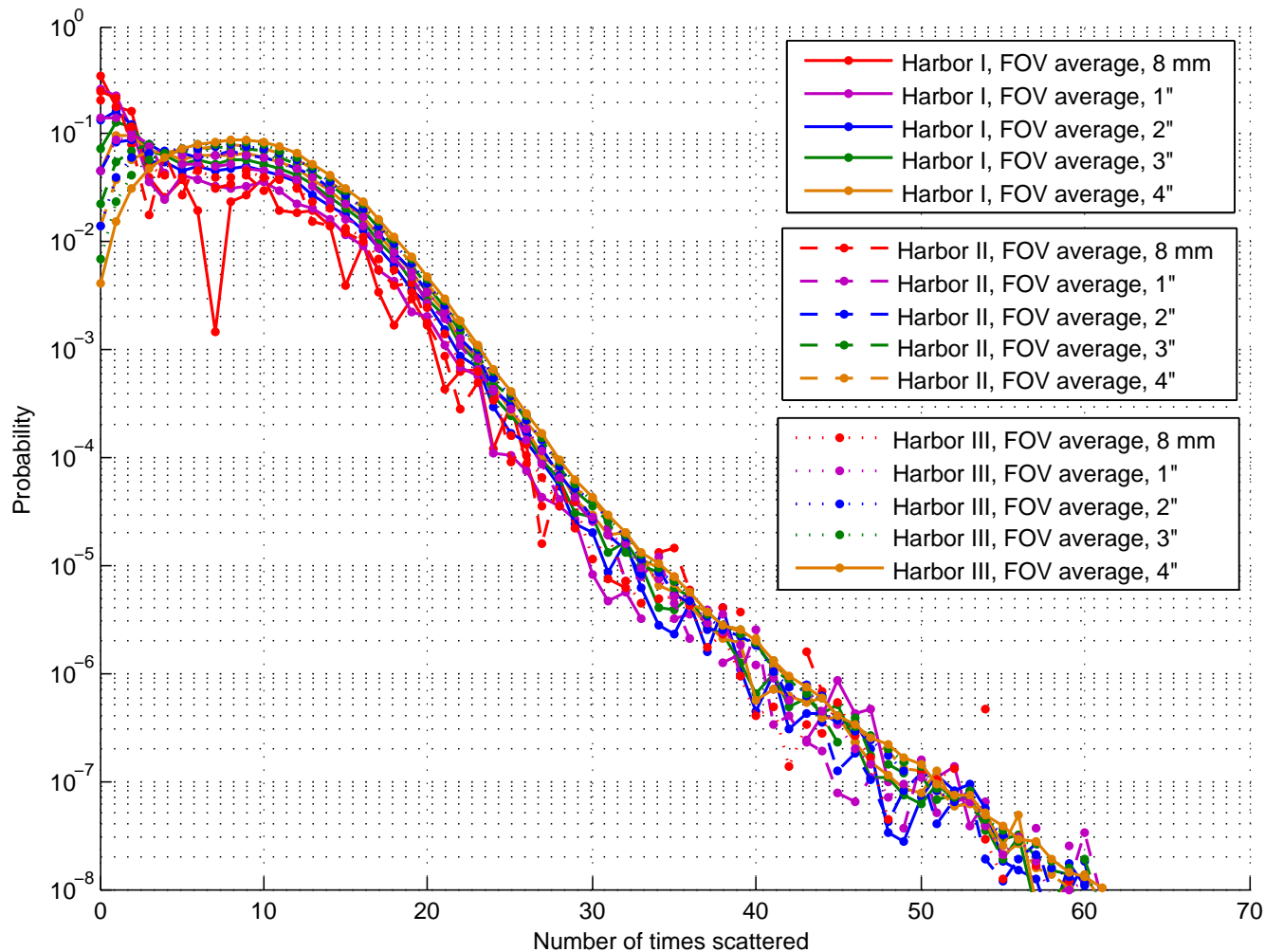


Figure 5.60: Scattering order PDF of received photons for all Harbor water types at 16 attenuation lengths. The average PDF of scattering orders is plotted for each aperture size at each water type.

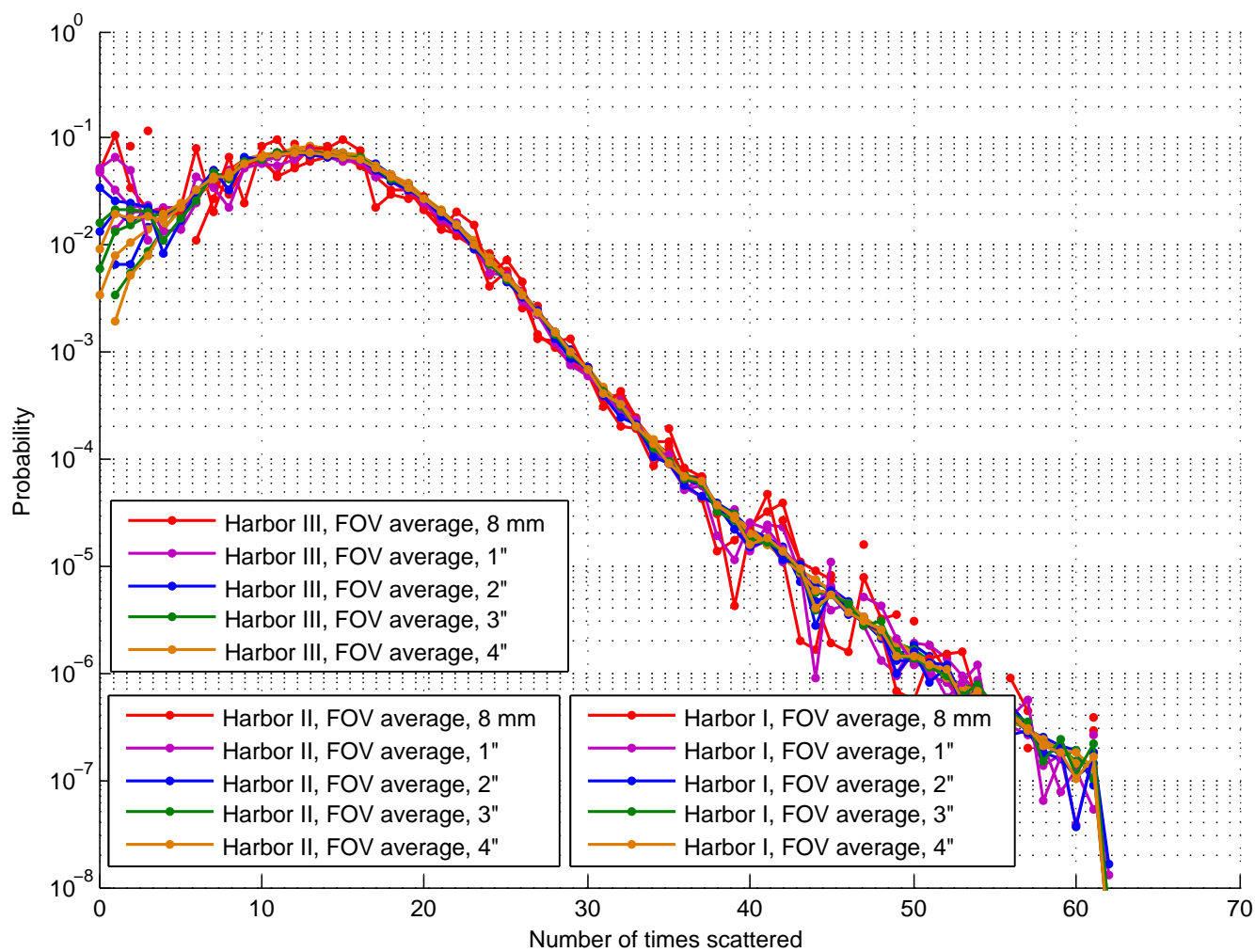


Figure 5.61: Harbor water average scattering histogram - 20 cz

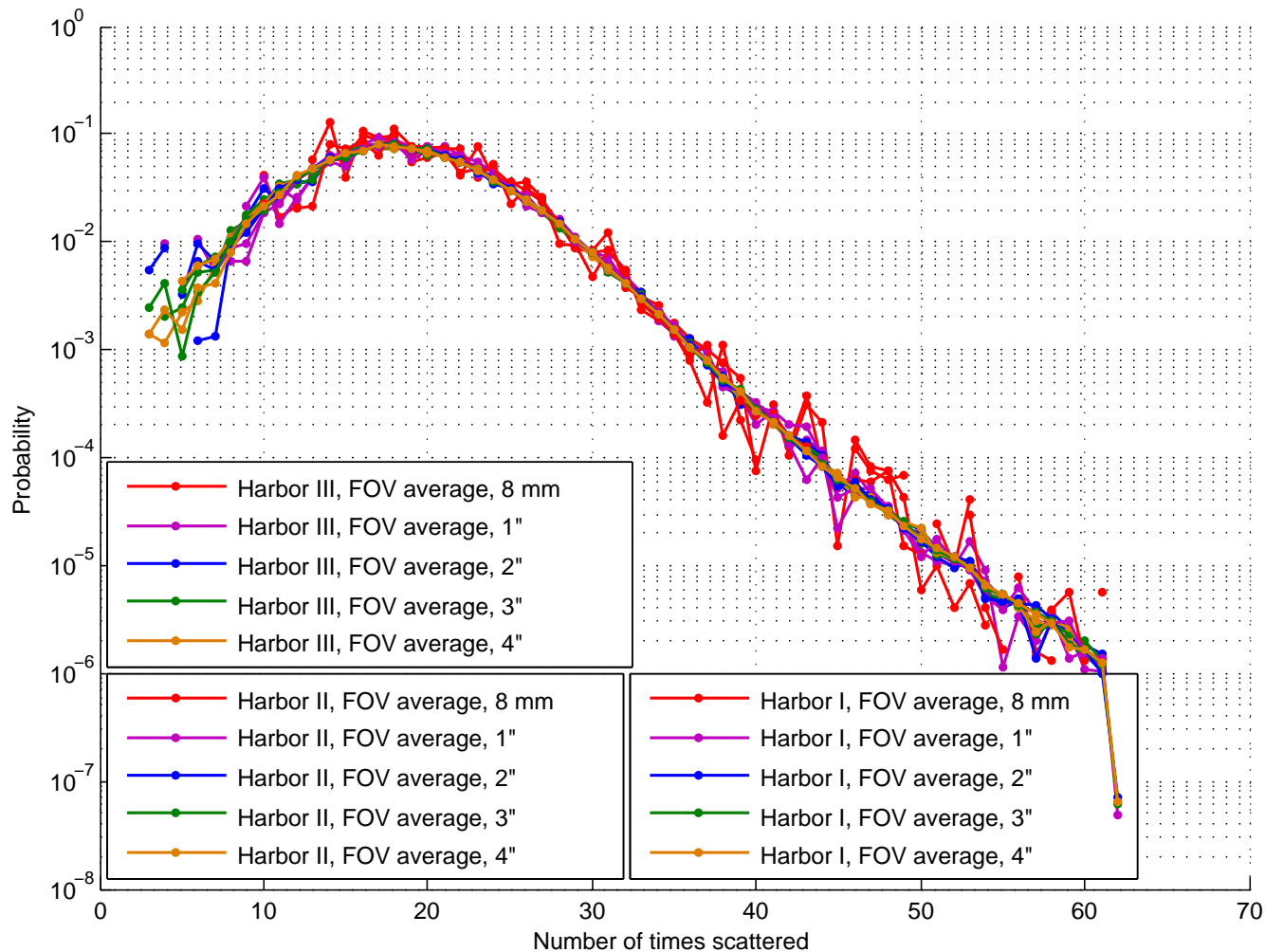


Figure 5.62: Scattering order PDF of received photons for all Harbor water types at 25 attenuation lengths. The average PDF of scattering orders is plotted for each aperture size at each water type.

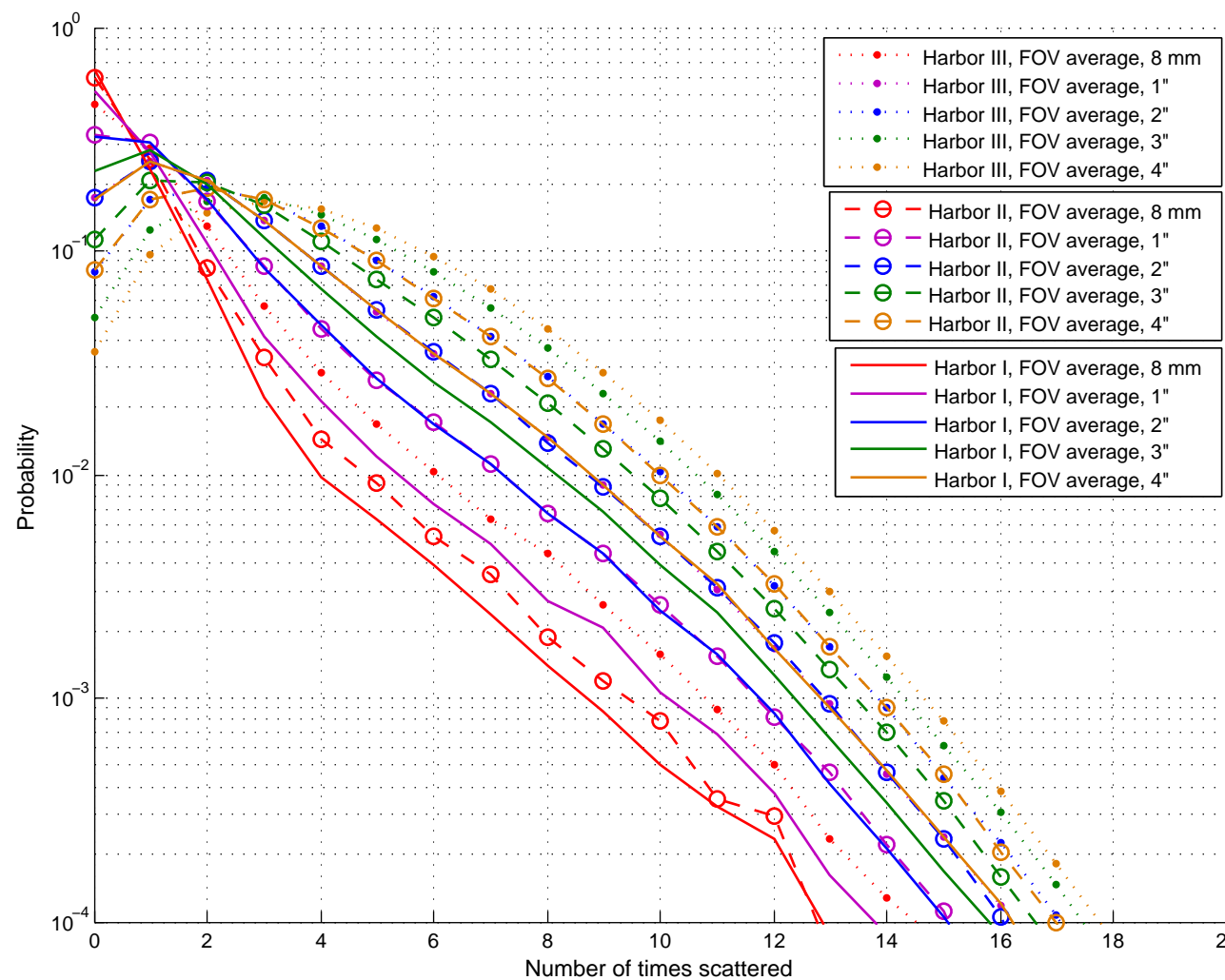


Figure 5.63: A closer view of Fig. 5.59, which shows the scattering order PDF of various water types, and aperture sizes averaged over all simulated FOVs at $10\text{ }cz$.

5.9 Temporal Response

The MCNS simulation can be used to gain discrete information on the temporal response of the channel. Each photons path distance is tracked, and for a homogeneous medium, yields a time-of-flight. The calculations for computing the impulse response and channel bandwidth are described in Section 4.4 on page 36. The results below use these calculations and show the frequency response up to about 2 GHz for the various Harbor water channels.

5.9.1 Frequency Response of Harbor Water

The frequency response for Harbor II type water, for various aperture sizes is shown in Fig. 5.64 on page 139. Only curves that contain at least 100 received photon packets are plotted. As the number of total received photon packets drops, the frequency response curves tend to become more noisy as there are less points in the time-of-arrival (TOA) histogram by which to estimate the frequency response.

From the data presented in Fig. 5.64, it appears that the frequency response changes little based on the size of the aperture. This is intuitive, based on the scattering results from the previous section, as the scattering orders change little based on the aperture, and the multiple scattering is what contributes to the change in frequency response. Using this observation, the frequency response of all aperture sizes are plotted together, at each chosen attenuation length. The images in Fig. 5.65 through Fig. 5.73 (page 140 through page 148) show the frequency response of Harbor I, II and III type water conditions over various attenuation lengths, aperture sizes and FOVs.

5.9.2 Temporal Response of Harbor Water Figures

The figures in this section correspond to the discussion in Section 5.9 and are presented below for readability.

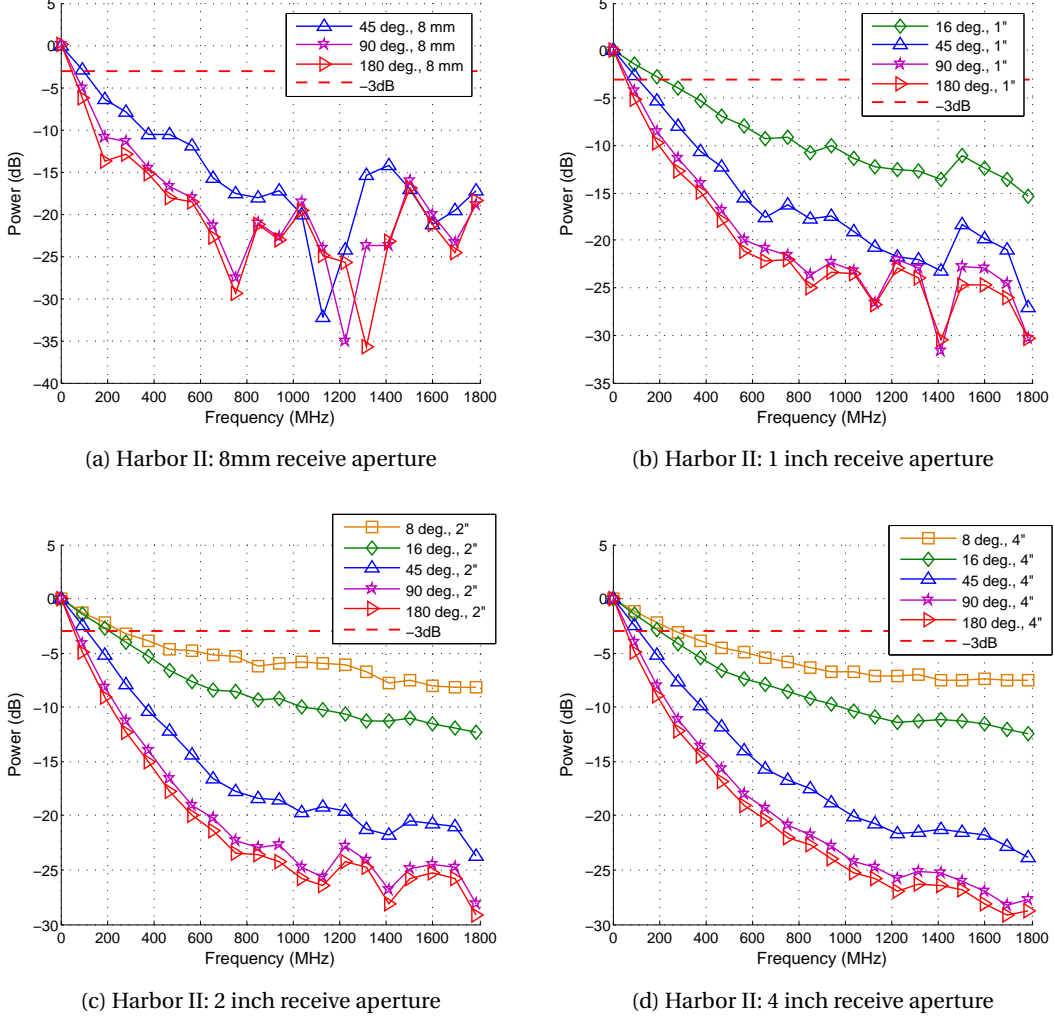


Figure 5.64: Harbor II: Frequency response at 25 attenuation lengths. Each FOV frequency response is plotted when there are more than 100 photon packets that can be used for an estimate of the response. It is clear from these plots that the frequency response appears to be independent of the aperture size.

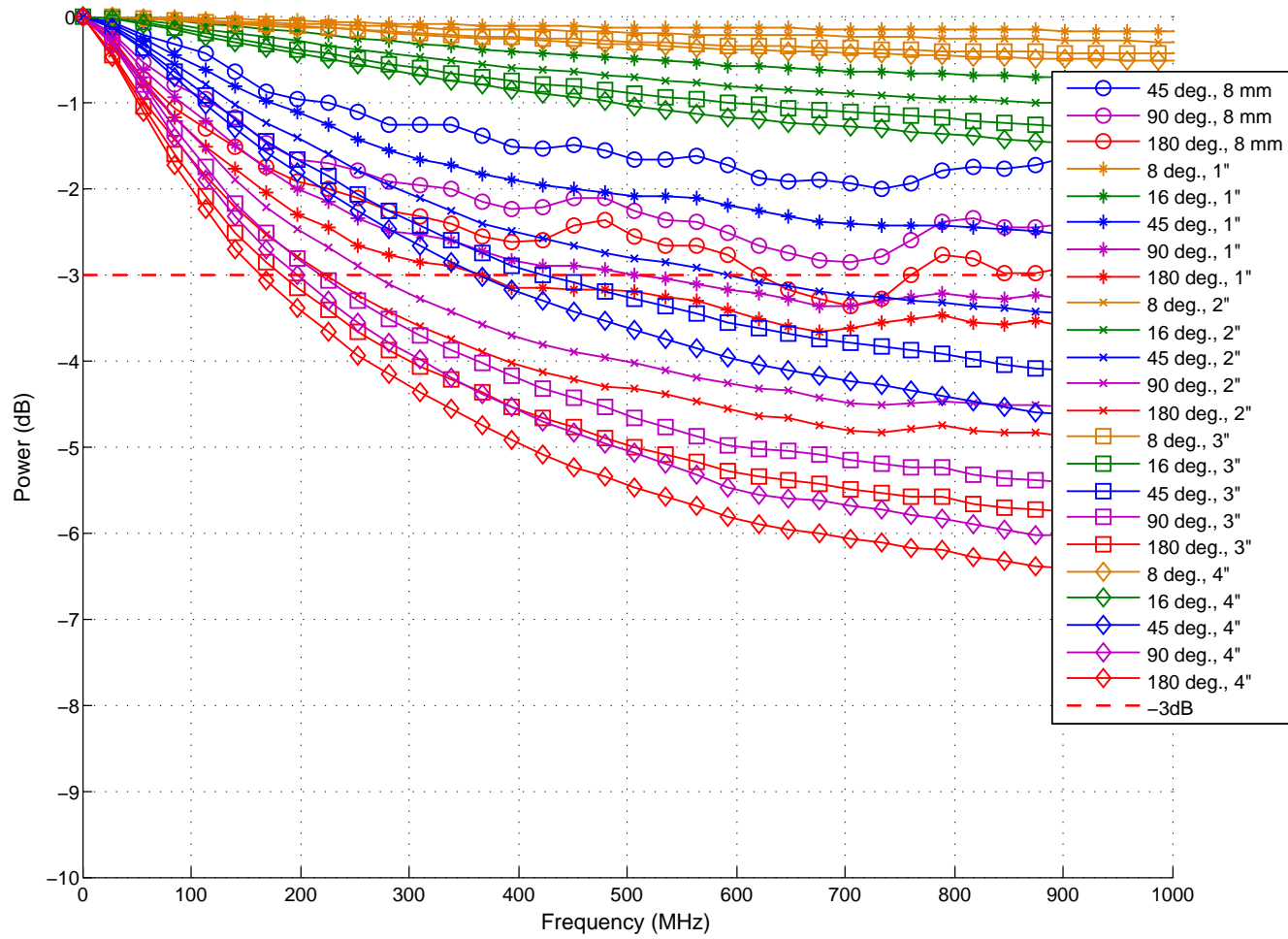


Figure 5.65: Harbor I water frequency response at 16 attenuation lengths ($d_{rx/tx}$ of 14.5 meters).

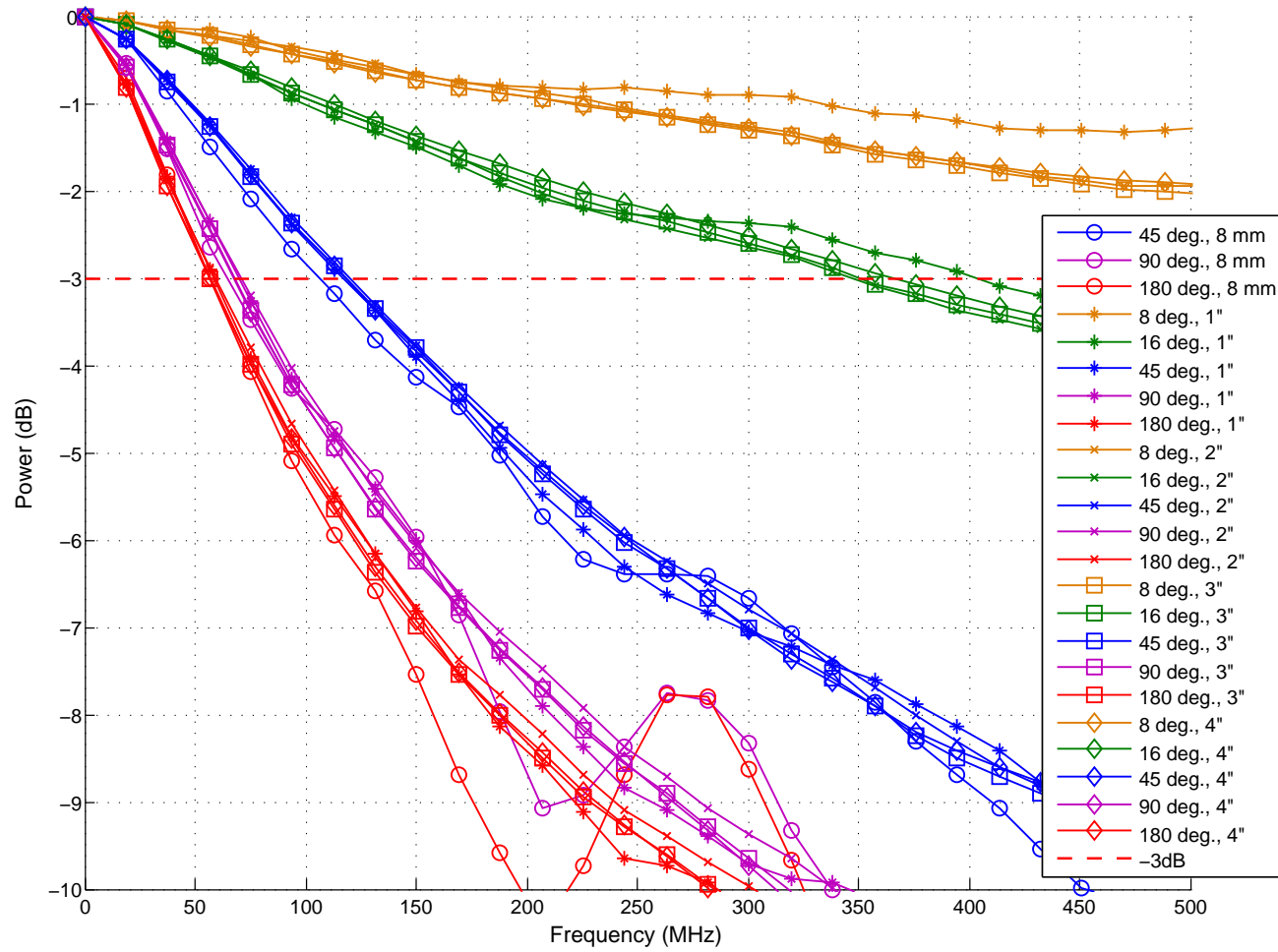


Figure 5.66: Harbor I water frequency response at 20 attenuation lengths ($d_{rx/tx}$ of 18.2 meters).

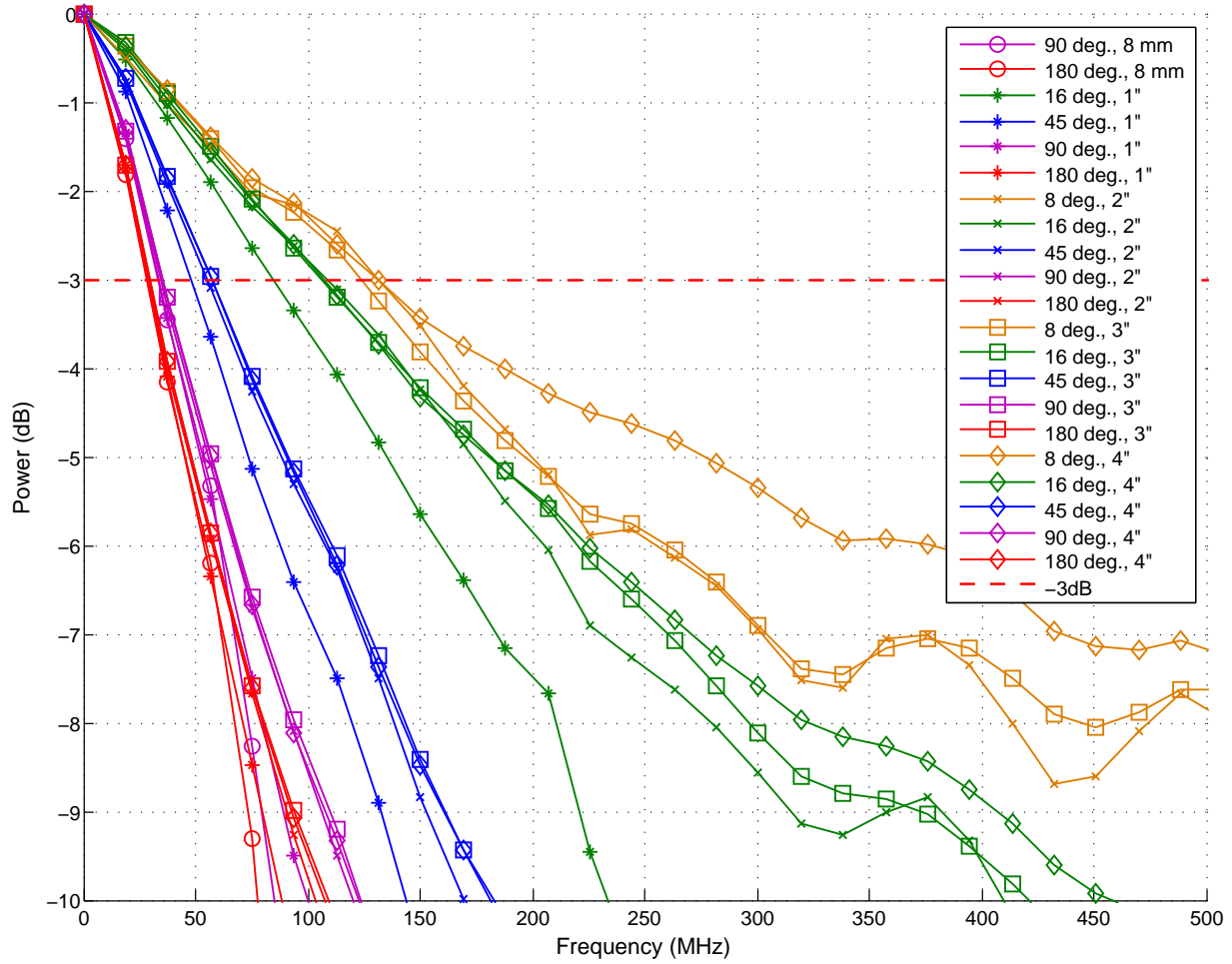


Figure 5.67: Harbor I water frequency response at 25 attenuation lengths ($d_{rx/tx}$ of 22.7 meters).

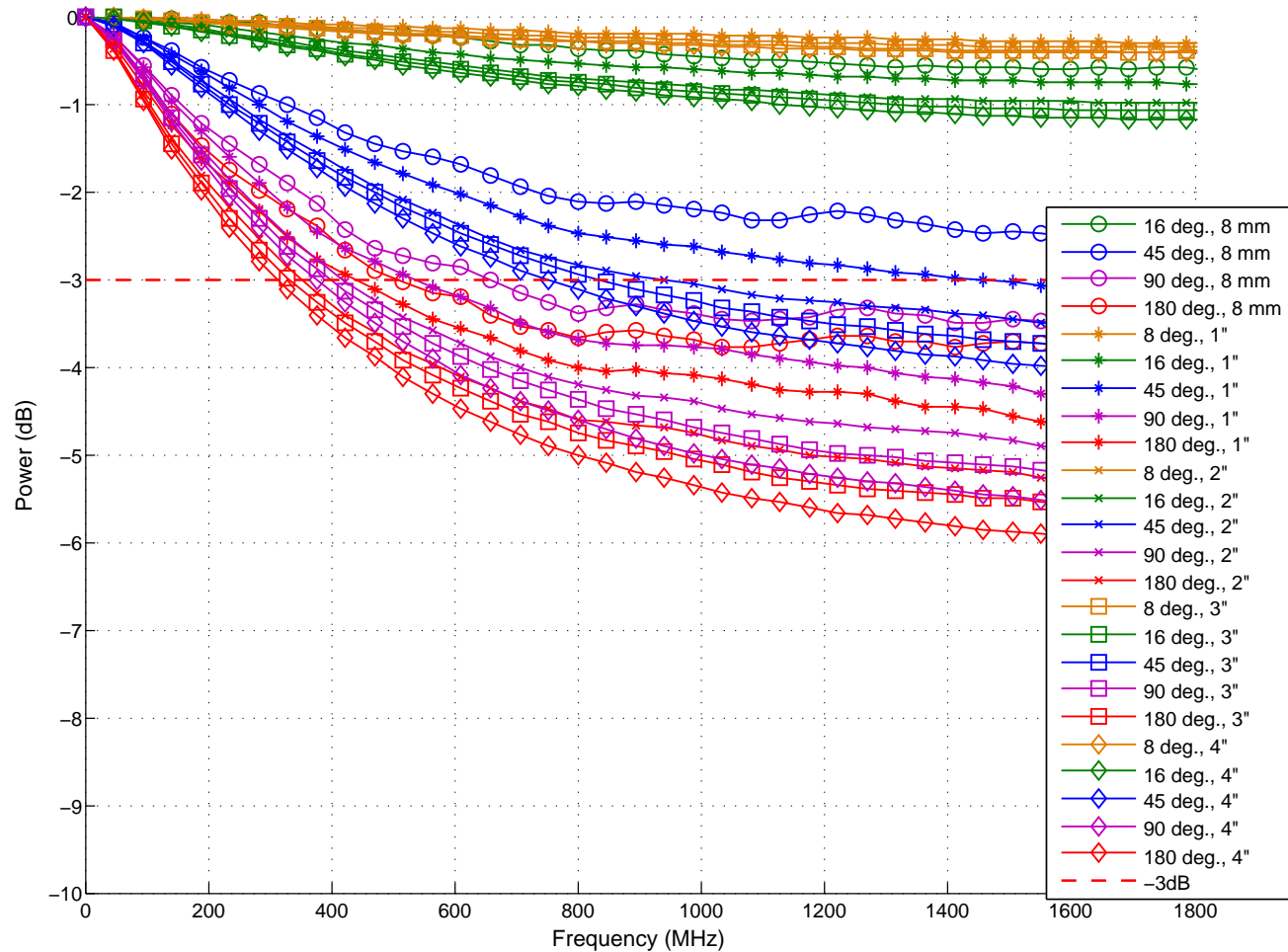


Figure 5.68: Harbor II water frequency response at 16 attenuation lengths ($d_{rx/tx}$ of 7.3 meters).

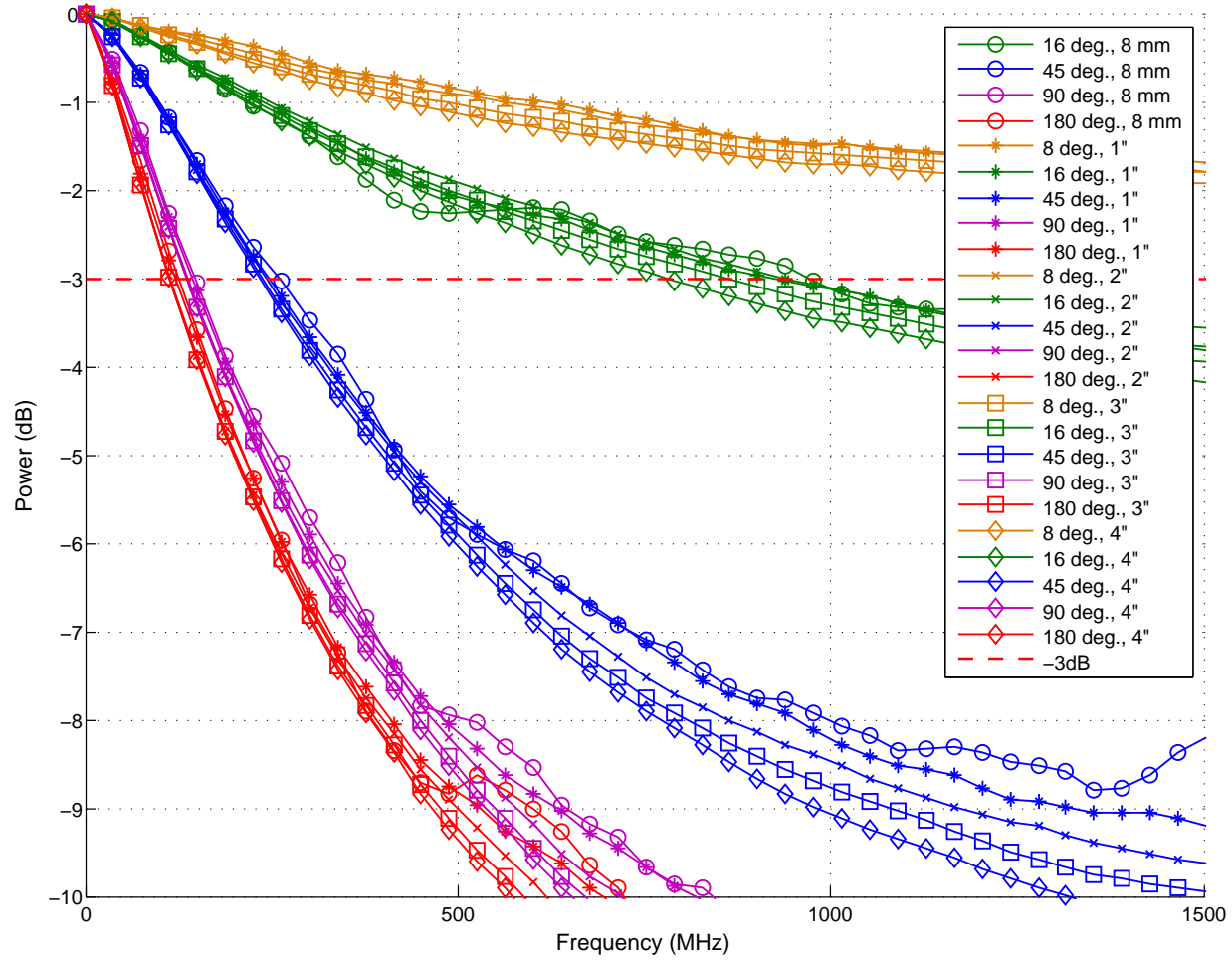


Figure 5.69: Harbor II water frequency response at 20 attenuation lengths ($d_{rx/tx}$ of 9.1 meters).

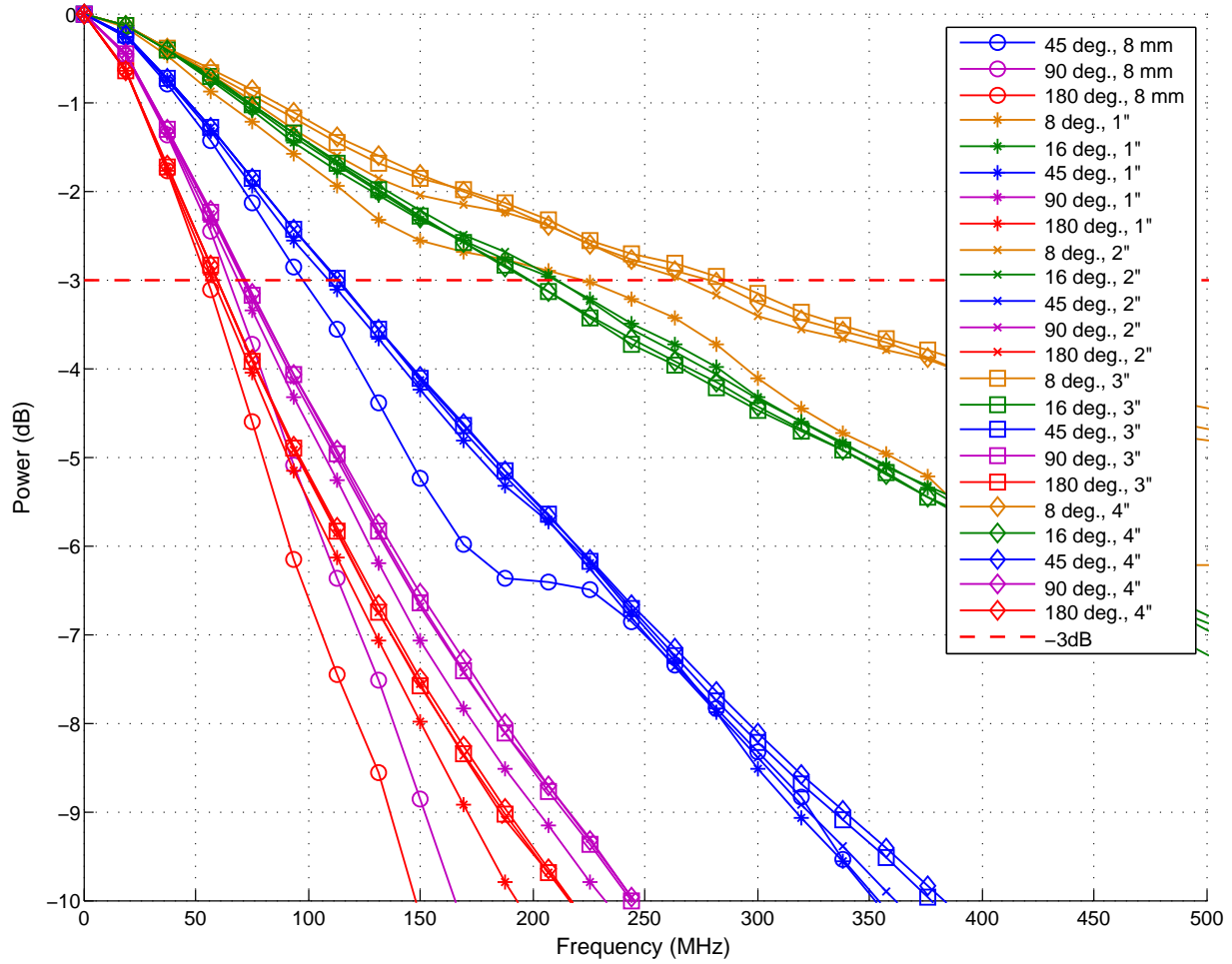


Figure 5.70: Harbor II water frequency response at 25 attenuation lengths ($d_{rx/tx}$ of 11.3 meters).

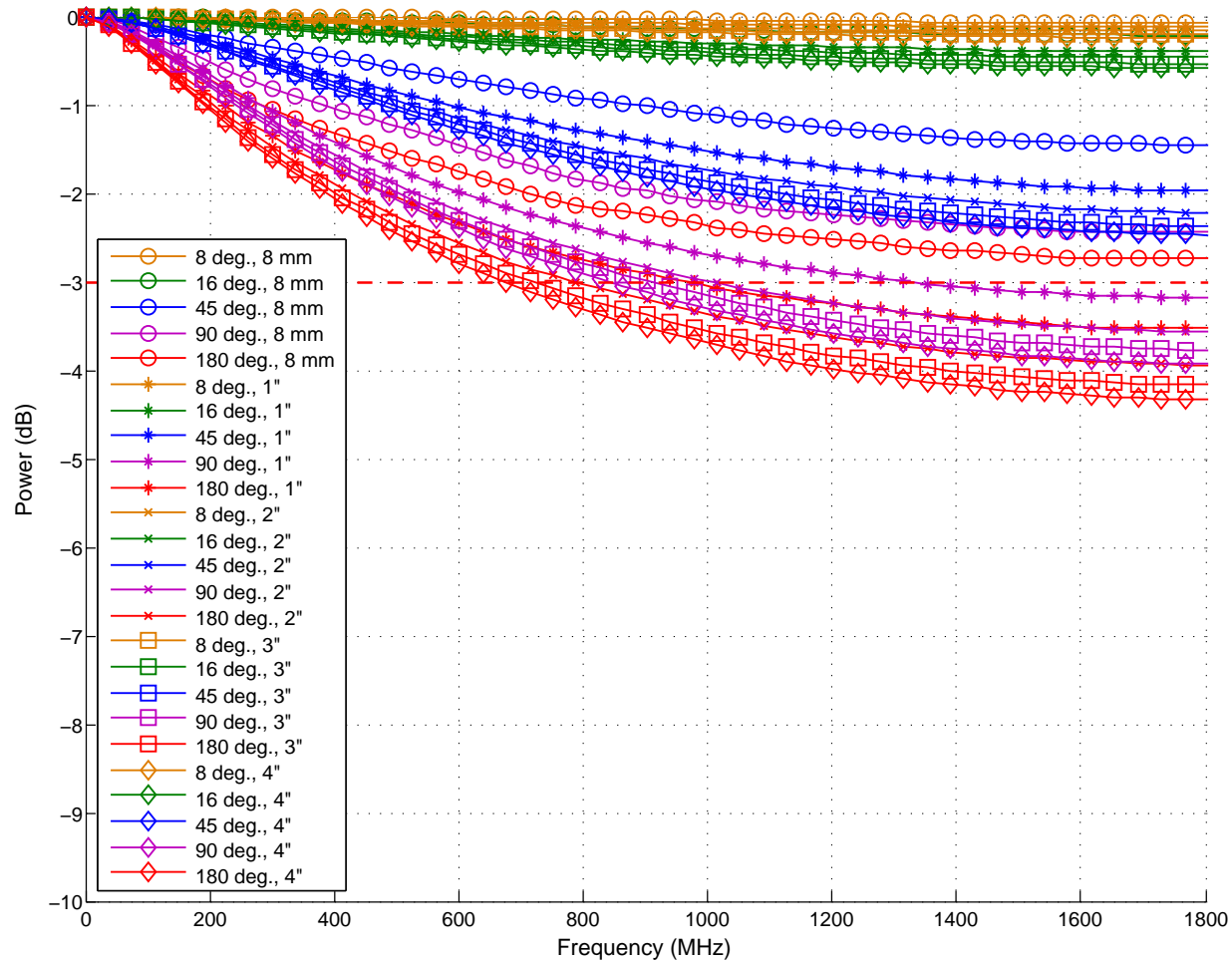


Figure 5.71: Harbor III water frequency response at 16 attenuation lengths ($d_{rx/tx}$ of 3.6 meters).

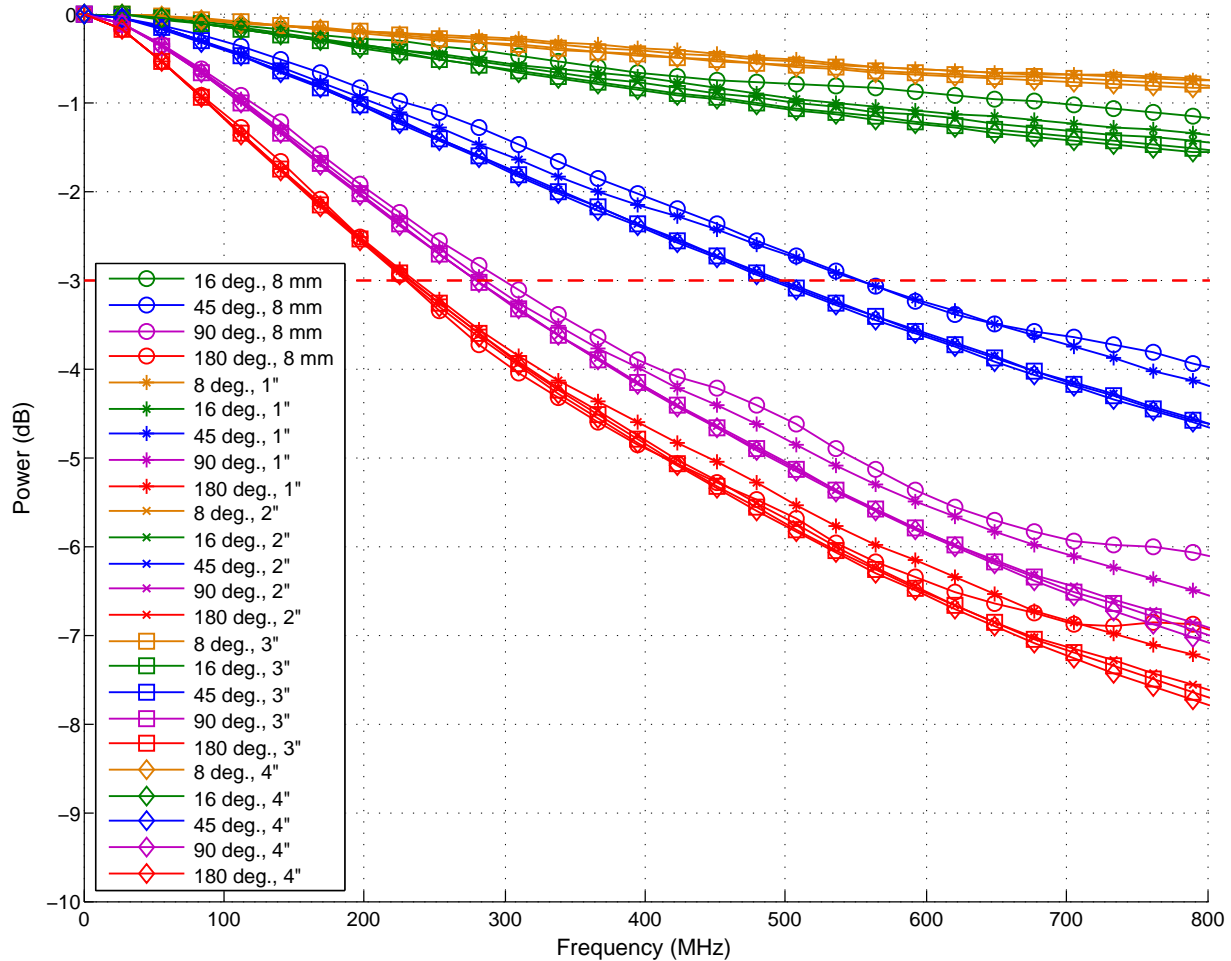


Figure 5.72: Harbor III water frequency response at 20 attenuation lengths ($d_{rx/tx}$ of 4.5 meters).

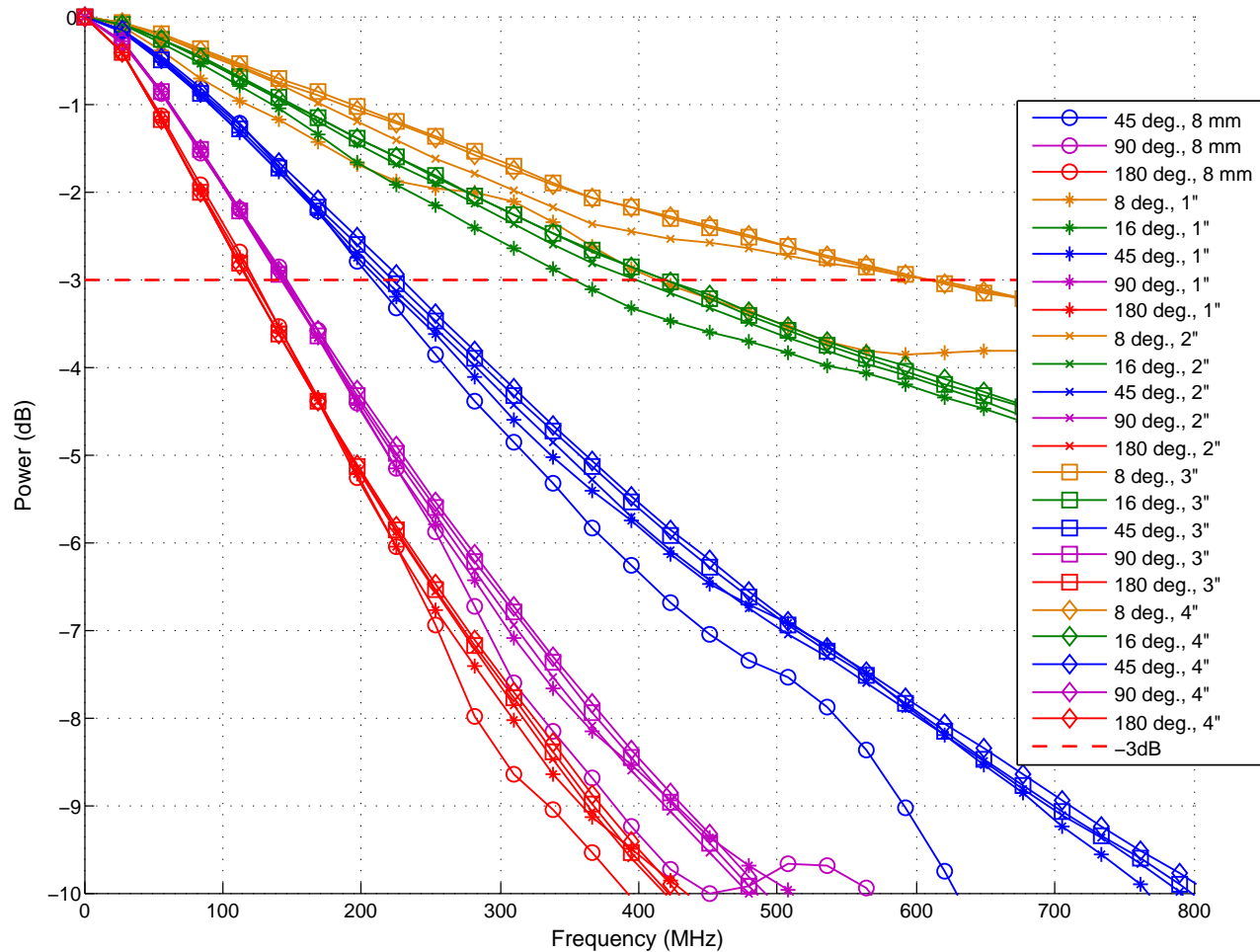


Figure 5.73: Harbor III water frequency response at 25 attenuation lengths ($d_{rx/tx}$ of 5.7 meters).

5.10 Received Power Versus Misalignment of Receiver/Transmitter

A functional optical communication system will need to deal with the effects of angular and position offsets between the receiver and transmitter. Previous simulations have dealt with on-axis reception of optical signals. A misalignment of the receiver's position relative to the transmitter, or an angular pointing error between receiver and transmitter will result in power loss. The simulations below help to quantify the effects of this offset.

Misalignment can characterized by four factors, transmitter angular misalignment, receiver angular misalignment, transmitter position misalignment, and receiver position misalignment. These four terms are illustrated in Fig. 5.2 on page 65. Since the simulation geometry is such that the receiver plane is always on the x/y-plane, these four misalignments must be modeled as just transmitter angular misalignment, transmitter position misalignment, and receiver position on the x/y-plane. In practice, the terms can be reduced such that only the transmitter's position and pointing angle needs to be changed in order to simulate angular and positional differences between the two. This conversion is discussed in Section 5.2.1. For the following sections, the offset is measured for a positional offset of the receiver on the receiver x/y-plane. This roughly translates into an angular offset on the transmitter, and a slight angular offset of the receiver, as it is not directly pointing towards the transmitter.

5.10.1 Computing the Distance Misalignment Power

There are two methods by which the total received power for a receiver misalignment can be computed. The first method, which is the most simple, involves simulating a physical distance offset of the receiver aperture on the receiver plane. Essentially, the received power is computed over a receiver aperture at a fixed position on the receiver plane. While this method is simple, better statistical data could be gathered if the radially symmetric nature of the medium could be leveraged. The second method takes advantage of this fact, and instead of computing the 2d integral over the x and y dimension to find the receiver power, it instead computes the 2d integral over the radial distance and the circular section comprising the receiver aperture. This concept is best illustrated rather than explained. Fig. 5.75 illustrates the concept.

Using the second method, each photon's radial distance from the center of the x/y receiver plane is computed, with the center being the intersection of the ballistic photons on the receiver plane. This is universally defined as coordinate (0, 0). Since the nature of natural water scattering is radially symmetric, a receiver aperture at any radial distance from the center of the receiver plane should receive the same power. The receiver power is computed by calculating the area of an annular ring intersecting the area of the receiver aperture, where each annular ring is the width of each bin of the radial power distribution. Essentially, the power distribution in 2d cartesian space is converted to a one dimensional power distribution based on radius. Fig. 5.74 and Fig. 5.75 illustrate this concept.

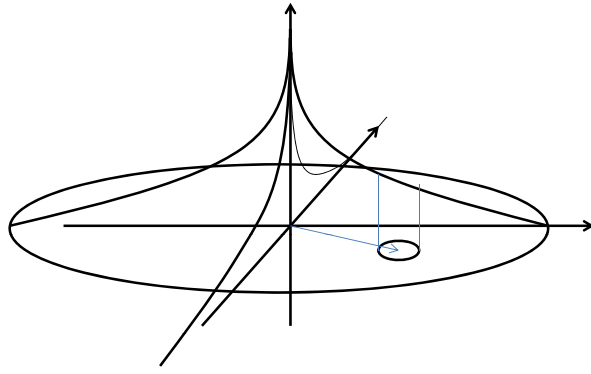


Figure 5.74: Illustration showing the concept of offset received power.

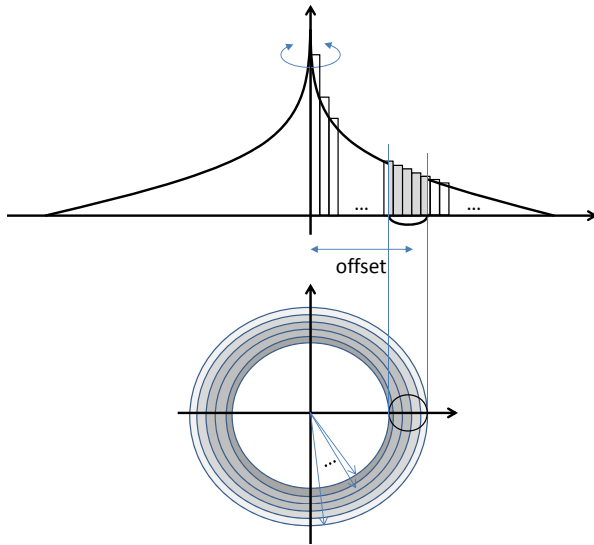


Figure 5.75: Illustration showing how the received power is calculated via the radial power distribution. Each annular ring represents the power in a specific radial bin.

The advantage to this second method is that it leverages all of the received photon path weights when building an estimate of offset received power, instead of using just path probabilities that intersect the plane only at the specific 2d coordinates that fall within any given receiver.

5.10.2 Misalignment Effects in Harbor Waters

Harbor I type waters ($c = 1.1 \text{ m}^{-1}$)

The figures presented in this section represent the misalignment affects in Harbor I-type waters. Harbor I type waters have an attenuation coefficient of 1.1 m^{-1} , and the results are presented at three different attenuation lengths of 10, 16, and 20. Attenuation lengths greater than 20 are not presented

since the number of simulated photons limit the statistical accuracy at each radial power bin. It would be possible to increase the radial bin size, essentially reducing the precision of the power distribution, however as can be seen in Fig. 5.78d, the power distribution is nearly flat over the radial offsets being considered.

As shown in Fig. 5.76, at 10 attenuation lengths there is a significant power loss associated with any distance deviations of the receiver from the central beam. For apertures smaller than 4 inches, a receiver that is more than 5 cm radially offset from the central beam will experience greater than 3 dB of loss. For a 4 inch receiver with a 180 degree FOV, this 3 dB loss point expands to 7 or 8 cm. The best case scenario presents a loss of 80 % of the signal power with a radial offset of 30 cm. In Harbor I type waters, at 10 attenuation lengths, this presents an angular offset of approximately 33 mrad using the equation below

$$\theta_{offset} = \tan^{-1} \frac{cz/c}{d_{offset}} \quad (5.22)$$

where θ_{offset} is the pointing angle offset at the transmitter to achieve a distance offset on the receiver plane of d_{offset} , cz is the attenuation length and c is the attenuation coefficient of the water.

At a distance of 16 attenuation lengths, shown in Fig. 5.77, the power distribution on the receiver plane has begun to spread considerably, since this is past the diffusion length of the channel. This is visible in the power loss plots with the large power spread between small FOVs and large FOVs (Fig. 5.16 for example). For instance, with a 2 inch aperture, nearly eight times the power is received with a 180 degree FOV than with a 1 degree FOV at an offset distance of 5 cm (see Fig. 5.76c). While there is still a distinct central beam, observed by the initial sharp transition in the first few centimeters of offset distance, past this point the power has been begun to spread, illustrated by the gently sloping curves past the initial drop. In fact, shown in Fig. 5.76d, with a 4 inch, 180 FOV, receiver, moving from an offset of 5 cm to 30 cm only reduces the received power by approximately 12 % (~ 0.92 to ~ 0.72 normalized power in the figure). It should be noted, however, that for small FOVs, there is still considerable loss associated with receiver/transmitter misalignment.

The final Harbor I type plot, shown in Fig. 5.78, presents power loss from receiver/transmitter misalignment at 20 attenuation lengths. At this distance, limited number of photons make the curves more noisy than previous curves, but there is enough detail to observe general trends. By 20 attenuation lengths the radial power distribution is nearly uniform for large FOVs, with only a 5% to 10% power drop being observed between 0 and 5 cm of offset distanced.

Fig. 5.79 and Fig. 5.80 show the effects of receiver and transmitter offsets at 16 cz and 20 cz respectively for fields-of-view of 1 deg., 16 deg. and 180 deg. This shows a range from a tightly coupled lens and detector, to a large FOV PMT detector system. While this data is also presented in the previous plots, it is helpful to visualize the losses at various aperture sizes together. Each plot shows the power loss as apertures of various sizes are swept laterally away from the transmit beam.

The difference between the 1 deg. FOV systems (shown marked with circles) drop off very quickly as the receiver is moved laterally away from the transmit beam, while the 180 deg. FOV systems loose power very gradually. If one were to compare a large FOV system with a small aperture (much like a small PMT-based detector) to the performance of a large aperture, small FOV system (much like a PIN photodetector coupled with a large lens), each crosses the -3 dB point at about 5 cm of lateral offset distance, but the slope difference between the two response curves is drastically different, with the small FOV system leaving very little margin for error in pointing.

Harbor II type waters ($c = 2.19 \text{ m}^{-1}$)

The figures presented in this section represent the misalignment affects in Harbor II-type waters. Harbor II type waters have an attenuation coefficient of 2.19 m^{-1} , and the results are presented at three different attenuation lengths of 10, 16, and 20. These correspond to distance of 5.6 m, 7.3 m, and 9.1 m separating the receiver and transmitter respectively. As discussed in Section 3.5.2, the data presented at 16 and 20 attenuation lengths are beyond the diffusion length of the channel and therefore represent a link that is operating with a significant amount of multiple scattering.

The offset power measured at 10 attenuation lengths (Fig. 5.81) shows a very strong dependency on accurate pointing, with a very sharp cutoff happening above 10 cm of lateral offset. This number is slightly wider than the data from Harbor I-type waters, as the beam is traveling over a larger distance and therefore is larger due to geometric expansion from the divergence. Regardless of aperture size, by 30 cm of lateral offset, the power has dropped by greater than 75 % for even the best case scenarios (Fig. 5.81d).

At 16 attenuation lengths, the offset distance power loss slope has sharply decreased, with the larger FOVs experiencing relatively little loss over a much larger range of offset distances. For small FOVs, 1 deg. and 2 deg., there is still a sharp fall-off at distances greater than 5 cm. For a system operating with a large FOV and a small aperture, the power loss between 5 cm and 30 cm only amounts to reduction of approximately 10 % (Fig. 5.82a and Fig. 5.82b).

Fig. 5.83 presents the power loss as a function of lateral offset between receiver and transmitter at a distance of 20 attenuation lengths. In Harbor II-type water, this corresponds to approximately 9 m distance separating the two. At this distance, the lightfield has very little predominant forward scattering beam, as evidenced by the lack of strong peak at the 0 cm offset distance in Fig. 5.83a. For apertures larger than 8 mm, there is even less evidence of a central peak, with the 4 in aperture exhibiting less than 10 % of power loss over the full range of 30 cm of lateral offset distance. While the small FOV detectors still exhibit a large loss over the full offset distance, the effect is not nearly as pronounced as with the plots at smaller attenuation lengths. When comparing the received power at small FOVs between Harbor I and Harbor II-type waters, the Harbor II-type waters show about 10 % less received powers than in Harbor I-type waters. This is due to the geometric beam spreading and

the light field scattering into a larger area, thereby reducing the received power.

Harbor III type waters ($c = 4.4 \text{ m}^{-1}$)

The figures presented in this section represent the misalignment affects in Harbor III-type waters. Harbor III type waters have an attenuation coefficient of 4.4 m^{-1} , and the results are presented at three different attenuation lengths of 10, 16, and 20. These correspond to distance of 2.3 m, 3.6 m, and 4.5 m separating the receiver and transmitter respectively. As discussed in Section 3.5.2, the data presented at 16 and 20 attenuation lengths are beyond the diffusion length of the channel and therefore represent a link that is operating with a significant amount of multiple scattering. Harbor III waters represent very turbid water that might be found in semi-closed bodies of water like a Sound or close to shore in a harbor environment. Potential uses may be non-contact docking and data transfer for underwater vehicles, or communication between vehicle swarms, since the shallow seabed makes acoustic communication difficult in this scenario.

When comparing the offset power loss between the Harbor III and Harbor I waters at 10 cz , it is apparent that the curves are more tightly coupled in Harbor I waters than in Harbor III. Increasing the FOV of the receiver in Harbor III waters produces a stronger response. This is due to the fact that the are on the transmitter plane subtended by the FOV is smaller, since the physical distance between receiver and transmitter is smaller. For a 4" aperture, shown in Fig. 5.86d, the -3 dB point shifts from 5 cm to 10 cm offset distance based on the FOV of the receiver. For a small 8 mm aperture, transitioning from on-axis to 1 cm off-axis produces a 70 % drop in power (see Fig. 5.86a).

The data presented in Fig. 5.87 shows the power loss resulting from receiver and transmitter misalignment in Harbor III water at 16 attenuation lengths. This corresponds to approximately a distance of 3.6 m, as opposed to 7.3 m and 14.5 m in Harbor II and Harbor I waters. The initial power drops from on-axis to slightly off-axis alignment is not quite as severe in Harbor III waters as it is in Harbor I waters, with a 8 mm aperture still receiving 60 % of the transmitted power as opposed to 50% in Harbor I waters. Since the scattering lengths are shorter in the more turbid waters, the beam has less distance over which to spread. This is, however, mitigated by the smaller, central, ballistic beam. The slope of the power loss curve at distances greater than 5 cm are much more steep than in Harbor I waters, suggesting that the shorter scattering lengths also keeps the beam from becoming as diffuse as in Harbor I waters.

Finally, the offset power loss curves for 20 attenuation lengths (4.5 m distance between receiver and transmitter) are shown in Fig. 5.88. At FOV's larger than 16 degrees, the initial power loss when moving from on-axis to off-axis is nearly invisible, and the loss curves for large FOVs is constant. This, compared to the initial drop of about 10% in Harbor I waters, with a nearly flat loss profile out to 30 cm, shows that at 20 attenuation lengths, the light field in Harbor III-type waters still is not completely homogenous out to a radius of 30 cm. For a system with a 1" aperture and a 16 deg. FOV (Fig. 5.88b),

Table 5.5: -3 dB offset distances and angles for various water types at 20 attenuation lengths for a 2 inch aperture with 4 deg. FOV.

| Quantity | Harbor I | Harbor II | Harbor III |
|--------------|----------------------|----------------------|----------------------|
| C value | 1.1 m^{-1} | 2.2 m^{-1} | 4.4 m^{-1} |
| -3 dB radius | 0.14 m | 0.1 m | 0.07 m |
| -3 dB angle | 7.7 mrad | 110 mrad | 220 mrad |

at 30 cm, the system has loss 50% power, whereas in Harbor I waters (Fig. 5.78b) the power loss is less than 30%.

The data shown in Fig. 5.89 and Fig. 5.90 repeat the data presented above, but for a limited set of FOVs (1, 16, and 180 deg.), and plotted together for easier comparison. In Fig. 5.90 the 180 deg. and 16 deg. families of curves are tightly grouped together, suggesting that at that distance the ballistic center of the beam has all but disappeared, whereas in Fig. 5.89, there are still considerable differences between the smaller and larger apertures. If, however, the system has a very tight FOV, as in the 1 deg. case, there is still a sizable power loss when transitioning from on-axis to off-axis at both 16 cz and 20 cz , with 90 % of the power being lost by 5 cm of offset distance in 20 cz water with a small 8 mm aperture. That number is nearly 99% power loss when in 16 cz water. It should be noted, however, that while the relative power loss is greater at 16 cz than at 20 cz for small FOVs and apertures, the absolute power received will be greater due to the shorter transmission distance.

Equating Linear Rx/Tx Mismatch to Angular Mismatch

When comparing power loss for linear offset between receiver and transmitter, it should be noted that the physical distance between receiver and transmitter is not constant between the various simulated water types, while the linear offset distance is. This effectively means that for a fixed attenuation length, the required angular pointing accuracy increases as the water quality improves. Essentially, as you transmit over a longer distance, you need to maintain a tighter angular pointing accuracy in order to keep the same linear distance.

For example, for a 2" 4 deg. FOV receiver at 20 attenuation lengths, the -3 dB point for various water types is shown in Table 5.5. The -3 dB angle is calculated using the formula

$$\theta_{3dB} = \tan^{-1}\left(\frac{r_{offset}}{z_{rx/tx}}\right) \quad (5.23)$$

where θ_{3dB} is the pointing angle accuracy needed to maintain a radial distance r_{offset} from the on-axis beam at a distance of $z_{rx/tx}$ away from the transmitter.

5.10.3 Misalignment Result Figures

The figures below are presented here for readability, and are referred to throughout Section 5.10.

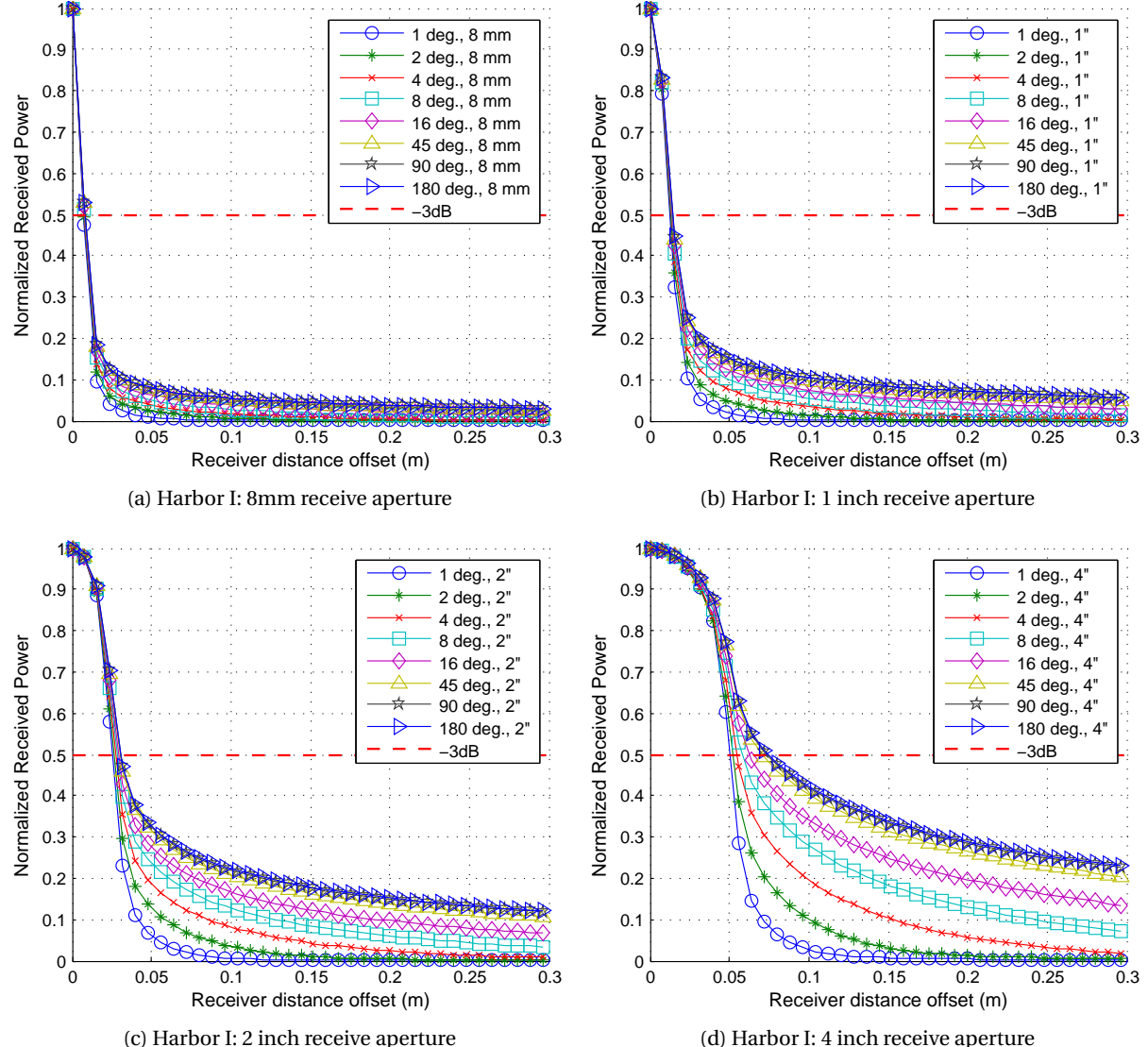


Figure 5.76: Harbor I, 10 Attenuation Lengths: Normalized power received for the given aperture, as it is swept from the beam center (0 offset) to 0.3 meters radial distance from the transmitted beam center.

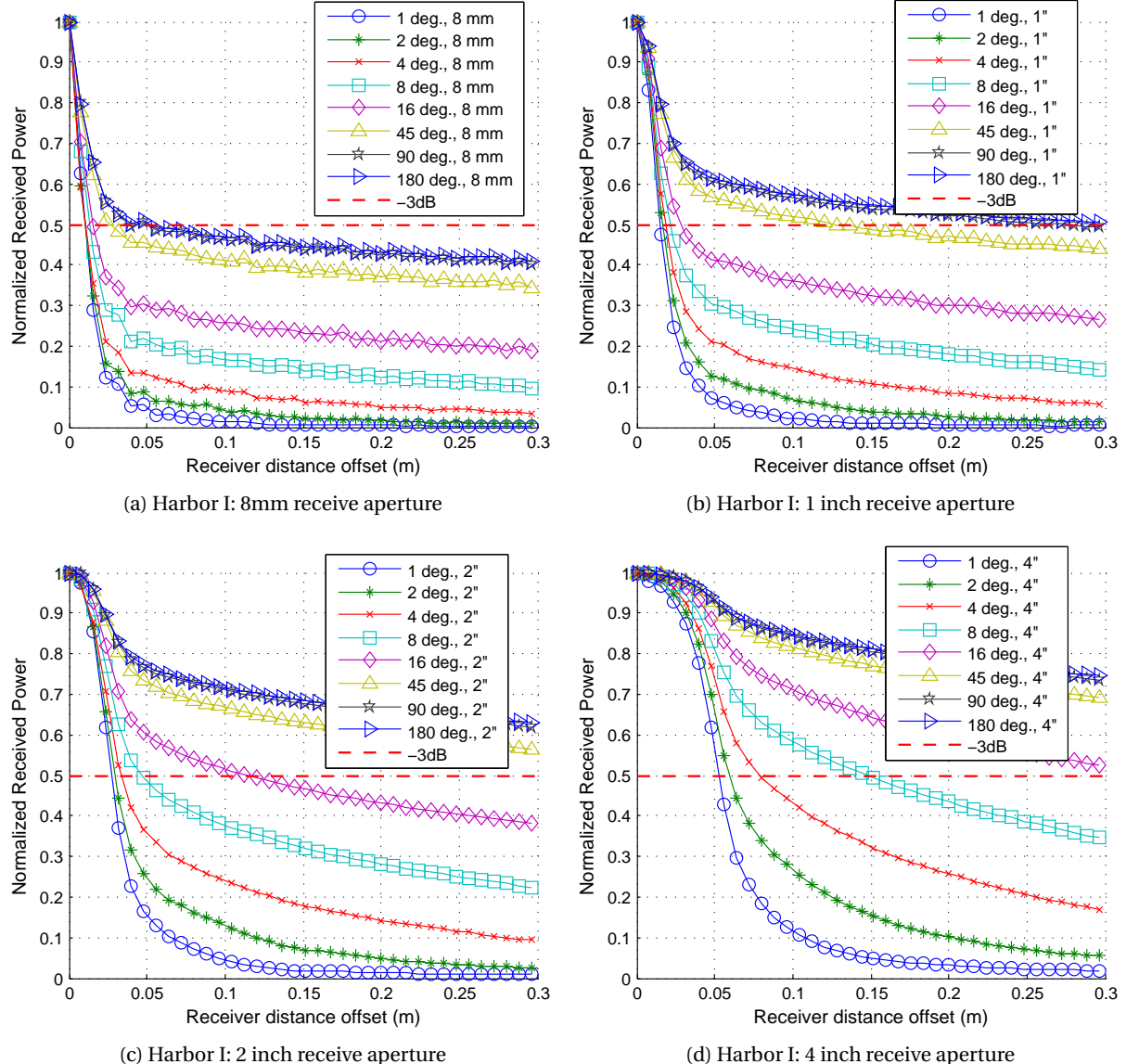


Figure 5.77: Harbor I, 16 Attenuation Lengths: Normalized power received for the given aperture, as it is swept from the beam center (0 offset) to 0.3 meters radial distance from the transmitted beam center.

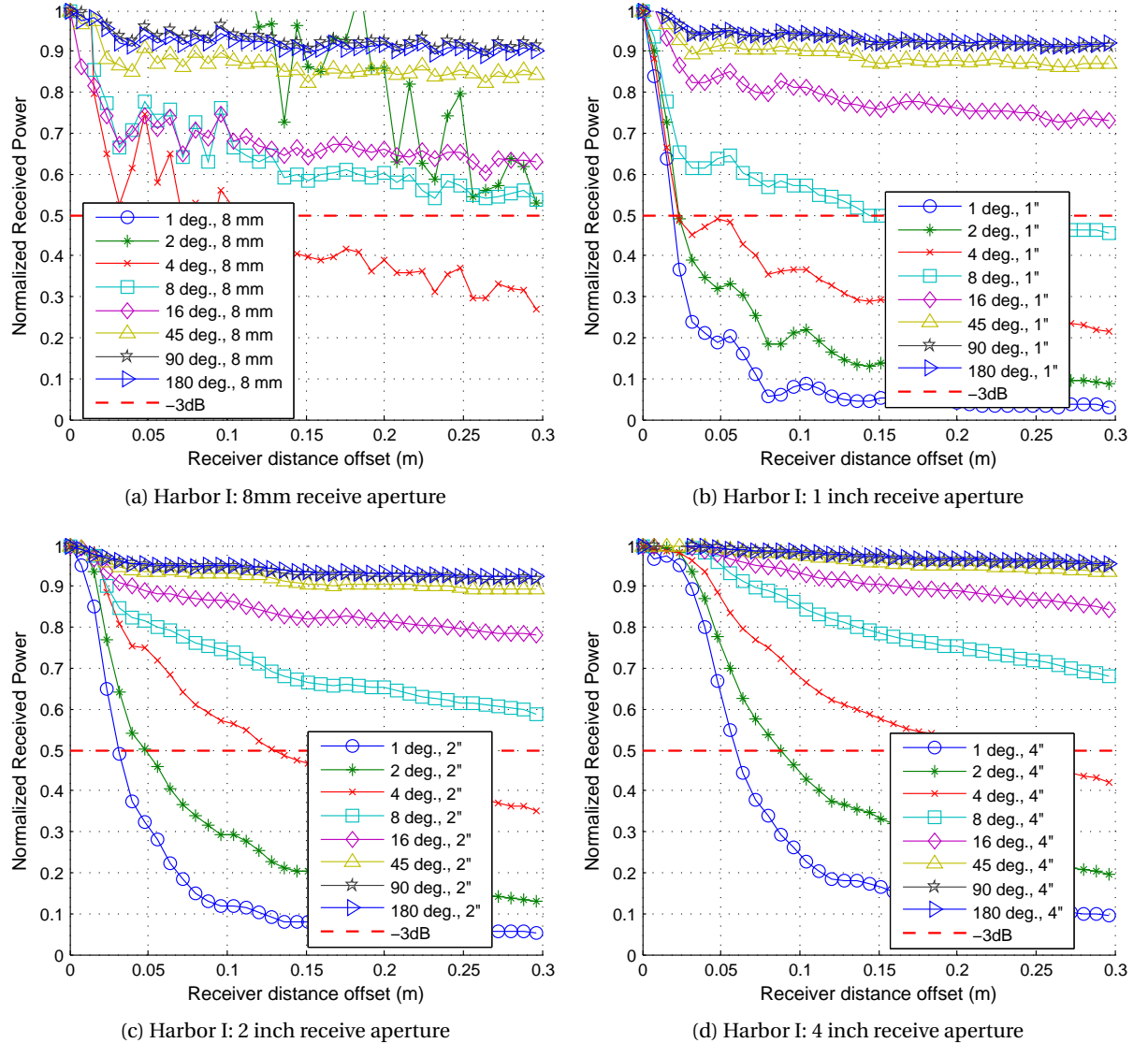


Figure 5.78: Harbor I, 20 Attenuation Lengths: Normalized power received for the given aperture, as it is swept from the beam center (0 offset) to 0.3 meters radial distance from the transmitted beam center.

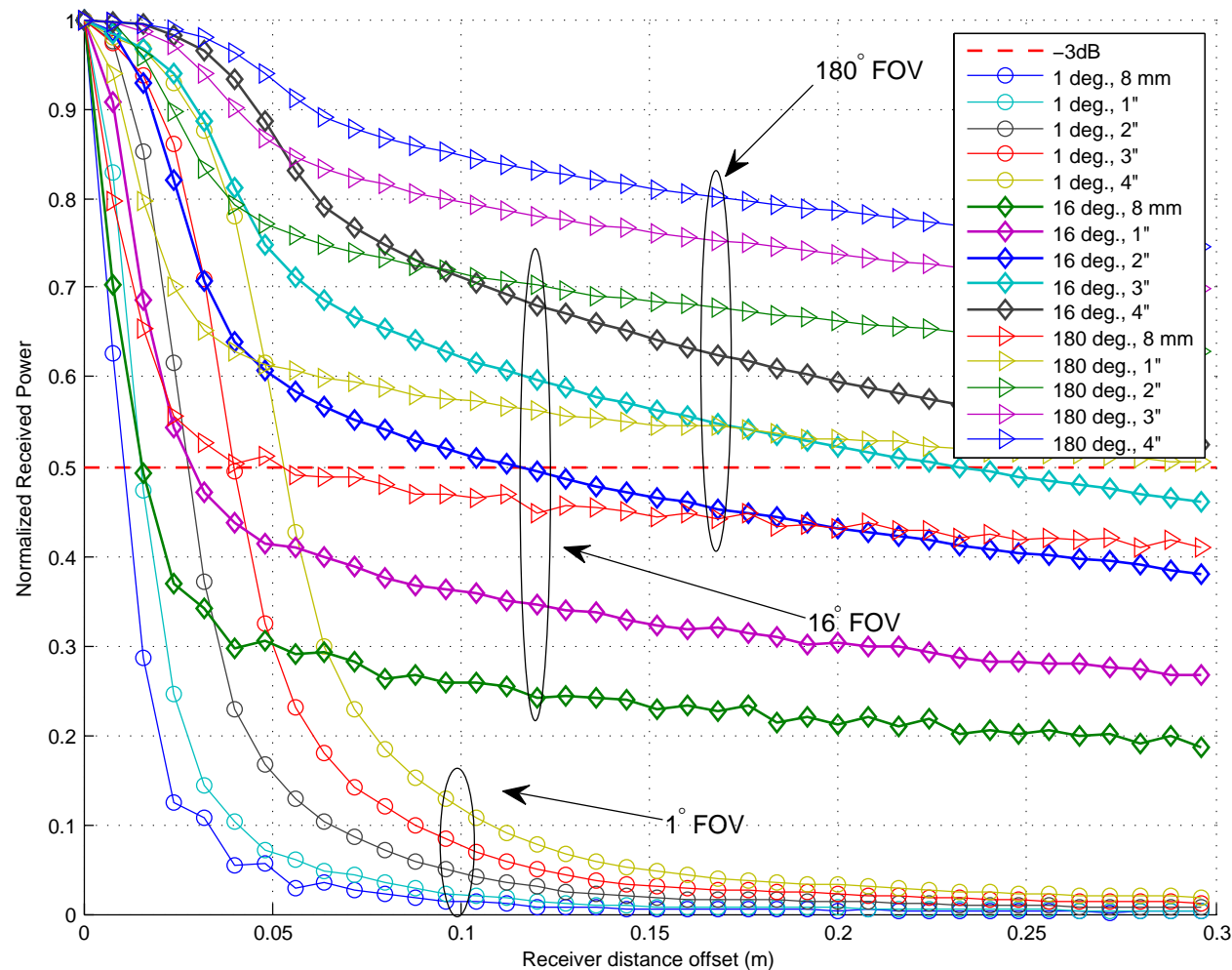


Figure 5.79: Harbor I: Normalized received power for various apertures and FOV's, at a given offset distance from the center of the transmitted beam. This is for simulated data at 16 attenuation lengths, or approximately 15 meters distance.

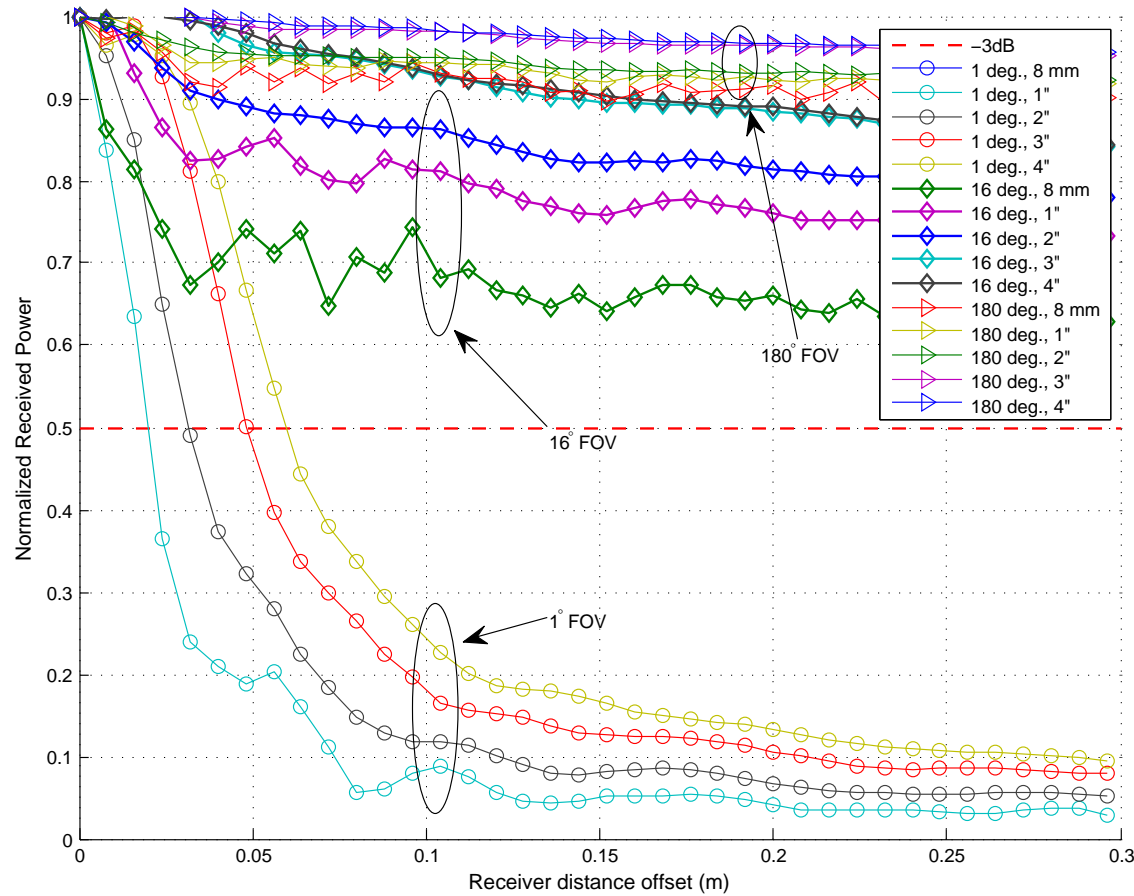


Figure 5.80: Harbor I: Normalized received power for various apertures and FOV's, at a given offset distance from the center of the transmitted beam. This is for simulated data at 20 attenuation lengths, or approximately 18 meters distance.

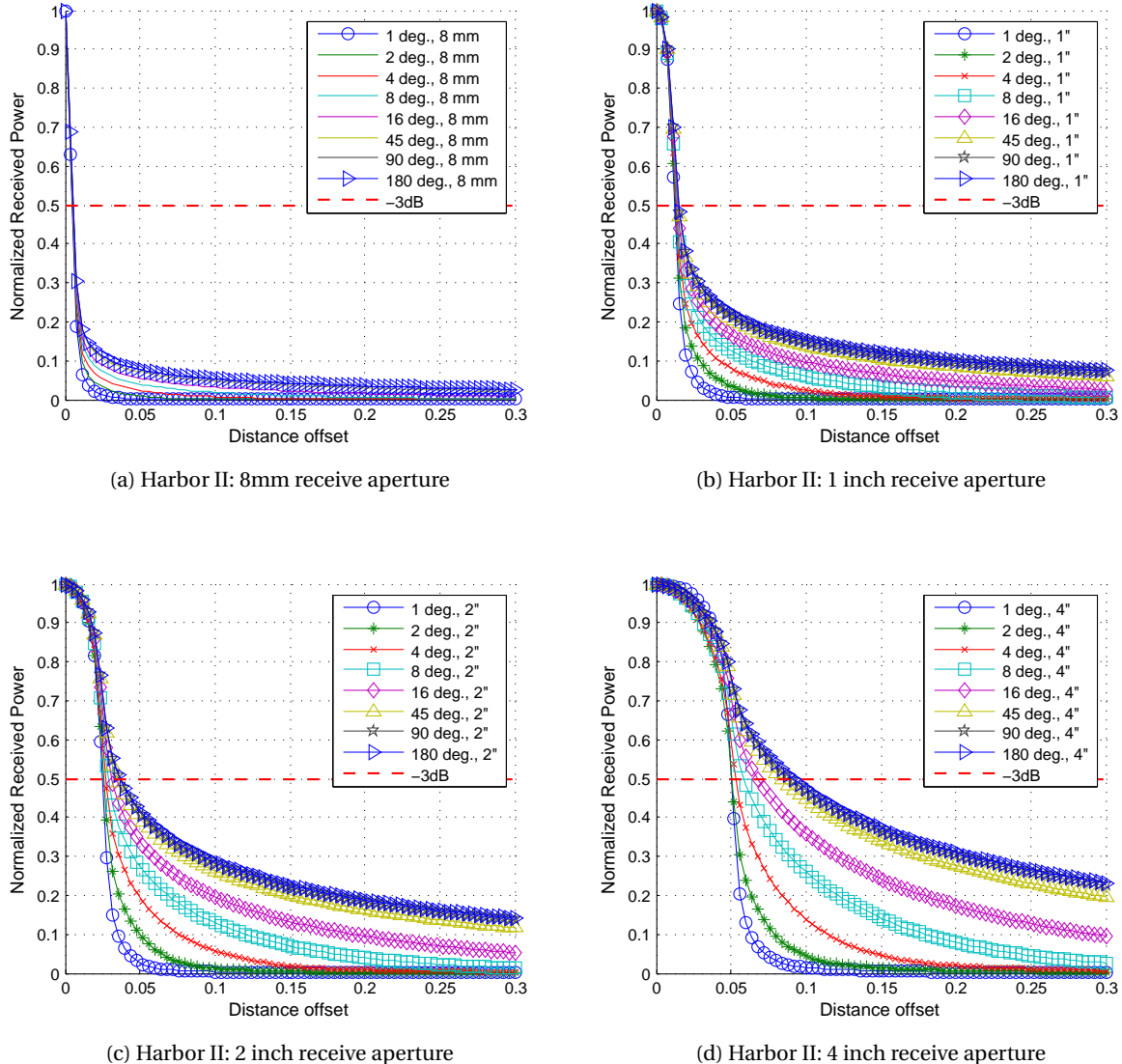


Figure 5.81: Harbor II, 10 Attenuation Lengths: Normalized power received for the given aperture, as it is swept from the beam center (0 offset) to 0.3 meters radial distance from the transmitted beam center.

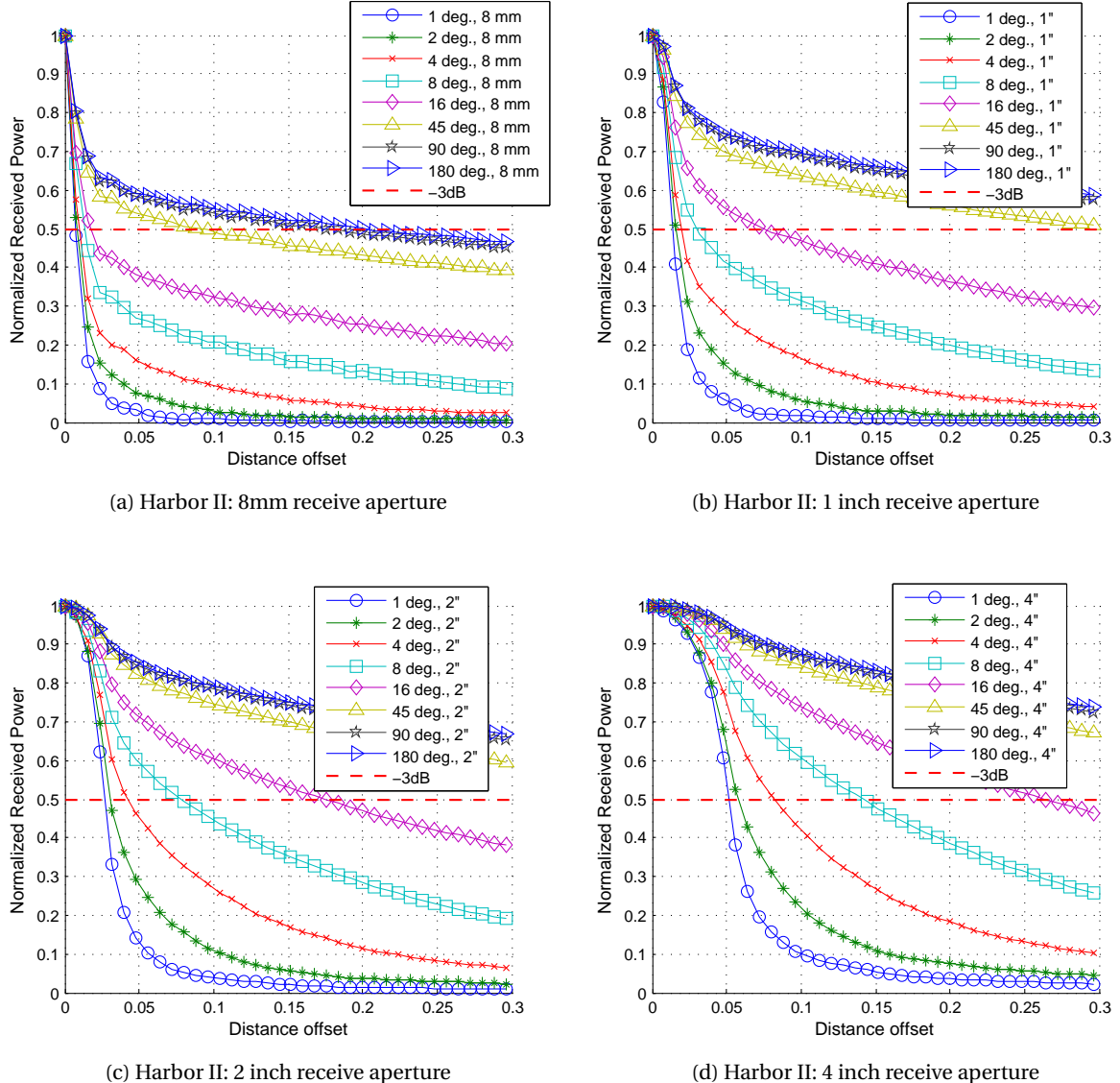


Figure 5.82: Harbor II, 16 Attenuation Lengths: Normalized power received for the given aperture, as it is swept from the beam center (0 offset) to 0.3 meters radial distance from the transmitted beam center.

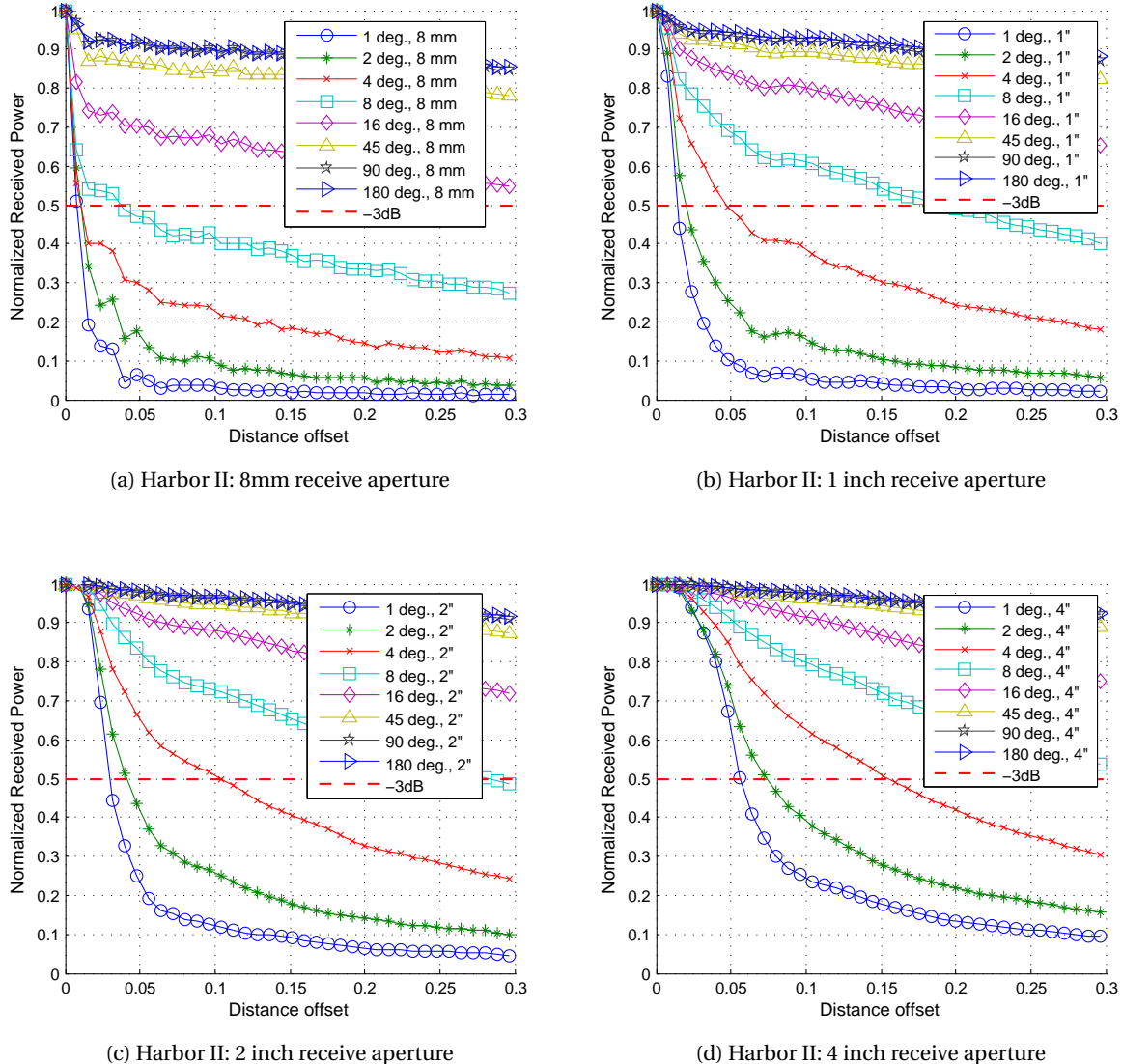


Figure 5.83: Harbor II, 20 Attenuation Lengths: Normalized power received for the given aperture, as it is swept from the beam center (0 offset) to 0.3 meters radial distance from the transmitted beam center.

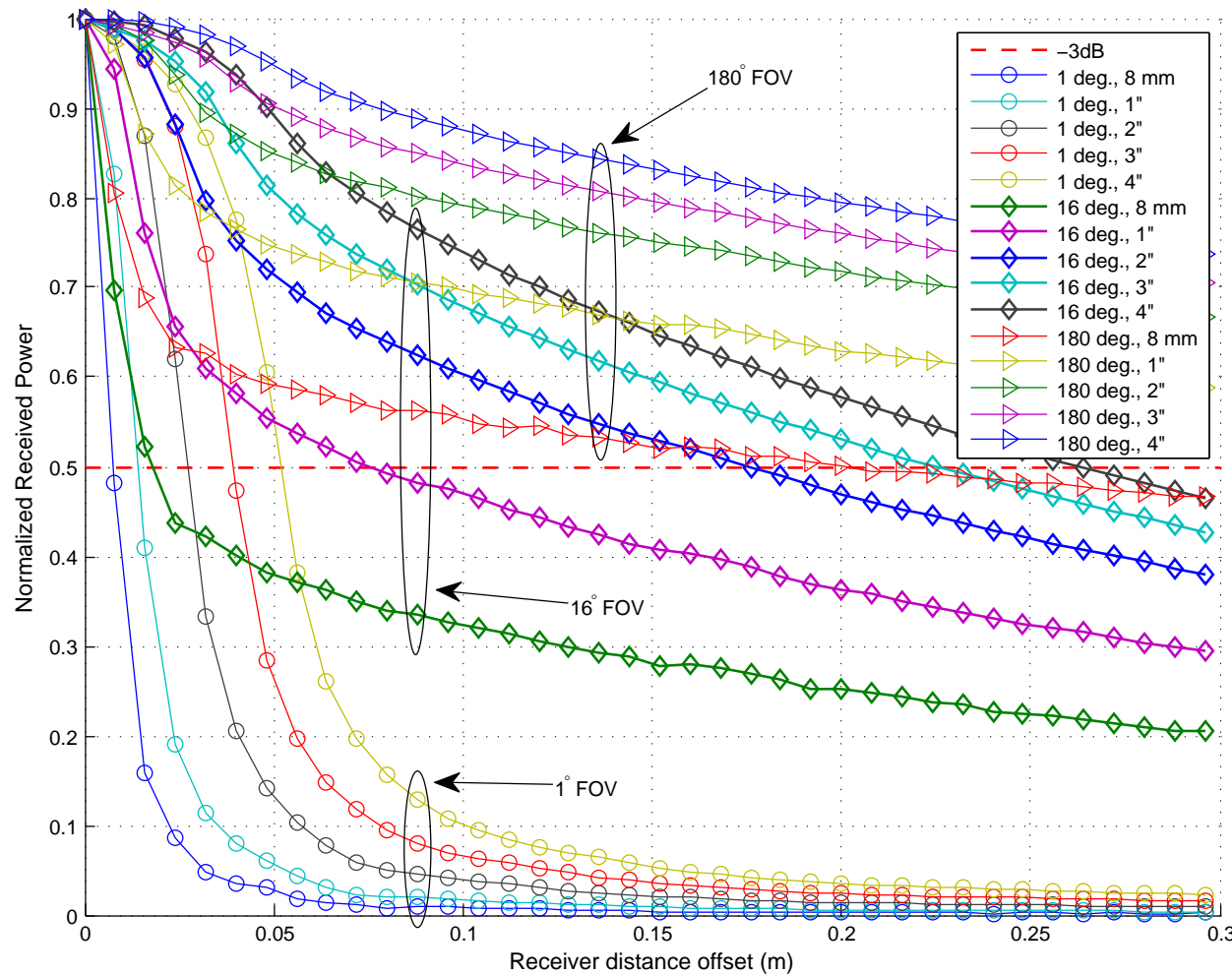


Figure 5.84: Normalized received power for various apertures and FOV's, at a given offset distance from the center of the transmitted beam. This is for simulated data at 16 attenuation lengths in Harbor II water, or approximately 7.3 meters distance.

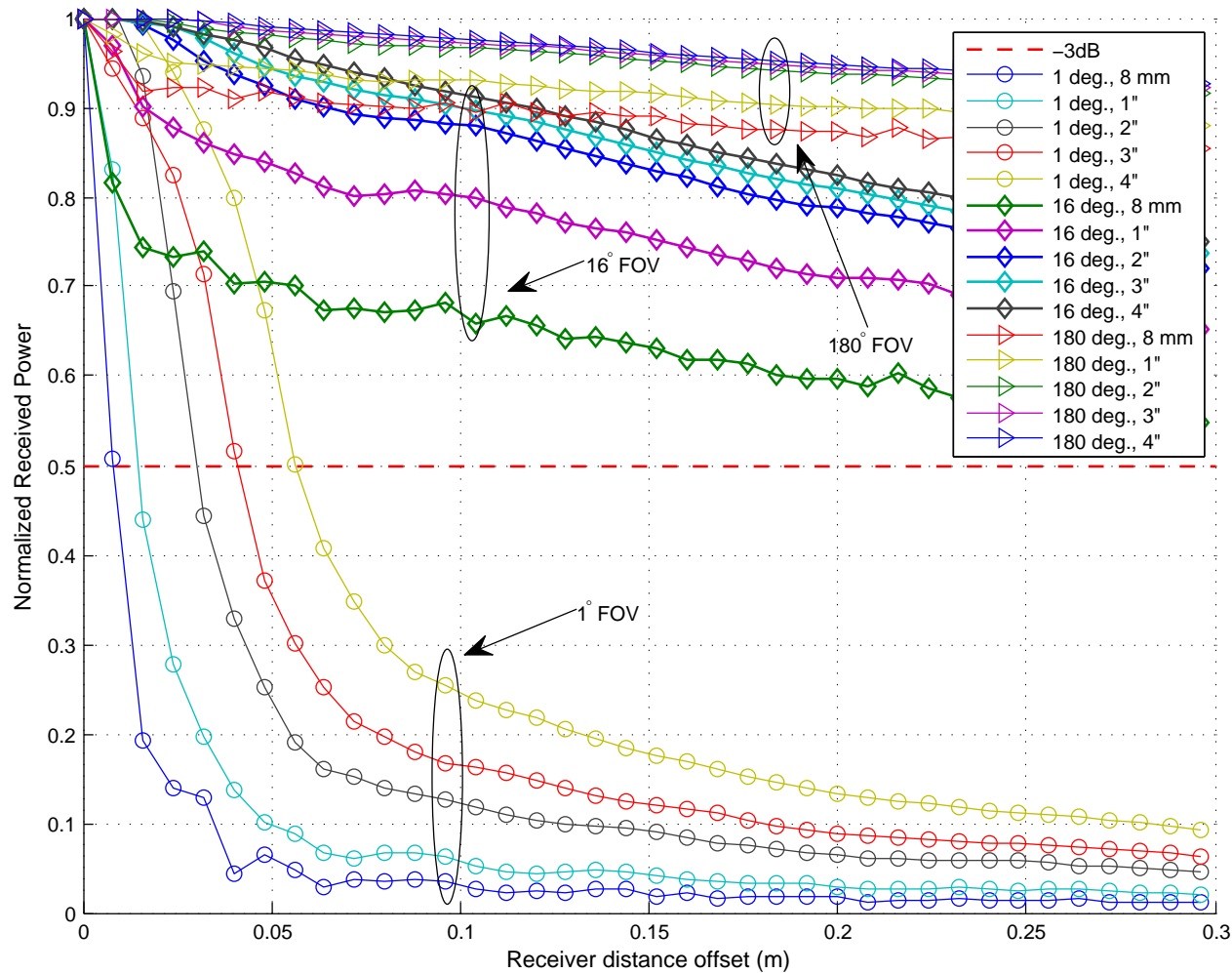


Figure 5.85: Normalized received power for various apertures and FOV's, at a given offset distance from the center of the transmitted beam. This is for simulated data at 20 attenuation lengths in Harbor II water, or approximately 9 meters distance.

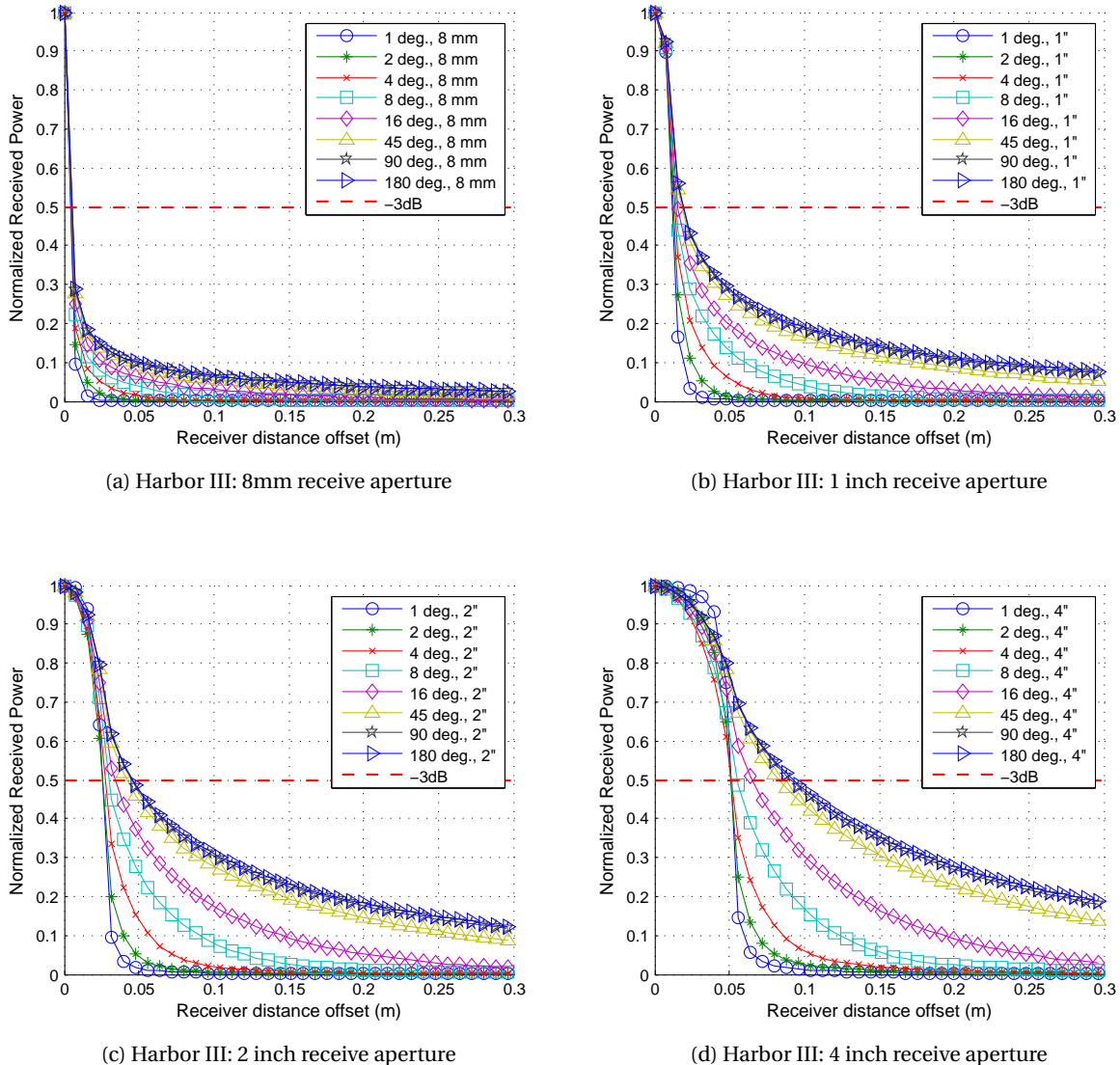


Figure 5.86: Harbor III, 10 Attenuation Lengths: Normalized power received for the given aperture, as it is swept from the beam center (0 offset) to 0.3 meters radial distance from the transmitted beam center.

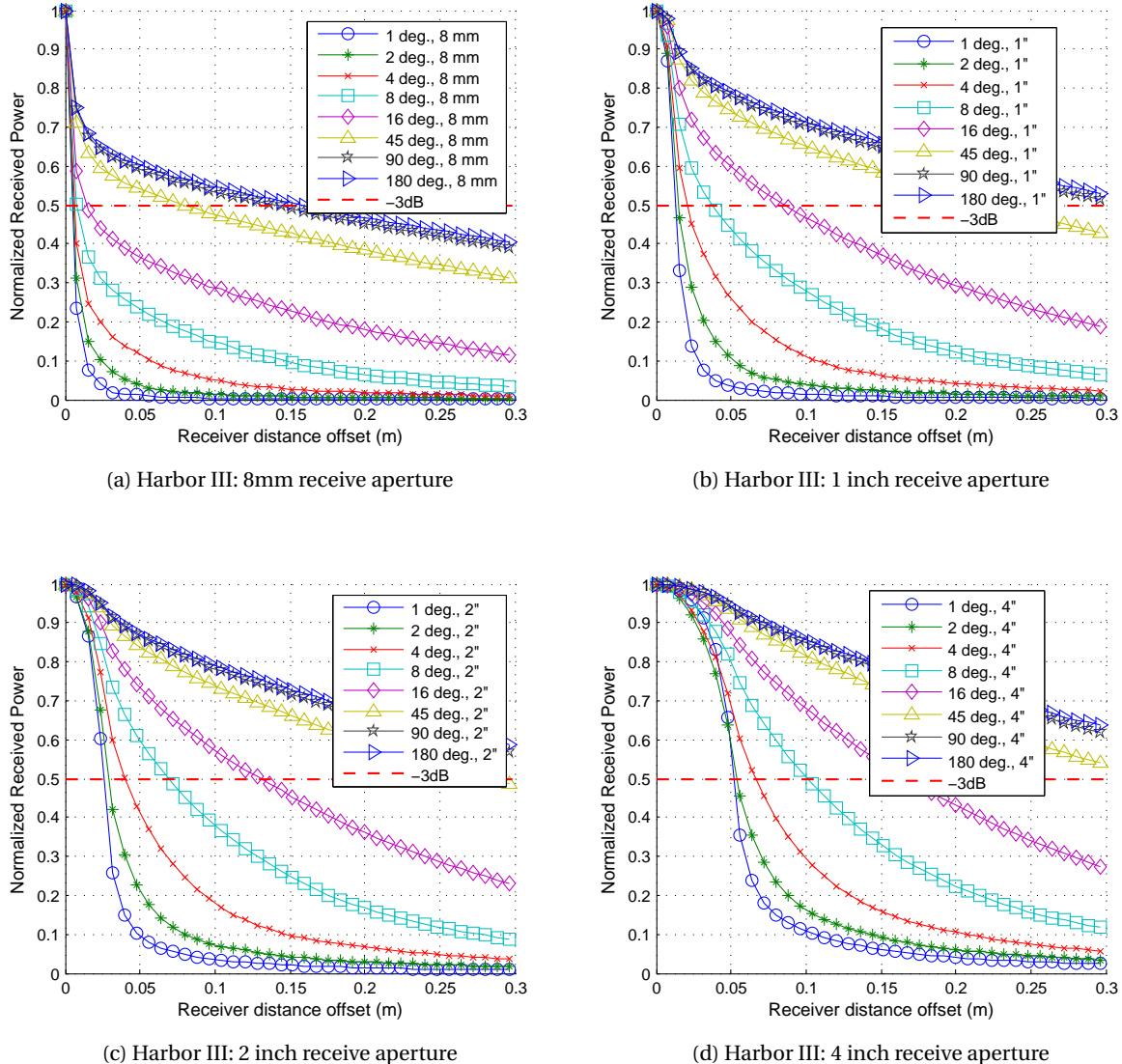


Figure 5.87: Harbor III, 16 Attenuation Lengths: Normalized power received for the given aperture, as it is swept from the beam center (0 offset) to 0.3 meters radial distance from the transmitted beam center.

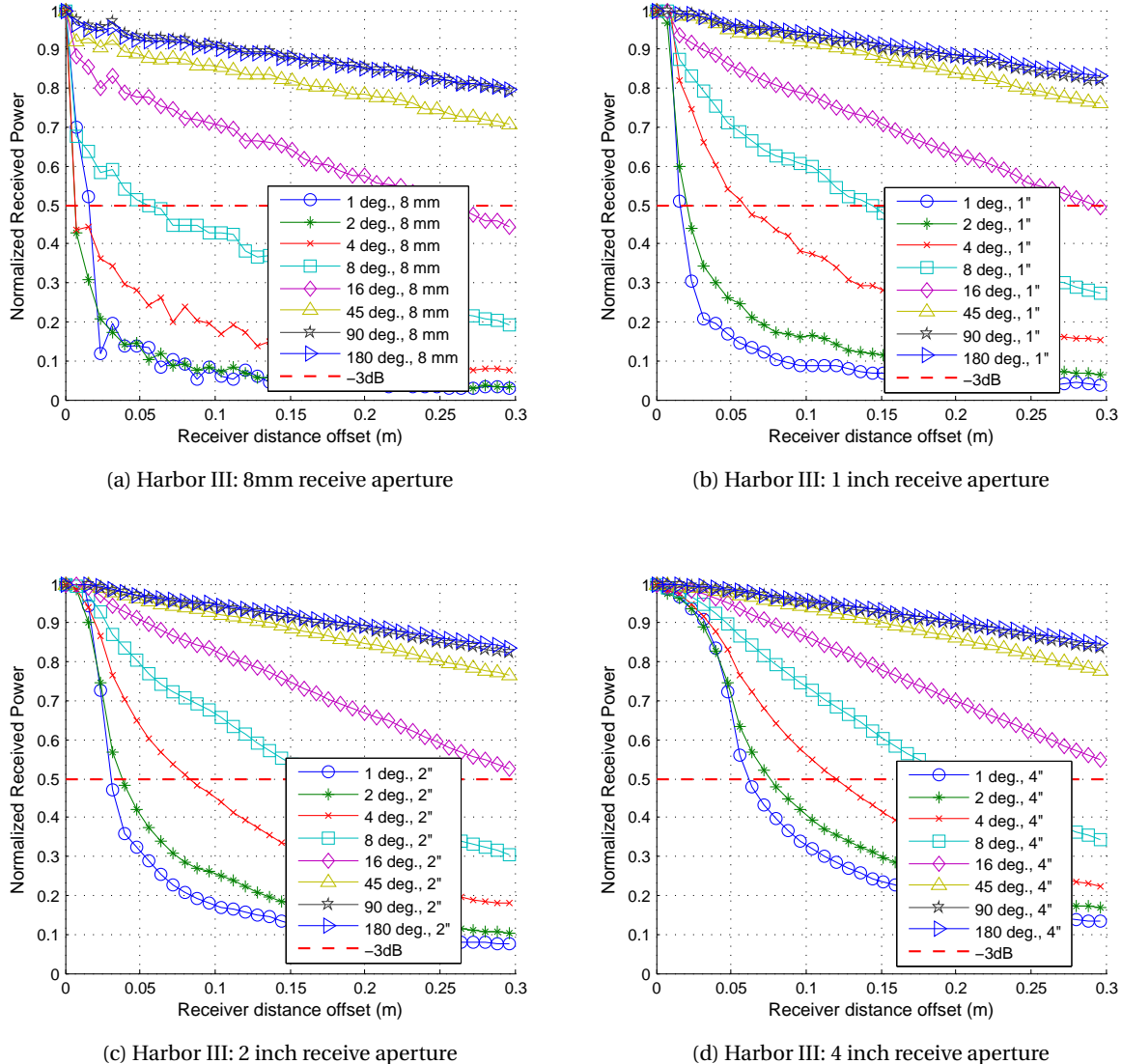


Figure 5.88: Harbor III, 20 Attenuation Lengths: Normalized power received for the given aperture, as it is swept from the beam center (0 offset) to 0.3 meters radial distance from the transmitted beam center.

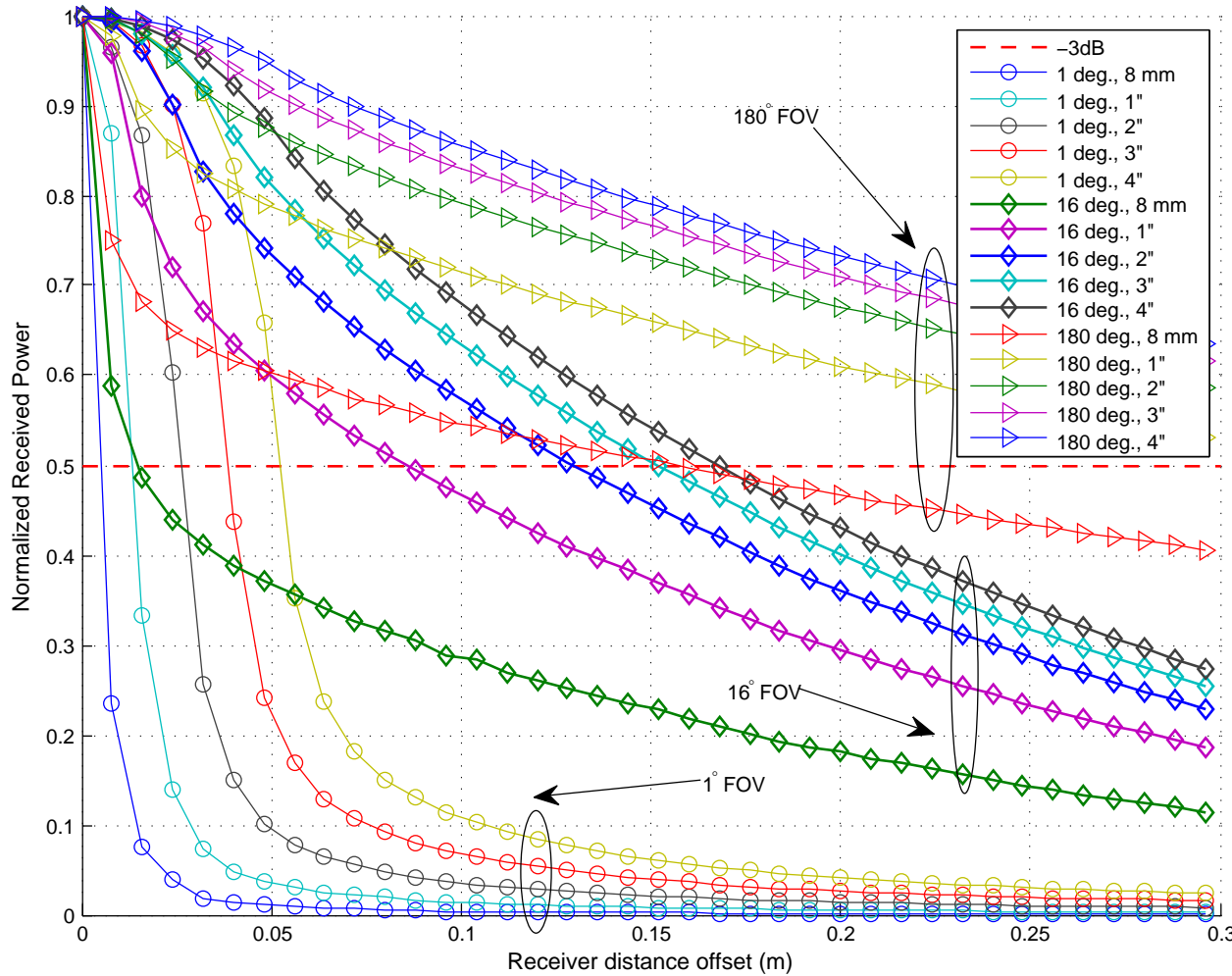


Figure 5.89: Normalized received power for various apertures and FOV's, at a given offset distance from the center of the transmitted beam. This is for simulated data at 16 attenuation lengths in Harbor III water, or approximately 4.5 meters distance.

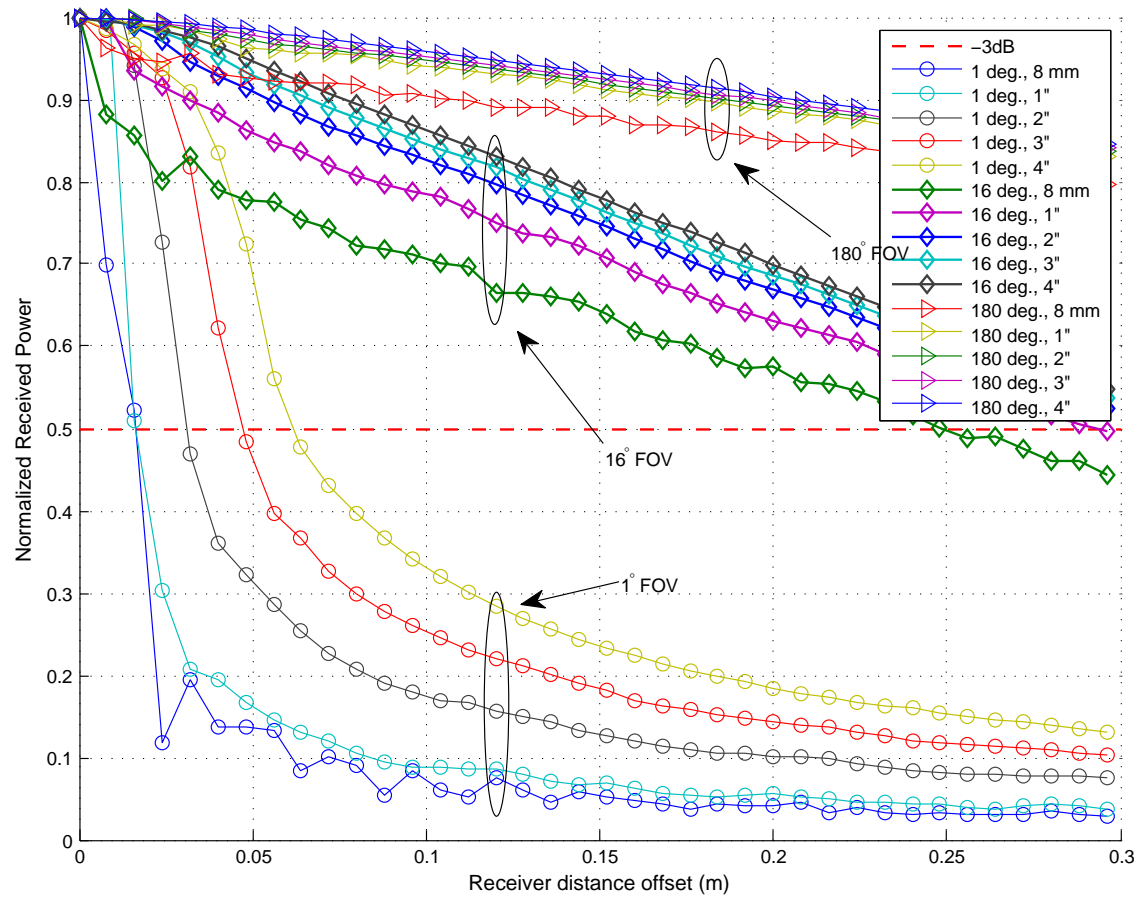


Figure 5.90: Normalized received power for various apertures and FOV's, at a given offset distance from the center of the transmitted beam. This is for simulated data at 20 attenuation lengths in Harbor III water, or approximately 4.5 meters distance.

5.11 Conclusion

In conclusion, this chapter presented simulated results for a variety of communication situations in natural waters. These included received power for Harbor, Clear and Coastal water, the scattering orders of received photons, temporal data for channel bandwidth, and finally the received power for offsets in the receiver. These results are summarized below.

5.11.1 Received Power Conclusion

The received power for a variety of receiver arrangements was presented in Section 5.4. These included both Harbor and Clear/Coastal waters. The Harbor waters were subdivided into three categories, each with a different c value, representing increasing turbidity, while the albedo of the water was constant at 0.83, which represented a highly scattering environment. A series of plots showing the absolute normalized received power versus distance was shown. These plots showed a strong dependence on FOV and aperture when comparing the total received power. This is not unexpected, and predicted by link budget equations, such as are developed in Chapter 6, however the shapes of the curves are somewhat surprising, in that they tend to deviate significantly from Beer's-Law type loss at higher attenuation lengths. Due to the collection of multiply scattered light, which was seen in Section 5.8, the total received power begins to approach the limit of pure absorption, especially for the receivers with a larger FOV and aperture, as many scattered photons are still received. For the very small FOVs, the received power tended to be very close to Beer's Law-type loss, with some gains coming from the increased aperture size, as this would still collect single-scattered photons (as explored in Section 6.4).

When comparing the received power at a fixed attenuation length, as shown in Fig. 5.25 - Fig. 5.36, there is a clear indication, at higher attenuation lengths, that there is a power-law response to increasing the FOV of the receiver. It also appears that there is nearly a linear relationship between received power and the area of the receiver. This is shown more in Fig. 5.37 - Fig. 5.39, which shows how the intensity (W/m^2) of the received signal is the same for various apertures at high attenuation lengths. At lower attenuation lengths, the intensity for a greater apertures is less, because the beam is still well collimated and confined to the receiver aperture. In this case, increasing the area of the receiver causes little gain in the received power. Both of these facts can be used to help develop a theoretical model for the received power.

Coastal and Clear waters were shown in Section 5.5 and Section 5.6. These were for an albedo of 0.55 and 0.25 respectively, and for attenuation coefficients, c of 0.40 m^{-1} and 0.15 m^{-1} respectively. Coastal water has approximately $1/10^{th}$ of the attenuation of Harbor III-type waters, and Clear water has approximately $1/10^{th}$ the attenuation of Harbor I-type waters.

The results show that for Clear and Coastal waters the strong bend in the received power, seen in Harbor waters, is not present. This is predicted, in part, by the higher diffusion length (see Section 3.5.2) in these type waters (31 attenuation lengths) as opposed to Harbor-type waters (15

attenuation lengths). Also, due to geometric losses from the much longer transmission distances the actual received power can be less than predicted by Beer's Law. This is accentuated for smaller apertures and longer distances (like Clear water compared to Coastal water).

5.11.2 Scattering Orders Conclusion

By using a Monte Carlo numerical simulation, a statistical picture of how many times a photon scatters before it is received can be produced. This is a unique feature of a Monte Carlo simulation, as opposed to an analytical solution, which practically would only produce a mean value for the scattering orders. While not relating directly to the important question of received power, a picture of how the statistical properties of how photons scattering can tell us a few things about the channel. This could be especially useful if we wished to build a statistical picture of the polarization of photons, as each scattering event will rotate the polarization vectors. Additionally, each scattering event will tend to increase the distance a photon travels (and thus the time of travel), as the direction vector changes.

Section 5.8 showed the scattering statistics of the Harbor-type water channels for various apertures and FOVs. It is clear that as the attenuation length of the transmission increases, the mean value of the scattering PDF increases, with the peak for 10 attenuation lengths being near 0. This means that the largest percentage of received photons were ballistic, with the peak moving to near 10 scattering events at 16 attenuation lengths. For 20 and 25 attenuation lengths the peak number of scattering events moved to 15 and 20 scattering events, respectively. Additionally, even at 10 attenuation lengths for the largest FOV case, the peak of the PDF is around 2-4 scattering events, showing that even at these "low" attenuation lengths there can be a significant amount of scattering.

The figures in Fig. 5.59 - Fig. 5.62 show that the scattering probability densities change very little between the Harbor I, II and III types of water. Fig. 5.63 illustrates a zoomed view of the 10 c_z scattering orders for various water types and shows similarities, with the multiple scattering orders being accentuated for the higher turbidity water. This is mostly likely due to the fact that at lower turbidities, scattering will tend to distribute the light over a larger area (due to the longer propagation distance), and as such, these multiple scattered photons will be less likely to intersect the receiver aperture.

Perhaps one of the most striking aspects of these plots is the large number of scattering events that take place on the received photons. At 25 attenuation lengths, with a large FOV, the average number of scattering events can approach 20. This is one of the reasons why the water albedo has such a strong affect on the received power, as at each optical event the water albedo effectively "selects" whether a photon will be scattered or absorbed, so whereas in strongly scattering water these photons can arrive at the receiver, in more absorbing water they are much less likely to propagate without being absorbed.

5.11.3 Temporal Dispersion Conclusion

Since each photon is tracked individually, the total transit distance, and thereby transit time, can easily calculated for each simulation output. This enables the simulation to compute the temporal response of the channel. The temporal response is integral to understanding the channel bandwidth and how the channel will spread information pulses in time. A common method to analyze this temporal response is to measure it in the frequency domain.

The precision of the temporal response measurements determine the window over which the frequency response can be estimated. As discussed in Section 5.9 by choosing smaller measurement bins the frequency response can be estimated to a larger maximum frequency. This has to be balanced with the number of simulated photons, as many bins will contain no values. The simulation frequency response estimates were estimated to a maximum frequency of 1.8 GHz. The results show that for small FOVs, the frequency response generally extends past 1.8 GHz, while the FOVs greater than 45° exhibit -3 dB frequency points down to 50 MHz, depending on the water quality. The more turbid the water, the lower the frequency response, as scattering causes temporal spread. Also seen in the results for the temporal spread of the data is that increasing the size of the aperture has little effect on the frequency response of the system. The FOV seems to be the controlling factor for determining the system bandwidth (other than the detector and receiver's bandwidth).

5.11.4 Received Power with Receiver Offset Conclusion

Another aspect of the simulation is the ability to choose the location and angles of the transmitter and the receiver. This allows simulated results to be computed for off-axis rx/tx alignment or for angular mismatch. This is important to understand as angular or lateral offsets will cause drops in signal power, which need to be accounted for in a proper system design.

The results in Section 5.10 show the effects moving the receiver off-axis from the transmit beam. The simulations results are corollary to the theoretical derivations for off-axis received power shown in Section 6.1. For Gaussian transmit beams with a small divergence, the power drops off quickly as the receiver moves away from the central beam. The scattering of light in turbid Harbor waters, along with the geometric beam spreading at longer distances (in Clear and Coastal waters) alleviates this effect somewhat, however Table 5.5 shows the angular requirements imposed on the transmitter in order to keep the receiver within the 3 dB loss region.

The receiver's aperture plays a large role in the degree to which offset distances reduce the received power, as the larger aperture effectively “averages” over the power loss curve. Additionally, the receiver's FOV plays a large part in how much power is received as the receiver transitions from the beam's center. In harbor waters at large distances (e.g. > 20 attenuation lengths) the lightfield is nearly homogeneous in regards to small distance offsets, and a larger FOV receiver is able to maintain a quality link with a large degree of distance offset. The smaller FOVs do not fare as well, as they tend

to reduce the reception of large angle photons caused by multiple scattering.

CHAPTER 6

Link Equation for Underwater Optical Communication

Determining a correct link equation is a difficult task due to the variable nature of the underwater channel, as we have seen in Chapter 5. Additionally, the detection method, such as direct detection, subcarrier coherent detection or optical coherent detection, will affect the SNR at the detector, which will fundamentally affect the ability to detect a signal. Finally, some assumptions about the size of the beam at the receiver must be made in order to determine the received power, along with the type of light source – diffuse point source, modified Lambertian, or Gaussian beam, for example.

A link equation will take into account all signal gains and losses to determine the received signal-to-noise ratio, which gives indication of how well the system will perform in a variety of situations. We will take into account received signal power using analytical models and the simulation results from Chapter 5, along with sources of noise, such as environmental light sources and electrical noise sources. Finally, the ratio of signal-to-noise power will be used to derive bit-error-rate (BER) equations for various modulation formats.

6.1 Received Power

A link equation describing the received optical power can be expressed as

$$P_{rx} = P_{tx} \tau_{optics} \tau_{channel} \tau_{pointing} \tau_{geo} \quad (6.1)$$

where τ_{optics} is the loss from the receiver and transmitter optics, $\tau_{pointing}$ is the loss from angular and spatial mismatch between transmitter and receiver, $\tau_{channel}$ is loss from absorption and scattering, and τ_{geo} is the geometric loss described below. The conversion between electrical and optical power

at the transmitter and receiver will be covered in Section 6.2.2.

6.1.1 Diffuse Point Source

To determine the received power from any source, we begin by defining the power of the transmitter in the far field in terms of Watts/m². This value, known as “irradiance” can be expressed as

$$I_{rx} = \frac{P_{tx}}{A_{tx}} \quad (6.2)$$

where A_{tx} is the surface area of the lightfield at the measurement distance and P_{tx} is the transmitted power in Watts.

For a point source, we can express A_{tx} as

$$A_{tx} = \pi R^2 \tan(\theta/2)^2 \quad (6.3)$$

where R is the distance from the transmitter to the receiver plane, and θ is the full angle of the transmitter optics.

By using the first order approximation of tangent from its Taylor series($\tan \theta \approx \theta$), we arrive at the equation

$$A_{tx} = \frac{\pi}{4} (R\theta)^2. \quad (6.4)$$

The power at the receiver will be the ratio of the area of the light field at the receiver distance and the area of the receiver aperture. The receiver power for a diffuse point source is therefore expressed as

$$P_{rx} = \frac{P_{tx} D_{rx}^2}{(R\theta)^2}. \quad (6.5)$$

The term, $D_{rx}^2/(R\theta)^2$ can be thought of as a loss term expressing the geometric loss of the system. We will call this τ_{geo}

$$\tau_{geo} = \frac{D_{rx}^2}{(R\theta)^2} \quad (6.6)$$

which applies for a homogeneously illuminated receiver surface [83].

Assuming that the beam irradiance is uniform over the receiver aperture, a simple approximation of the pointing loss is expressed by

$$\tau_{pointing} = \cos \phi \quad (6.7)$$

where ϕ is the angle the incident beam makes with the surface normal of the receiver aperture [81].

This equation assumes that the beam is incident on the receiver aperture and that there is no distance offset between the beam and the receiver. In this case, the equation becomes more complicated and is a function of the beam profile.

6.1.2 Generalized Lambertian Source

For a transmitter with azimuthally symmetric transmission pattern, the geometric loss is given by

$$\tau_{geo} = \begin{cases} \frac{A_{rx}}{R^2} \Psi_0(\phi) & \text{if } 0 < \phi \leq FOV/2 \\ 0 & \text{if } \phi > FOV/2 \end{cases} \quad (6.8)$$

where $\Psi_0(\phi)$ is the azimuthally symmetric polar angle distribution of radiant intensity, in W/sr, and normalized such that $2\pi \int_0^\pi \Psi_0(\phi) \sin \phi d\phi = 1$, and FOV is the full angle field of view of the receiver [84]. For a receiver with a non-imaging optic in front, such as a compound parabolic concentrator, Karp et al. [84] has equations for adding the gain term into the geometric loss equations.

For a generalized Lambertian radiant intensity light source, $\Psi_0(\phi)$ can be approximated as

$$\Psi_0(\phi) = \frac{m+1}{2\pi} \cos^m(\phi) \quad (6.9)$$

[84, 85] where m is related to the transmitter's semi-angle at half-power, modeled as

$$\cos^m \phi_{1/2} = 0.5 \quad (6.10)$$

where $\phi_{1/2}$ is the angle at which power falls to half its peak value [83]. This yields the following equation for m

$$m = -\frac{\ln 2}{\ln(\cos \phi_{1/2})}. \quad (6.11)$$

In practice, this number, m , ranges from 1, for a $\phi_{1/2}$ of 60° , to 20, for a $\phi_{1/2}$ of 15° . In other words, m functions as a directional gain term.

Thus, for a generalized Lambertian source the geometric loss between receiver and transmitter is

$$\tau_{geo} = \begin{cases} \frac{m+1}{2\pi} \frac{A_{rx}}{R^2} \cos^m \phi_{tx} \cos \gamma_{rx} & \text{if } 0 < \phi_{tx} \leq FOV/2 \\ 0 & \text{if } \phi_{tx} > FOV/2 \end{cases} \quad (6.12)$$

where the geometry is illustrated in Fig. 6.1, ϕ_{tx} is the transmitter offset angle, and γ is the receiver angular misalignment.

6.1.3 Gaussian Beam Received Power

For Gaussian beams the geometric losses are similar to Eq. 6.8, in that the amount of the source irradiance falling on the receiver aperture, controlled by the source's angular distribution, is what defines the geometric loss of the system. For laser systems, however, the power spread can be much smaller than LED systems, and as such, the calculations for aperture offsets become more complicated, since we cannot assume that the aperture area is small compared to the transmitted beam area.

For a Gaussian beam, the loss equation is defined as

$$\tau_{geo,Gaussian} = 1 - \exp\left(-\frac{2r^2}{W(z)^2}\right) \quad (6.13)$$

where r is the aperture radius, $W(z)$ is the beam width at a distance z , which is approximated as $\phi_{diverg} z$ due to the beam divergence angle, ϕ_{diverg} . This equation holds for an on-axis receiver, however if the receiver is moved off-axis, this loss equation becomes more complicated. A plot showing τ_{geo} for on-axis Gaussian beams is shown in Fig. 5.3.

To compute the off-axis received power from a Gaussian beam, we consider a Gaussian beam whose center is distance d from the center of an aperture of radius r , the received power in the aperture is calculated by

$$\tau(d; z)_{geo,Gaussian} = \int_{-r}^r \int_{-\zeta}^{\zeta} \frac{2}{\pi W^2(z)} \exp\left(-2 \frac{(x' - d)^2 + y'^2}{W^2(z)}\right) dy' dx' \quad (6.14)$$

where $\zeta = \sqrt{(r^2 - x'^2)}$ and $W(z)$ is the beam width on the receiver plane. An approximation, and method of calculation is proposed in [86], and given by the equations

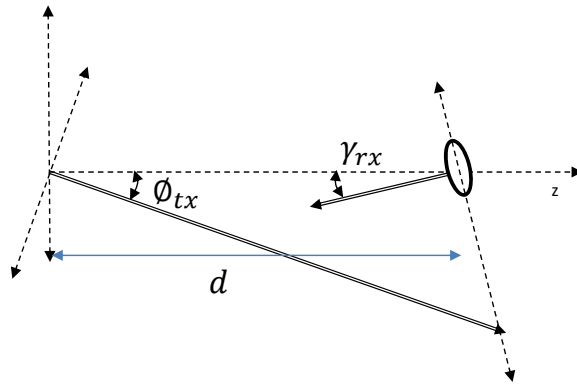


Figure 6.1: Diagram showing the geometry of the receiver and transmitter. The receiver's area is reduced by the cosine of its pointing angle, and the source's intensity is determined by the angle between it and the receiver.

$$\tau(d)_{geo,Gaussian} \approx A_0 \exp\left(-\frac{2d^2}{w_{eq}^2}\right) \quad (6.15)$$

$$v = (\sqrt{\pi}r)/(\sqrt{2}W(z)) \quad (6.16)$$

$$A_0 = [\operatorname{erf}(v)]^2 \quad (6.17)$$

$$w_{eq}^2 = W^2(z) \frac{\sqrt{(\pi)\operatorname{erf}(v)}}{2v \exp(-v^2)} \quad (6.18)$$

where $W(z)$ is the beam waist on the receiver plane and d is the radial distance between the receiver center and the beam center. This equation does not take into account angular differences between the receiver plane and the transmit plane, but it is common to reduce the aperture area by the cosine of the offset angle. This equation also does not hold very well when the Gaussian beam waist is less than the aperture radius. Best agreement is for a $W(z)/r > 6$.

Eq. 6.14 can be evaluated using numerical integration in MATLAB or similar program.

6.1.4 Channel loss

The channel loss is a combination of absorption and scattering. These are expressed in terms of two commonly used coefficients, a and b , which are in units of m^{-1} . These terms are generally combined to form the total attenuation coefficient, c which also has units of m^{-1} . c is used to express the exponential loss in the channel due to absorption and scattering. This equation is commonly known as Beer's Law and is dependent on the scattering coefficient and the transmission distance. This loss model is discussed in Chapter 3, and as shown in Chapter 5 represents the minimum loss for the channel. In practice, for water types that are highly scattering, this underestimates the actual received power by a significant amount. Beer's Law is defined as

$$\tau_{channel} = \exp(-cR) \quad (6.19)$$

where R is the transmission distance and c is the attenuation coefficient. The combined term, cR is a unit-less term known as the "attenuation length". Each attenuation length represents a loss of $\exp(-1)$ or approximately 63%. Expressed in terms of dB

$$dB_{loss} = 10 \log_{10}(\exp(-cR)) = -4.34(cR). \quad (6.20)$$

The Beer's Law-type loss assumes that no scattered photon ever returns to the receiver. This assumption is only valid for certain types of links. This can be viewed as a maximum loss as photons that are scattered back into the beam will only contribute to the power. It should be noted, however, that such photons may contribute to pulse spread which could certain types of communication links.

Combining these terms we can arrive at a minimum receiver power statement for a diffuse point source, such as an LED.

$$P_{rx} = P_{tx} \frac{\tau_{optics} \exp(-cR) \cos \phi D_{rx}^2 \cos \gamma_{rx}}{(R\theta)^2} \quad (6.21)$$

6.1.5 Ocean water measurements for channel loss

Some of the most comprehensive measurements of ocean quality have reported optical attenuation in terms of the diffuse attenuation coefficient, due to its ease of measurement. This value underestimates the amount of attenuation for a collimated beam and therefore a conversion must be made between the diffuse attenuation coefficient, k , and the attenuation coefficient, c . Unfortunately this conversion is not straightforward since k is measured using the solar radiation propagating through the water. As such, variations of zenith angle and cloud cover affect these numbers. Various conversions have been suggested (see [87, 88] for examples).

Fig. 6.2 shows the ratio of k to c versus the scattering albedo of the water [88]. It is parameterized by g , which is a measure of how strongly the scattering phase function is forward peaked. g is typically >0.9 for natural waters [89]. From this plot it is evident that the attenuation coefficient, c , is 1 (for “typical Mediterranean”) to 5 (for “dirty lake”) times greater than k .

Knowledge of the diffuse attenuation coefficient allows us to use many sources of ocean information, including the comprehensive work done by Jerlov in the 1970’s [90]. Fig. 6.3 illustrates how various water types have different wavelength dependent diffuse attenuation coefficients. The water classes that Jerlov assigned range from I (cleanest) to III (dirtiest) and from 1 to 9 (odd numbers only) for coastal waters. Fig. 6.3 shows these values.

Fig. 6.4 shows a global map of various water types. These values allow a system designer to determine approximately the amount of attenuation that the channel will impose on the optical signal [91]. For example, at 400 nm the diffuse attenuation coefficient is $\sim 0.04 m^{-1}$ for ocean type I. For albedos between 0.6 and 0.7, the ratio of k/c would range from ~ 0.4 to 0.5 , giving approximate c values ranging from $0.1 m^{-1}$ to $0.08 m^{-1}$. These values would be good starting points for a channel loss estimate of a system operating in the mid-Pacific.

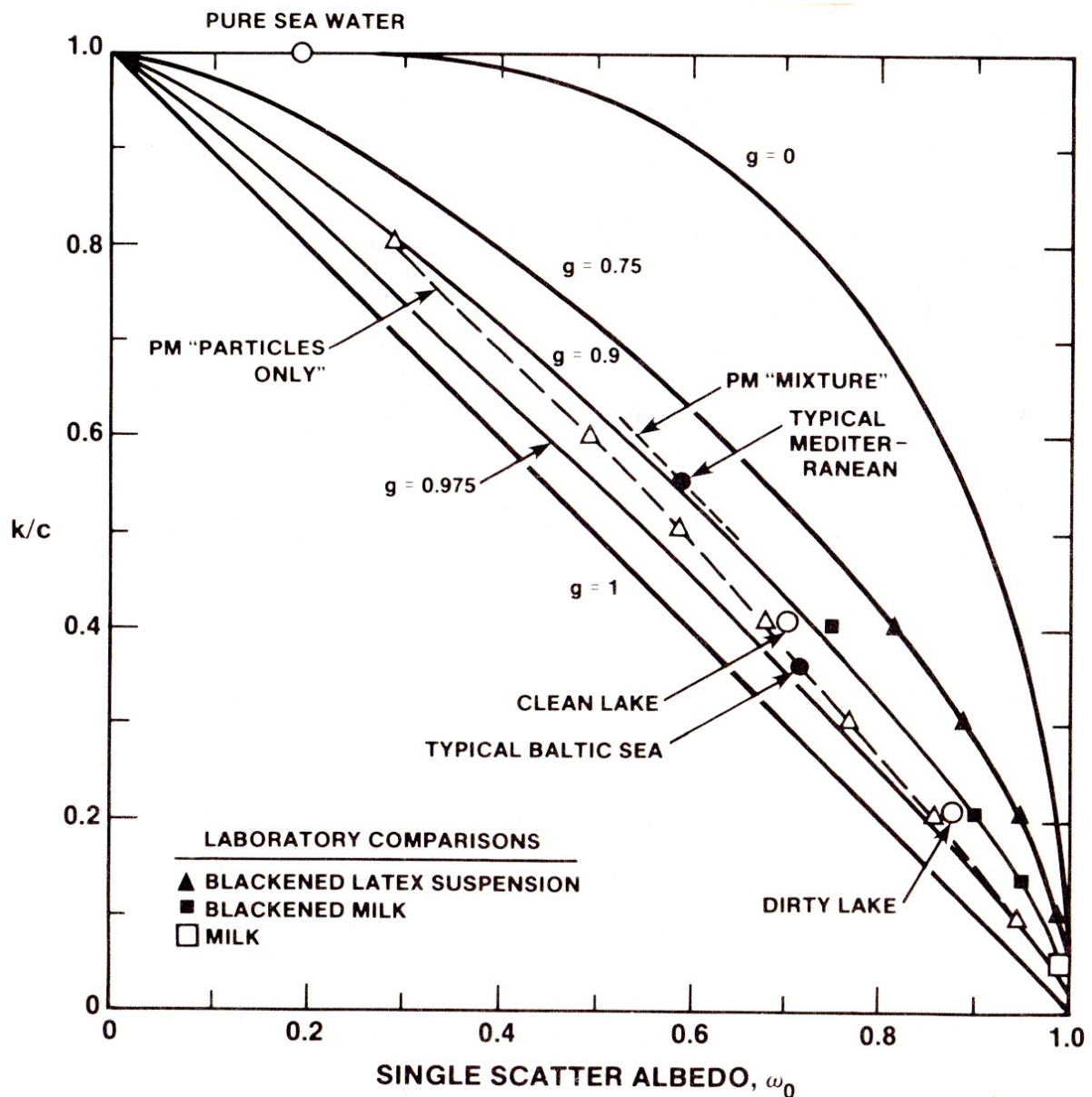


Figure 6.2: The ratio of k and c vs. the water albedo. Various water conditions are indicated on the chart [88].

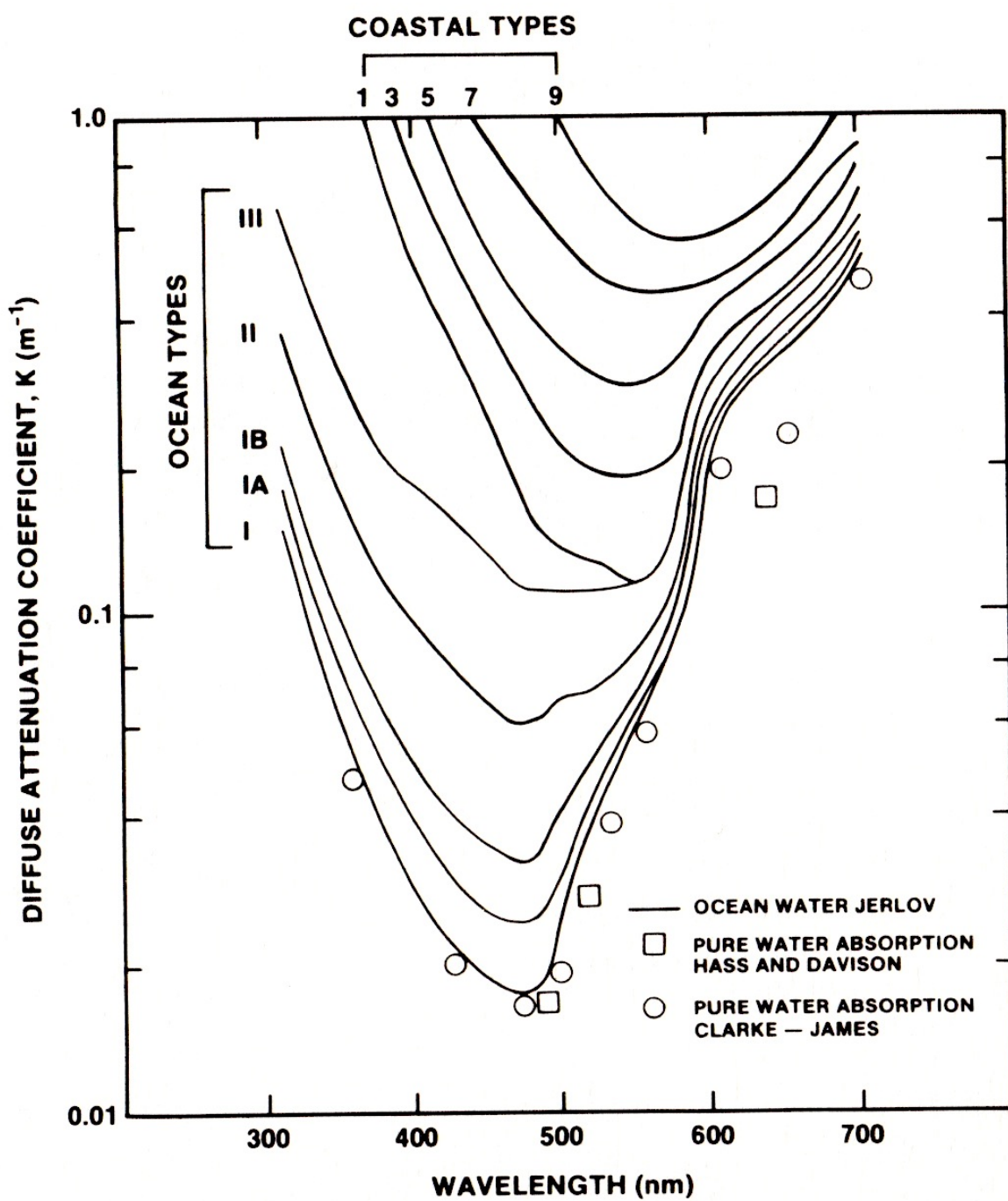


Figure 6.3: Plot of diffuse attenuation coefficient vs. wavelength for various Jerlov water types [90].

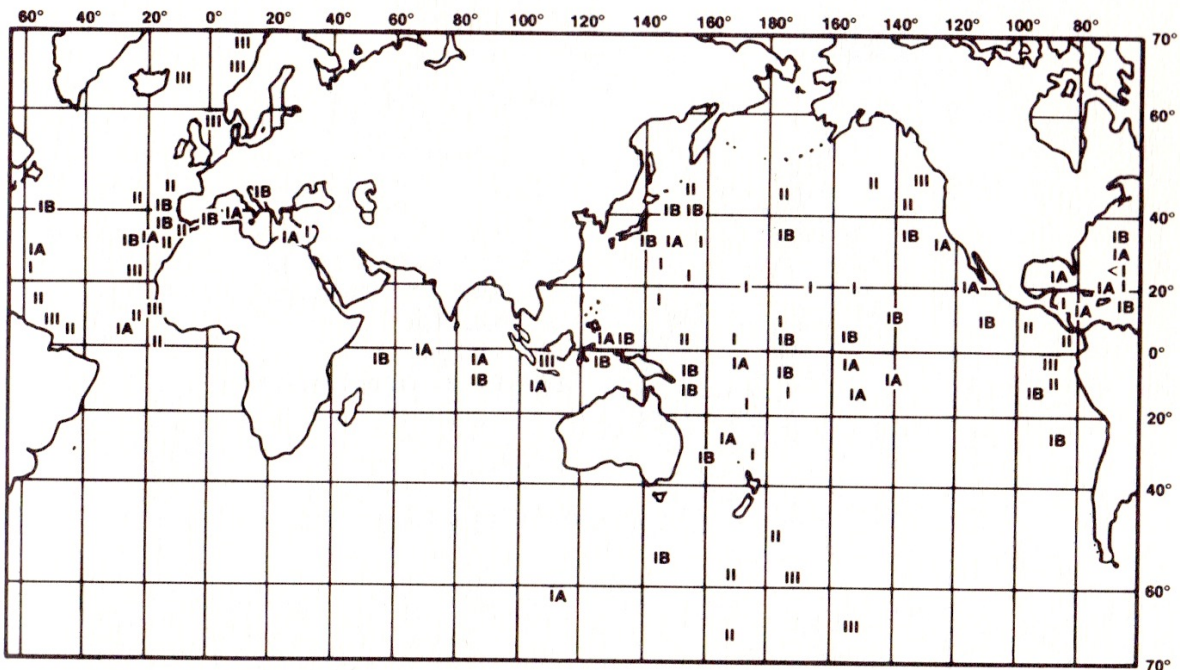


Figure 6.4: World map showing water conditions [90].

6.2 Receiver Noise

Receiver noise is determined by both water conditions and receiver hardware. Diffuse radiation from sunlight, receiver dark current and thermal noise all contribute. Environmental noise is determined by operating depth and receiver FOV, while other noise sources are dependent on the specific type of detector used.

6.2.1 Environmental Optical Background Noise

Environmental noise is primarily caused by diffuse solar radiation penetrating into the ocean water. Below the depth of solar penetration bioluminescence can contribute to the noise, but will not be considered here. The solar radiance in $\text{W}/(\text{m}^2 \text{ sr nm})$ is given by [91]

$$L_{sol}(\lambda) = \frac{1}{\pi} E_d R_d L_{fac} e^{-K_d D} \quad (6.22)$$

where E_d is the downwelling irradiance in $\text{W}/(\text{m}^2 \text{ nm})$, R_d is the downwelling reflectance, L_{fac} is a direction dependence factor, K_d is the diffuse attenuation coefficient, and D is the operating depth. This is a function of wavelength. Typical values for L_{fac} range from 1 while looking straight down (180 degrees from upward surface normal) to 2.9 at 90 degrees and 333 for straight up at 532 nm [91]. These values are also dependent on the operating depth, along with the absolute depth at which the system is operating. In reality, the equation for L_{sol} is quite complicated for regions near the ocean surface or ocean floor. Mobley [92] contains useful information on arriving at the asymptotic radiance distribution, which only depends on the polar angle, θ .

Data from [93] suggests that it may require up to 20 diffuse attenuation lengths before a truly asymptotic solar radiation distribution is reached. Until that point, the angular peak of radiance is in the direction of the sun's refracted rays. At shallow depths the proportional difference in radiance between an upward and downward looking system can be several thousand, while the difference is a factor of a few hundred at depths where the asymptotic lightfield distribution has been reached. Fig. 6.5 shows this behavior [93].

To compute the received background power, the solar radiance is multiplied by the receiver FOV (in steradians), optical filter bandwidth, and receive aperture [94]

$$P_{sol} = L_{sol}(\lambda) 2\pi (1 - \cos \theta_{fov/2}) \Delta\lambda_{filter} \frac{(\pi D_{rx})^2}{2} \tau_{optics} \quad (6.23)$$

where $\theta_{fov/2}$ is the half-angle field of view, $\Delta\lambda_{filter}$ is the width of the optical filter in nm, D_{rx} is the receive aperture diameter, and τ_{optics} is the efficiency of the receiver optics. Using the 2nd order approximation of the cosine function, and inserting the full field of view angle, the equation becomes

$$P_{sol} = L_{sol}(\lambda) \Delta\lambda_{filter} \pi \theta_{fov}^2 \frac{(\pi D_{rx})^2}{8} \tau_{optics}. \quad (6.24)$$

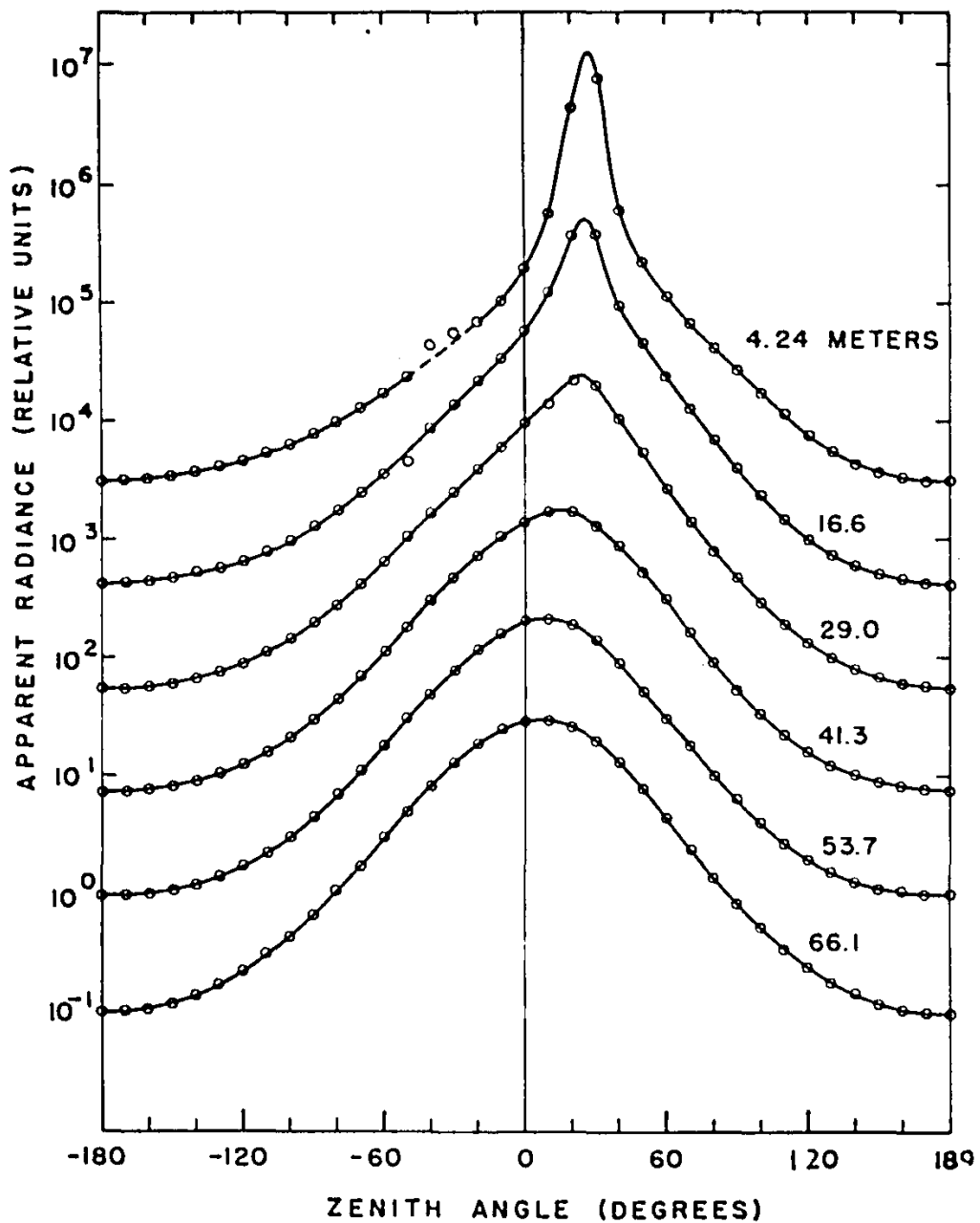


Figure 6.5: Plot from [93] showing underwater radiance distributions in the plane of the sun on a clear, sunny day. Lines show measurements at various depths. 41 meters represents 16 attenuation lengths, and 100 m is 20 attenuation lengths.

Surface solar radiation used to compute the subsea solar irradiance is a complicated process involving the time of year, location on the earth's surface, and atmospheric components. Typical values for visible wavelengths between 400 nm and 532 nm range from 1.2 W/(m² nm) to 1.5 W/(m² nm) [95].

It should be noted that solar radiation almost entirely contributes to the DC power of the noise, while other noise sources are broadband. Therefore, for a bandpass communication channel its contribution would be to lower the dynamic range of the system, and not necessarily directly add to the system noise.

6.2.2 Electrical Noise

The choice of detector determines the amount and type of electrical noise in the system. Three common choices are amplified photodiode, avalanche photodiode or a photomultiplier tube. The latter two choices are valued for their large gains, but are expensive and require high voltage power supplies. The electrical noise will only be considered for direct-direction receivers.

Detector signal current can be expressed by [96]

$$i_{sig} = \frac{qP_{rx}G_{det}QE}{hv}. \quad (6.25)$$

The detector signal power can then be expressed by

$$P_{sig} = i_{sig}^2 R_L = R_L \left(\frac{qP_{rx}G_{det}QE}{hv} \right)^2 \quad (6.26)$$

where q is the electron charge, P_{rx} is the optical power received, G_{det} is the electrical gain of the detector, and QE is the quantum efficiency of the detector. hv describes the Joules of energy per photon. Noise will come from Schottky shot noise of the signal, background radiation and dark current of the detector, along with thermal noise of the load. Dark current power, and thermal noise power are expressed below in Watts.

$$P_{dark} = 2qG^2 i_d BR_L \quad (6.27)$$

$$P_{thermal} = 4kTB \quad (6.28)$$

where B is the detector bandwidth, R_L is the equivalent load resistance of the detector, i_d is the detector dark current, k is Boltzmann's constant, and T is the detector temperature in Kelvin. Noise from background radiation and shot noise inherent in the signal are expressed by

$$P_{noise_{bg}} = 2qG_{det}i_{bg}BR_L = 2q^2G_{det}^2 \left(\frac{P_{sol}QE}{hv} \right) R_L B \quad (6.29)$$

$$P_{noise_{sig}} = 2qG_{det}i_{sig}BR_L. \quad (6.30)$$

The full noise term can then be expressed as a summation of the various powers, P_{dark} , $P_{thermal}$, $P_{noisebg}$, and $P_{noise-sig}$.

$$P_{noise} = 2qG^2i_dR_LB + 4kTB + 2q^2G_{det}^2\left(\frac{P_{sol}QE}{hv}\right)R_LB + 2q^2G_{det}^2\left(\frac{P_{rx}QE}{hv}\right)R_LB. \quad (6.31)$$

This equation rearranged becomes

$$P_{noise} = 2qG_{det}^2R_LB\left(i_d + \frac{qQE}{hv}(P_{sol} + P_{rx})\right) + 4kTB. \quad (6.32)$$

6.3 Signal to Noise Ratio

Once the signal power and noise power are known, the signal-to-noise ratio is easily derived. The full equation is expressed by

$$SNR = \frac{P_{sig}}{P_{noise}} = \frac{R_L\left(\frac{qP_{rx}G_{det}QE}{hv}\right)^2}{2qG_{det}^2i_dR_LB + 2q^2G_{det}^2\left(\frac{P_{sol}QE}{hv}\right)R_LB + 2q^2G_{det}^2\left(\frac{P_{rx}QE}{hv}\right)R_LB + 4kTB}. \quad (6.33)$$

Simplified, this becomes

$$SNR = \frac{P_{rx}^2R_L\left(\frac{qG_{det}QE}{hv}\right)^2}{2qG_{det}^2R_LB\left(\frac{qQE}{hv}(P_{sol} + P_{rx}) + i_d\right) + 4kTB}. \quad (6.34)$$

Note that this equation may not represent fully the noise component of some devices, such as an avalanche photodiode, as they have an additional noise term contributed by the intrinsic gain of the system. This term expresses the noise generated by the inherent random nature of the gain process. This term is present for both APDs and PMTs. However, for situations where $P_{sig} \gg P_{noise}$, the SNR term collapses into [96]

$$SNR_{P_{sig} \gg P_{noise}} = \frac{P_{rx}QE}{2Bhv}. \quad (6.35)$$

This equation represents the best possible direct direction receiver scenario where the only noise source is the emitted signal photon variance [97]. This can be a useful term for quick calculations, but should be avoided for robust system design considerations.

Using the SNR equations defined above, along with Shannon's equation, a best-case datarate can

be established for the communications link. Shannon's famous equation [98] shows that the link datarate is dependent on the system SNR and bandwidth

$$C = B \log_2(1 + SNR) \quad (6.36)$$

where C is the capacity in bits/sec, B is the system bandwidth and SNR is the signal-to-noise ratio of the link.

For applications where the receiver is photon limited, Majumdar et al. [17] suggests an alternate calculation for maximum bit rate. This equation is

$$C = \frac{P_{rx}}{N_b h \nu} \quad (6.37)$$

where N_b is the receiver sensitivity in photons/bit.

6.4 Modeling Channel Loss

The goal of this thesis is not to create a unified analytical model for channel loss, but it is helpful to distill the results from Chapter 5 into a loss model that can be the basis for future work.

If we were to consider the power loss as a function of two exponentials, one which describes the loss at attenuation lengths less than the diffusion length, and one to describe the loss at attenuation lengths greater than the diffusion length, then we could arrive at the following equation

$$I = I_o \exp(-cr\psi) + \beta \exp(-cr\xi) \quad (6.38)$$

where I and I_o are the final and initial powers, c is the attenuation coefficient, r is the distance between the receiver and transmitter, ψ and ξ are gain terms, and β is the initial power for the diffuse exponential. Intuitively this equation can be thought of as an expression for the initial Beer's Law-like power loss at small attenuation lengths, and then the second term to describe the diffuse power loss from absorption and multiple scattered light. At small attenuation lengths, the 2nd term contributes little to the total power, and at high attenuation lengths, the 1st term contributes little to the total power.

Cochenour [34] notes that the diffuse gain, for turbid water conditions, is contributed from a reduced scattering coefficient, not any change in the absorption of the water, and therefore expresses ξ as $1 - \eta w_o$, where η ranges from 1 to 0. When η is 0, the equation reduces to Beer's Law, while when $\eta = 1$, the loss is expressed as absorption loss only. Making this substitution yields

$$I = I_o \exp(-cr\psi) + \beta \exp(-[1 - \eta w_o]cr) \quad (6.39)$$

which is dependent on three unknowns: ψ , β , and η . The latter two are determined by the lightfield

in highly scattering environments, while the first, ψ is determined by the receiver aperture at small attenuation lengths. Essentially, the receiver's aperture reduces the effects of scattering, since at small receiver/transmitter separations, not all scattered photons are lost, but are merely scattered into the receiver aperture. This effect can be modeled by analyzing the differential loss equation for a differential volume of absorbing/scattering medium.

6.4.1 Modified b value

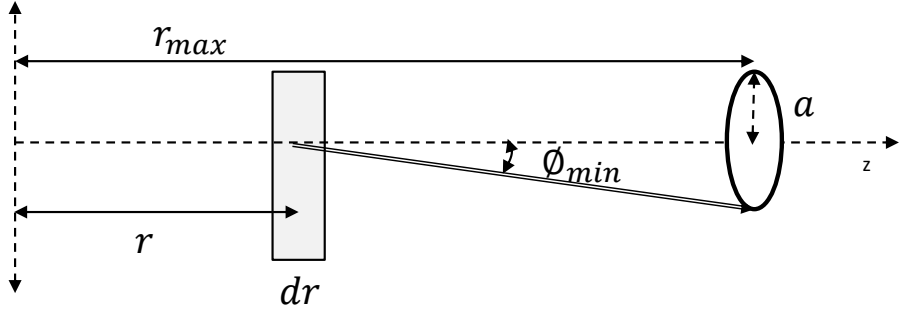


Figure 6.6: Geometry for calculating the modified b value.

As described by Mobley [40], the differential loss over this volume is expressed by

$$\frac{dI}{dr} = -aI - bI \quad (6.40)$$

where a is the absorption coefficient, described as the ratio of transmitted to absorbed power over a differential distance in the medium, and b is the scattering coefficient, described by the following equation

$$b = 2\pi \int_0^\pi \beta(\theta) \sin(\theta) d\theta \quad (6.41)$$

where $\beta(\theta)$ is the volume scattering function, describing the power scattered into a differential volume at a polar angle θ from the incident beam. However, this equation presumes that all polar scattering from $0 < \theta \geq \pi$ is accounted for in this coefficient. However, if the receiver has a finite aperture, some scattering will contribute to the received power. This is illustrated in Fig. 6.6. Instead, this equation should be modified to be

$$b_{mod} = 2\pi \int_{\phi_{min}}^\pi \beta(\theta) \sin(\theta) d\theta \quad (6.42)$$

where ϕ_{min} is the minimum angle for which a scattered photon is counted as a loss. This term is defined by the distance from the aperture, r_{dist} and the aperture radius, a as

$$\phi_{min} = \tan^{-1}\left(\frac{a}{r_{dist}}\right) \quad (6.43)$$

yielding

$$b_{mod}(r_{dist}) = 2\pi \int_{\tan^{-1} a/r_{dist}}^{\pi} \beta(\theta) \sin(\theta) d\theta \quad (6.44)$$

Now, using Eq. 6.44, and substituting b_{mod} for b in Eq. 6.40 yields

$$\frac{1}{I} dI = -a dr - b_{mod} dr \quad (6.45)$$

Integrating both sides results in

$$\ln(I) = -ar - 2\pi \int_{\tan^{-1} a/(r_{max}-r)}^{\pi} \beta(\theta) \sin(\theta) d\theta dr \quad (6.46)$$

since $\int 1/I dI = \ln(I)$, and $r_{dist} = r_{max} - r$, where r_{max} is the maximum separation between receiver and transmitter. It should be noted that this equation only applies to open field-of-views. For a limited FOV the equation would be modified such that the lower limit on the inner-most integration was $\min[FOV/2, \tan^{-1} a/(r_{max})]$.

This allows us to define the 1st term of Eq. 6.39 as

$$I_{ballistic} = \exp(-ar - 2\pi \int_{\tan^{-1} a/(r_{max}-r)}^{\pi} \beta(\theta) \sin(\theta) d\theta dr) \quad (6.47)$$

The results of this integration are such that very small receiver/transmitter ($d_{rx/tx}$) separations the b_{mod} term is greatly reduced, as the scattered light often is captured by the larger aperture, while for larger distances, this only affects the differential losses near the receiver aperture. This is illustrated in Fig. 6.7, which shows the differential b_{mod} value along the transmit path. For the differential distances near the receiver, the b_{mod} value drops as single scattered photons in this area are captured. Also, as the scattering phase function, $\beta(\theta)$ becomes more forward peaked, the b_{mod} term becomes smaller.

When comparing the final loss equation to the original first term in Eq. 6.39, it is clear that the resulting expression cannot easily be reduced to one term, ψ , but must instead be integrated as a whole. It should also be noted that this equation tends to underestimate the total received power, since it only accounts of single scatter events. In practice, as seen by the scattering order plots in Section 5.8 on page 121, even at smaller attenuation lengths, there is multiple scatter received by the aperture. Therefore, in practice, Eq. 6.47 will need to be adjusted higher.

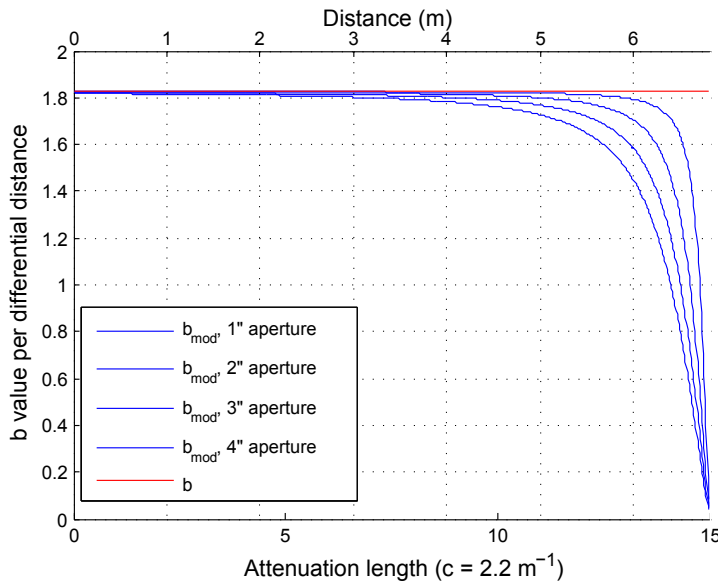


Figure 6.7: Plot showing the modified b value for each differential distance between the receiver and transmitter. For distances close to the receiver, the b value is much smaller, as single scattered photons are still received by the aperture.

6.4.2 Defining turbid water loss

Having discussed the first term of Eq. 6.39, now we should address the two remaining terms, β and η . If we approximate the loss function, such that the intersection of the two exponentials happens at the diffusion length (an appropriate assumption given that that distance marks the transition between generally forward scattering light and diffuse light), we can derive the following expression for β by setting the Beer's Law equation to be equal to the diffuse loss equation

$$I_o \exp(-cr) |_{r=L_d} = \beta \exp(-[1 - \eta w_0]cr) |_{r=L_d} \quad (6.48)$$

where L_d is the diffusion length. Simplifying the equation above yields

$$\beta = I_o \exp(-\eta b L_d) \quad (6.49)$$

where L_d is the diffusion length in meters. In turn, the 2nd term of the power loss equation, Eq. 6.39 becomes

$$I_{diffused} = I_o \exp(-([1 - \eta w_0]cr + \eta b L_d)) \quad (6.50)$$

While this reduces the complexity of the equation to being dependent on only one variable, this variable is in turn dependent on many system design characteristics (FOV, aperture, water type, etc.).

Also, in practice, looking at the simulated power curves in 5.4, it appears that the diffuse exponential term, instead of intersecting with the Beer's Law loss curve, instead intersects with the modified loss term, shown in Eq. 6.47, making the value of β dependent on the integration term.

6.4.3 Model examples

MCNSUsing the dual exponential power loss model defined in Section 6.4, we can solve for the various components using the output data from the MCNS simulation discussed in Chapter 4 on page 17 and following. Fig. 6.8 shows the result of the MCNS simulation for some FOV's and apertures, plotted along with the dual-exponential loss model. The model parameters are calculated by applying an exponential fit to the first five datapoints in the simulation (low turbidity values) and an exponential fit to the last four values in the simulation (high turbidity). These two exponential fits were summed to produce the solutions shown in Fig. 6.8.

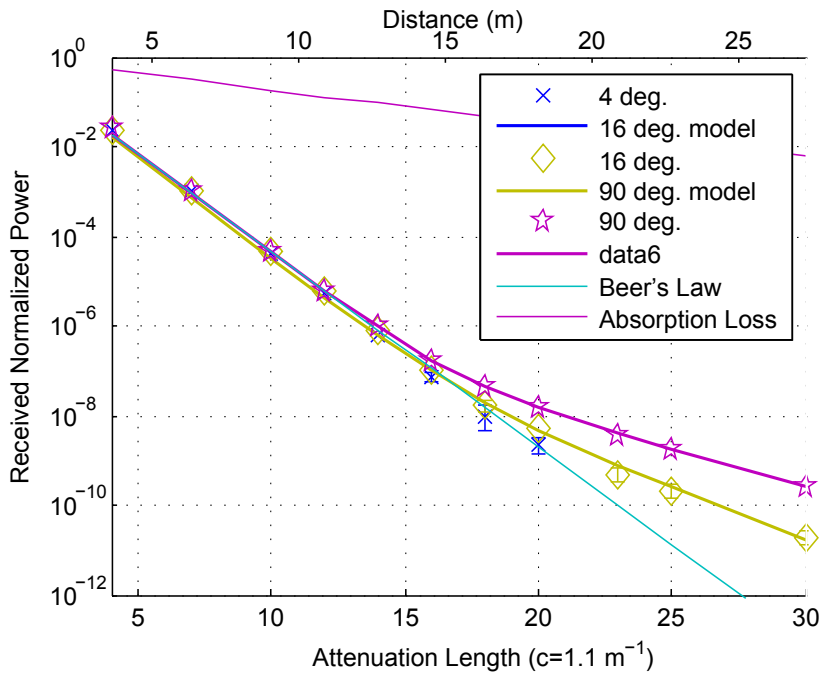
In order to be able to compare accuracy of a model to the truth data, we use a mean absolute percentage error (MAPE) as this functions well over the vast range of values in the simulation output. The equation for the MAPE is

$$Err = E(|\frac{model - sim}{sim}|) \quad (6.51)$$

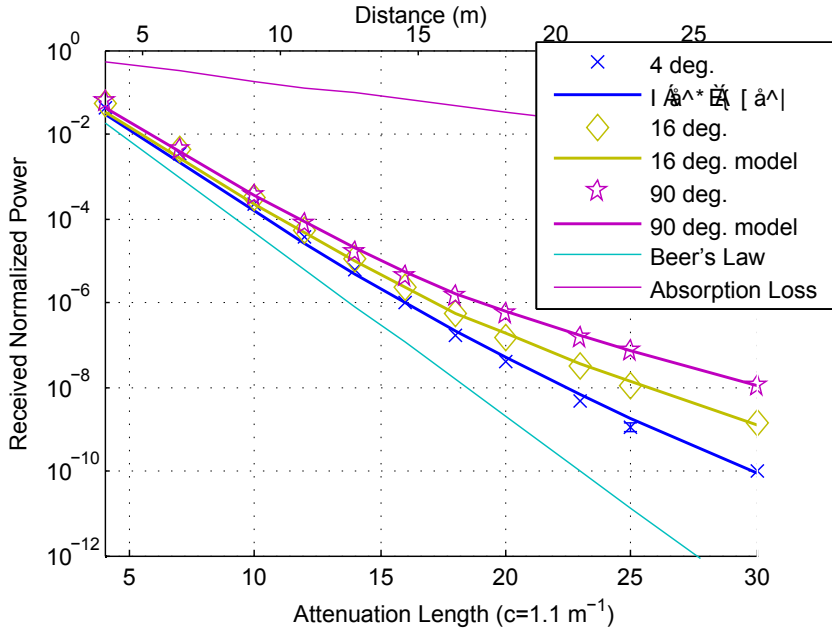
where *model* and *sim* are the outputs from the model and the simulation respectively. Using this equation and the data from the simulation outputs yields the MAPE values shown in Fig. 6.9. The MAPE values for the results in Fig. 6.8 are shown in Table 6.1. The MAPE results shown in Fig. 6.9 show that the values are generally within 20% of the true value, except for FOVs $< 15^\circ$. The higher MAPE's at smaller FOVs appears to be a combination of having noise from lower photon path counts in these regions, along with a less distinct "knee" in the data shape that happens at the diffusion length. Regardless, the model seems to achieve good agreement, especially considering the values range over many orders of magnitude. Future work will involve parameterizing the diffuse exponential term based on the aperture and FOV of the detector.

Table 6.1: MAPE values for simulation and model comparison.

| FOV | MAPE 8 mm aperture | MAPE 2" aperture |
|-----|-----------------------|---------------------|
| 4° | na | 0.30 |
| 16° | 0.23 | 0.19 |
| 90° | 0.08 | 0.14 |

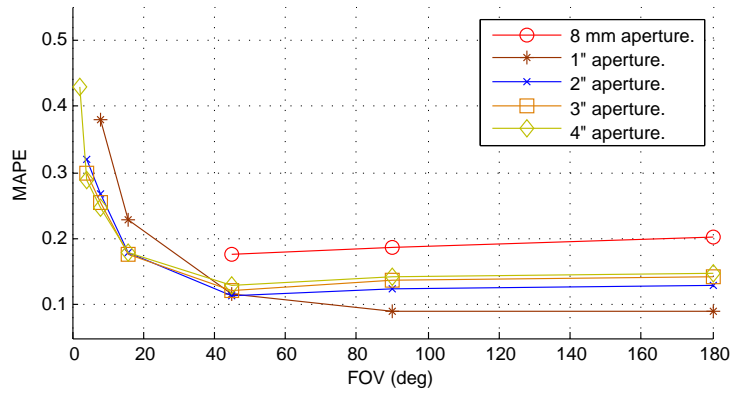


(a) Harbor II: 8mm receive aperture

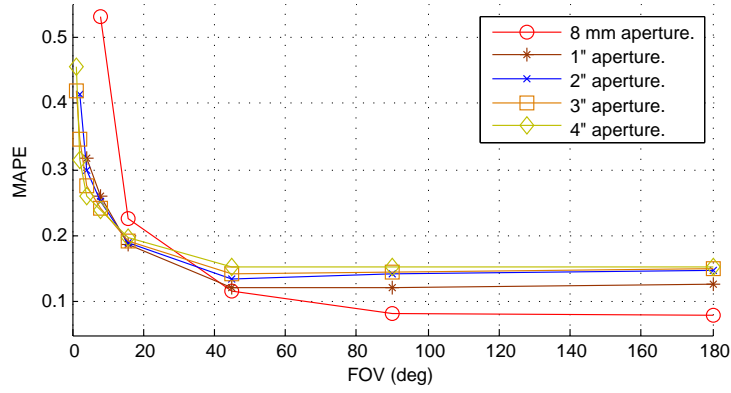


(b) Harbor II: 2 inch receive aperture

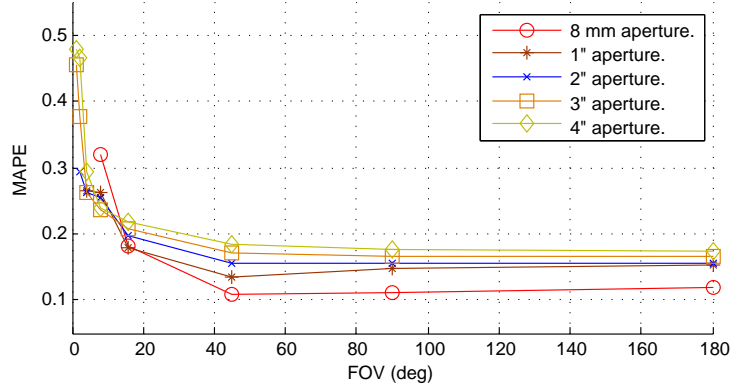
Figure 6.8: Simulation results for Harbor II-type water for a selection of apertures and FOV's, along with a two term exponential model fit line.



(a) Harbor I MAPE



(b) Harbor II MAPE



(c) Harbor III MAPE

Figure 6.9: The mean absolute percentage error (MAPE) for three harbor water types at various FOVs. Each line represents a different aperture size. The quantitative fit measurement is listed in Table 6.1

6.5 Design Considerations

Design considerations for an underwater optical communication system consist of many codependent criteria. In general we can divide this between the transmitter, receiver, and overall system components. These considerations are summarized below.

6.5.1 Transmitter Considerations

Optical Source The optical source determines average and peak optical output power. Lasers are typically easier to collimate and propagate over a longer distance. Peak output power can be very high and is especially useful for pulsed communication systems. Optical coherence can be used for communication. Lasers have a smaller optical bandwidth than LEDs, which allows them to be more effectively filtered. LEDs are inexpensive and useful for creating a Lambertian source, which can make pointing and tracking easier.

Modulation Format Baseband modulation has been implemented on most systems in the past. Many laser systems are capable of outputting high peak powers at low repetition-rates, which make them ideal for pulse-position modulation. On-off keying is a simple modulation format that does not require advanced circuitry. LEDs are limited in their bandwidth and therefore limit the datarate of communication when using modulation formats that only modulate one bit per symbol. Subcarrier intensity modulation allows for high-order constellations by modulating a RF signal onto the intensity of the optical beam. Modulation schemes like this allow the communications engineer to employ the vast capabilities of RF modulation standards and research. Such schemes may be limited in very low light situations where photon counting is employed. Sophisticated systems may employ optical coherence to directly change the phase/frequency/polarization of the optical signal. The propagation of ballistic photons can be significantly lower than scattered photon propagation and therefore may limit communication distances for such systems.

Transmitter Divergence Wide angle optical sources, such as LEDs or diode lasers without a collimating lens, may eliminate or reduce the need for beam steering apparatus on the transmitter, but also reduce the power at the receiver since the transmitted photons are being spread over a much larger surface area than the receiver aperture. Tightly collimated laser sources require precise alignment and are more likely to suffer beam wander from turbulence or signal fades from particulate matter or sea creatures.

6.5.2 Receiver Considerations

Optical Filtering Optical filters play a large part in determining the receiver's sensitivity to background radiation. A wider bandwidth filter will need to be employed for optically broadband sources like LEDs, while extremely narrow filters can be used for laser sources. These narrow filters, however, have very limited acceptance angles, and will reduce the system field of view.

Receiver Optics The receiver optics control the aperture and, to some extent, field of view. One of the downsides to utilizing wide angle receivers is the increase in background noise, which as seen in Eq. 6.24, is directly proportional to the receiver area and proportional to the square of the receiver FOV. Very wide field of view optics may be difficult to design, especially when paired with small detector surface areas.

Optical Detector The choice of optical detector limits system bandwidth and field-of-view. Choices include photodiode, avalanche photodiode (APD) or photomultiplier tube (PMT). APDs and PMTs have built-in electrical gain of many orders of magnitude, with the downside being added expense, high-voltage power requirements, and possibly higher noise due to dark currents and excess noise. These devices will have a larger detector area than an equivalent bandwidth photodiode, which exhibits no electrical gain, but is very inexpensive and easy to electrically bias.

Modulation Format The modulation format will affect the receiver circuitry. Analog receivers may be low cost, but are inferior to digital demodulation methods and are difficult to tune to varying channel conditions. Digital systems will need to digitize the signal with an ADC, which may be more difficult with baseband modulation formats, as the signal cannot be easily AC-coupled to the input (as the DC-component is used to transmit information). Careful consideration will need to be made in regards to bandwidth, datarate, and processing power needed for demodulation.

6.5.3 Overall Design Considerations

The system size, weight and power (SWaP) will need to carefully balanced. Water weighs approximately 62 lbs/ft³ which determines the corresponding amount of weight the system will need vs. the volume to remain neutrally buoyant. System power will be a combination of optical source, electronics power, and any heating/cooling needed to maintain the electronics and reduce receiver noise. While operating underwater the system may function fine, once on the surface or in direct sunlight, internal temperatures can rise rapidly. While the receiver may need to continuously operate in order to detect a transmission, the modulation type can determine the difference between peak and average optical power. Subcarrier or carrier modulation formats require nearly constant optical power, while baseband methods, such as PPM, allow for significantly lower average optical powers.

Table 6.2: Simulation parameters for different detector types. Values are used in the SNR equation listed in Eq. 6.34.

| Parameter | PMT | Photodiode |
|-----------|---------|------------|
| FOV | 90° | 16° |
| Aperture | 8 mm | 2" |
| Gain | $5e^5$ | 1 |
| i_d | 0.15 pA | 5 pA |
| QE | 0.18 | 0.85 |

Table 6.3: Simulation parameters that are the same for the various detectors listed in Table 6.2. Values are used in the SNR equation listed in Eq. 6.34.

| Parameter | Value |
|-----------------|-------------------|
| λ | 532 nm |
| bandwidth | 10 MHz |
| temperature | 50° F |
| filter | 10 nm |
| τ_{optics} | 0.85 ² |
| P_{tx} | 1 W |

6.6 Comparing Various System Performance

By using the data presented in Chapter 5 we can model some power loss equations and compare against the simulated results. A natural method of comparison will be the bit error rate (BER) of the system compared to its operating distance.

In order to arrive at a operating SNR for a system, various system parameters must be chosen. Two major types of systems will be compared, a large FOV, small aperture PMT-based system, and a large aperture, small FOV, photodiode-based system. For these examples, the values in Table 6.2 and Table 6.3 are used for the various constants expressed in Eq. 6.34.

Using the two term exponential power loss model derived in Section 6.4, the SNR equation in

Table 6.4: Constants to compute background solar power.

| Parameter | Value |
|-----------|----------------|
| K_d | $0.03 m^{-1}$ |
| E_d | $1.2 W/m^2 nm$ |
| R_d | 0.01 |
| depth | 25 m |
| L_{fac} | 3 |

Eq. 6.34, and the background solar power calculations in 6.2.1, we can simulate the performance of a variety of optical communication links. Using the parameters in Tables 6.2, 6.3, and 6.4 and the curve parameters from the Harbor I-type waters simulated in Section 5.4, the power and SNR curves in Fig. 6.10 and Fig. 6.11 were generated. Also plotted are the same values but using the standard Beer's Law channel loss model, which underestimates the received power.

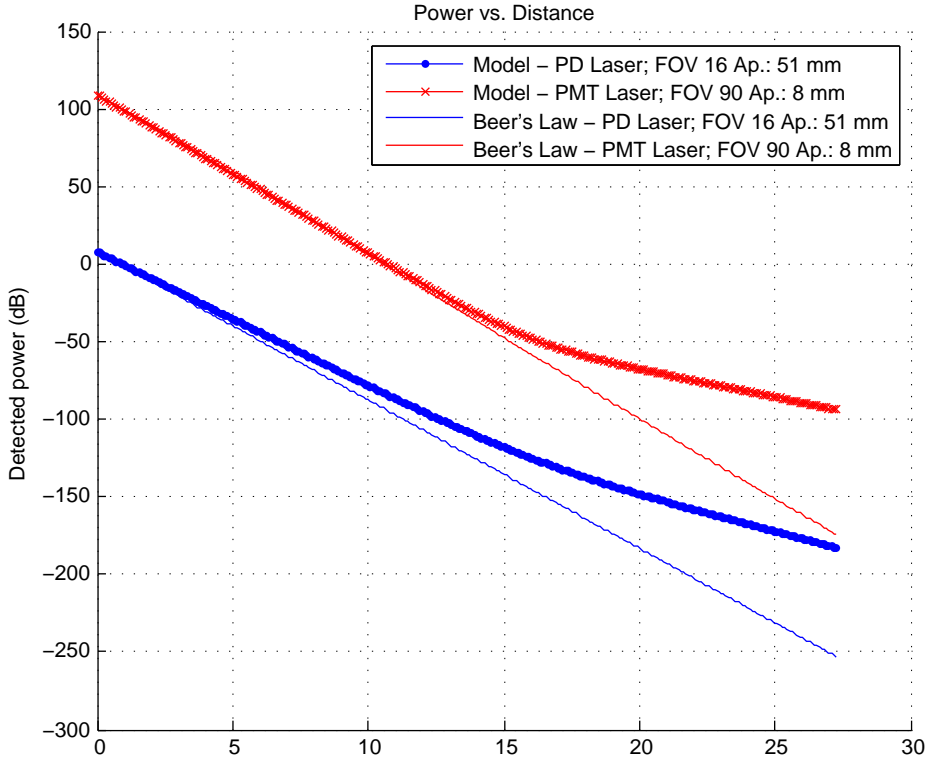


Figure 6.10: Simulated power vs. distance for Harbor I-type waters, with a PMT and a photodiode-based detector. This is simulated for a fixed PMT gain, yielding power values at small distances which are clearly unreasonable.

Fig. 6.10 shows the received electrical power versus distance for a link operating in Harbor I ($c = 1.1 \text{ m}^{-1}$) water. Since the PMT gain was simulated as fixed, clearly the received power is unrealistic at small distances, where a real link would adjust the gain and aperture down to compensate. Consequently, as see in Fig. 6.11 the SNR for the photodiode based receiver (shown in blue) is actually higher at smaller distances than the SNR for the PMT based system. This is due to the large amplification of the shot noise of the detector.

Using one equation for bit error rate,

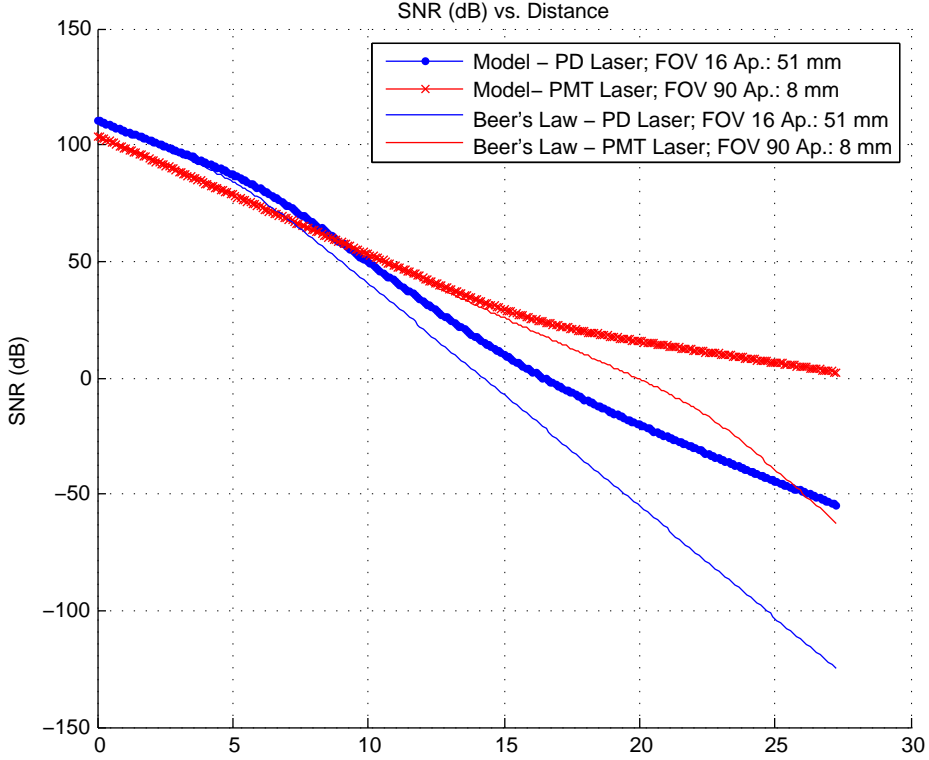


Figure 6.11: Simulated SNR vs. distance for a PMT and PD detector in a Harbor I-type environment. This is simulated for a fixed PMT gain and aperture, so the SNR values are very high.

$$BER_{qpsk} = Q(\sqrt{SNR}) \quad (6.52)$$

we can plot the BER for the system versus the distance the link is operating at. This is shown in Fig. 6.12. Clearly there is a significant improvement in the BER estimate from using the common Beer's Law-type power loss model. Significant additional gains could be had from using forward error correction on the optical links. For more information, the work by Everett is very helpful [99].

6.7 Experimental Systems

Several experimental systems were constructed and tested during the course of this research. Heavy emphasis was placed on practical and experimental results, with the ultimate goal of allowing bi-directional data traffic between two optical modems. Discussed below are three of the experimental systems, each emphasizing different aspects of the communication link, including novel modulation with polarization, novel transmission with a modulating retroreflector and novel reception using software defined radio.

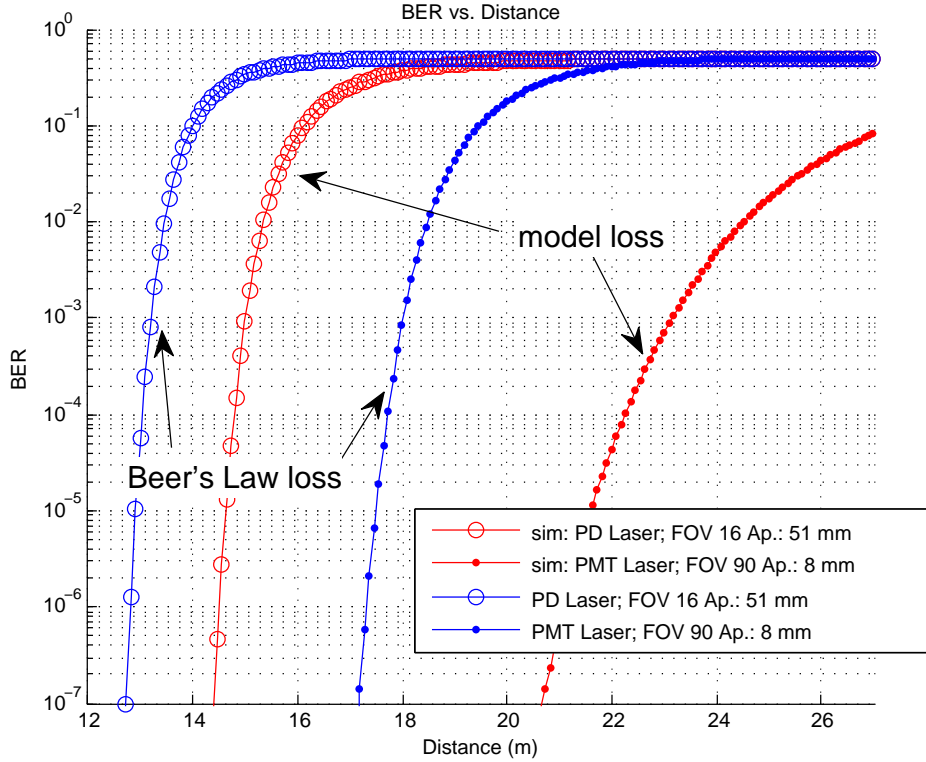


Figure 6.12: Bit error rate versus distance for PMT and Photodiode based links.

6.7.1 Polarization Modulation using Diode Lasers

A laser based polarization modulation system was built in order to explore the feasibility of using low-cost polarization modulation (PolModSK) for sending optical data underwater. The system was designed to use two diode lasers, along with two PMT detectors in order to detect two orthogonal linear polarizations. By adding polarization to the measurements, the system could be used to block feedback between receiver and transmitter (backscatter suppression) or it could be used for additional channel sensing.

A block diagram of an experimental system is shown in Fig. 6.13 and further discussed in Cox et al. [100]. The transmitter was accomplished using two diode lasers mounted at right angles on a polarizing beamsplitter. The detector was similar in that two detectors were mounted to the faces of a polarizing beamsplitter. The two diode lasers were rotated such that each transmitted either horizontal or vertical polarized light, which was then detected by the appropriate detector based on polarization. The reception of the signal was done in software, where the difference of the two detected signals was taken. The system used a modified binary on-off-keying (OOK) transmission, with “1”s being sent on one diode and “0”s on the other.

The system performance was measured against the system performance of a single diode, on-off-

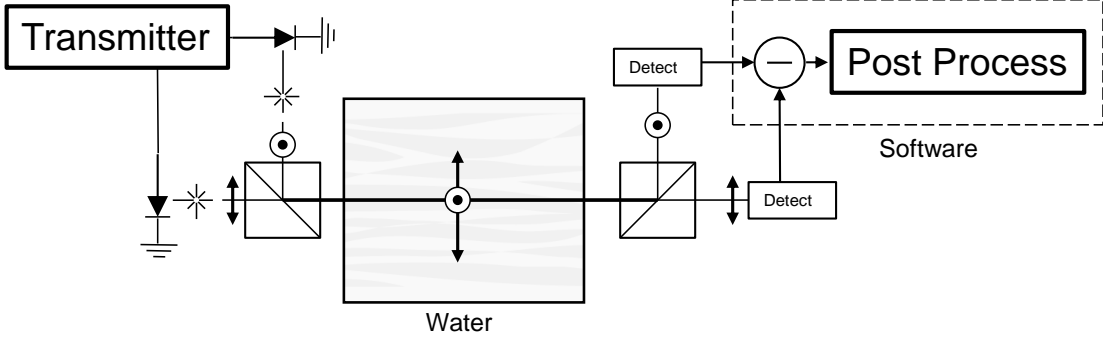


Figure 6.13: Block diagram of polarization modulation system using two diode laser and two orthogonal detectors.

keying system. Since the PolModSK system utilized two diode lasers and two detectors, the signal to noise ratio was the same for a single laser, single detector system. This is illustrated in Fig. 6.14. However, the system performance, compared to attenuation length, was somewhat degraded over the OOK system, in that scattering in the channel changes the polarization of the light, causing the signal to degrade. This is illustrated in Fig. 6.15. It can be seen that the PolModSK system causes a loss of about two attenuation lengths for the systems operating with the UMTS Turbo Code error control code. The uncoded system performance is nearly equal. This seems to be because the system SNR becomes too low for proper bit detection before there is a significant amount of multiple scattering that lowers the degree of polarization (DOP).

While the absolute system performance is not as good as the OOK system, one potential use of this setup is for simultaneous communication and channel sensing. By using a simple depolarization model, we can make some general observations about the viability of this method. If the degree of polarization (DOP) is measured as

$$g = \frac{P_{co} - P_{cross}}{P_{co} + P_{cross}} \quad (6.53)$$

where P_{co} is the co-polarized light power and P_{cross} is the cross-polarized light power, then a simple model for how the light depolarizes through water is given by Vasilkov et al [101]

$$g = g_0 \exp(-\phi br) \quad (6.54)$$

where g_0 is the initial degree of polarization, ϕ is a term called the depolarization factor, b is the scattering coefficient, and r is the transmission distance.

The value ϕ is a measured quantity that is dependent on the Mueller matrix of the transmission medium, but appears to range from 0.002 – 0.009 for natural waters.

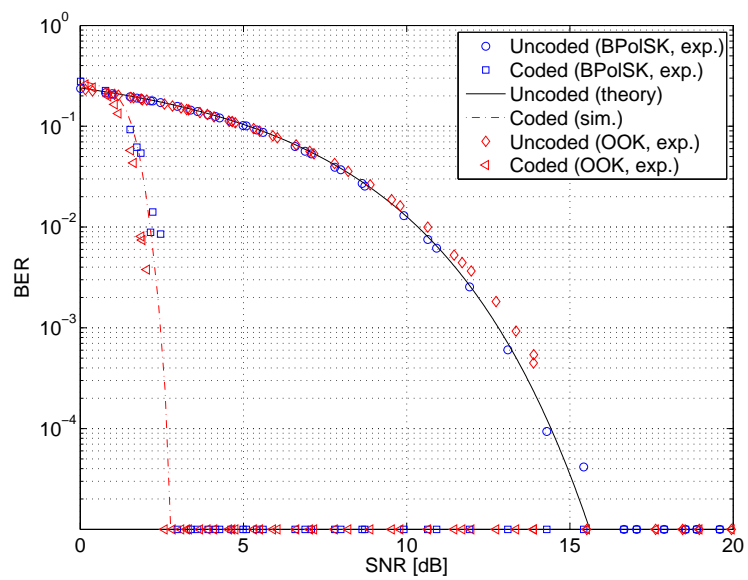


Figure 6.14: Bit error rate versus SNR of the received data for both a single laser OOK system, and the PolModSK system. Also shown is the system performance using a UMTS Turbo Code.

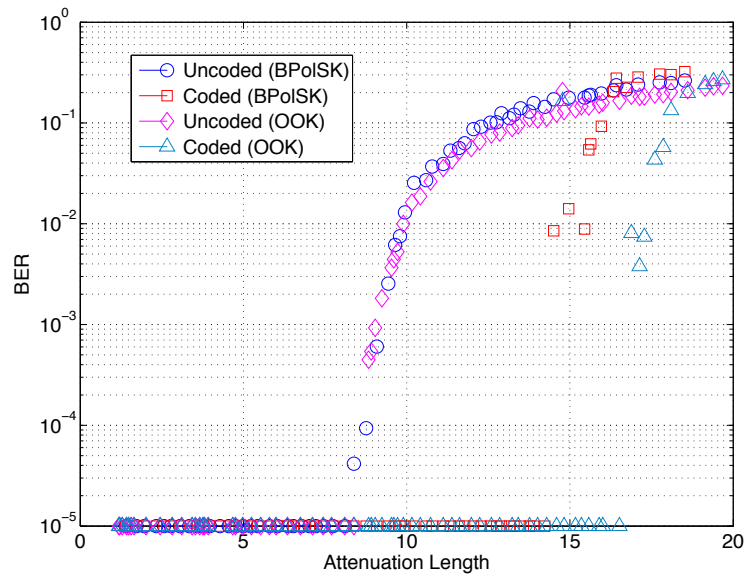


Figure 6.15: Bit error rate versus the attenuation length of the systems (for a fixed distance of 3.66 m). Also shown is the system performance using a UMTS Turbo Code.

If we assume the basic Beers-Law power loss model, it can be expressed as

$$P = P_0 \exp\left(-\frac{b}{\omega_0} r\right) \quad (6.55)$$

where P and P_0 are the initial and received power and ω_0 is the albedo of the water.

Ideally we'd like to solve for both r and ω_0 as this would eliminate some ambiguity in the received signal. i.e. The receiver doesn't "know" if the transmitter is at a great distance in lightly scattering water, or at a short distance in highly scattering water.

Substituting Eq. 6.54 into Eq. 6.55, we arrive at the following expression for ω_0

$$\omega_0 = \frac{\ln(g/g_0)}{\phi \ln(P/P_0)} \quad (6.56)$$

which depends only on the (measured) DOP and received power, and requires knowledge of the transmitter's initial power and DOP. ϕ is the only unknown and would have to be measured, or assumed. By using the above equation for ω_0 , along with a loss model for power, which depends on the albedo and distance, the type of water in the channel can be determined.

Simulated example values for DOP versus received power and DOP versus distance for various water types are presented in Fig. 6.16 and Fig. 6.17. This assumes a Beer's Law-type loss model. Using a better loss model would probably accentuate the differences between the water types, as the multiple scattering of the Harbor waters would increase the DOP loss for those water types. The plots are for a fixed depolarization factor, ϕ , of 0.005. One way these type of plots could be used would be to take the total received power, along with the DOP to find the closest water-type match. For instance, if the DOP was 0.95 and the received power was $10^{-6} W$, then it could be assumed that the system was operating with a Clear water-type channel. Furthermore, it could be assumed that with that type of water and DOP, that the transmission distance was $> 50m$ from the plot in Fig. 6.16.

Clearly such an implementation would require refinement, along with a better understanding of the depolarization of water through the channel. Currently Photonator MCNS does not support polarization measurements of the lightfield, however it could be added without too much difficulty. The figures in 6.16 and 6.17 are meant to illustrate potentially how such a system would behave, and the advantages of adding a second degree of observation to the communication system.

Conclusion

In conclusion, a novel method for underwater optical communication has been demonstrated. This method, utilizes the polarization of light to send data, and can be used to both gain extra information about the communication channel, or to distinguish between backscattered light and the incoming data signal. While further exploration needs to be made, the system proposed is practical and takes advantage of the natural polarization of diode lasers.

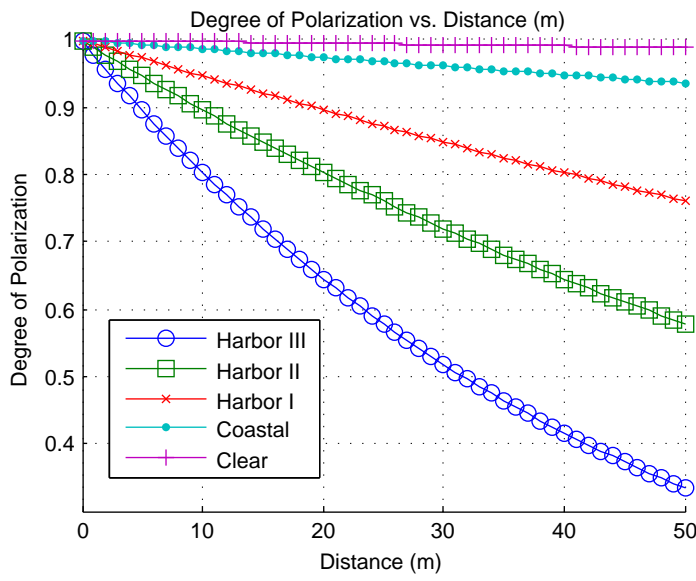


Figure 6.16: Degree of polarization (DOP) versus transmission distance for several different water types.

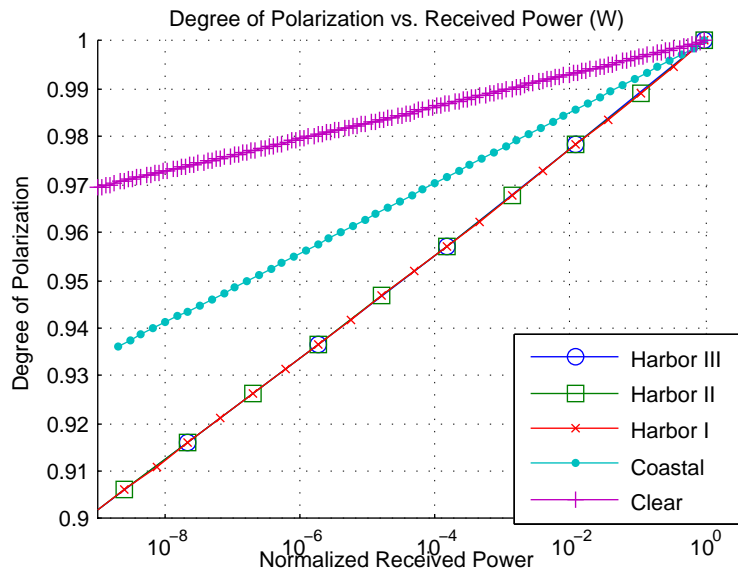


Figure 6.17: Degree of polarization (DOP) versus received power for various water types.

6.7.2 Using a Modulating Retroreflector for Underwater Optical Communications

Another interesting method for underwater optical communications is the use of a modulating retroreflector (MRR). This device allows a high-power system to send data to a low-power system, containing the retroreflector, which can then modulate the return signal at very low power. This is illustrated in Fig. 6.18. The use of such a system was explored by the author [12]. The difficulty with such a system, however, is the severity of the bi-directional geometric loss, which is dependent on 4th power of the distance, instead of the square of the distance for a one-way link, shown in Eq. 6.5.

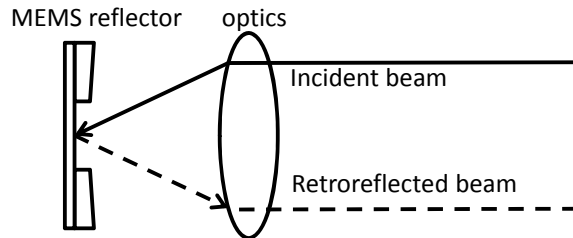


Figure 6.18: Diagram showing the retroreflection process.

The link budget for a MRR system is

$$P_{rx} = P_{tx} L_{tx} L_{rx} L_{ch,tx} L_{ch,rx} \quad (6.57)$$

where L_{tx} is the geometric loss in the forward direction, L_{rx} is the geometric loss from the MRR back to the interrogating system's receiver, and $L_{ch,tx}$ and $L_{ch,rx}$ are the channel loss for both directions. Both of these are expressed as the ratio of lightfield to aperture area, or

$$L = \frac{D^2}{4r^2\phi^2} \quad (6.58)$$

where D is the receiver diameter, r is the link distance, and ϕ is the half-angle divergence of the source function. For a Gaussian laser transmitter, ϕ_{tx} is approximately $\lambda/\pi W$, where W is the transmit aperture. For the MRR, the divergence could be estimated to be

$$\phi_{MRR} = d_{MRR}/f_l \quad (6.59)$$

where d_{MRR} is the diameter of the MRR itself ($250\mu m$ in our system) and f_l is the focal length of the lens in front of the device.

As can be seen from the link budget equation, the MRR system exhibits a loss that is related to

$1/r^4$, as opposed to the standard loss for a non-retroreflector that is proportional to $1/r^2$. Hence, MRR systems are generally not suitable for links operating at high attenuation lengths.

The MRR described by Cox et al. [12] was a MEMS device, fabricated from a silicon nitride bridge. By placing a voltage between the bridge and the substrate (shown in Fig. 6.22) the distance between the two was changed. By interrogating the bridge normal to the surface, the bridge and substrate formed a fabry-perot cavity, whose resonance could be changed by adjusting the plate distance with a voltage. The optical spectrum of this device, with and without a driving voltage, is shown in 6.23, and illustrates how, by changing the bridge voltage, the reflectivity or transmissivity of the device can be dynamically controlled.

For the system described by Cox et al. [12], the system values are listed in Table 6.5.

Table 6.5: System parameters for the modulating retroreflector system further discussed by Cox et al. [12].

| Parameter | Value |
|-------------|------------|
| λ | 532 nm |
| P_{tx} | 20 mW |
| ϕ_{tx} | < 1.5 mrad |
| d_{MRR} | 25 mm |
| f_l | 25 mm |
| d_{rx} | 50 mm |
| r | 3.66 m |

The experimental system block diagram is shown in Fig. 6.19. The transmitter block diagram is shown in Fig. 6.20, and the demodulator, written in MATLAB, is diagramed in Fig. 6.21. A diagram of the MRR is shown in Fig. 6.22. The MRR is pictured in Fig. 6.24. The device has 144 modulators patterned on it, which are the small squares surrounding the four large central squares. A picture of the mounted MRR is shown in Fig. 6.25 with the interrogating laser shown focused onto the MRR. Fig. 6.26 shows the interrogator setup, along with the parabolic mirror and photodiode receiver.

The transmitter was formed using an FPGA-based transmitter that would take an incoming bitstream from the USB port and modulate the output of a DAC at one of four voltage levels. This variable voltage signal was fed into an arbitrary waveform generator (Arb.), which shifted the phase of a carrier signal in proportion to the incoming voltage. In this manner a basic quadrature phase-shift keying (QPSK) modulation system was established. This QPSK modulated carrier waveform was amplified using a high-power amplifier, which was then used to change the voltage across the MRR's bridge.

The bandwidth of the device was measured by sending a frequency sweep into the input and

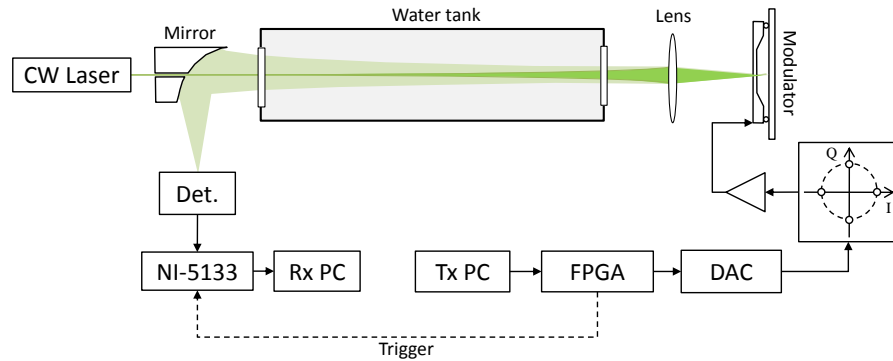


Figure 6.19: Experimental block diagram for MRR communication system.

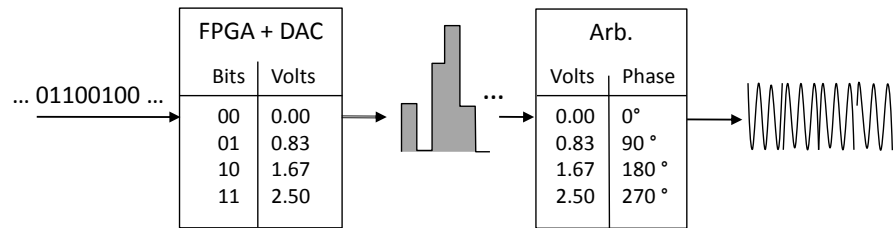


Figure 6.20: Block diagram of transmitter for the MRR communication system.

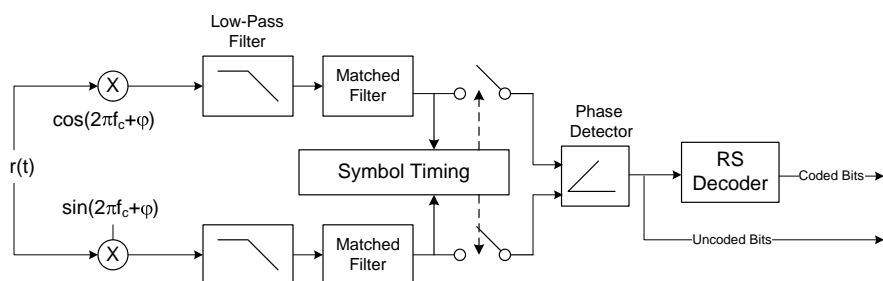


Figure 6.21: Receiver diagram for MRR system. This was implemented in software in MATLAB.

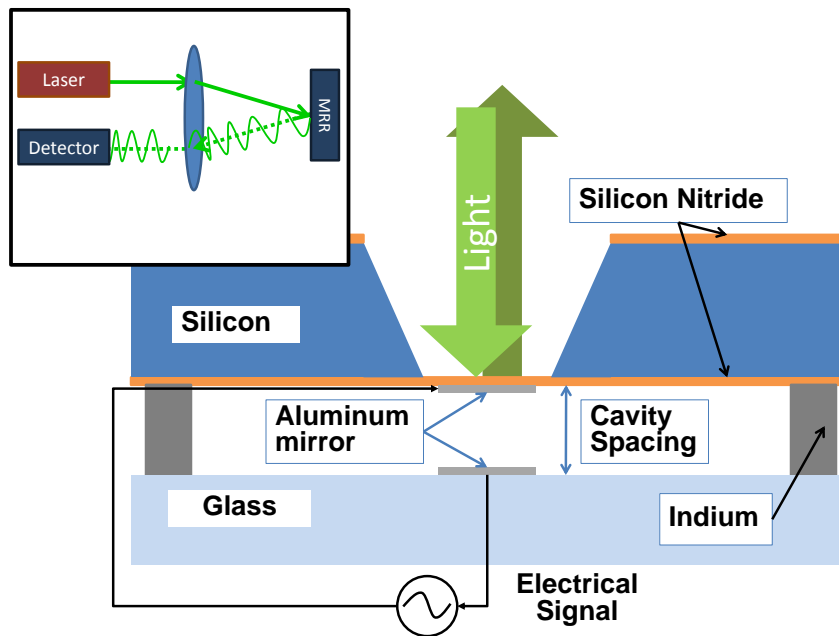


Figure 6.22: Cross section diagram of a MEMS modulating retroreflector. The device can be used for ultra-low power underwater optical communication.

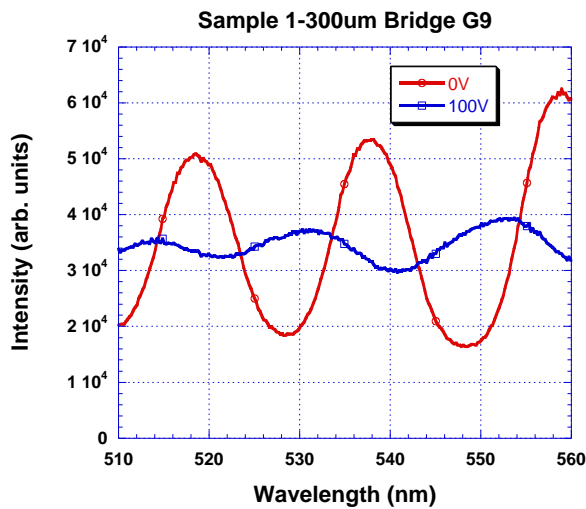


Figure 6.23: Optical transmission spectrum of a bridge with and without a voltage load. By interrogating the bridge with a fixed optical wavelength, the transmission or reflection of the device can be changed.

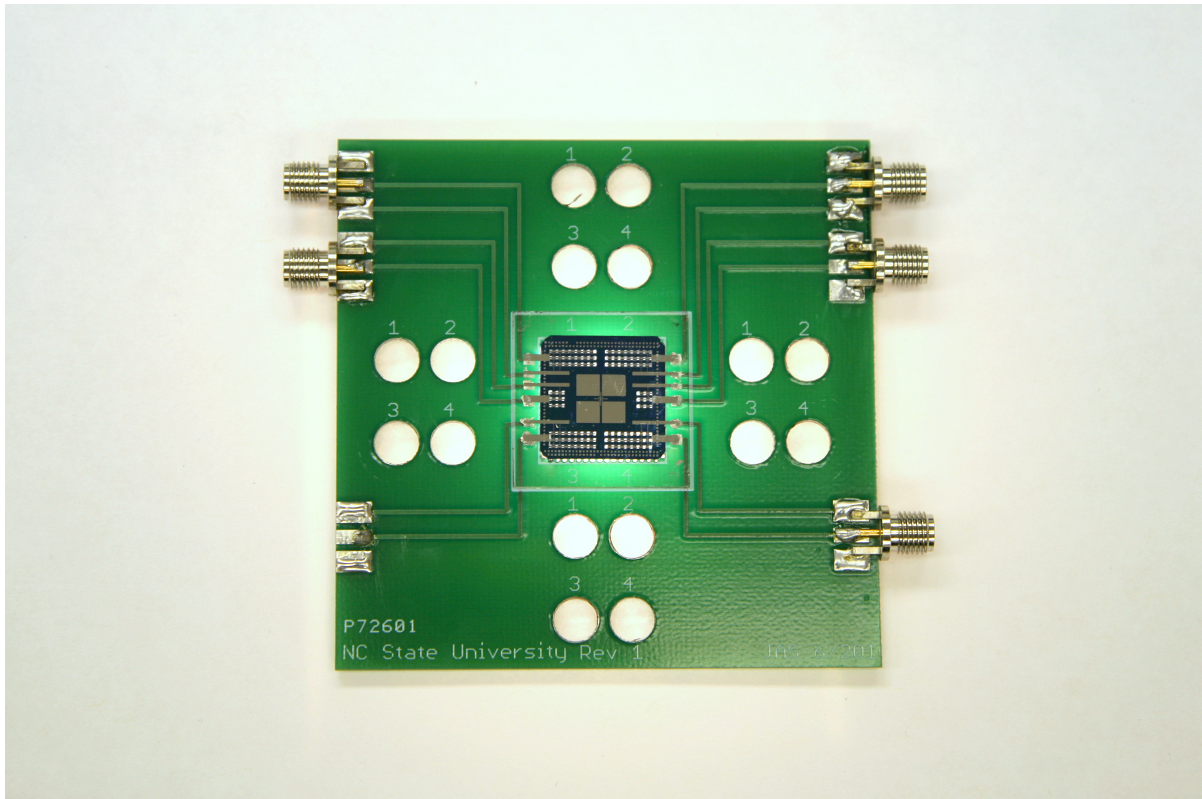


Figure 6.24: Top-down picture of the MRR. The small squares surrounding the four central squares are 144 individual modulators.

measuring the output at the optical detector. The image in Fig. 6.27 shows the frequency response of the high-power amplifier, the laser itself, finally the MRR with the input frequency sweep. Depending on which bridge was used, and where the spot was focused, the response can exhibit large dips, due to mechanical resonance, but in general the frequency is flat till about 1 MHz, where it begins to roll off. The response was measured by digitizing the signal and using the MATLAB `periodogram()` command.

While the spectrum can change depending on the particular device interrogated, along with the specific spot on the bridge that the laser is focused on, in general the bridges exhibit about 1 MHz of flat bandwidth before the frequency response starts to drop. Using this spectrum, the QPSK data signal was modulated with a 750 kHz carrier. The information was transmitted via a 20 mW 532 nm interrogating laser, over a 3.66 m water tank. Maalox was added to the water to increase the attenuation coefficient, c , in order to attenuate the beam. Data-rates of 250 kbps, 500 kbps, and 1 Mbps were selected to transmit 40k databits, which were encoded with a (256, 129) Reed-Solomon error correction code, which outputs 80k encoded bits.

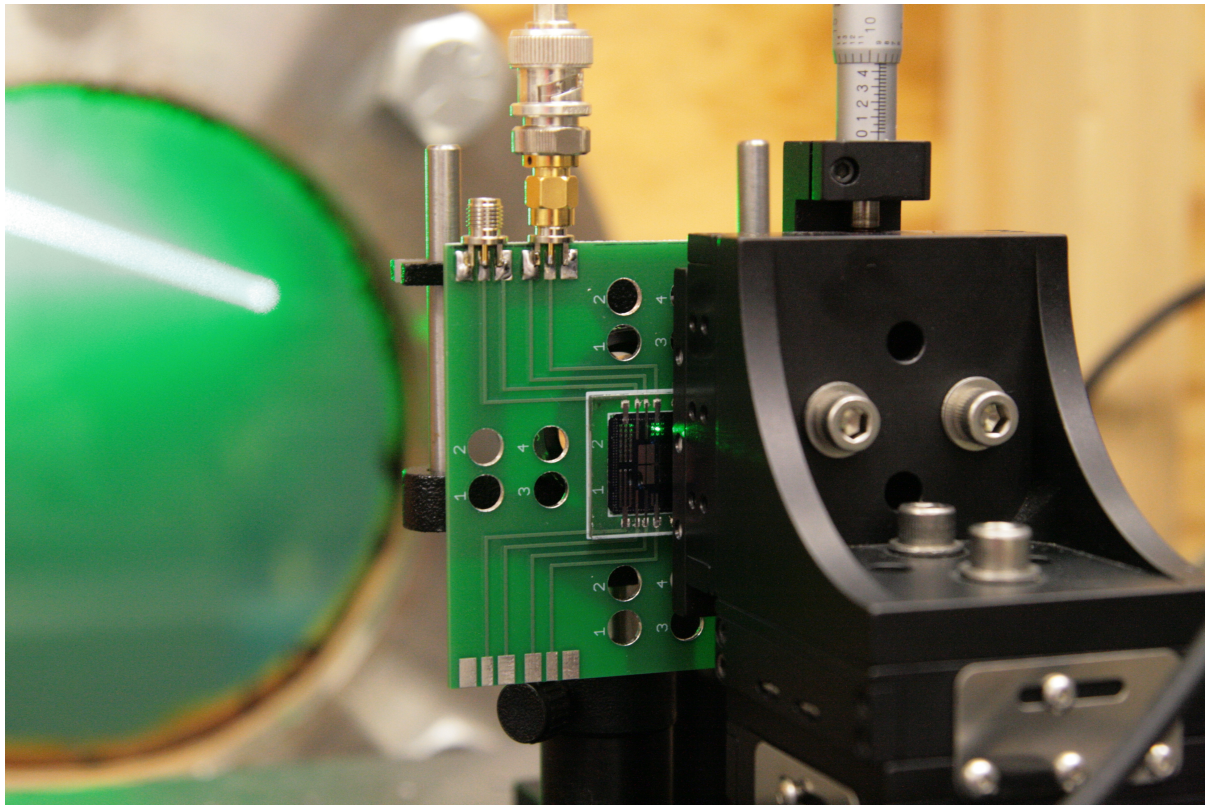


Figure 6.25: Mounted view of the MRR with interrogating laser.

The results are shown in Fig. 6.28 for both bit-error rate (BER) versus attenuation length (Fig. 6.28a through Fig. 6.28c), and for BER vs. the estimated received optical power (Fig. 6.28d through Fig. 6.28f). By using the Reed-Solomon error control code, error-free transmission was achieved at close to 7 attenuation lengths (out and back distance), and with a detected optical power of about $5 \mu W$ (-23 dBm) of optical power. This number increases to $8 \mu W$ (-21 dBm) of optical power for 1 Mbps datarate, and the maximum transmission distance drops to 5.5 attenuation lengths. It should also be noted that the uncoded data for the 1 Mbps datarate case exhibits an error floor at about 10^{-2} . This is most likely due to the limited bandwidth of the device when paired with the larger bandwidth of the 1 Mbps data. The Reed-Solomon code, however, removes this error floor and allows error free transmission (i.e. no errors in the sent packet).

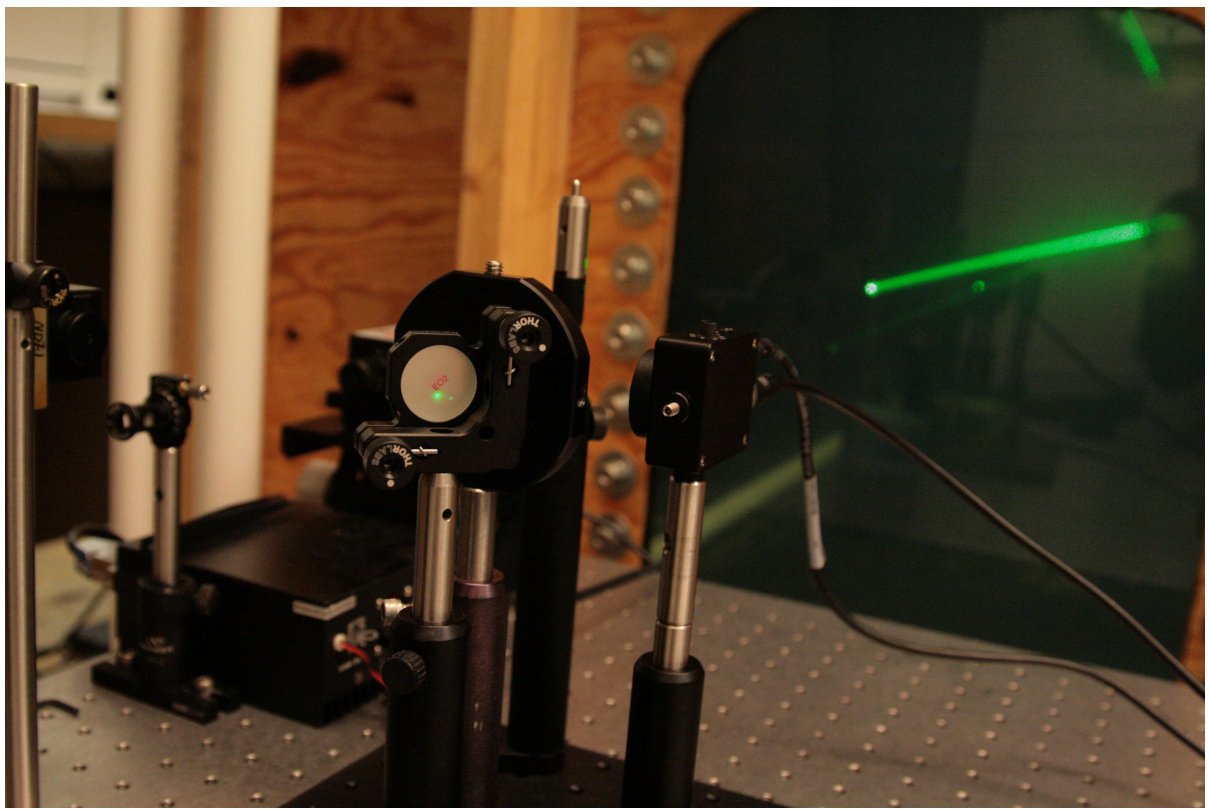


Figure 6.26: View of the MRR interrogating system.

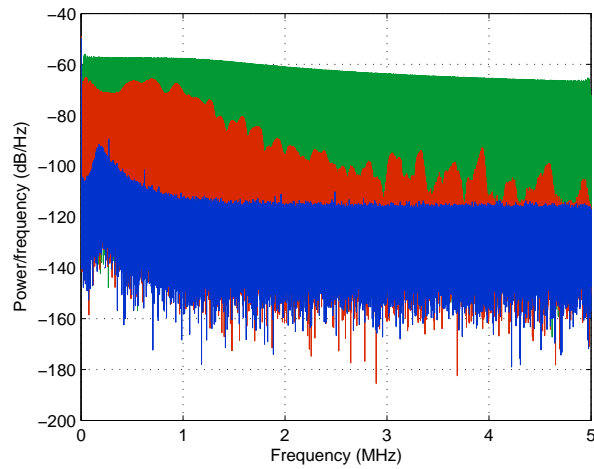
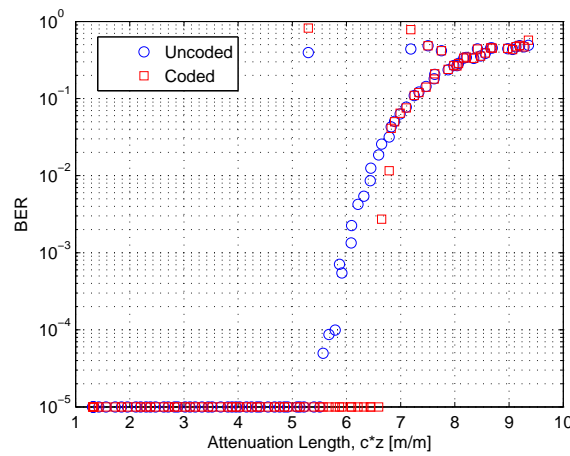
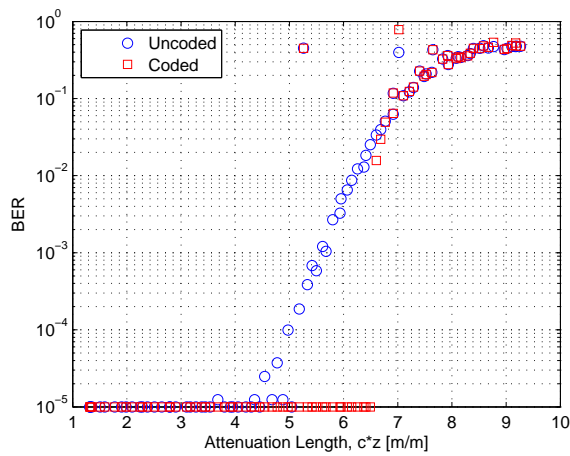


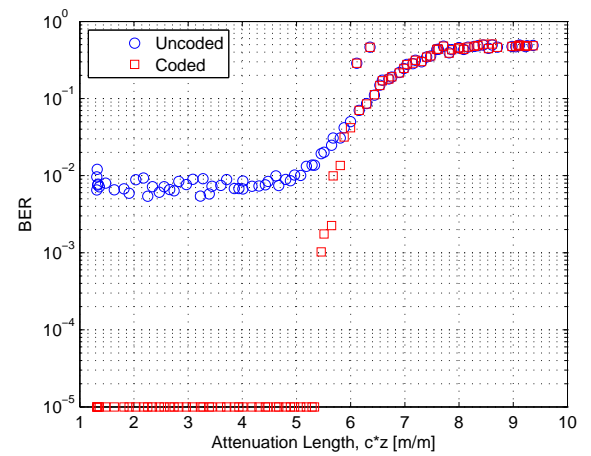
Figure 6.27: Frequency response of the (green) high-power amplifier, full system (red) and the interrogating laser and detector (blue).



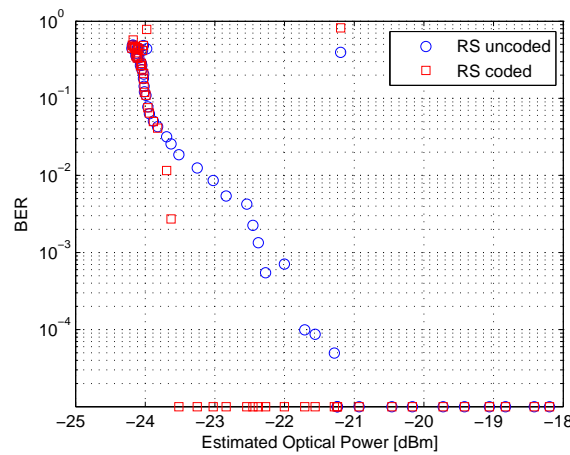
(a) 250 kbps BER versus AL



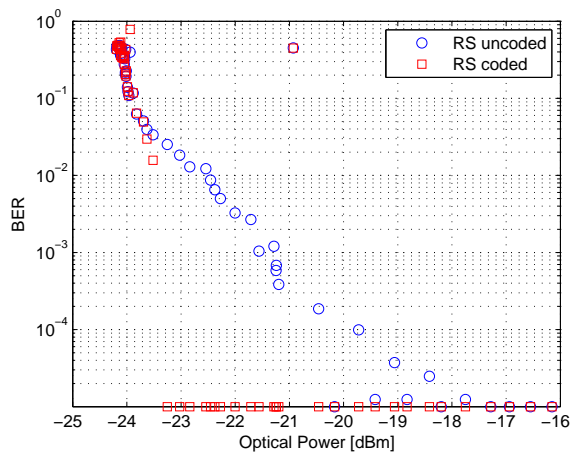
(b) 500 kbps BER versus AL



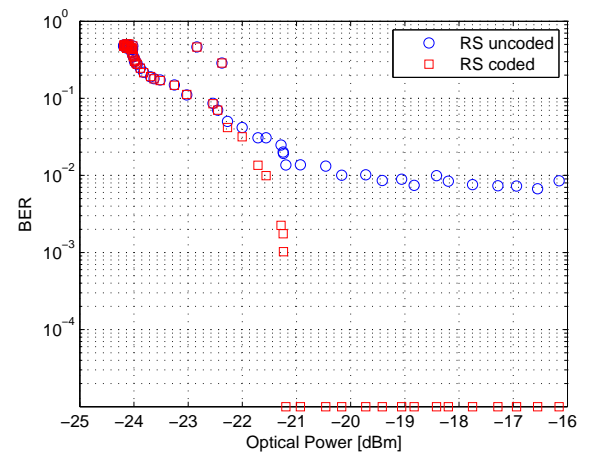
(c) 1 Mbps BER versus AL



(d) 250 kbps BER versus Power



(e) 500 kbps BER versus Power



(f) 1 Mbps BER versus Power

Figure 6.28: Bit error rate measurements for the MEMS MRR compared with the attenuation length and received optical power.

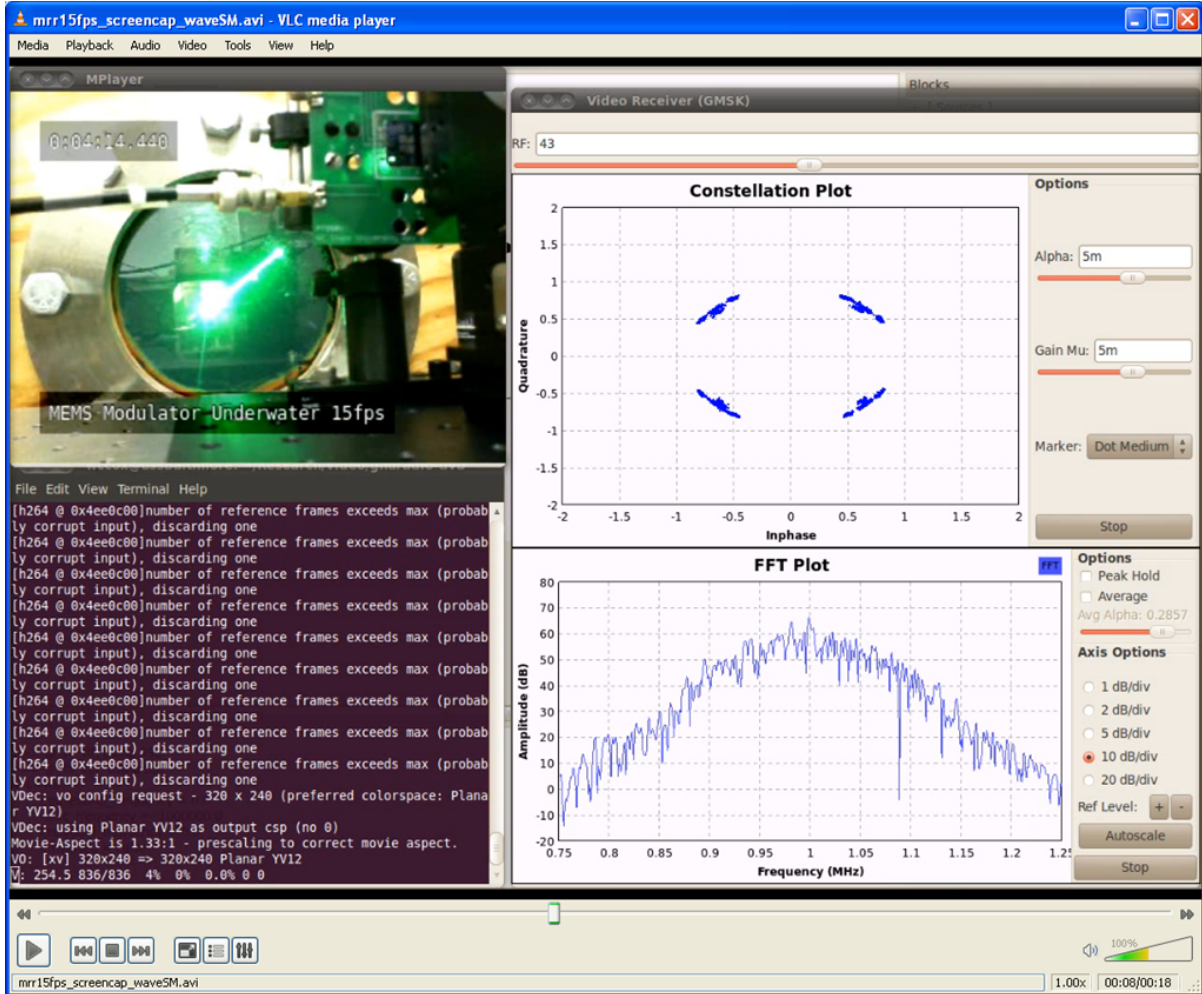


Figure 6.29: Screen capture showing the MRR working with the GNURadio software defined radio package to send streaming video from the MRR to the interrogating receiver.

Extending the performance

Using $5 \mu W$ as the minimum power needed for error-free transmission, the link budget equation from Eq. 6.7.2, and the system parameters from Table 6.5, we can arrive at the following equation relating the system parameters to the transmitter power

$$\frac{P_{rx}}{P_{tx}} = \frac{D_{MRRlens}^2 D_{rx}}{16r^4 \phi_{laser}^2 \phi_{lens}^2} \exp(-2cr) \quad (6.60)$$

where P_{rx} and P_{tx} are the received and transmitted optical powers, $D_{MRRlens}$ and D_{rx} are the diameters of the lenses and receiver aperture, r is the distance between the MRR and receiver, ϕ_{laser} and ϕ_{lens} are the beam widths of the laser and lens, and c is the speed of light.

ters of the receiver lens and MRR focusing lens, ϕ_{laser} and ϕ_{lens} are the divergence of the laser and the MRR lens transmitter. Using this equation we can plot the required transmit power to close the link at various distances. This is shown in Fig. 6.30. In most cases, very little is gained, in terms of transmission distance, by increasing the transmitter power past a few hundred mW. For example, with Harbor II-type waters, a link distance of 3 m can be achieved with 110 mW of optical transmit power, however by increasing the power by over 3x, to 370 mW, the link distance only moves to 3.2 m. It should be noted, however, that this only applies to the basic Beer's Law-loss model, and if a better model was used, the gain from increased power would be accentuated, however the r^{-4} loss will still dominate.

Conclusion

In conclusion, we have demonstrated using a MEMS modulating retroreflector for underwater optical communication at up to 7 attenuation lengths at a datarate of 1 Mbps. Using a theoretical link budget for this device, system performance can be estimated for a variety of water types. While a MRR system suffers a large loss due to transmission distance (r^{-4} , as opposed to r^{-2}) it can be a very useful tool for allowing a high power system to communicate with a low power system and in reverse. The physical power required by the MRR system is very small, since all that is required is mechanically moving a $250 \mu m^2$ bridge a few nm. This provides a unique solution for low power sensor nodes operating in the ocean, as they can achieve non-contact communication with very low power and at much higher datarate than are offered by acoustic communication systems.

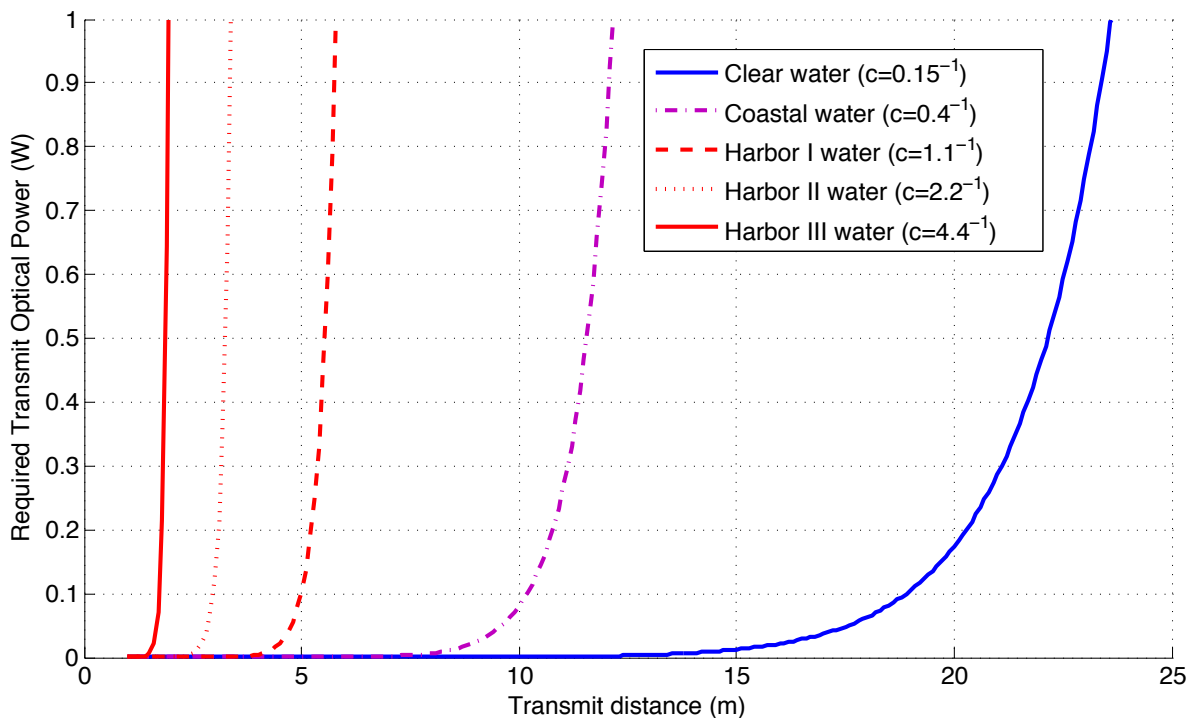


Figure 6.30: Required transmit power to achieve $5 \mu\text{W}$ of received power at the receiver. Plot shows required power at various water conditions, and various distances between the interrogator and the MRR. This assumes perfect alignment and that the MRR is normal to the interrogating beam.

6.7.3 Using GNURadio and LEDs for Underwater Optical Communication

Using high powered LEDs for underwater optical communication has been explored in several papers [102, 10, 5] since these devices allow for moderately high optical output power and have a diffuse beam which eases the pointing and tracking requirements (see Section 6.1). These systems utilized baseband modulation schemes, such as on-off keying, which, while simple to implement, suffers from poor performance when the background light level can fluctuate and when maximum receive power is not known prior to the bit estimate. Additionally, it is difficult to implement multi-bit-per-symbol modulation schemes, such as M-PAM, with this method. In order to overcome these limitations, and to take advantage of existing RF communication systems, a passband modulation scheme for using LEDs to communicate underwater was proposed and explored by Cox et al. [13].

A LED and photodiode-based bidirectional communication system was established using the GNURadio software defined radio system. A block diagram of the system is shown in Fig. 6.31, and shows the difference between the optical front-end, the RF hardware, and the system software. A picture of one of the transceivers is shown in Fig. 6.32. The LED transmitter is shown on the left, which is hooked to a Bias-T and a RF amplifier in order to amplify the output signal from the SDR hardware, and bias the signal past the turn-on voltage of the LED. A 1" lens is in front of the LED to reduce the divergence. The detector is an amplified photodiode with a 2" collection lens in front. The detector output is AC-coupled to the RF receiver via a DC block.

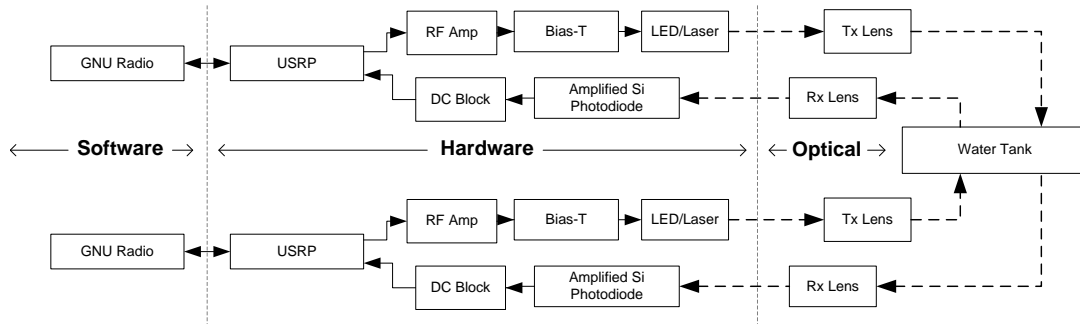


Figure 6.31: System block diagram for LED-based passband communication system using software defined radio.

In order to test the system performance, various LED wavelengths were chosen, along with a 410 nm diode laser transmitter. These were compared via the GNURadio `bert_tester.py` program in order to look at the signal SNR and the system BER. Additionally, the system was also compared to the operating attenuation length in a fixed length tank, by adding Maalox to the water to attenuate the signal. Plots of the SNR versus BER for the various systems are shown in Fig. 6.33. Also plotted

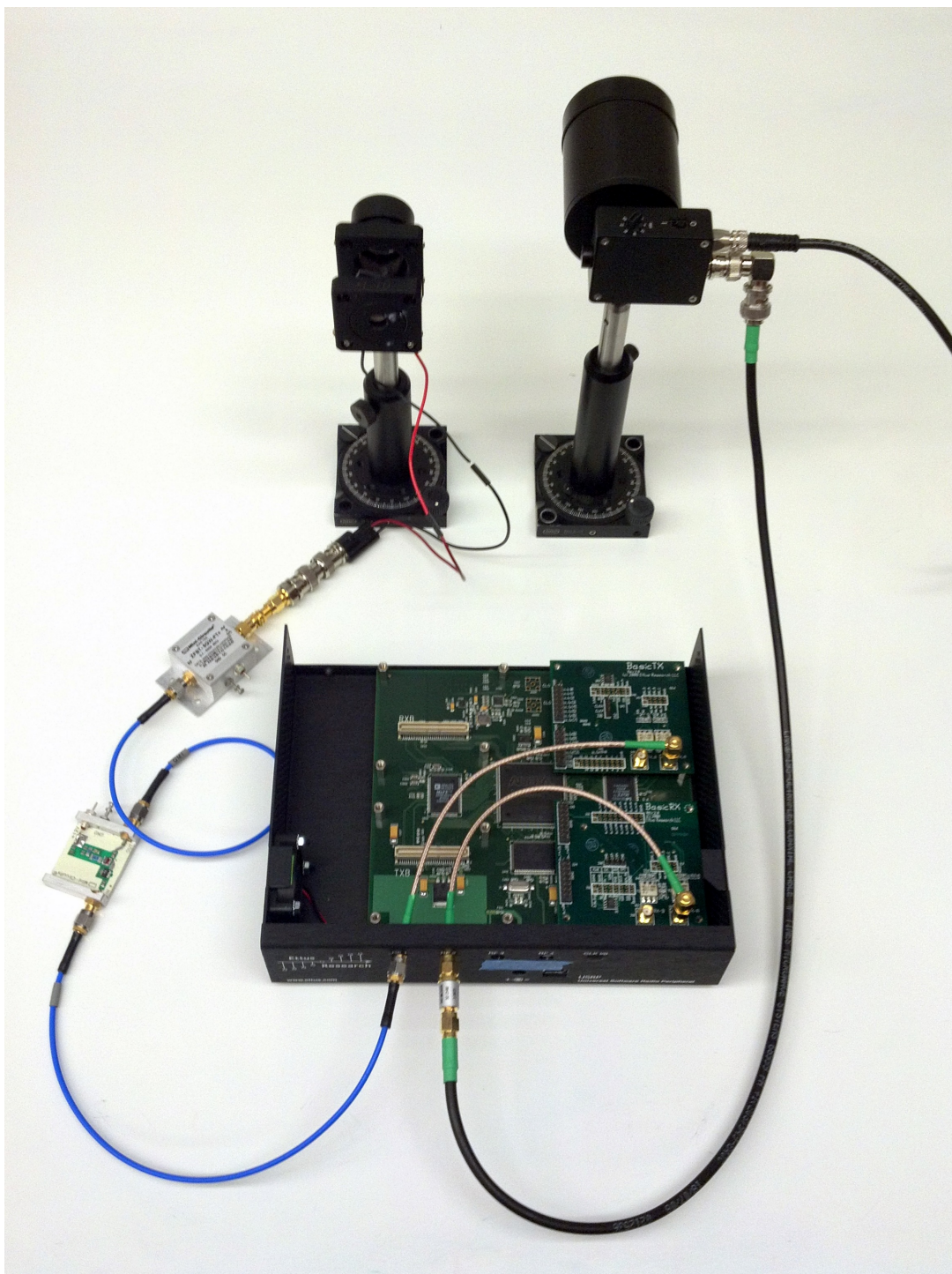


Figure 6.32: Picture of one of the SDR transceivers. Image shows the PD receiver and LED transmitter, along with the USRP digitizer.

is the theoretical system performance. It can be seen that the system performs within 3 dB of the theoretical limit. When comparing the system performance versus the c value of the water, in Fig. 6.34, the variability of the data is removed, indicating that the SNR estimator used in the GNURadio system may be what is causing the noisy data in Fig. 6.33. The electrical power of the three transmitters was approximately equal, however the optical output power of the green LED was much lower than the blue LED and the diode laser. The added performance of the laser is due to the limited geometric at the link operating distance (3.66 m). It should also be noted that this system operated without an error control coding.

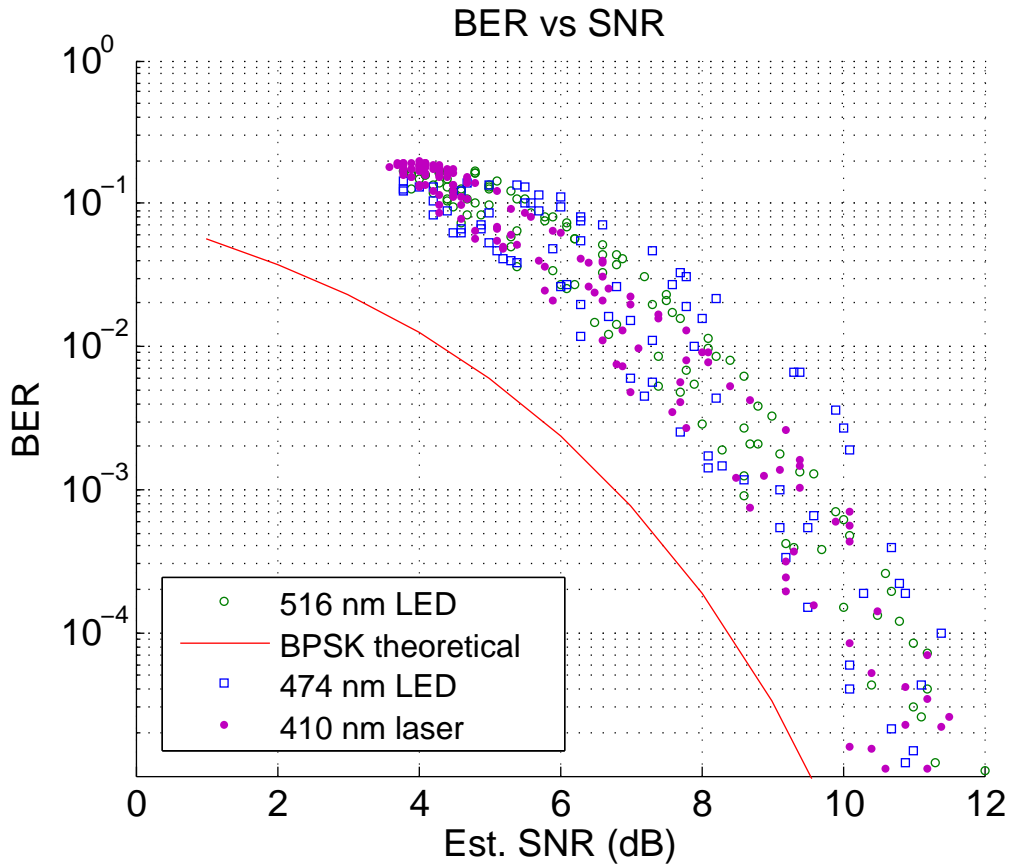


Figure 6.33: Theoretical and experimental BER versus SNR system performance. The experimental system does not perform as well as theory, but is generally within 3 dB of the performance. Also, the system operating with two different wavelength LEDs, and with a 410 nm diode laser have similar performance when compared on this metric.

Using two sets of optical receivers and transmitters allowed a bi-directional network link to be

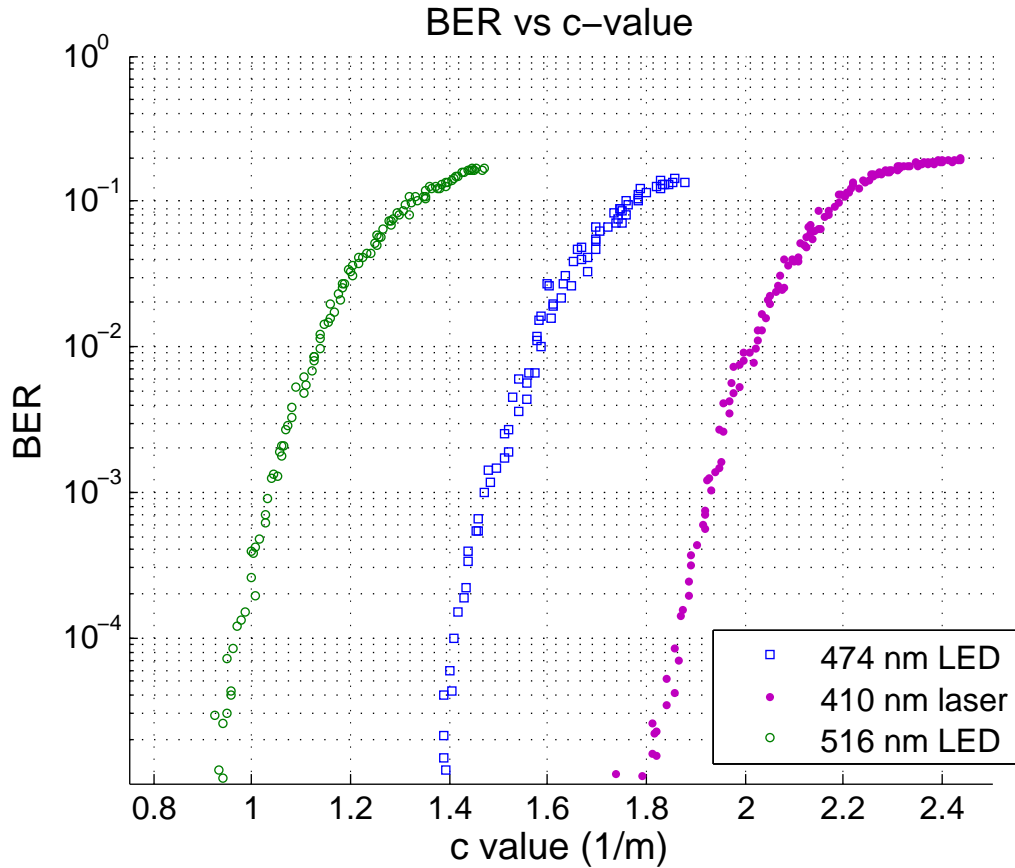


Figure 6.34: Experimental BER versus attenuation length. The different optical output powers of the various systems is very clear, along with the lack of geometric loss for the laser transmitter.

established. Using the GNURadio example program, `tunnel.py`, a virtual network connection was established across the optical link. The network benchmark tool, `netperf`, was used to test the performance of the network link, including throughput and latency. This was tested for a bidirectional link consisting of two LEDs at different wavelengths (474 nm and 516 nm) and at similar wavelengths (474 nm and 448 nm), and for a bidirectional link consisting of two diode lasers at 410 nm. The performance for the LED duplex link is shown in Fig. 6.35 and the results for the laser-based duplex link are shown in Fig. 6.37. The network latency is shown in Fig. 6.36 for the LED system and Fig. 6.37 for the laser-based system.

The throughput performance of the LED-based systems shows that, due to the lower optical power of the 516 nm LED, the link throughput drops well before the 474 nm LED. Also, for the system utilizing similar wavelength LEDs, the link performance for both extends further than the 516/474nm system. The system latency reflects this behavior.

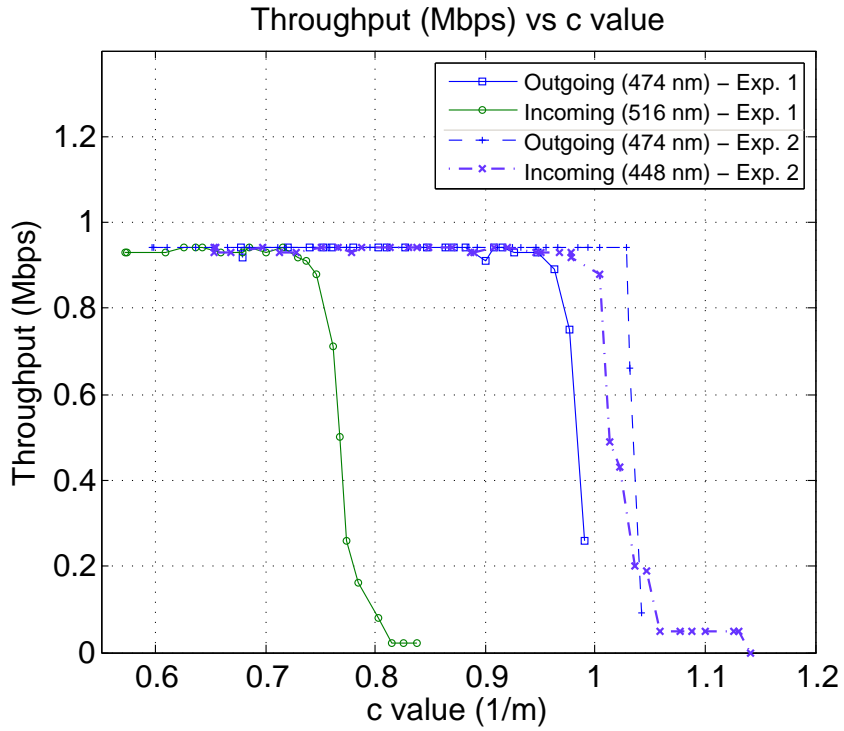


Figure 6.35: Throughput for the two sets of LED-based network links.

For the laser-based system, the throughput is maintained to a greater c value than the LED-based systems due to reduction in geometric losses - e.g. the laser beam is contained within the 2" receiver optic on the photodiode receiver.

Conclusion

In conclusion, a LED and laser based optical communication link was established using a software defined radio system. The system operated with a subcarrier intensity modulation scheme that could potentially allow for multi bit-per-symbol modulation schemes that can increase the datarates of a system with a fixed bandwidth. This is important with LED-based transmitters, as LEDs tend to have limited bandwidth (usually < 10 MHz). The system operated with a network throughput of nearly 1 Mbps and delivered bidirectional communication. Future work will include expanding the range of the system and packaging it for underwater experiments.

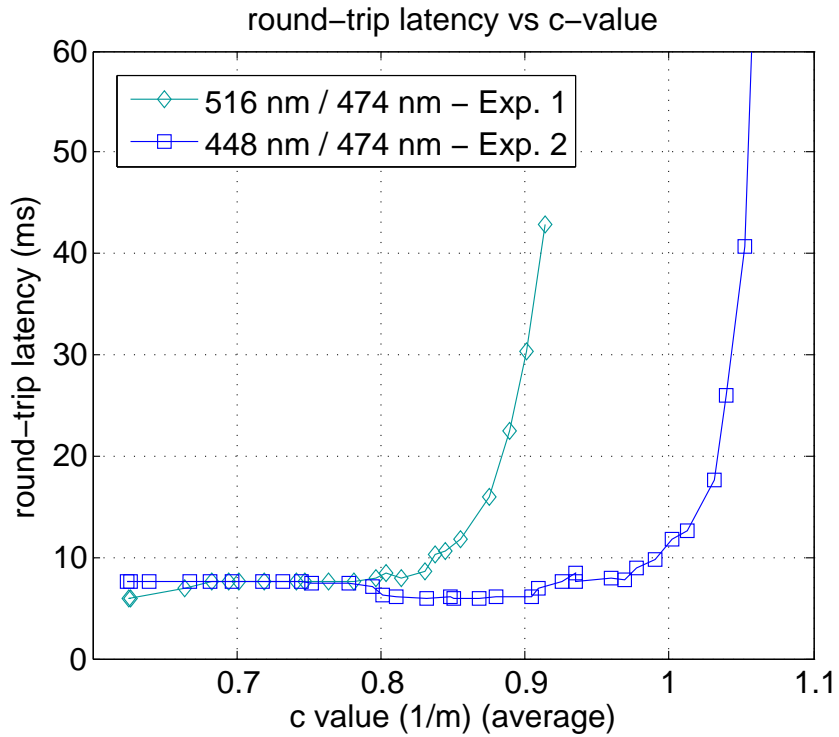


Figure 6.36: Network latency for the two sets of LED-based network links.

6.8 Conclusion

In this chapter we have explored the link budget and applications of underwater optical communication. The results from previous chapters were compared to theoretical link budget calculations that take into account both the received signal power, the background radiation and the electrical noise of the system. Received power from LEDs, laser beams, and diffuse points sources were considered. Additionally, a basic model for defining the optical power loss between receiver and transmitter was proposed and compare with the simulated results in Chapter 5. A two-term exponential function was used to fit the experimental results and a fit metric was shown. The two-term model showed good agreement over many orders of magnitude in received power. Matching the fit parameters to channel and link parameters is still an active area of study, though a basic model for accounting for single scattered light in the low turbidity region was shown in Section 6.4.1. Finally, link considerations for both the transmitter and receiver were discussed.

In addition to the link budget and models, this chapter also presented several practical applications and experiments of underwater optical communication. A polarization modulation system, MEMS modulating retroreflector system, and a SDR optical network connection were presented. The results show the practicality of using many different system implementations for achieving an optical link in

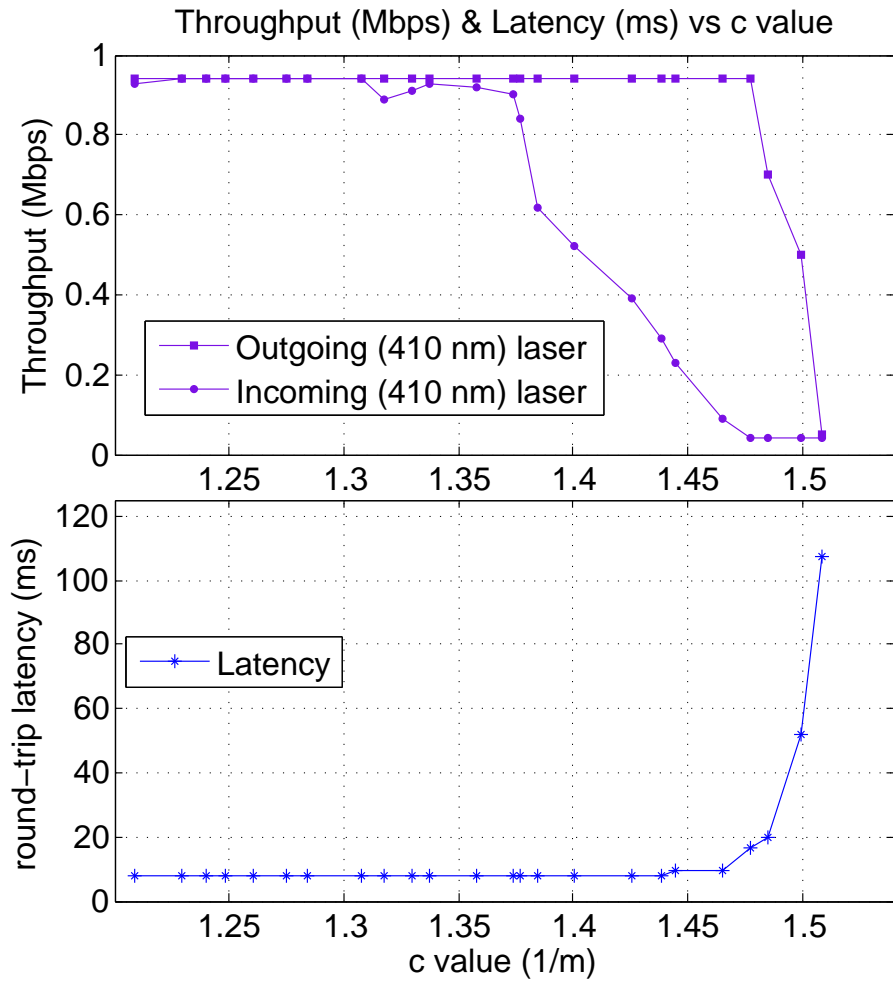


Figure 6.37: Throughput and latency for laser based optical network link.

the water environment. Each system has its own unique advantages and concerns, and are appropriate in a variety of situations.

In conclusion, this chapter has established a theoretical understanding of the signal and noise parameters of an underwater optical communication system. Analytical forms of power loss were proposed and compared with simulated results. A practical link budget is an important part of closing the loop between experimental and theoretical systems and ultimate fielding useful optical communication systems in natural bodies of water.

CHAPTER 7

Conclusion and Future Work

Underwater optical communication presents a unique opportunity for high data-rate, low-latency communication in the oceans. Previously, underwater communication was limited to tethered applications using a cable or very low data-rates using acoustic communication. While this has served as a viable solution for many years, real-time control of underwater vehicles or applications involving large amounts of data, such as real-time video, have been unachievable. Many possible applications could be explored using the advantages that underwater optical communication present. Several of these examples are discussed in the following paragraphs.

For example, an underwater sensor network could be outfitted with an optical modem. The sensor network would collect data over a long period of time and store its data. In order to retrieve the data from the network, an unmanned vehicle or submarine could maneuver past the network, initiating a data transfer, and collect the stored data in a fraction of the time that it would take for an acoustic link. Additionally, such a method would be covert and feasible for a non-stationary up-link, which would be impossible for a tethered connection.

A second example would be for non-contact data transfer during docking. Instead of having a vehicle dock and make a physical connection in order to exchange data, the docking station could be outfitted with modulating retroreflectors which would both provide a means of data transfer over a short distance, and also a way to exchange localization data to aid the vehicle in docking. This would be appropriate in shallow waters which causes severe multi-path interference with acoustic links.

A third possible use-case would be for real-time video feedback and teleoperation of remote vehicles underwater using an optical link. The high latency of an acoustic communication link make it prohibitive for this type of use, along with the high data-rate requirements for streaming video. In

this case, an optical communication link could provide both the low latency for teleoperation and the necessary bandwidth for streaming video operation. This type of arrangement could be used for underwater inspection or mining operations. For a multi-agent system, omnidirectional transmission of the optical source would most likely be necessary, along with omnidirectional reception. A multi-hop network could be used to relay information between the different operating vehicles and the controller.

A final example case would be equipping low power sensor nodes, perhaps which are powered by the ocean's internal currents, with low power optical communicators, like the modulating retro-reflector discussed previously. In this case, the sensor node would be able to detect an interrogating optical source and then return the requested data to the interrogator. Such a sensor node could be nearly passive while not exchanging data, and exchange data in a higher power mode only when necessary.

These examples are meant to provide inspiration to future scientists and engineers. They are also meant to show the varied nature of optical communication in the oceans. As scientists seek to understand and exploit the ocean's benefits to humanity, additional sensing is required. Underwater optical communication is an attractive means of filling gaps left by other communication methods.

7.1 Future Work

Future work involves both the MCNS and its applications. In regards to the MCNS, Photonator, the speed of the simulation is a major factor in determining whether or not a simulation is feasible. Current simulations, such as the results at 30 attenuation lengths, feature billions of photons scattered through the channel. Typically these types of simulations can range from several to tens of hours. Future improvements would involve additional parallelization that would allow the simulation to not only run on multiple computers at once, but also to divide the simulation into much larger blocks than are currently supported. The simulation has been tested running up to eight simultaneous tracking threads, and using the MATLAB parallel toolbox and the parallel server, this number could easily be expanded. A second method of speed improvement would be to compile the program to run in a language other than MATLAB. It is expected that this would boost performance significantly, but it would involve a potentially lengthy validation process in order to make sure that the results were the same as when running in MATLAB. Finally, the major component of the simulation that takes the most time is choosing the polar scattering angles from the scattering phase function. Improvements to this method would include reducing the size of the lookup table, using an analytical function, or remapping the phase function such that the probability indices of the CDF were linearly spaced, and could be used as the index of the scattering angle array.

Future work involving the use of the simulation tool would involve using it to simulate different types of light sources, such as LEDs or a purposefully diffused laser source. Additionally, it would be

helpful to quantize the ability to do off-axis communication or sensing, such as using a receiver and transmitter pair to analyze the backscattering from the signal for channel sensing. This kind of result could easily be simulated with Photonator. Also, there is much work to be done in parameterizing the slope of the highly scattering power loss curve, as this is a function of both the VSF, receiver FOV and aperture.

Another potential expansion to the MCNS would be to add polarization information to the propagating photons. This would complicate matters in that each scattering event would be directionally dependent, in that not only would the photon's electric field components need to be tracked, but depending on the random orientation of the scattering particle, the scattering angle would differ. This type of simulation would add complication but would also help validate the use of a polarization modulation system, as shown in Section 6.7.1, or the use of a polarization dependent receiver/transmitter for filtering out backscattered light.

Finally, it would be very helpful to catalog and make available simulated datasets for other researchers. Since simulations can take a long amount of time, running them multiple times isn't very efficient for the research community. Having the MCNS automatically upload and catalog the lightfield on a plane, along with storing the appropriate initial conditions, would be a useful tool to the research community, and could also be used for cataloging actual water data that could be used for additional validation of the simulation.

7.2 Conclusion

The goal of this research was to present several tools to the underwater optical communication system designer. These were a validated numerical simulation for computing the received optical signal power, along with theoretical calculations for computing the SNR of the received signal. These two aspects were shown in Chapter 4 and in Chapter 6, with the results from the simulation tool principally shown in Chapter 5.

The simulation tool, a Monte Carlo numerical simulation, "Photonator", is a very flexible simulation tool that allows any number of source functions, scattering phase functions, or receiver configurations to be simulated prior to fielding a system in natural waters. This allows a system designer to first prove the concept before spending the time and effort to test a design in the costly and dangerous ocean environment. The simulation output, coupled with theoretical SNR calculations will allow a system designer to determine how effective a given modulation scheme or detector will function prior to building or testing, and can be used to test novel communication ideas, such as a modulating retroreflector, or non-line-of-sight transmission and detection, where existing theoretical channel models may not be valid. The MCNS also allows for accurate channel bandwidth calculations, along with understanding the probability density function of various scattering orders of the received signal. These results are difficult or impossible to arrive at with analytical solutions. Finally, the source

code for the simulation is freely available and approachable to other researchers and engineers in the field. It is hoped that the code will be used for future work and expanded and shared by others who continue in this field. While other models exist, the author feels that by making the computer simulation code public, the results are easily verifiable and can be used to bootstrap continuing expansion in the field of underwater optical communication.

Among the major contributions of this research are showing that the FOV and aperture of an optical system are independent in highly turbid waters, and that increasing one does not necessarily affect the other. Additionally, a power-law relationship between FOV and received power was shown for turbid water environments for fields-of-view up to about 45 degrees. Thirdly, the first ever simulated results for the scattering orders at the receiver of an underwater optical communication system were shown, which provides a physical underpinning to the temporal results also demonstrated. Fourthly, it was shown that the temporal bandwidth of an underwater optical communication system is largely impacted by the field-of-view, with very little response due to changes in the aperture size. Finally, the first ever open-source, validated, Monte Carlo numerical simulation for underwater optical communication was presented.

In conclusion, this research has presented an experimentally validated simulation tool for computing various aspects of an underwater optical communication system. Additionally, simulated results and theoretical models for designing an optical communication system have been shown, along with example uses for such data.

REFERENCES

- [1] X. Che, I. Wells, G. Dickers, P. Kear, and X. Gong. Re-evaluation of RF electromagnetic communication in underwater sensor networks. *Communications Magazine, IEEE*, 48(12):143–151, 2010.
- [2] William C. Cox. *A 1 Mbps Underwater Communication System Using a 405 nm Laser Diode and Photomultiplier Tube*. M.s. thesis, North Carolina State University, Raleigh, NC, 2007.
- [3] J.A. Simpson. *A 1 Mbps Underwater Communications System using LEDs and Photodiodes with Signal Processing Capability*. PhD thesis, NC State University, 2008.
- [4] Clifford Pontbriand, Norman Farr, Jonathan Ware, James Preisig, and Hugh Popenoe. Diffuse high-bandwidth optical communications. In *Proc. OCEANS Conf. 2008*, pages 1–4. Ieee, 2008.
- [5] N Farr, J Ware, C Pontbriand, and T Hammar. Optical communication system expands CORK seafloor observatory’s bandwidth. In *Proc. OCEANS Conf. 2010*, Seattle, WA, 2010.
- [6] Frank Hanson and Stojan Radic. High bandwidth underwater optical communication. *Applied optics*, 47(2):277–83, January 2008.
- [7] Davide Anguita and Davide Brizzolara. Optical wireless communication for underwater Wireless Sensor Networks: Hardware modules and circuits design and implementation. In *Proc. OCEANS Conf. 2010*, Seattle, WA, 2010.
- [8] Brandon Cochenour, Linda Mullen, Alan Laux, and Tom Curran. Effects of multiple scattering on the implementation of an underwater wireless optical communications link. In *Oceans 2006*, pages 1–6, 2006.
- [9] William C. Cox, Jim A. Simpson, Carlo P. Domizioli, John F. Muth, and Brian L. Hughes. An underwater optical communication system implementing Reed-Solomon channel coding. In *Proc. OCEANS Conf. 2008*, pages 1–6, Quebec, Canada, 2008. Ieee.
- [10] Marek Doniec and Daniela Rus. BiDirectional Optical Communication with AquaOptical II. In *Embedded Networked Sensor Systems*, Zurich, Switzerland, 2010.
- [11] Marek Doniec, Carrick Detweiler, Iuliu Vasilescu, and Daniela Rus. Using Optical Communication for Remote Underwater Robot Operation, 2010.
- [12] William C. Cox, Kory F Gray, Jim A Simpson, Brandon Cochenour, Brian L Hughes, and John F Muth. A MEMS Blue / Green Retroreflecting Modulator for Underwater Optical Communications. In *Proc. OCEANS Conf. 2010*, Seattle, WA, 2010.
- [13] William C Cox, Jim A Simpson, and John F Muth. Underwater Optical Communication Using Software Defined Radio Over LED and Laser Based Links. In *Military Communications Conference, 2011. MILCOM 2011. IEEE*, Baltimore, MD, 2011.
- [14] Edward Leonardo. *The notebooks of Leonardo da Vinci*. G. Braziller, New York, 1954.

- [15] A. Quazi and W. Konrad. Underwater acoustic communications. *IEEE Communications Magazine*, 20(2):24–30, March 1982.
- [16] M. Stojanovic. Underwater acoustic communications. In *Proceedings of Electro/International 1995*, pages 435–440. IEEE, 1995.
- [17] Arun K Majumdar and Jennifer C Ricklin, editors. *Free-Space Laser Communications: Principles and Advances (Optical and Fiber Communications Reports)*. Springer, 2007.
- [18] D. R. McConathy. Submarine laser communications. *EASCON '82; Annual Electronics and Aerospace Systems Conference*, -1:277–282, 1982.
- [19] T. Wiener and S. Karp. The Role of Blue/Green Laser Systems in Strategic Submarine Communications. *IEEE Transactions on Communications*, 28(9):1602–1607, September 1980.
- [20] John D. Feichtner. Satellite to Submarine Laser Communications (SLC): Advanced filter technology. *Lockheed Missiles and Space Co. Report*, -1, January 1992.
- [21] Dennis Killinger. Free Space Optics for Laser Communication Through the Air. *Optics and Photonics News*, 13(10):36, October 2002.
- [22] WC Cox Jr. A 1 Mbps Underwater Communication System Using a 405 nm Laser Diode and Photomultiplier Tube. Master of, 2008.
- [23] Hoa Le Minh, Dominic O'Brien, Grahame Faulkner, and Lubin Zeng. 80 Mbit/s Visible Light Communications using pre-equalized white LED. In *2008 34th European Conference on Optical Communication*, pages 1–2. IEEE, 2008.
- [24] Kaiyun Cui, Gang Chen, Qunfeng He, and Zhengyuan Xu. Indoor optical wireless communication by ultraviolet and visible light, 2009.
- [25] J.A. Simpson, B.L. Hughes, and J.F. Muth. A spatial diversity system to measure optical fading in an underwater communications channel. In *OCEANS 2009*, pages 1–6, Biloxi, MS, 2009. IEEE.
- [26] S. Karp. Optical communications between underwater and above surface (satellite) terminals. *Communications, IEEE Transactions on*, 24(1):66–81, 1976.
- [27] Judith Bannon Snow, James P Flatley, Dennis E Freeman, Mark A Landry, Carl E Lindstrom, Jacob R Longacre, and Joshua A Schwartz. Underwater propagation of high data rate laser communications pulses. In *Ocean Optics XI*, volume 1750. SPIE, 1992.
- [28] Sermsak Jaruwatanadilok. Channel Modeling and Performance Evaluation using Vector Radiative Transfer Theory. 26(9):1620–1627, 2008.
- [29] Linda Mullen, Alan Laux, and Brandon Cochenour. Propagation of modulated light in water: implications for imaging and communications systems. *Applied optics*, 48(14):2607–12, May 2009.
- [30] A. Laux, R. Billmers, L. Mullen, Brian Concannon, J. Davis, J. Prentice, and V. Contarino. The a, b, cs of oceanographic lidar predictions: a significant step toward closing the loop between theory and experiment. *Journal of Modern Optics*, 49(3):439–451, March 2002.

- [31] Linda Mullen, Brandon Cochenour, William Rabinovich, Rita Mahon, and John Muth. Backscatter suppression for underwater modulating retroreflector links using polarization discrimination. *Applied Optics*, 48(2):328–37, January 2009.
- [32] Brandon Cochenour, Linda Mullen, and Alan Laux. Phase Coherent Digital Communications for Wireless Optical Links in Turbid Underwater Environments. In *Oceans 2007*, volume 1, pages 1–5. Ieee, 2007.
- [33] Brandon Cochenour, Linda J. Mullen, and Alan E. Laux. Characterization of the Beam-Spread Function for Underwater Wireless Optical Communications Links. *IEEE Journal of Oceanic Engineering*, 33(4):513–521, October 2008.
- [34] Brandon Cochenour, Linda Mullen, and John Muth. Effect of scattering albedo on attenuation and polarization of light underwater. *Optics letters*, 35(12):2088–90, June 2010.
- [35] Shlomi Arnon and Debbie Kedar. Non-line-of-sight underwater optical wireless communication network. *Journal of the Optical Society of America. A, Optics, image science, and vision*, 26(3):530–9, March 2009.
- [36] Debbie Kedar and Shlomi Arnon. Optical wireless communication through fog in the presence of pointing errors. *Applied optics*, 42(24):4946–54, August 2003.
- [37] Frank Hanson and Mark Lasher. Effects of underwater turbulence on laser beam propagation and coupling into single-mode optical fiber. *Applied Optics*, 49(16):3224–3230, June 2010.
- [38] Shlomi Arnon, D. Sadot, and N. S. Kopeika. Analysis of Optical Pulse Distortion Through Clouds for Satellite to Earth Adaptive Optical Communication, August 1994.
- [39] Binbin Wu, Brian Marchant, and Mohsen Kavehrad. Channel modeling of light signals propagating through a battlefield environment: analysis of channel spatial, angular, and temporal dispersion. *Applied Optics*, 46(25):6442, September 2007.
- [40] Curtis D Mobley. *Light and Water : radiative transfer in natural waters*. Academic Press, San Diego, 1994.
- [41] Dominique Toublanc. Henyey-Greenstein and Mie phase functions in Monte Carlo radiative transfer computations. *Applied Optics*, 35(18):3270, June 1996.
- [42] JTO Kirk. Monte Carlo study of the nature of the underwater light field in, and the relationships between optical properties of, turbid yellow waters. *Marine and Freshwater Research*, 32(4):517, 1981.
- [43] Kirk Jonathan (U.C. Santa Barbara) Waters. *Monte Carlo modeling of the open ocean light field*. PhD thesis, 1994.
- [44] Jing Li, Yong Ma, Qunqun Zhou, Bo Zhou, and Hongyuan Wang. Channel capacity study of underwater wireless optical communications links based on Monte Carlo simulation. *Journal of Optics*, 14(1):015403, January 2012.
- [45] Curtis Mobley. Ocean Optics Web Book.

- [46] Richard W Spinrad, Kendall L Carder, and Mary Jane Perry. *Modeling and Simulating Radiative Transfer in the Ocean*. Oxford monographs on geology and geophysics ; no. 25. Oxford University Press ; Clarendon Press, New York, 1994.
- [47] MA Chancey. *Short range underwater optical communication links*. PhD thesis, NC State University, Raleigh, 2005.
- [48] Alan Weidemann. Evaluating Realistic Volume Scattering Functions on Underwater Imaging System Performance. Technical report, 2008.
- [49] TJ Petzold. Volume scattering functions for selected ocean waters. Technical report, Scripps Institute of Oceanography, San Diego, CA, 1972.
- [50] Vladimir I Haltrin. phase function for light scattering in seawater. *Applied Optics*, (5), 2002.
- [51] Curtis D Mobley, Lydia K Sundman, and Emmanuel Boss. Phase function effects on oceanic light fields. *Applied optics*, 41(6):1035–50, March 2002.
- [52] G.R. Fournier and M. Jonasz. Computer-based underwater imaging analysis. In *Proceedings of SPIE*, volume 3761, page 62, 1999.
- [53] G.R. Fournier and J.L. Forand. Analytic phase function for ocean water. In Jules S. Jaffe, editor, *Proceedings of SPIE*, volume 2258, page 194, Bergen, Norway, 1994.
- [54] H C Van De Hulst and Light Scattering. H. C. van de Hulst, Light Scattering by Small Particles, Wiley, NewYork 1957. *Small*, 1957.
- [55] A Morel. BIO-OPTICAL MODELS, 2001.
- [56] J.R.V. Zaneveld, M.S. Twardowski, K.S. Shifrin, W.S. Pegau, E. Boss, and I. Zolotov. Inversion of light scattering measurements to obtain biogeochemical parameters. Technical report, Oregon State University, Santa Fe, New Mexico, 2002.
- [57] Włodzimierz Freda and Jacek Piskozub. Improved method of Fournier-Forand marine phase function parameterization. *Optics express*, 15(20):12763–8, October 2007.
- [58] Victor F Weisskopf. Neutron Diffusion. In Clark Goodman, editor, *The science and engineering of nuclear power*, chapter 3, pages 87–97. Addison-Wesley Press, Cambridge, 2nd edition, 1952.
- [59] Robert M. Lerner and John D. Summers. Monte Carlo description of time- and space-resolved multiple forward scatter in natural water. *Applied Optics*, 21(5):861, March 1982.
- [60] Brandon Cochenour and Linda Mullen. Free Space Optical Communications Underwater. In Shlomi Arnon, John Barry, George Karagiannidis, Robert Schober, and Murat Uysal, editors, *Advanced Optical Wireless Communication Systems*. Cambridge University Press, 2012.
- [61] Jules S. Jaffe. Monte Carlo modeling of underwater-image formation: validity of the linear and small-angle approximations. *Applied Optics*, 34(24):5413, August 1995.

- [62] RA Leathers, Trijntje Downes, CO Davis, and CD Mobley. Monte Carlo Radiative Transfer Simulations for Ocean Optics: A Practical Guide. Technical report, Naval Research Laboratory, 2004.
- [63] Jessica C Ramella-Roman, Scott a Prahl, and Steven L Jacques. Three Monte Carlo programs of polarized light transport into scattering media: part II. *Optics express*, 13(25):10392–405, December 2005.
- [64] Oswaldo González, Silvestre Rodríguez, Rafael Pérez-Jiménez, Beatriz R Mendoza, and Alejandro Ayala. Comparison of Monte Carlo ray-tracing and photon-tracing methods for calculation of the impulse response on indoor wireless optical channels. *Optics express*, 19(3):1997–2005, January 2011.
- [65] Lihong Wang and S.L. Jacques. Monte Carlo modeling of light transport in multi-layered tissues in standard C. *The University of Texas, MD Anderson Cancer Center, Houston*, 1992.
- [66] Duncan Forgan. An Introduction to Monte Carlo Radiative Transfer. Technical report, Institute for Astronomy Royal Observatory Edinburgh, Edinburgh, 2009.
- [67] VI Haltrin. Monte Carlo Modeling of Light Field Parameters in Ocean with Petzold Laws of Scattering. *Environmental Research*, I(March):17–19, 1997.
- [68] Eric Veach. *Robust Monte Carlo methods for light transport simulation*. PhD thesis, Stanford University, 1997.
- [69] Vladimir I Haltrin. THEORETICAL AND EMPIRICAL PHASE FUNCTIONS FOR MONTE CARLO CALCULATIONS OF LIGHT SCATTERING IN SEAWATER * I-509 I-510. *Environmental Research*, I(March):17–19, 1997.
- [70] Eric W. Weisstein. Circle-Circle Intersection – from Wolfram MathWorld.
- [71] Peter (Stanford) Glynn. The Central Limit Theorem , Law of Large Numbers and Monte Carlo Methods. In *CME308: Stochastic Methods in Engineering Course Notes*, volume 2, chapter 3, pages 23–61. 2009.
- [72] Athanasios Papoulis, NCSU Retired Faculty Endowment., Staff Library, and S. Unnikrishna Pillai. *Probability, random variables, and stochastic processes*. McGraw-Hill series in electrical and computer engineering. McGraw-Hill,, Nyew York, NY, 4th ed. edition, 2002.
- [73] E. E. (Elmer Eugene) Lewis and W. F Miller. *Computational methods of neutron transport*. Wiley,, New York, 1984.
- [74] M Jeruchim. Techniques for estimating the bit error rate in the simulation of digital communication systems. *Areas in Communications, IEEE Journal on*, (1):153–170, 1984.
- [75] B.P Welford. American Society for Quality. *Technometrics*, 4(3):419–420, 1962.
- [76] Donald Knuth. Seminumerical Algorithms. In *The Art of Computer Programming*, page 232. Addison-Wesley Press, Boston, 3rd edition, 1988.

- [77] T.F Chan, G.H. Golub, R.J. LeVeque, and STANFORD UNIV CALIF DEPT OF COMPUTER SCIENCE. Updating formulae and a pairwise algorithm for computing sample variances. Technical report, Stanford University, 1979.
- [78] E. Berrocal. *Multiple scattering of light in optical diagnostics of dense sprays and other complex turbid media*. PhD thesis, Cranfield University, 2006.
- [79] Scott Prahl. Mie Scattering Calculator.
- [80] PK Milsom. A ray-optic, Monte Carlo, description of a Gaussian beam waist applied to reverse saturable absorption. *Applied Physics B: Lasers and Optics*, 70(4):593–599, 2000.
- [81] Eugene Hecht. *Optics*, volume 1. Addison Wesley, 4th edition, 2001.
- [82] Bahaa E. A. B.E.A. Saleh and Malvin Carl M.C. Teich. Beam Optics. In *Fundamentals of Photonics*, Wiley series in pure and applied optics, page 85. John Wiley & Sons; 1st edition, New York, 1st edition, 1991.
- [83] F.R. Gfeller and U. Bapst. Wireless in-house data communication via diffuse infrared radiation. *Proceedings of the IEEE*, 67(11):1474–1486, 1979.
- [84] J.M. Kahn and J.R. Barry. Wireless infrared communications. *Proceedings of the IEEE*, 85(2):265–298, 1997.
- [85] Hongming Yang, Jan W M Bergmans, Tim C W Schenk, Jean-Paul M G Linnartz, and Ronald Rietman. An analytical model for the illuminance distribution of a power LED. *Optics express*, 16(26):21641–6, December 2008.
- [86] A.A. Farid and Steve Hranilovic. Outage capacity optimization for free-space optical links with pointing errors. *Journal of lightwave technology*, 25(7):1702–1710, 2007.
- [87] Helgi Arst. *Optical Properties and Remote Sensing of Multicomponent Water Bodies*.
- [88] S Karp, R M Gagliardi, S E Moran, and L B Stotts. *Optical channels: fibers, clouds, water, and the atmosphere*, volume 424. Plenum Press, New York, 1988.
- [89] Curtis D Mobley. *Chapter 9 Eigenmatrix Methods*.
- [90] N G Jerlov. Optical Oceanography. volume 5, pages Pg 15, 51–62, 118–126. Elsevier Publishing Company, New York, 1968.
- [91] John W Giles and Isaac N Bankman. PART 2 : BASIC DESIGN CONSIDERATIONS. *Applied Physics*, pages 1–6.
- [92] Curtis D Mobley. Radiative Transfer Theory, 2010.
- [93] Seibert Q Duntley. Light in the sea. *Journal of the Optical Society of America*, 53(2):214–233, August 1963.
- [94] Shlomi Arnon. Optical wireless communication. In Ronald G. Driggers, editor, *Encyclopedia of optical engineering, Volume 2*, page 3104. Marcel Dekker, New York, 2003.

- [95] C A Gueymard, D Myers, and K Emery. Proposed reference irradiance spectra for solar energy systems testing. *Solar Energy*, 73(6):443–467, 2002.
- [96] David G. Aviv. *Laser Space Communications*. Artech House, Boston, MA, 2006.
- [97] William K Pratt. *Laser Communication Systems*. Wiley series in pure and applied optics. Wiley, New York, 1969.
- [98] C E Shannon. A Mathematical Theory of Communication. *Bell System Technical Journal*, 27(1):379–423, 1948.
- [99] J Everett. *Forward-Error Correction Coding for Underwater Free-space Optical Communication*. PhD thesis, Raleigh, NC, 2009.
- [100] William C. Cox, Brian L Hughes, and John F Muth. A Polarization Shift-Keying System for Underwater Optical Communications. In *Oceans 2009*, 2009.
- [101] Alexander P Vasilkov, Yury A Goldin, Boris A Gureev, Frank E Hoge, Robert N Swift, and C Wayne Wright. Airborne Polarized Lidar Detection of Scattering Layers in the Ocean. *Applied Optics*, 40(24):4353–4364, 2001.
- [102] Jim A Simpson, William C. Cox, John R Krier, Brandon Cochenour, Brian L Hughes, and John F Muth. 5 Mbps Optical Wireless Communication with Error Correction Coding for Underwater Sensor Nodes. In *Proc. OCEANS Conf. 2010*, pages 6–9, Seattle, WA, 2010.

APPENDICES

APPENDIX A

Errata and Changes

Corrections, changes and updates to this document or the Photonator source code can be found at the author's website:

<http://gallamine.com/thesis/>

APPENDIX B

Photonator MCNS Source Code

Complete source code and documentation for Photonator can be found online at <http://gallamine.com/thesis/> or directly at <http://www.github.com/gallamine/Photonator>. The copy below is for archival purposes.

```
% MC simulation for photon movementr
% V3 - changed propogation to z-axis, changed equations for updating
% position/angle
% V4 - Lots of changes to statistics calculations - mean and variance

% clear all
% clc

% Set the random stream seed to something ... wait for it ... random
RandStream.setDefaultStream ...
    (RandStream('mt19937ar','seed',sum(100*clock)));

% Change some things if we're running on Linux (i.e. on AWS)
if (isunix())
    userData = urlread('http://169.254.169.254/latest/user-data');
    if (~strcmp(userData, 'autorun_sim'))
        %error('No autorun');
    else
        autorun = 1;
        cd('/home/wccox/Dropbox/WCC Research/mc');
```

```

% Define these variables appropriately:
mail = 'from@gmail.com'; %Your GMail email address
load password

% Then this code will set up the preferences properly:
setpref('Internet','E_mail',mail);
setpref('Internet','SMTP_Server','smtp.gmail.com');
setpref('Internet','SMTP_Username',mail);
setpref('Internet','SMTP_Password',password);
props = java.lang.System.getProperties();
props.setProperty('mail.smtp.auth','true');
props.setProperty('mail.smtp.socketFactory.class', ...
    'javax.net.ssl.SSLSocketFactory');
props.setProperty('mail.smtp.socketFactory.port','465');

% Send the email. Note that the first input is the address you are ...
    sending the email to

sendmail('to@gmail.com','Simulation started on AWS.')
end
end

if (isunix())
    dataDir = '/home/wccox/';
    simDir = '/home/wccox/Dropbox/WCC Research/mc';
else
    %dataDir = 'C:\Users\wccox\Documents\ThesisData\TankSimulations\Harbor';
    dataDir = 'D:\Simulation Data\Practice';
    simDir = 'C:\Users\wccox\Dropbox\WCC Research\mc';
end

usersEmail = 'to@gmail.com';      % This user will be emailed info about the ...
    finished simulation.

useVCL = 'false';                % save output file to k drive
sendEmail = 'true';               % Send email at start and stop of simulation
saveOutput = 'true';              % Save the output data to a folder
ftpData = 'false';                % FTP data back to FTP server at ...
    conclusion of simulation

num_photons = 1e6;                % number of photons simulated per ...
    batch/group
num_sims = 10;                   % number of groups to simulate
n_water = 1.33;                  % index of refraction of water
n_window = 1.585;                % index of refraction of polycarbonate

```

```

diverg = 0;
g = 0.93;
wallReflect = 1; % This flag isn't used for infinite ...
environments (like open ocean)
%[cdf_scatter,angle] = generate_scatter('measured','petzold_harbor');
%[cdf_scatter,angle] = generate_scatter('measured','petzold_coastal');
[cdf_scatter,angle] = generate_scatter('measured','petzold_clear');
% [cdf_scatter,angle] = generate_scatter('measured','petzold_maalox');
% [cdf_scatter,angle] = generate_scatter('measured','widemann_maalox');
% [cdf_scatter,angle] = generate_scatter('measured','petzold_avg');
% [cdf_scatter,angle] = generate_scatter('measured','mie_1_micron');
%[cdf_scatter,angle] = generate_scatter('calc','hg',g);

% Create an average VSF from Harbor and Coastal
% [cdf_scatter2,angle] = generate_scatter('measured','petzold_coastal');
% cdf_scatter = (cdf_scatter + cdf_scatter2) ./ 2;

% albedo = (c-a)/c; % Water albedo is scattering coef./atten. coef. (b/c ...
unitless)
%% Albedo of Maalox (ranges from 0.8 to 0.95) - IF YOU CHANGE THIS, BE SURE ...
TO CHANGE THE MINIMUM POWER VALUE!!! %%%
%albedo = 0.83;
% albedo = 0.55;
% albedo = 0.69; % Coastal/Harbor water albedo
% albedo = 0.7366;
albedo = 0.25;

attenuationLength = 12;
%c = 0.40; % Harbor ~= 2.19, ...
Coastal ~= 0.49, Clear ~= 0.15
c = 0.15;
%c = 2.19;
% c = 1.3;
receiver_z = attenuationLength/c; % Z position of the ...
receiver (in meters)

b = c * albedo;
a = c - b;
wallAbsorption = 1; % Photons lose half their weight when ...
colliding with a wall

beamDiverg = 0.0015/2; % Half angle divergence at the beam waist

```

```

beamWidth = 0.001;                                % 1.6 mm (half width). Hecht pg. 595

% beamDiverg = 0;
% beamWidth = 0;

rec_pos = [0,0];

sizeRecPos = size(rec_pos);
num_rx = sizeRecPos(1);

rec_aperture = ones(num_rx,1).*0.8;
rec_fov = ones(num_rx,1).* pi./2;

% rec_aperture = [0.0079, 0.0508, 0.0508]; % rec_aperture = ...
%   ones(num_rx,1).*0.0508; % 0.0508 m = 2 inches
% rec_fov = ones(num_rx,1).*0.314159;      % 0.314159 = 18 deg FOV; ; % ...
%   0.0508 m = 2 inches
% rec_fov = [2.27, 0.0785, 0.1745];       % 0.314159 = 18 deg FOV, 2.27 = 130 ...
%   deg, 0.0785 = 5 deg

attenLen = round(receiver_z*c);

scattering_events = ceil((c-a)*receiver_z*7)        %five times the scattering ...
% attenuation length
if scattering_events < 10
    scattering_events = 10;
end

photonDist = 0;          % Array to hold receiver distances of photons from ...
% receiver
photonAngles = 0;
photonWeights = 0;

init_angle = 0;          % Point transmitter at receiver
init_angle2 = 0;         % Point transmitter at receiver

if (strcmp(saveOutput,'true'))
   折りたたみ = sprintf('outputData-%s',datestr(now,'HH-MM-SS_yyyy-mm-dd'));
    mkdir(sprintf('%s/%s',dataDir,foldername));
    fid = fopen(sprintf('%s/%s/whatHere.txt',dataDir,foldername),'w');
    fprintf(fid,'Experiment run on %s \n\r Atten. Length: %d \n\r Rx. dist: ... ...
    %d c: %d a: %d b: %d albedo: %d\n\r Num. photons: %d Num. sims %d',...
    foldername,attenLen,receiver_z,c,a,b,albedo,num_photons,num_sims);

```

```

    save(sprintf('%s/%s/simVariables.mat',dataDir,foldername));
    fclose(fid);
end

total_time = zeros(num_sims,1);
total_rec_power = zeros(num_sims,1);
total_rec_packets = zeros(num_sims,1);
received_location = [];
travel_distance = [];

total_power = zeros(num_rx,1);
total_photons = zeros(num_rx,1);

angleVarSum = zeros(num_rx,1);
angleMean = zeros(num_sims,num_rx);
distVarSum = zeros(num_rx,1);
distMean = zeros(num_sims,num_rx);
weightVarSum = zeros(num_rx,1);
weightMean = zeros(num_sims,num_rx);

allWeights = 0;
allAngles = 0;
allDist = 0;

tStart = tic;

poolSize = 8;
if (matlabpool('size')==0)
    matlabpool('open','local',poolSize)
end

totalPhotonsAtRxPlane = 0;
run_counter = 0;

recPosX = 0;
recPosY = 0;
finalPhotonPos = zeros(1,5);
finalPhotonDist = 0;
finalPhotonWeight = 0;

parfor simcount = 1:num_sims
    %%
    simcount

```

```

[total_time(simcount), ...
total_rec_power, ...
total_rec_packets, ...
rec_loc_final, ...
total_rec_dist, ...
rec_weights] = ...

...
mc_func_r6(num_photons, ...
scattering_events, ...
c, ...
a, ...
receiver_z, ...
cdf_scatter, ...
angle, ...
init_angle, ...
init_angle2, ...
beamDiverg,beamWidth, ...
wallAbsorption);

totalPhotonsAtRxPlane = totalPhotonsAtRxPlane + total_rec_packets;

if (strcmp(saveOutput,'true'))
    parsave(foldername,simcount,dataDir,rec_loc_final, ...
    total_rec_dist,rec_weights);
end
end

% Check to make sure total_photons > 1, otherwise these values below will ...
% be NaN

sim_time = toc(tStart) / 60

if (matlabpool('size')>0)
    %matlabpool close
end

findfigs

sprintf('Simulation on DATE with %d photons, %d scattering events.', ...

```

```

    num_photons*num_sims, scattering_events)
sprintf('C = %d (1/m), A = %d (1/m).',c,a)
% sprintf('Receiver at %d, %d, %d (meters)',receiver_x, receiver_y, receiver_z)
% sprintf('Travel distance delta %d (m). Time of arrival delta %d (sec)', ...
    distance_delta, time_delta)
% sprintf('Time delta between histogram bins: %d (sec), %d (Hz)',T,bandwidth)

beep
beep
beep
beep

if (strcmp(useVCL,'true'))
    cd('K:\MC_data')
    save output.mat
end

filename = sprintf('outputData-%s.mat',datestr(now,'HH-MM-SS_YYYY-mm-dd'));

if (strcmp(ftpData,'true'))
    % zip output data folder
    cd('~/');
    tar(foldername,foldername,'/home/wccox/');
    filename = sprintf('%s.tar',foldername);
    cd('/home/wccox/Dropbox/WCC Research/mc');
    dir = '~/';
    saveDataFTP(filename,dir);
end

if (strcmp(sendEmail,'true'))

    [ret, name] = system('hostname');

    if ret ~= 0,
        if ispc
            name = getenv('COMPUTERNAME');
        else
            name = getenv('HOSTNAME');
        end
    end
    name = lower(name);

    subject = sprintf('Simulation on %s with %d photons, %d scattering ...
events completed.', name, num_photons*num_sims, scattering_events)
body = sprintf('C = %d (1/m), A = %d (1/m). Simulation took %d minutes ...

```

```

    to run.\n Data saved to folder: %s',c,a,sim_time,foldername);\n
    %save output.mat\n\n

% Define these variables appropriately:
mail = 'wccoxresearch@gmail.com'; %Your GMail email address
load password

% Then this code will set up the preferences properly:
setpref('Internet','E_email',mail);
setpref('Internet','SMTP_Server','smtp.gmail.com');
setpref('Internet','SMTP_Username',mail);
setpref('Internet','SMTP_Password',password);
props = java.lang.System.getProperties;
props.setProperty('mail.smtp.auth','true');
props.setProperty('mail.smtp.socketFactory.class', ...
    'javax.net.ssl.SSLSocketFactory');
props.setProperty('mail.smtp.socketFactory.port','465');

% Send the email. Note that the first input is the address you are ...
    sending the email to

sendmail(usersEmail,'Simulation complete',[subject body])
end

```

```

% set up an array for the photons,
% x, y, z, mu_x, mu_y, mu_z, weight, received
% 0, 0, 0, 0 , 0 , 1 , 1 , 1 - initial values
% 1, 2, 3, 4 , 5 , 6 , 7 , 8 - Position
% photon(:,1) == X POSITION
% photon(:,2) == Y POSITION
% photon(:,3) == Z POSITION
% photon(:,4) == ux
% photon(:,5) == uy
% photon(:,6) == uz
% photon(:,7) == WEIGHT
% photon(:,8) == RECEIVED? 1 = No, 0 = Yes (detected), -1 = terminated

% index from origin, 0 theta (angle between x and z), 0 phi (angle between
% x and y) along x-axis

% V5 - change scattering equations. Change direction of propagation to
% z-axis.
% V6 - Lots of changes:

```

```

% - Added size limits to the simulation. Photons terminate when
% encountering boundaries
% - Added unlimited scattering. Scattering is dependant on minimum weight
% - added rouletting to remove photons of low weight
% - added window effects to the receiver
% - changed events to be based on 'c', not 'b'
% - changed how weights are calculated/updated

function [total_time, total_rec_power, total_rec_packets, ...
    rec_loc_final, total_rec_dist, rec_weights] = ...
    mc_func_r6(num_photons, scattering_events, c, a, receiver_z, ...
    cdf_scatter, angle, init_angle, init_angle2, ...
    beamDiverg, beamWidth, wallAbsorption)

useLimits = 'false';
reflection = 0;

rxPlaneLimits = 1; % Use dimension limits on the receiver ...
plane. This reduces the size of the dataset
rxXLimMax = 3; % 3 meters
rxXLimMin = -3;
rxYLimMax = 3;
rxYLimMin = -3;

nAir = 1;
nWater = 1.33;
surfCritAngCos = sqrt(1 - (nAir/nWater)^2); % sine T1 = ...
    nair/nwater sine T3

sizeMult = 1;

zLimMin = 0;

if strcmp(useLimits, 'true')
%     xLimMax = 0.61*sizeMult;
%     xLimMin = -.61*sizeMult;
%     yLimMax = 0.61*sizeMult;
%     yLimMin = -.61*sizeMult;
%     zLimMax = receiver_z;
%     zLimMin = 0;

% Actual tank dimensions from exp in 7_11
xLimMax = 0.61*sizeMult;
xLimMin = -.61*sizeMult;
yLimMax = 0.1905*sizeMult;

```

```

yLimMin = -.5842*sizeMult;
zLimMax = receiver_z;

end

photon = zeros(num_photons,8);
photon(:,7) = ones(num_photons,1); % set weights to one
photon(:,8) = ones(num_photons,1); % set all active
totaldist = zeros(num_photons,1); % record total distance traveled by ...
    each photon
rec_dist = zeros(num_photons,1); % total distance photon traveld at ...
    point of reception
rec_loc = zeros(num_photons,4); % location of the received photon on ...
    the z,y rec. plane
total_rec_packets = 0; % Total number of packets to cross detector
total_rec_power = 0; % Total power to cross detector

prob_of_survival = ((c-a)/c); % b/c
rouletteConst = 10; % 1/rouletteConst determines the ...
    probability of a low power photon surviving
rouletteConst_inv = 1/rouletteConst;
inv_c = 1/c;

if prob_of_survival >= 0.90
    min_power = 1e-4; % minimum power value for photons ...
        before they are terminated by rouletting
    %min_power = 0.5
elseif prob_of_survival >= 0.8299
    min_power = 1e-5;
elseif prob_of_survival >= 0.70
    min_power = 1e-5;
else
    min_power = 1e-7;
end
max_uz = 1-1e-12;

tic;
%
% theta = diverg.*rand(1,num_photons); % uniform rand. dist over ...
    divergence ang.
% phi = (2*pi).*rand(1,num_photons); % uniform rand. dist over ...
    azimuthal angles
%

```

```

% beta = init_angle;    % direction the transmitter is pointing (zenith)
% alpha = init_angle2;      % direction the transmitter is pointing (azimuth)

[photon(:,1),photon(:,2),photon(:,4),photon(:,5),photon(:,6)] = ...
beamProfile(num_photons,beamWidth,beamDiverg,'gaussian');

% % point down z-axis
% photon(:,4) = zeros(num_photons,1);           % x = 0
% photon(:,5) = zeros(num_photons,1);           % y = 0
% photon(:,6) = ones(num_photons,1);            % z = 1
photonsRemaining = num_photons;                 % count down for each photon ...
received/terminated

clear theta phi x y z beta alpha

% for j = 1:scattering_events
while photonsRemaining > 0                      % which is faster? create ...
    random values on the fly??  <- check
    rand_array = rand(num_photons,3);           % generate a matrix for ...
        each photon with rand propagation, roll, and pitch
    rand_array(:,3) = rand_array(:,3).*2.*pi;    % Uniformly distributed ...
        over (0,2Pi)

    % iterate over every single photon to calculate new position and
    % whether it was received or not.
    for i = 1:num_photons

        % if the photon is still active (1 - active, 0 - received, -1 - ...
        terminated
        if (photon(i,8) == 1)

            r = -inv_c*log(rand_array(i,1));       % randomly generate ...
                optical path length

            %Generate scattering angle from beam spread function
            minIndex = 2;
            maxIndex = length(cdf_scatter);
            midIndex = minIndex + ceil((maxIndex - minIndex)/2);

            while rand_array(i,2) ~= cdf_scatter(midIndex) && maxIndex >= ...
                minIndex           % Changed > to >=
                    midIndex = minIndex + ceil((maxIndex - minIndex)/2);
                    if rand_array(i,2) > cdf_scatter(midIndex)
                        minIndex = midIndex + 1;
                    end
                end
            end
        end
    end
end

```

```

elseif rand_array(i,2) < cdf_scatter(midIndex)
    maxIndex = midIndex - 1;
end

end
midIndex = minIndex + ceil((maxIndex - minIndex)/2);
k = midIndex;

theta = angle(k-1) + (rand_array(i,2) - ...
    cdf_scatter(k-1))*(angle(k) - angle(k-1))/(cdf_scatter(k) - ...
    cdf_scatter(k-1)); % Linear interpolation from "angle" vector
phi = rand_array(i,3); % Phi is uniformly distributed over 0-2pi

% find new position increment based on PREVIOUS direction ...
vectors (ux,uy,uz). This
% takes care of the initial condition problem where photons
% were scattered immediately on the first iteration.
x_step = r*photon(i,4); % x step size
y_step = r*photon(i,5); % y step size
z_step = r*photon(i,6); % z step size

% if the photon moves past the receiver plane <- photons that
% should be reflected are not counted properly (i.e. they
% aren't reflected before being received)
if ((photon(i,3) + z_step) >= receiver_z)

    if photon(i,6) ~= 0 % If the photon ...
        has a z-component, mu_z != 0
        % z distance to receiver plane
        z_dist_rec_intersection = receiver_z - photon(i,3); ...
        % Zrec - Zphoton
        % y distance to receiver plane
        y_dist_rec_intersection = ...
        % z_dist_rec_intersection*photon(i,5)/photon(i,6);
        % x distance to receiver plane
        x_dist_rec_intersection = ...
        % z_dist_rec_intersection*photon(i,4)/photon(i,6);
    else
        disp('how can the photon cross the receiver plane when ...
            it''s pointing straight up??');
    end

    % euclidian distance to the reciever plane

```

```

dist_to_rec = z_dist_rec_intersection / photon(i,6);      % z ...
/ mu_z

if rxPlaneLimits == 1                                     % If we're limiting ...
the dimensions of the receiver plane (to reduce the ...
dataset)
if ((photon(i,1) + x_dist_rec_intersection) > rxXLimMax ...
|| (photon(i,1) + x_dist_rec_intersection) < ...
rxXLimMin ...
|| photon(i,2) + y_dist_rec_intersection > ...
rxYLimMax || photon(i,2) + ...
y_dist_rec_intersection < rxYLimMin)    % ...
Photon exceeds the limits
photon(i,8) = -1;                                         % mark ...
as terminated
photonsRemaining = photonsRemaining - 1;      % ...
decrement outstanding photons
continue;                                              % ...
Continue on to the next photon, skipping the ...
code below
end
end

rec_loc(i,1) = photon(i,1) + x_dist_rec_intersection;    % ...
x-axis location of reception
rec_loc(i,2) = photon(i,2) + y_dist_rec_intersection;    % ...
y-axis location of reception
rec_loc(i,3) = photon(i,4);                                % ...
for statistics, should be uniform (mu_x)
rec_loc(i,4) = photon(i,5);                                % ...
for statistics, should be uniform (mu_y)
rec_loc(i,5) = photon(i,6);                                % ...
incident angle, mu_z

total_rec_packets = total_rec_packets + 1;
total_rec_power = total_rec_power + photon(i,7);          % ...
total power at the receiver plane (sum of received photons)

rec_dist(i) = totaldist(i)+ dist_to_rec;                  % ...
individual photon's distance traveled.
photon(i,8) = 0;                                         % ...
mark photon as received
photonsRemaining = photonsRemaining - 1;      % ...
decrement number of outstanding photons

```

```

% update the total distance the photon has traveled
totaldist(i) = totaldist(i) + dist_to_rec;

else % if the photon didn't move into the detector, reduce its ...
      power & move it

photon(i,1) = photon(i,1) + x_step;           % move to new x ...
      position
photon(i,2) = photon(i,2) + y_step;           % move to new y ...
      position
photon(i,3) = photon(i,3) + z_step;           % move to new z ...
      position

% update the total distance the photon has traveled
totaldist(i) = totaldist(i) + r;

if (reflection == 1)                         % Check to make ...
      sure we're using reflection in our simulation (perfect ...
      reflectors)
      % While any of the boundaries are exceeded, reflect
      % around that boundary. Keep doing this till the photon
      % is contained in the boundaries.
      while ((photon(i,1) > xLimMax) || (photon(i,1) < ...
          xLimMin) || (photon(i,2) > yLimMax) || ...
          (photon(i,2) < yLimMin))
          if (photon(i,2) > yLimMax)                   % If ...
              the photon leaves the top of the volume, ...
              reflect downwards

          if (photon(i,5) < surfCritAngCos)        % TOTAL ...
              INTERNAL REFLECTION
              photon(i,5) = -1*photon(i,5);           ...
                  % reflect the light beam by flipping ...
                  the sign of the mu_y vector
              photon(i,2) = yLimMax - (photon(i,2) - ...
                  yLimMax);             % New y_pos is Y-Max - ...
                  (Y_pos - Ymax). Remove the part that ...
                  "sticks out" of the top of the surface.
          else                                % OTHERWISE, Lose power out the top
              % Calculate fresnel loss
              cosExitAng = sqrt(1 - ...
                  (nWater/nAir)^2*(1-photon(i,5)^2));
              rp = (photon(i,5) - ...
                  nWater*cosExitAng)/(photon(i,5) + ...
                  nWater*cosExitAng);    % Thanks to -> ...

```

```

        Small Monte Carlo by Scott Prahl ...
        (http://omlc.ogi.edu)
rs = (cosExitAng - ...
      nWater*photon(i,5))/(cosExitAng + ...
      nWater*photon(i,5));
R = (rp^2 + rs^2)/2; ...

...
% unpolarized reflection coefficient
photon(i,7) = photon(i,7)*R; ...
% Reduce the photon weight

photon(i,5) = -1*photon(i,5); ...
% reflect the light beam by flipping ...
% the sign of the mu_y vector
% X and Z position stay the same
photon(i,2) = yLimMax - (photon(i,2) - ...
yLimMax); % New y_pos is Y-Max - ...
(Y_pos - Ymax). Remove the part that ...
"sticks out" of the top of the surface.
end
elseif (photon(i,2) < yLimMin) % ...
Leaves the bottom of the container
photon(i,5) = -1*photon(i,5); ...
reflect the light beam by flipping the sign ...
of the mu_y vector
photon(i,2) = yLimMin - (photon(i,2) - yLimMin);
photon(i,7) = photon(i,7)*wallAbsorption;
photon(i,8) = -1; ...
%
mark as terminated
photonsRemaining = photonsRemaining - 1; ...
decrement outstanding photons
continue;
end

if (photon(i,1) < xLimMin) % ...
Leaves the side of the container
photon(i,4) = -1*photon(i,4); ...
reflect the light beam by flipping the sign ...
of the mu_x vector
photon(i,1) = xLimMin - (photon(i,1) - xLimMin);
photon(i,7) = photon(i,7)*wallAbsorption;
photon(i,8) = -1; ...
%
mark as terminated
photonsRemaining = photonsRemaining - 1; ...
decrement outstanding photons

```

```

%
    continue;
elseif (photon(i,1) > xLimMax) % ...
    Leaves the side of the container
    photon(i,4) = -1*photon(i,4); % ...
        reflect the light beam by flipping the sign ...
        of the mu_x vector
    photon(i,1) = xLimMax - (photon(i,1) - xLimMax);
    photon(i,7) = photon(i,7)*wallAbsorption;
    photon(i,8) = -1; % ...
%
mark as terminated
photonsRemaining = photonsRemaining - 1; % ...
decrement outstanding photons
%
    continue;
end
end
end

% If the photon collides with the back wall, terminate
if (photon(i,3) < zLimMin)
    photon(i,8) = -1; % mark as ...
        terminated
    photonsRemaining = photonsRemaining - 1; % decrement ...
        outstanding photons
    continue;
else % if the photon is still in the boundaries

    photon(i,7) = photon(i,7)*prob_of_survival; % ...
        reduce weight
    if photon(i,7) < min_power
        if rand() > (rouletteConst_inv) % ...
            if the photon is randomly chosen to be ...
            terminated ...
            photon(i,8) = -1; ...
                % -1 indicates a photon was terminated, but ...
                not received
            photonsRemaining = photonsRemaining - 1; ...
                % decrement outstanding photons
        else % ...
            ... otherwise the photon gets the energy of ...
            terminated photons
            photon(i,7) = photon(i,7)*rouletteConst; % ...
                shift power of terminated photons to new photon
    end
end

```

```

        if abs(photon(i,6)) > max_uz           % if uz ~ 1
            photon(i,4) = sin(theta)*cos(phi);
            photon(i,5) = sin(theta)*sin(phi);
            photon(i,6) = sign(photon(i,6))*cos(theta);
            %disp('mu_z near 1')
        else
            sqrt_uz = sqrt(1 - photon(i,6)^2);
            old_ux = photon(i,4);
            old_uy = photon(i,5);
            old_uz = photon(i,6);
            photon(i,4) = ...
                (sin(theta)/sqrt_uz)*(old_ux*old_uz*cos(phi) - ...
                old_uy*sin(phi)) + old_ux*cos(theta);    % ux
            photon(i,5) = ...
                (sin(theta)/sqrt_uz)*(old_uy*old_uz*cos(phi) + ...
                old_ux*sin(phi)) + old_uy*cos(theta);    % uy
            photon(i,6) = (-sin(theta)*cos(phi))*sqrt_uz + ...
                old_uz*cos(theta); ...
                % uz
        end

        % Normalize the pointing vectors -> ux^2 + uy^2 + uz^2 ...
        = 1^2
        if abs(1 - (photon(i,4)^2 + photon(i,5)^2 + ...
        photon(i,6)^2)) > 1e-11
            normLength = sqrt(photon(i,4)^2 + photon(i,5)^2 + ...
            photon(i,6)^2);
            photon(i,4) = photon(i,4) / normLength;
            photon(i,5) = photon(i,5) / normLength;
            photon(i,6) = photon(i,6) / normLength;
            %disp('Vector normalization wrong!');
        end
    end
end
end
end
end
end

total_time = toc;

% Do this after the loop above, so we can allocate the array once (instead
% of growing dynamically as we receive individual photons - SLOW)
rec_loc_final = ones(total_rec_packets,5);
j = 1;
for i = 1:num_photons                      % iterate over all photons

```

```

if (photon(i,8) == 0)                                % if the photon was received
    rec_loc_final(j,:) = rec_loc(i,:);                % record the receive ...
    location and angles
j = j +1;                                              % increment the number of ...
    received photons
end
end

if ((j-1) ~= total_rec_packets)
    disp('Error! Total received photons doesnt equal j iterator. ');
    disp(sprintf('j = %d and total_rec_packets = %d',j, total_rec_packets));
end

j = 1;
total_rec_dist = zeros(total_rec_packets,1);
rec_weights = zeros(total_rec_packets,1);
total_rec_power = 0;
for i = 1:num_photons
    if (photon(i,8) == 0)
        total_rec_dist(j) = rec_dist(i);            % store the distance ...
        traveled by each photon
        rec_weights(j) = photon(i,7);                % store the weights of ...
        received photons
        j = j + 1;
    end
end

if ((j-1) ~= total_rec_packets)
    disp('Error! Total received distances doesnt equal j iterator');
    disp(sprintf('j = %d and total_rec_packets = %d',j, total_rec_packets));
end

```

```

% standaloneReceiver
% This program reads in stored datafiles of photons on the receiver plane,
% and passes the data to the receiver function for processing. This allows
% the photon movement (to the Rx plane) and the "reception" to be
% separated.
% VERSION 2 - 10/8/11 - Add ability to take histogram of how many times
% photons have scattered. Adds flags to mainfile to control this behavior,
% changes also made to the receiver code.

clear all;clc

if (isunix() && ~ismac())

```

```

    dataDirectory = '/home/wccox/outputData-21-16-31_2011-09-07';
else
    disp('Windows');
    dataDirectory = 'D:\Simulation ...
                    Data\Practice\outputData-16-27-51_2012-03-14';
end

% a = 0.396;
% num_photons = 1e6;
load(sprintf('%s/simVariables.mat',dataDirectory));

file_list = dir(fullfile(dataDirectory,'*outputData*.mat'));

num_sims = size(file_list,1);

% rec_fov = [3;6;18;27;45;90;130;180;3;6;18;27;45;90;130;180].*pi./180;
rec_fov = [1;2;4;8;16;45;90;180;...
            1;2;4;8;16;45;90;180;...
            1;2;4;8;16;45;90;180;...
            1;2;4;8;16;45;90;180 ...
            ].*pi./180;
sizeRecPos = size(rec_fov);
num_rx = sizeRecPos(1);

rec_pos = zeros(num_rx,2);
% rec_aperture = [ones(num_rx/2,1).*0.0508; ones(num_rx/2,1).*0.1016];
rec_aperture = [ones(num_rx/5,1).*0.008;...
                ones(num_rx/5,1).*0.0254;...
                ones(num_rx/5,1).*0.0508;...
                ones(num_rx/5,1).*0.0762;...
                ones(num_rx/5,1).*0.1016];

% rec_fov = 180;
% num_rx = 1;
% rec_pos = [0,0];
% rec_aperture = 0.008;

% rec_fov = 26*pi/180;
% num_rx = 1;
% rec_pos = [0,0];
% rec_aperture = 0.05;

```

```

recordScatEvents = 0;           % Set to 1 in order to record histogram of ...
                                % scattering event count (0 otherwise)
if (recordScatEvents)
    binEdges = [0:100];          % Edges of the bins for the count ...
                                % histogram
    numBins = length(binEdges);   % How many bins?
    scatHistTotal = zeros(num_rx,numBins);   % Histogram for each receiver ...
                                % combination
else
    binEdges = 0;
    numBins = 0;
    %scatHist = 0;
end

recordDistanceHist = 1;
if (recordDistanceHist)
    distBinWidth = 0.0025;        % Bin spacing is 10 mm or ~10GHz bandwidth
    distBinWindow = 2.25;         % Record out to 2 meters from balstic length
    distHistTotal = zeros(num_rx,round(distBinWindow/distBinWidth));
else
    distBinWidth = 0;
    distBinWindow = 0;
end

angleVarSum = zeros(num_rx,1);
angleMean = zeros(num_sims,num_rx);
distVarSum = zeros(num_rx,1);
distMean = zeros(1,num_rx);
weightVarSum = zeros(num_rx,1);
weightMean = zeros(num_sims,num_rx);

total_power = zeros(num_rx,1);
total_photons = zeros(num_rx,1);
total_rec_packets = zeros(num_sims,1);
photonCount = zeros(num_sims,num_rx);

photonDist = 0;
photonAngles = 0;
photonWeights = 0;

tic;
parfor simcount = 1:num_sims
    %%
    simcount
    S = load(sprintf('%s/%s',dataDirectory,file_list(simcount).name));

```

```

%      foldername = S varargin{1}
%      simcount = S varargin{2}
%      dataDirectory = S varargin{3}           <- this changed after 1st ...
data set!
%      rec_loc_final = S varargin{4}
%      total_rec_dist = S varargin{5}
%      rec_weights = S varargin{6}

%===== CODE FOR RECEIVER =====
[power,ph_cnt,angle_mean,angle_var,dist_mean,dist_var,weight_mean,%
 weight_var,reflected,distances,angles,weights,scatHist,distHist] ...
 = mc_rec_r6(a,S varargin{4},S varargin{5},S varargin{6},rec_pos,%
 rec_aperture,rec_fov,num_photons,binEdges,%
 albedo,receiver_z,distBinWidth,distBinWindow);

total_power = total_power + power'; % ...
    Vectorized sum of the weights of received photons (sum received ...
    photons weights over all groupings)
total_photons = total_photons + ph_cnt'; % ...
    Vectorized sum of number of photons
photonCount(simcount,:) = ph_cnt; % Store the ...
    total received photons/detector - used to weight statistics at the end

%      photonDist = [photonDist distances];
%      photonAngles = [photonAngles angles];
%      photonWeights = [photonWeights weights];

% Scattering histogram
if (recordScatEvents)
    scatHistTotal = scatHistTotal + scatHist; % Add the ...
        incremental histogram count to the overall count
end

if (recordDistanceHist)
    distHistTotal = distHistTotal + distHist;
end

% Calculate MEAN and VARIANCE of the ANGLE

angleMean(simcount,:) = angle_mean; % Receiver ...
    angle means for each sub-simulation
angleVarSum = angleVarSum + (ph_cnt' - 1).*angle_var';

```

```

% Calculate MEAN and VARIANCE of the DISTANCE

distMean = distMean + dist_mean.*power;                                % Divide by ...
    the sum of weights (total_power) at end of sim.
distVarSum = distVarSum + (ph_cnt' - 1).*dist_var';

% Calculate MEAN and VARIANCE of the WEIGHT (each sub-simulation has a
% constant number of samples, so that's why the equation is different)

weightMean(simcount,:) = weight_mean;
weightVarSum = weightVarSum + weight_var';

%reflec = reflected/total_rec_packets;

end

time = toc/60

% ====== CALCULATE SOME STATISTICS FROM OUTPUT OF RECEIVER ======
totalMeanAngle = sum(photonCount.*angleMean,1)./total_photons';
% total variance is broken for weighted samples ... too hard to fix. Use
% the histogram of the data to figure it out!
%totalVarAngle = (1./(total_photons'-1)).*(angleVarSum' + ...
    sum(photonCount.* (angleMean - ...
    repmat(totalMeanAngle,size(angleMean,1),1)).^2,1));

totalMeanDist = distMean./total_power';
% total variance is broken for weighted samples ... too hard to fix. Use
% the histogram of the data to figure it out!
%totalVarDist = (1./(total_photons'-1)).*(distVarSum' + ...
    sum(photonCount.* (distMean - ...
    repmat(totalMeanDist,size(distMean,1),1)).^2,1));

totalMeanWeight = sum(weightMean,1)./num_sims;
totalVarWeight = ((num_photons-1)/(num_photons*num_sims - ...
    1)).*weightVarSum' + ((num_photons)/(num_photons*num_sims - ...
    1)).*sum(weightMean - repmat(totalMeanWeight,size(weightMean,1),1),1).^2;

%stdErr = sqrt(totalVarWeight./(num_photons*num_sims));

if (num_rx == 1)
    scatteringNumber = log(photonWeights(2:end))/log(albedo);
end

```

```

disp('total_power/(num_photons*num_sims) = ');
normRxPower = total_power./(num_photons*num_sims) % Total ...
    received power / total transmitted photon packets SHOULD EQUAL ...
    total_mean_weight
%sd_dist = sqrt(totalVarDist);
%total_photons = total_photons';
totalMeanWeight = totalMeanWeight';

```

```

% VERSION LOG
% Rev 1 - first creation, record power and count for each receiver
% Rev 2 - add statistics, mean and variance for power, angle(s)
% Rev 3 - changed receiver plane to x/y instead of y/z - photons move along
% the z-axis now
% Rev 3b/4 - 5/3/11 - added window affects, changed power calculations <- ...
    SIMPLE BASIC, VERIFIED VERSION
% Rev 5 - Added FOV function, which is matched to experimental data ...
    measuring the FOV of the actual receiver.
% Rev 6 - 10/8/11 - SAME AS Rev. 4, but with scattering histogram
% calculations, temporal histogram calcuations, changes to distance
% mean/variance calculations (added bug fix by adding in weight)

function [power,ph_cnt,angle_mean,angle_var,dist_mean,dist_var, ...
weight_mean,weight_var,reflected,distances,angles,weights,scatHist,distHist] ...
= ...
mc_rec_r6(a,rec_loc_final,total_rec_dist,rec_weights,rec_pos,rec_aperture, ...
rec_fov,numTxPhotons,binEdges,albedo,rxDist,distBinWidth,distBinWindow)

sizeRecPos = size(rec_pos);
num_rx = sizeRecPos(1); % total number of receivers

size_num_photons = size(rec_loc_final); % total number of received photons
num_photons = size_num_photons(1);

if distBinWidth > 0 % If we're taking the histogram of distances ...
    traveled
    histDist = 1;
    numDistBins = round(distBinWindow/distBinWidth);
    distHist = zeros(num_rx,numDistBins); % Creat an array for the ...
        distance bins for each receiver

else
    histDist = 0;
    distHist = 0;

```

```

end

numBins = length(binEdges);
if (numBins > 1)
    recScat = 1;
    logAlbedo = log(albedo); % Calculate this once to make ...
        things faster
    scatHist = zeros(num_rx,numBins);
else
    recScat = 0;
    scatHist = 0;
end

ph_cnt = zeros(1,num_rx);
power = zeros(1,num_rx);

angle_mean = zeros(1,num_rx); % weighted mean of the incident angle for ...
    each Rx
angle_var = zeros(1,num_rx); % variance of incident angle for each Rx - ...
    HARD TO CALCULATE for weighted value < SKIP

dist_mean = zeros(1,num_rx); % weighted mean distance traveled for each Rx
dist_var = zeros(1,num_rx); % Variance of dist traveled for each Rx - ...
    HARD TO CALCULATE for weighted value < SKIP

weight_mean = zeros(1,num_rx); % Mean weight for each Rx
weight_var = zeros(1,num_rx); % Variance of weight for each Rx

distances = zeros(1,num_photons); % Distances from photon to 0,0 ...
    point - Initailize to full size, crop at end
angles = zeros(1,num_photons); % Angle of received photon
weights = zeros(1,num_photons); % Weight of received photon

reflected = 0;

% if (num_rx > 1)
%     disp('You need to change how the distance array is stored!');
% end

for i = 1:num_photons % iterate over every photon on ...
    receiver_plane
    ph_x = rec_loc_final(i,1);
    ph_y = rec_loc_final(i,2);
    mu_z = rec_loc_final(i,5);

```

```

for j = 1:num_rx                      % iterate over every receiver
    rx_x = rec_pos(j,1);
    rx_y = rec_pos(j,2);
    radius = rec_aperture(j)/2;          % 1/2 diameter of receiver

    cos_rec_fov = cos(rec_fov(j)/2);      % ...
    cos(fov/2) to compare with photon's incident angle

    distance = sqrt((ph_x-rx_x)^2 + (ph_y-rx_y)^2);        % ...
    Euclidian distance to receiver center

    if ((distance <= radius) && (mu_z >= cos_rec_fov))           % Photon ...
        received
        power(j) = power(j) + rec_weights(i);                     % ...
        Adjust power of received photons
        ph_cnt(j) = ph_cnt(j) + 1;                                % ...
        Increment number of received photons
        ph_dist = total_rec_dist(i);

        if histDist
            distBinNum = floor((ph_dist - rxDist) / distBinWidth); ... % ...
            % Partition the distances past the ballistic distance into ...
            bins of distBinWidth
            if (distBinNum < numDistBins)
                distHist(j,distBinNum+1) = distHist(j,distBinNum+1) + ... % ...
                rec_weights(i);   % Add the received weight into the ...
                appropriate bin
            else
                % Something screwed up here ...
                ph_dist;
                rec_weights(i);
            end
        end
    end

    angle_delta = rec_weights(i)*(rec_loc_final(i,5) - angle_mean(j));
    dist_delta = rec_weights(i)*(ph_dist - dist_mean(j));          % ...
    Distance times weight
    weight_delta = rec_weights(i) - weight_mean(j);

    %distWeightSum(j) = distWeightSum(j) + rec_weights(i)

    if recScat                         % Record ...
        the scattering event histogram

```

```

scatEventNum = round(log(rec_weights(i))/logAlbedo);      % ...
    This should be an integer
if (scatEventNum < binEdges(end))
    scatHist(j,scatEventNum+1) = scatHist(j,scatEventNum+1) + ...
        1;  % Increment bin count for this number of scattering ...
        events
else
    scatHist(j,end) = scatHist(j,end) + 1;
end
end

% if j == 1
%     weights(ph_cnt(j)) = rec_weights(i);
%     angles(ph_cnt(j)) = rec_loc_final(i,5);
%     distances(ph_cnt(j)) = ph_dist;
% end

% Record stats on incident angle
angle_mean(j) = angle_mean(j) + (angle_delta) / power(j);    % ...
    MODIFIED FOR WEIGHTED AVERAGE!!!!!! - E'[uz] = E[uz] + (uz - ...
    E[uz]) / N+1 - See Knuth's Art of Comp. Programming & ...
    http://en.wikipedia.org/wiki/Algorithms_for_calculating_variance
% Record stats on distance traveled
dist_mean(j) = dist_mean(j) + (dist_delta) / power(j);          % ...
    MODIFIED FOR WEIGHTED AVERAGE!!!!!!
% Record stats on photon weight
weight_mean(j) = weight_mean(j) + (weight_delta)/ph_cnt(j);    ...
    % E'[D] = E[D] + (D - E[D]) / N+1

    % Calculating weighted variance isn't this simple. DON'T USE
    % THIS CODE! Weighted variance is tricky to calculate.
%angle_var(j) = angle_var(j) + angle_delta*(rec_loc_final(i,5) - ...
    angle_mean(j));    % Var[uz] = 1/N-1 * (Var[uz] + (uz - ...
    E[uz]_N-1)(uz - E[uz]_N))
%dist_var(j) = dist_var(j) + dist_delta*(rec_weights(i)*ph_dist - ...
    dist_mean(j));
weight_var(j) = weight_var(j) + weight_delta*(rec_weights(i) - ...
    weight_mean(j));

    if (num_rx == 1)
        distances(ph_cnt(j)) = distance;
        angles(ph_cnt(j)) = mu_z;
        weights(ph_cnt(j)) = rec_weights(i);
    end
end

```

```

    end
end

for j = 1:num_rx

    if (num_rx == 1)
        distances = distances(1:ph_cnt(j));
        angles = angles(1:ph_cnt(j));
        weights = weights(1:ph_cnt(j));
    end

    weight_var(j) = (weight_var(j) + ...
        weight_mean(j).^2*(ph_cnt(j).* (numTxPhotons - ...
            ph_cnt(j))/numTxPhotons)) / (numTxPhotons - 1);
    weight_mean(j) = ph_cnt(j)*weight_mean(j) / numTxPhotons;

    % if weight_mean(j) ~= power(j)/numTxPhotons
    %     disp('Problem counting up the weight mean');
    %     weight_mean(j) = power(j)/numTxPhotons
    %     weight_mean(j)
    %     power(j)
    % end

    % if ph_cnt(j) > 1
    %     angle_var(j) = (1./(ph_cnt(j)-1)).*angle_var(j);
    %     dist_var(j) = (1./(ph_cnt(j)-1)).*dist_var(j);
    % end

    %
    % if isnan(angle_var(j))
    %     disp('angle_var(j) is NaN (in correction loop)');
    % end
    % if isnan(dist_var(j))
    %     disp('dist_var(j) is NaN (in correction loop)');
    % end
    % if isnan(weight_var(j))
    %     disp('weight_var(j) is NaN (in correction loop)');
    % end
    % if isinf(angle_var(j))
    %     disp('angle_var(j) is Inf');
    % end
    % if isinf(dist_var(j))
    %     disp('dist_var(j) is Inf');
    % end

```

```
%      if isinf(weight_var(j))
%          disp('weight_var(j) is Inf');
%      end

end

%dist_mean.*ph_cnt - power
```